
# Technique Development for Investigation of Axisymmetric Graphite Sample Oxidation in Hypersonic Flow

A Thesis submitted by

Daniel Odion Iyinomen, BEng, M.Sc

For the award of

**Doctor of Philosophy**

2019

# Abstract

Characteristics of graphite performance in a hypersonic blunt-body flow have been assessed experimentally and through simulation to determine mass loss. A 50 mm diameter graphite disc was heated from the downstream side with a plasma to approximately 2500 K, and then exposed to a cold Mach 4.5 flow. The disc was mounted on an experimental probe which was very similar to the European standard probe, normal to the flow. Surface temperatures were measured in the experiment using a correlation of the red pixel count of a high-speed camera, calibrated with a spectrometer.

The analysis shows that numerical simulation of the oxidation rate produced results that were within 50% of the mass loss measurements. Simulations indicate that oxidation through surface reactions producing CO was the major contributor to the ablation losses. Analysis involving comparisons between the experiments and simulations suggests that mechanical actions of the ablation process are only minor contributors to mass loss. The experiments show a significant spatial variation in thickness loss for the graphite test material over the disc radius though the spatial variation was still largely axisymmetric.

A new technique for preheating axisymmetric samples of heat shield material has been demonstrated through this work. Future applications for the technique are expected to be found in expansion tube facilities that can simulate the true flow energy under re-entry conditions.

# Certification of Thesis

This thesis is entirely the work of Daniel Odion Iyinomen except where otherwise acknowledged. The work is original and has not previously been submitted for any other award, except where acknowledged.

Student and supervisors signatures of endorsement are held at the University.

Daniel Odion Iyinomen

Principal Supervisor: Professor David Buttsworth

Associate Supervisor: Dr Ray Malpress

# Acknowledgments

I would like to acknowledge my Principal Supervisor Professor David Buttsworth for his technical support during my candidature. I thank him for pointing me in the right direction and for his contribution to my writing and overall learning during my candidature.

Many thanks also go to my Assistant Supervisor Dr Ray Malpress for his work and expertise to ensure the successful completion of the experiments. His contributions to my learning of data acquisition techniques, data analysis techniques and thesis writing were significant.

I also thank other friends at the University of Southern Queensland (USQ) including Dr Rishabh Choudhury for the MATLAB tutorials, Dr Mengmeng Zhao for the LaTEX basics, Byrenn Birch for computer software advice, and Brian Lenske and other technical staff for support for the experiments. I would also like to mention colleagues at the University of Queensland (UQ) including Dr Steven Lewis, Rory Kelly, and Ranjith Ravichandran for information about the spectrometer and the Princeton Instruments that assisted my experimental campaign.

Most importantly, I thank my lovely mother (Mrs Deborah Iyinomen), my beautiful wife (Love Daniel Udaze), and my lovely children for their heavy financial supports and tolerance over the years.

Daniel Odion Iyinomen

*February 2019*

# Contents

# List of Figures

# List of Tables

# Notation

## Symbols

| | |
|---|---|
| $A_r$ | pre-exponential constant in Arrhenius equation |
| $E_a$ | activation energy in Arrhenius |
| $\epsilon$ | emissivity |
| $k_f$ | forward rate of reaction |
| $k_b$ | backward rate of reaction |
| $M$ | Mach number |
| $n$ | temperature exponent in Arrhenius equation; mole fraction |
| $\rho$ | density |
| $R_a$ | surface roughness (arithmetic average) |
| $t$ | time |
| $T$ | temperature |
| $\Delta t$ | exposure time |
| $\mu$ | viscosity |
| $\gamma$ | specific heat ratio, $c_p/c_v$ |
| $\delta$ | boundary layer thickness |
| $\lambda$ | wavelength |
| $\sigma$ | Stefan-Boltzmann constant |

# Acronyms & Abbreviations

| | |
|---|---|
| ACHF | Alternating Current High Frequency |
| CCD | Charge Coupled Device |
| CFD | Computational Fluid Dynamics |
| CTE | Coefficient of Thermal Expansion |
| DCPR | Direct Current Reverse Polarity |
| DCSP | Direct Current Straight Polarity |
| FEA | Finite Element analysis |
| GTAW | Gas Tungsten Arc Welding |
| ICCD | Intensified Charge Coupled Device |
| NASA | National Aeronautics and Space Administration |
| PICA | Phenolic Impregnated Carbon Ablator |
| SIRCA | Silicon Impregnated Reusable Ceramic Ablator |
| TIG | Tungsten Inert Gas |
| TUSQ | Tunnel at the University of Southern Queensland |
| UQ | University of Queensland |
| USQ | University of Southern Queensland |

# Chapter 1

# Introduction

## 1.1 Aerospace Heat Shields

Reliable heat shielding is essential for aerospace vehicles travelling through terrestrial and extra-terrestrial atmospheres. This is because the high speeds of such vehicles generate local temperatures within the atmosphere which are well beyond the survivable, steady-state limit of most materials. For example, vehicle speeds of 11 km/s or higher will occur for spacecraft returning to Earth after visiting other planetary bodies, and within the shock layer around such spacecraft, stagnation temperature above 10,000 K will be reached during atmospheric re-entry (Porter, 2007). Because of the proximity of these hot gases to the vehicle, the rate of heat transfer to the vehicle will typically be high – for example, in the case of the Stardust capsule re-entry, a peak of around 11 $MW/m^2$ at 62 km altitude occurred (Eswein, Herdrich, Fasoulas and Röser, 2011). Unless spacecraft are fitted with carefully designed heat shields, the temperature of the vehicle structure will rapidly increase to values beyond its viable limit.

The physical processes that are present within the shock layer of a typical aerospace vehicle involve complex interactions which have a strong influence on the heat transfer to the vehicle. An illustration of some of the key processes associated with atmospheric entry vehicles is presented in Figure 1.1 (Potter, 2011).

For aerospace vehicles that travel within Earth's atmosphere at sub-orbital velocities (values less than about 8 km/s) the shock layer temperature will be sufficient to cause some dissociation of molecular oxygen ($O_2 \longrightarrow 2O$) if the speed is greater than about 2 km/s. If the speed is greater than about 4 km/s, then dissociation of the molecular oxygen will be almost complete, depending on the altitude, and some dissociation of molecular nitrogen ($N_2 \longrightarrow 2N$) can commence. For super-orbital velocities (values exceeding 9 km/s), almost complete dissociation of molecular nitrogen is likely and ionisation of the gas commences. At sub-orbital speeds, the dominant mechanism for heat transfer from the hot gases to the vehicle is convection, but for super-orbital speeds, radiation heat transfer from the gas to the vehicle can also make a significant contribution.

Different heat shield materials including C-C composite and Ultra-High Temperature Ceramics (UHTC) are used for nose-tip and wing leading edge components of aerospace vehicles (Marschall and Fletcher, 2010). Materials such as Avcoat, Phenolic Impregnated Carbon Ablator (PICA) and Silicone Impregnated Reusable Ceramic Ablator (SIRCA) are often used for super-orbital missions (Venkatapathy and Reuther, 2008). Heat shields consisting of carbon-based surface-ablating materials enable heat removal from the vehicle via mass loss processes associated with oxidation, nitridation, and sublimation (Bianchi, Nasuti, Paciorri and Onofri, 2013). For charring ablators like the matrix material of NASA's Phenolic Impregnated Carbon Ablator (PICA), reactions do not occur at the surface of the material but within a thin layer near the surface (Panerai, Mansour, Lachaud and Martin, 2014). The ejection of pyrolysis species from the surface into the boundary layer causes a reduction of the heat-flux (Martin and Boyd, 2015) thus increasing the efficiency of PICA relative to non-pyrolysing ablators. Pyrolysis blowing results in high porosity of heat shield material and enables oxygen diffusion into the porous layer, continuously causing in-depth oxidation and mass removal (Lachaud, Cozmuta and Mansour, 2010).

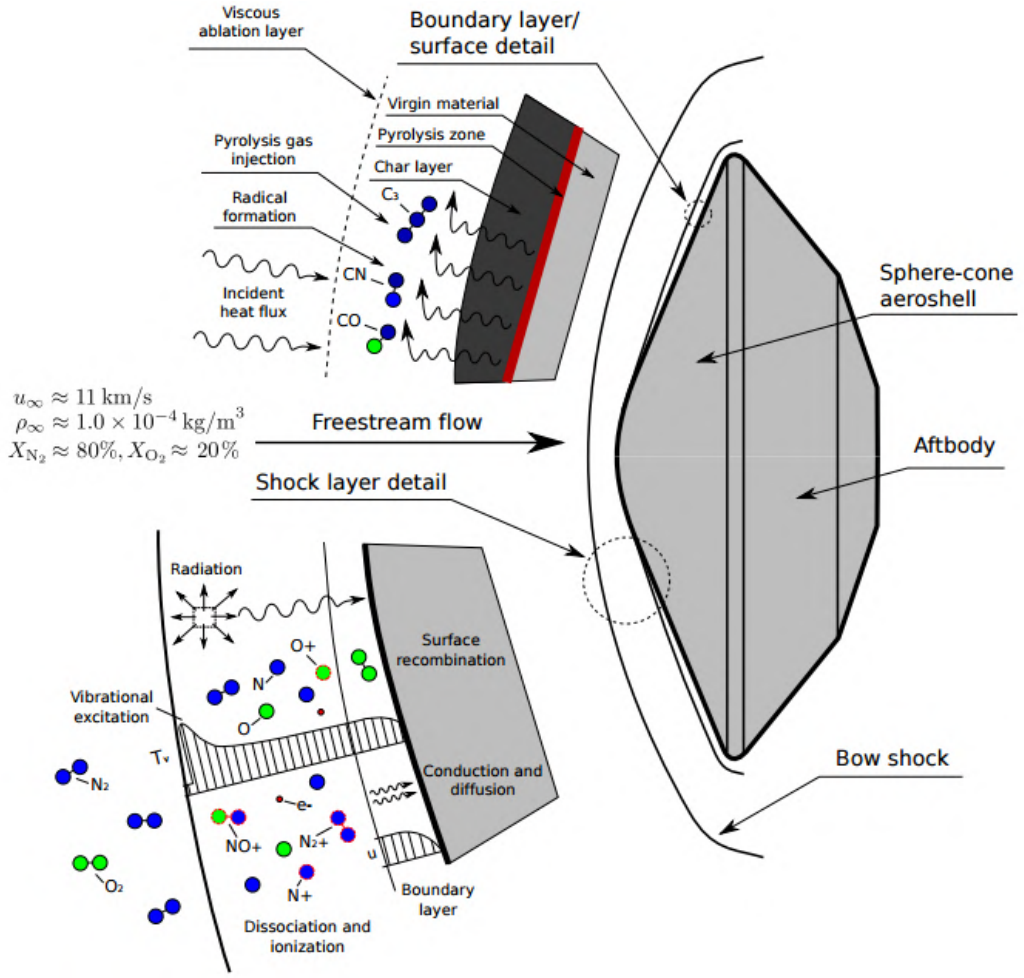


Figure 1.1: An illustration of thermochemical processes associated with a heat shield on a super-orbital vehicle (Potter, 2011).

## 1.2 Status of Other Contributions

Successful operation of heat shields for almost half a century does not mean they are optimally configured or that improvements cannot be made. Heat shields are typically over-designed to ensure vehicle integrity, but because of such design, missions objectives and potential outcomes are constrained because of the weight penalty. New heat shield configurations are subjected to extensive analysis, typically using models of the relevant physics in computational simulation tools. However, there remain significant uncertainties in the fundamental ablation models (Eswein et al., 2011).

Before a new heat shield material is certified for use, it typically undergoes extensive testing in plasma wind tunnels. However, plasma wind tunnels do not normally generate a hypersonic flow, and so the coupling between the shock layer and the ablating heat shield is not correctly simulated. Short duration shock tunnel testing with pre-heated samples has been used in an effort to physically simulate the coupling between the shock layer and the ablating heat shield. However, models used to date have not been axisymmetric, leading to complexities in the experimental analysis of results and the computational simulation of the flows.

## 1.3 Objectives and Overview

This thesis makes contributions primarily in the area of experimentation with heat shield materials by developing a new pre-heating method, suitable for testing axisymmetric models in short duration hypersonic wind tunnels.

The present work was motivated by the goal of quantifying ablation in short duration hypersonic wind tunnels which can simulate the coupling between the shock layer and the ablating heat shield. It is anticipated that such data will be used in the development and validation of models needed for the computational simulation of heat shield performance.

For the purpose of developing the measurement technique and demonstrating its viability through the production of some initial data sets that may be used for model validation, graphite material has been selected as a simple, low-cost, heat shield-like material.

Although the axi-symmetric model pre-heating technique may ultimately find application in impulse facilities, for the purpose of developing and demonstrating the technique, a much lower-energy hypersonic wind tunnel has been used in the present work. Impulse facilities, such as expansion tunnels, can most closely simulate the high-energy hypersonic flow conditions associated with super-orbital atmospheric entry. The experiments in the current work were performed in a Mach 4.5 flow produced using the TUSQ Ludwieg tube facility in the atmospheric blow-down configuration.

Measurements of the temperature distribution across the graphite were achieved, and a technique for identification of the material mass loss rate was also introduced. Computational simulation of the graphite samples in the hypersonic flow has also been performed to assess the capability to simulate the measured local mass loss rates in the hypersonic flow.

## 1.4 Thesis Overview

This present work comprises of seven chapters, inclusive of this introductory chapter. An outline of the work is provided at the beginning of each chapter while the main outcomes of the work are summarised at the end of each chapter.

**Chapter 2** outlines the literature relevant to the present work with hot graphite surfaces. A brief review of ablation models are provided including the various ablation stages associated with graphite combustion.

**Chapter 3** outlines the physical model development and the thermal heating of the graphite model. Temperature measurement techniques are described, and temperature profiles for the graphite samples for different plasma heating arrangements have been analysed.

**Chapter 4** presents the experimental results. The methods used in the experiments include the weighed mass loss technique and the volume-based method. To better understand the results, further measuring tools such as a measuring arm, a laser beam technique, and a Scanning Electron Microscope (SEM) were used to generate data. All the experimental data from the experiments are given in this chapter.

**Chapter 5** presents the CFD simulation results for the reacting stagnation region boundary layer and provides a calculation of the mass loss rate from the carbon surface.

**Chapter 6** investigates the results by analysing the influences of the various methods used to assess the material loss in the experiments. The information used as inputs for the simulations and the results from the simulations are explored; in particular, the

comparison between experimental results and simulation results are presented. Sensitivities to the various characteristics of the experiments and simulations are considered.

**Chapter 7** concludes the thesis by summarising the main findings of the present study and makes recommendations for future work. The experimental concerns, critique of the outcomes from the present work, assessments of the implications and research significance are presented.

# Chapter 2

# Literature Review

## 2.1 Introduction

This chapter discusses literature around the thermal behaviour of graphite materials, flow fields, and boundary layer conditions relating to heat shields and hot graphite models. Various techniques used in the development of heat shields are explored. The chemistry associated with ablation, and the various mechanical actions that effect the performance of heat shield are reviewed. Aspects of the techniques used for simulation are discussed.

## 2.2 Wind Tunnel Experiments on Heat Shields

### 2.2.1 Plasma Wind Tunnels

Plasma wind tunnels are high enthalpy facilities which do not require any pre-heating of models because they produce long duration high temperature flows as shown in Figure 2.1. A plasma wind tunnel uses an Inductively Coupled Plasma (ICP) such as the Plasmatron facility at the von Karman Institute (VKI) for Fluid Dynamics, Belgium. This facility is just one of many high enthalpy facilities currently being used by aerospace researchers to carry out heat shield studies.

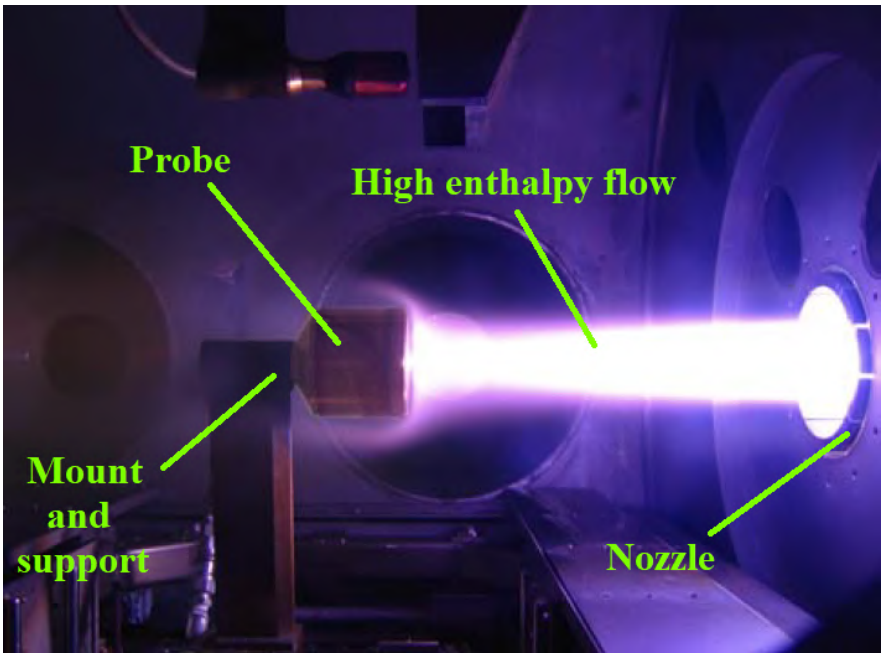


Figure 2.1: A typical experimental probe in the high enthalpy flow of the Plasmatron at von Karman Institute, Belgium (Chazot, 2006).

Plasma wind tunnels are not normally hypersonic and cannot generally produce true hypersonic shock layers. Typically, they produce only subsonic (Monteverde, Savino, Fumo and Di Maso, 2010) or supersonic flows (Savino, Fumo, Paterna, Di Maso and Monteverde, 2010) in durations measured in seconds or minutes (Luo, Wang, Liu, Duan, Wang and Lu, 2016). They go a long way to matching the correct flow enthalpy for hypersonic flight and they can achieve the correct heat flux as well by focussing on the subsonic stagnation region.

Figure 2.2 shows an experiment using a hemispherical heat shield specimen with a diameter of 50 mm and a length of 45 mm at the von Karman Institute (VKI). Figure 2.3 shows a Standard European probe used for re-entry studies at Institute of Space Systems (IRS). A drawing of the required water cooling system of the probe used in such facilities is also illustrated.

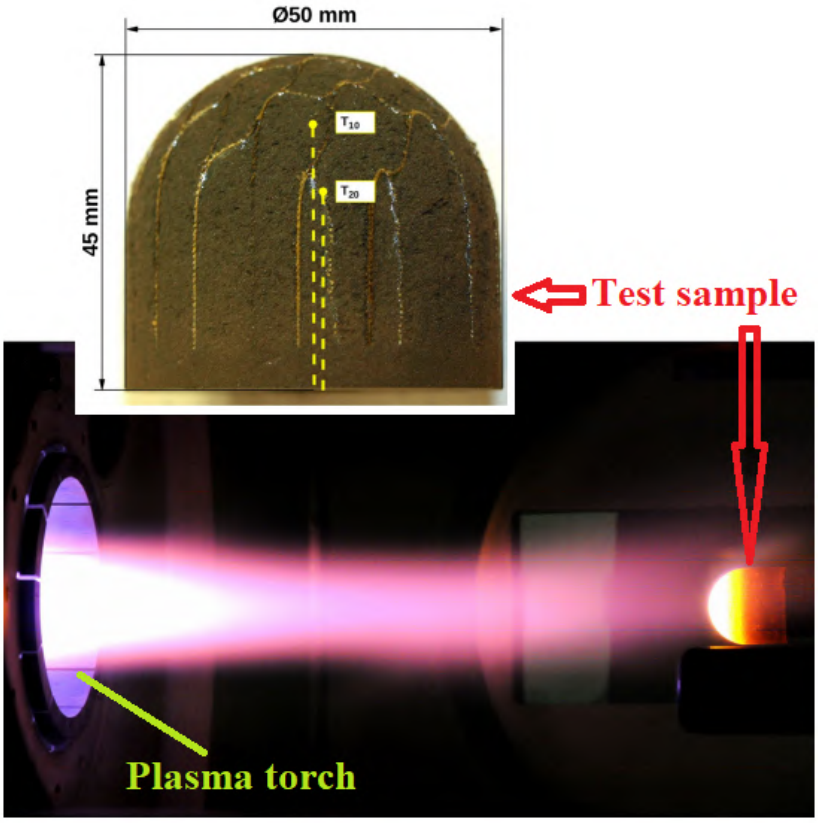


Figure 2.2: Ablation testing of a carbon composite at 1 MW/m$^2$ and 1.5 kPa (Helber et al., 2014).

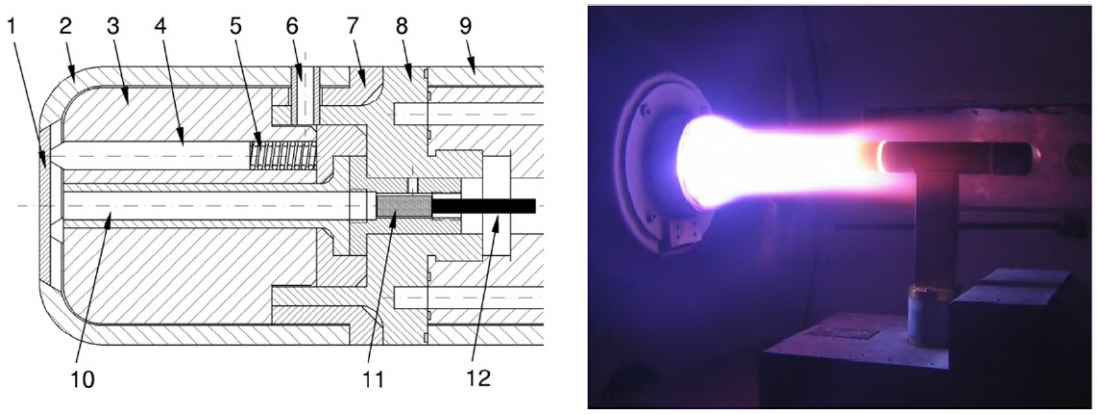


Figure 2.3: Drawing of water cooling system for probes used in high enthalpy facilities: (1) Material sample, (2) Ceramic cap, (3) Isolator foam, (4) Sample holding sticks, (5) Compression springs, (6) Ceramic fixation, (7) Isolator foam, (8) Water-cooled metallic adapter, (9) Water-cooled probe casing, (10) Ceramic tube allowing optical access to sample rear side, (11) Optic-fibre head and collimation lens, and (12) Optic-fibre. Institute of Space Systems (IRS) material probe in operation (Massuti-Ballester et al., 2015).

Figure 2.4 shows details of the arrangement used in a high-enthalpy air flow experiment at the Institute of Space Systems (IRS) plasma wind tunnel facilities. The material sample is a carbon-based cylindrical shape with a diameter of 39.8 mm and a length of 40 mm which was concentrically glued to a circular aluminium back plate (Pagan et al., 2017). Mach numbers of 1.26, 0.73 and 0.82 were used during the test at local enthalpies of 62 MJ/kg, 114 MJ/kg and 220 MJ/kg respectively.

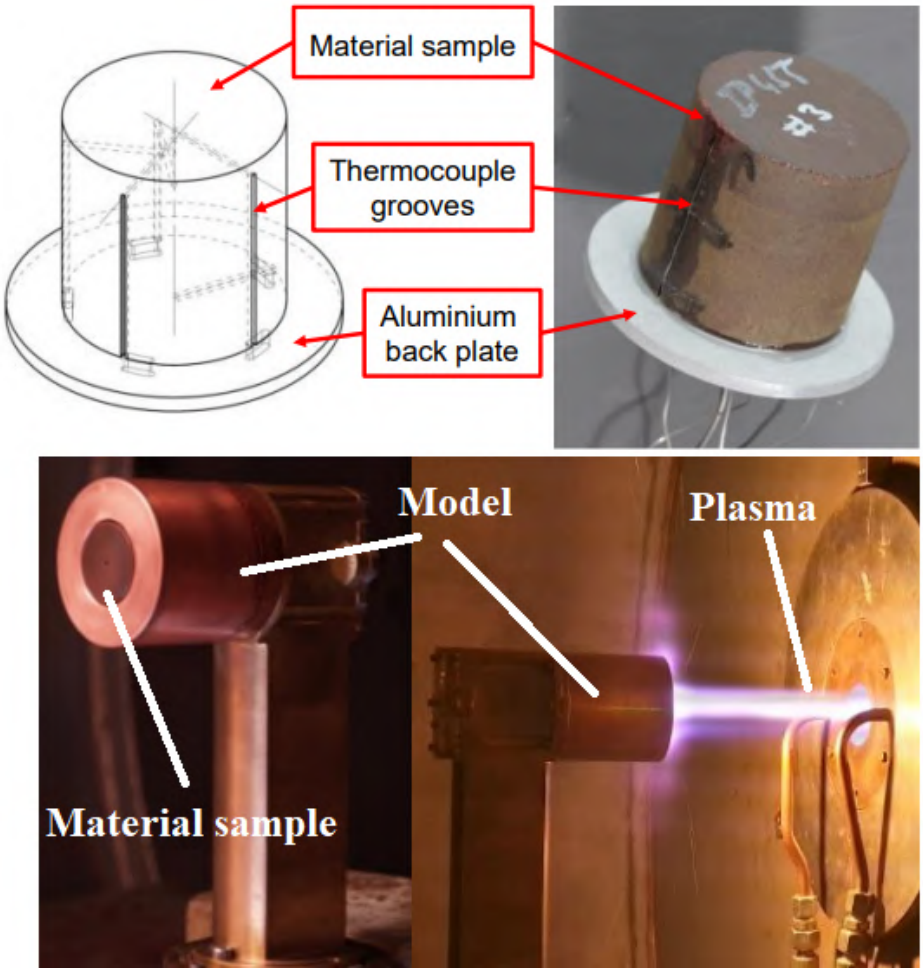


Figure 2.4: A cylindrical specimen in a high-enthalpy air flow facility (Pagan et al., 2017).

### 2.2.2 Electrical Pre-heating Methods

Shock and expansion tunnels (Mirels, 1964) do produce hypersonic shock layers (Erdos, Bakos, Castrogiovanni and Rogers, 1997) and can match the flow enthalpies for re-entry, but in the case of expansion tubes, they produce very short durations of flow up to

a few hundred microseconds (Miller, 1978). This makes it very difficult to quantify flow properties in such facilities. Impulse facilities have the ability to get shock layer characteristics correct, but they cannot undertake ablation work if cold-walled models are used. Unlike high enthalpy plasma facilities, which do not require any pre-heating of the model, the shock and expansion tubes do because of the very short flow durations. Presented here is a review of carbon-based pre-heating methods used in short duration wind tunnels.

Experiments with electrically pre-heated graphite samples have been conducted in the University of Queensland's X2 expansion tunnel, where air was used to study the surface ablation for Earth re-entry flow, as shown in Figure 2.5. The testing used a graphite specimen 10 mm high and 75 mm long. The surface temperature reached approximately 2500 K, when resistively heated by a 250 A.

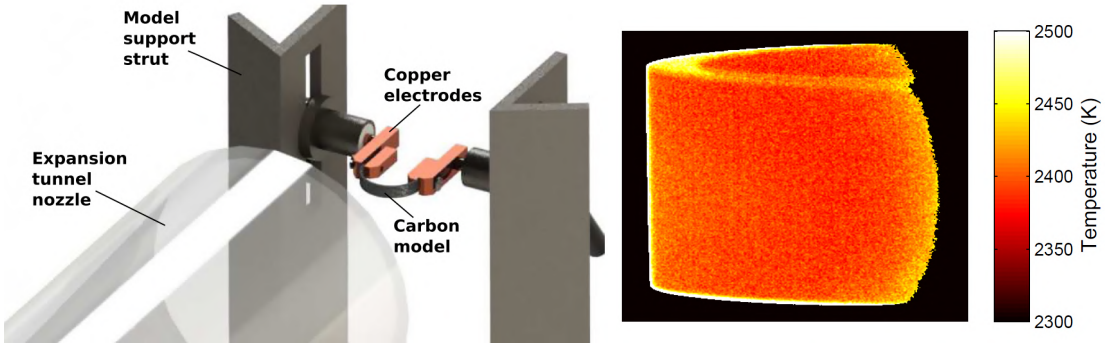


(a) Graphite sample and clamps. (b) Model temperature.

Figure 2.5: Pre-heating arrangements of a graphite model (Zander et al., 2012).

Copper was used for the electrodes at the contact regions because it has a very low electrical resistance, which allowed a high-efficiency energy transfer to the test model. Electrical insulation support structures capable of withstanding the temperature rises created in the sample and thermally conducted through the electrodes, were used to isolate the model mounts from the test-section. Figure 2.6 shows some failures that resulted from the electrical pre-heating method; highlighting some disadvantages of the technique.

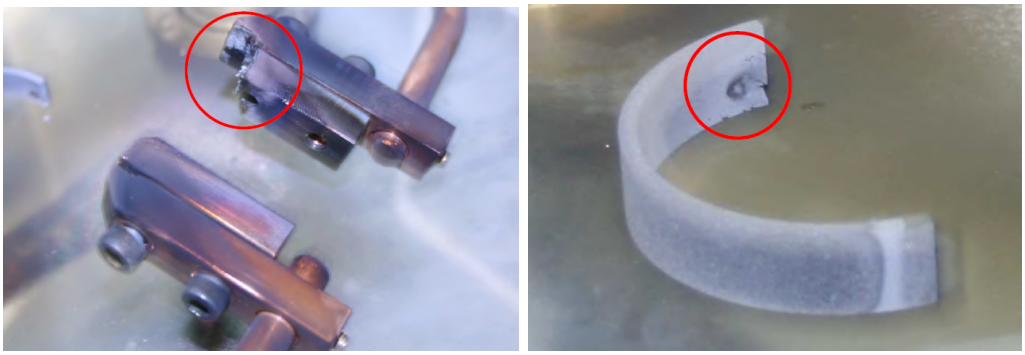

(a) Melted electrode due to arcing. (b) Damaged specimen due to arcing.

Figure 2.6: Arcing problems associated with the arrangement of Figure 2.5 (Lewis, 2017).

Figure 2.7 shows the hot-wall technique used in the past to heat a rectangular graphite plate in the short duration hypersonic wind tunnel, TUSQ. The test sample at the top surface was a 120 mm long graphite plate that used a 700 A power supply to resistively heat to a maximum temperature of about 2000 K (Vennik et al., 2017). The plate was mounted between forward and rear jaws made from 96 % alumina that acted as electrical and thermal insulators. Electrical contact to the plate was via tungsten electrodes between the carbon plate and the alumina jaws.

Due to the strong influence of surface temperatures on boundary layer species, the surface temperature profile needs to be well established. Previous pre-heating techniques in shock and expansion tunnels and in the hypersonic tunnel TUSQ have used resistive heating techniques utilising current passing longitudinally through a graphite element. This method restricts the samples' shape and orientation to arrangements that allow electrical connections at the ends of uniform width profiles. Pre-heating probe models with axisymmetric test specimens is not possible with this technique as will be demonstrated in Section 3.2.2. An alternative heating technique is needed to allow for an appropriate axisymmetric heating profile to allow for effective analysis of experiments using axisymmetric preheated models.

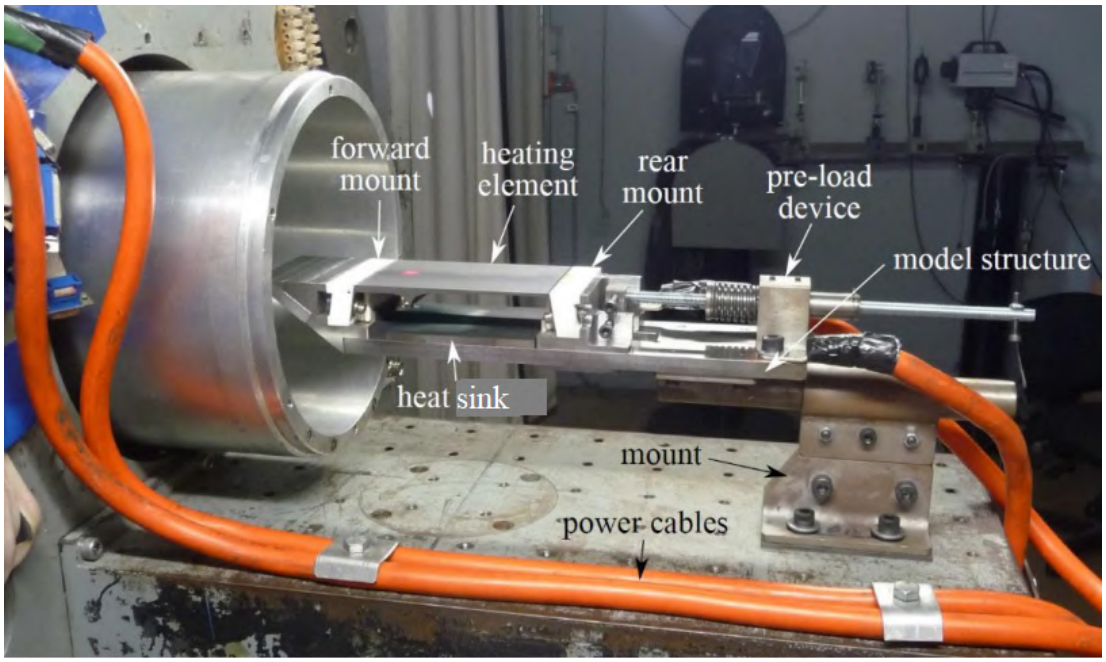


Figure 2.7: Heated model installed in the test section of TUSQ (Vennik et al., 2017).

## 2.3 Models for Carbon Surface Chemistry

### 2.3.1 Overview

Modelling of carbon ablation remains a central issue for accurate predictions of carbon based heat shield performance. For graphite test samples, the grade and properties have a significant influence on the over-all oxidation rate (Scala, 1962). The environmental conditions like pressure, temperature, flow velocity, gas mixture composition, and geometry of the model also play significant roles in determining graphite oxidation rates (Xiaowei, Jean-Charles and Suyuan, 2004).

Figure 2.8 reveals the changes at effectively steady state condition, in mass transfer regimes of graphite at hypersonic flight speeds as temperature increases from zero to 5500 K (Gilbert and Scala, 1965). The first phase was the reaction controlled oxidation regime (450 - 1100 K), followed by transition regime (1100 - 1450 K), followed by diffusion controlled oxidation regime (1450 - 2450 K), followed by sublimation regime (2450 - 3400 K) and finally changes on further heating to a condition where the vapour

pressure exceeds stagnation pressure (above 3400 K).

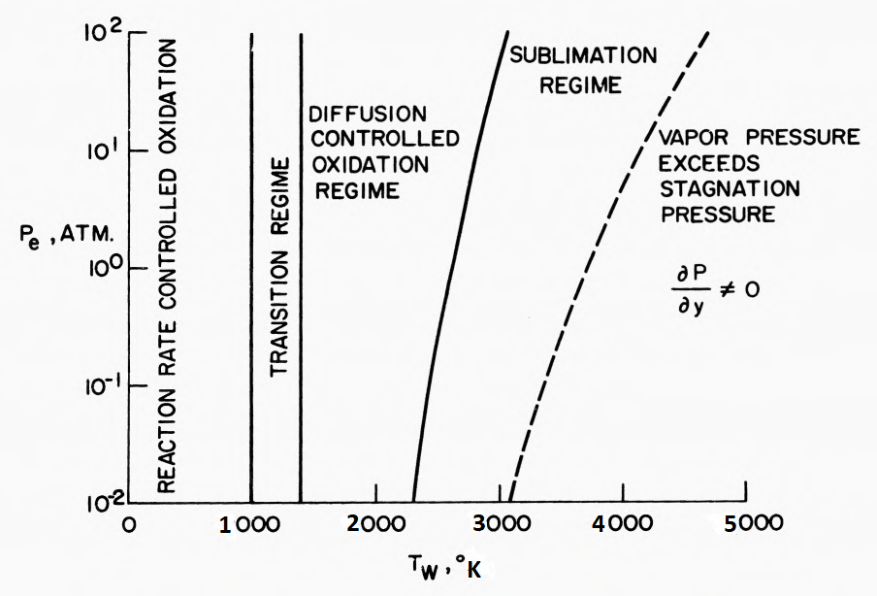


Figure 2.8: Reaction regimes of graphite (Gilbert and Scala, 1965).

The mass loss rate during a graphite ablation process is complex though graphite remains a very simple material with carbon being the only component. There are difficulties in deducing ablation rate data from an overall mass burning rate of graphite (Chelliah et al., 1996) because the overall effect does not explain the contribution of the individual regimes identified in Figure 2.8. Figure 2.9 gives an overview of the normalised surface mass flux of a graphite material across all ablation regimes. It shows that oxidation is dominant at temperatures below 2000 K, saturation occurs between 2000 K and 3000 K, and sublimation becomes dominant above 3000 K.

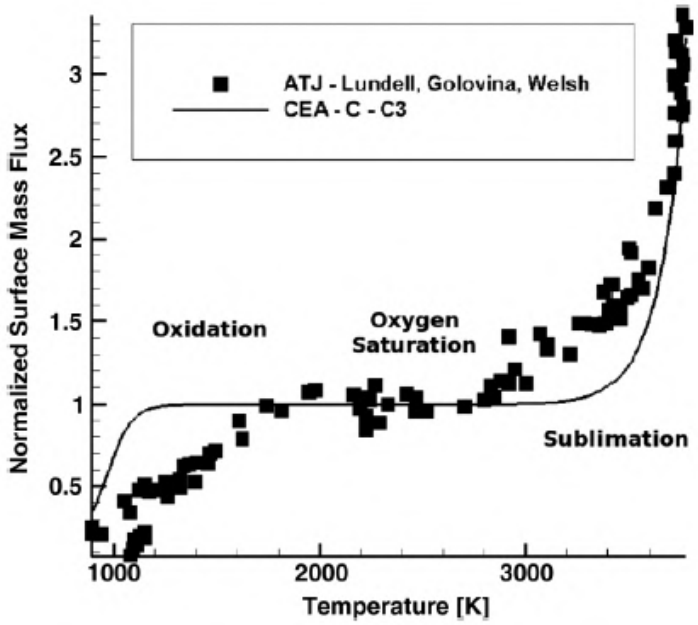


Figure 2.9: Graphite ablation from experiments at 1 atm (Gosse et al., 2012).

### 2.3.2 Oxidation

#### 2.3.2.1 Surface Oxidation

Through the process of species diffusion, the carbon monoxide resulting from surface oxidation, is moved into the neighbouring gaseous domain where it mixes and reacts with oxygen to produce carbon dioxide ($CO_2$) as illustrated in Figure 2.10. The wall interaction and the gas interaction become coupled when the $CO_2$ in the gas phase diffuses back to the wall to react with carbon surface to form additional CO.

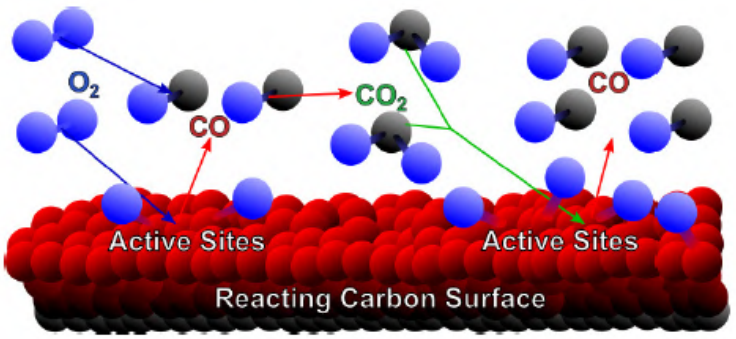


Figure 2.10: Reaction of hot graphite surface in air (Johnson and Chelliah, 2013).

The hot surface is usually exposed to oxidation, nitridation (at high enough temperature), phase changes (melting and sublimation), thermal action (heat flux), gas-surface interactions (surface catalysis and ablation) and mechanical actions (surface erosion and spallation), leading to radiation/convection/material coupling within the boundary layer. The transport phenomenon is affected by flow field, temperature and temperature gradient, pressure and pressure gradient and species concentration and concentration gradients.

The chemistry of carbon oxidation is complex (Shaddix, Holzleithner, Geier and Haynes, 2013). There is a coupling of surface recession (Scala, 1962), particle residence time (Zeng and Fu, 1996), pressure, temperature (Hayhurst and Parmar, 1998), laminar/turbulent/transition, and thermal energy balance (Zeng and Fu, 1996). There is a general agreement that CO production becomes dominant at high temperatures (Allouis, Esposito, Salatino, Savino and Senneca, 2014) which suggests combustion stoichiometry of $C + O_2 \underset{k_b}{\overset{k_f}{\rightleftharpoons}} CO + O$ changes to the forward reaction to produce more CO above $1700^0$C (Miller and Sutton, 1966).

#### 2.3.2.2 Oxidation of Hot Graphite Rod

A study of the combustion of hot carbon surfaces a using graphite rod revealed that water content in the flow can be an oxidiser at high temperatures (Acosta, Gross and Perram, 2016). Modelling of graphite oxidation in a stagnation-point flow field has been carried out using detailed homogeneous chemical kinetics and semi-global heterogeneous chemical kinetics by electrically heating a cylindrical graphite rod placed transversely in a uniform oxidiser flow-field as shown in Figure 2.11.

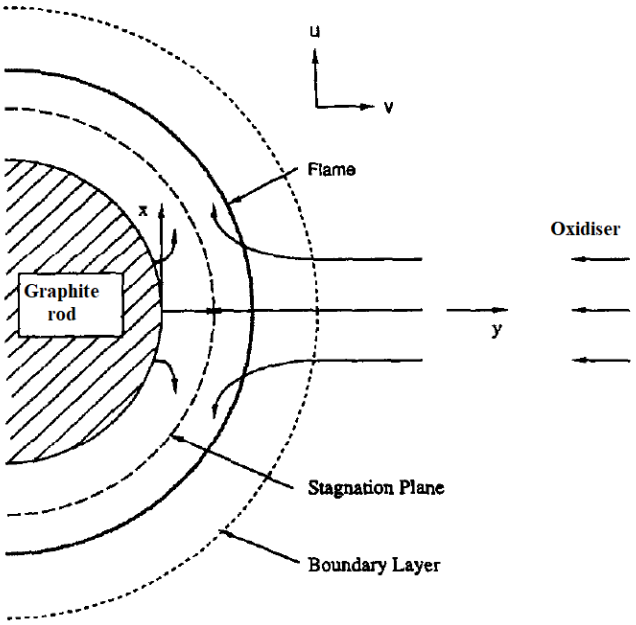


Figure 2.11: Schematic diagram of the stagnation-point flow field for a cylindrical graphite rod placed transversely to an oxidising flow (Chelliah et al., 1996).

In a typical gas-phase flame establishment, the CO transported towards the oxidiser stream either reacts with the oxidiser to produce $CO_2$ in the flame envelope or is simply convected away. A fraction of $CO_2$ produced in the flame diffuses to the surface and reacts with the graphite wall, to provide additional CO formation. The coupling between the gaseous and surface kinetics depends on: (1) surface temperature; (2) pressure; (3) oxidiser composition; (4) flow strain rate (as functions of model shape and amount of burn-off); and (5) material properties (porosity, impurities, and degree of graphitisation). Impurities could pose a threat (catalytic effect) to the reaction process which might reduce the activation energy of chemical reaction thereby increasing the reactivity between oxidising gas and graphite (Luo and Jean-Charles, 2003).

#### 2.3.2.3 Finite Rate Oxidation Models

The finite rate reaction model is generally used in modelling the surface chemistry of the flow regimes. This research work has adopted the commonly used finite rate carbon surface ablation models shown in Table 2.1, where the surface reactions are characterised by a reaction probability $\gamma_i$, an activation energy $E_i$, active site (s) and

carbon bulk C(b). Unlike the Zhluktov and Abe model which is a reversible process (Zhluktov and Abe, 1999), the Park model reaction set contains irreversibilities (Park et al., 1994) for all processes involving surface oxidation, nitridation, and sublimation. As the Park model adopts the kinetically controlled sublimation, it therefore depends on the surface reactions and Arrhenius rate parameters.

Table 2.1: Surface reactions (Park model) and Arrhenius rate (Park et al., 1994).

| No | Finite rate surface reaction | $\gamma_i$ | $E_i$ (kJ.mol$^{-1}$) |
|---|---|---|---|
| 1. | O + (s) + C(b) $\rightarrow$ CO + (s) | 0.63 | 9.644 |
| 2. | $O_2$ + 2(s) + 2C(b) $\rightarrow$ 2CO + 2(s) | 0.50 | 0 |
| 3. | N + (s) + C(b) $\rightarrow$ CN + (s) | 0.30 | 0 |
| 4. | 3(s) + 3C(b) $\rightarrow$ $C_3$ + 3(s) | $5.19\times10^{-13}$ | 775.81 |
| 5. | $C_3$ + 3(s) $\rightarrow$ 3(s) + 3C(b) | 0.10 | 0 |

The Park ablation model treats the finite rate surface reaction as a one-step process, ignores any adsorption and desorption steps, and assumes that the reverse reactions proceed slowly enough to be ignored. This reaction modelling approach is one of the most commonly used models for finite rate ablation studies. It represents irreversibility in oxidation (C and O to form CO), nitridation, and sublimation to form $C_3$ carbon vapour. Catalytic recombination of oxygen and nitrogen were ignored in the reaction scheme because of their negligible effects on the carbon surface. Assuming that every interaction of species $i$ with the surface generates a reaction with a given probability $\gamma_i$, the oxidation and nitridation reactions can be calculated. Previous work (Zhluktov and Abe, 1999) has reviewed the disagreements associated with Park's controlling parameters (Park et al., 1994) as to what values should be used for the finite rate reaction modelling and later proposed a more realistic physical representation of the surface chemistry with a total of twelve reversible surface reactions. The reactions correspond to adsorption/desorption of O and N, adsorption and catalytic recombination of $O_2$ and $N_2$, oxidation reaction to produce CO and $CO_2$, and sublimation of the surface into C, $C_2$, and $C_3$ vapour. The finite rate reaction models in Table 2.1 considered three distinct environments: the gas, the surface, and the carbon bulk environments.

#### 2.3.2.4 Graphite Oxidation and Reaction Probabilities

The three surface reaction processes of interest to graphite are oxidation, nitridation, and sublimation of which the oxidation process remains the most important. Oxidation is the principal emphasis in this section. Due to the ease of oxygen dissociation in relation to the atmospheric re-entry conditions, atomic oxidation becomes important and is shown in Table 2.2, where $T_w$ represents the wall temperature. The reaction probability $\gamma_1$ is from endothermic reaction while the reaction probabilities $\gamma_2$ and $\gamma_3$ are from exothermic reactions. The value of $\gamma_3$ is only valid for a range of wall temperatures ($T_w$) of $1500 \leq T_w \leq 2500$ K (Berkowitz, 1966).

Table 2.2: Finite rate surface reactions for non-equilibrium flows (Park, 1976).

| Surface reaction | Reaction probability ($\gamma$) |
|---|---|
| C(s) + $O_2$ $\rightarrow$ CO + O - 1.40 eV | $\gamma_1 = \frac{1.43\times10^{-3}+0.01exp(-1450/T_w)}{1+2\times10^{-4}exp(13000/T_w)}$ |
| C(s) + O $\rightarrow$ CO + 3.76 eV | $\gamma_2 = 0.63 \times exp\left(-\frac{1160}{T_w}\right)$ |
| C(s) + O + O $\rightarrow$ C(s) + $O_2$ + 5.08 eV | $\gamma_3 = \gamma_2 = 0.63 \times exp\left(-\frac{1160}{T_w}\right)$ |

The production rate of $CO_2$ at the surface is usually very slow and usually not considered by many authors compared to the production rate of CO. Hence the surface recession of a graphite surface is expressed in terms of the molar diffusion of carbon monoxide (CO) at the surface (Panerai et al., 2014). Figure 2.12 shows the reaction probability plots from molecular oxidation (left blue plot) and atomic oxidation (right red plot) using the information in Table 2.2. It shows a temperature range of 0 - 5000 K with atomic and molecular reaction probabilities of 0.396 and 0.0068 respectively at 2500 K. This makes the atomic reaction probability ($\gamma_2$) to be about 58 times more likely to occur on the graphite surface than the molecular reaction probability ($\gamma_1$) at 2500 K.

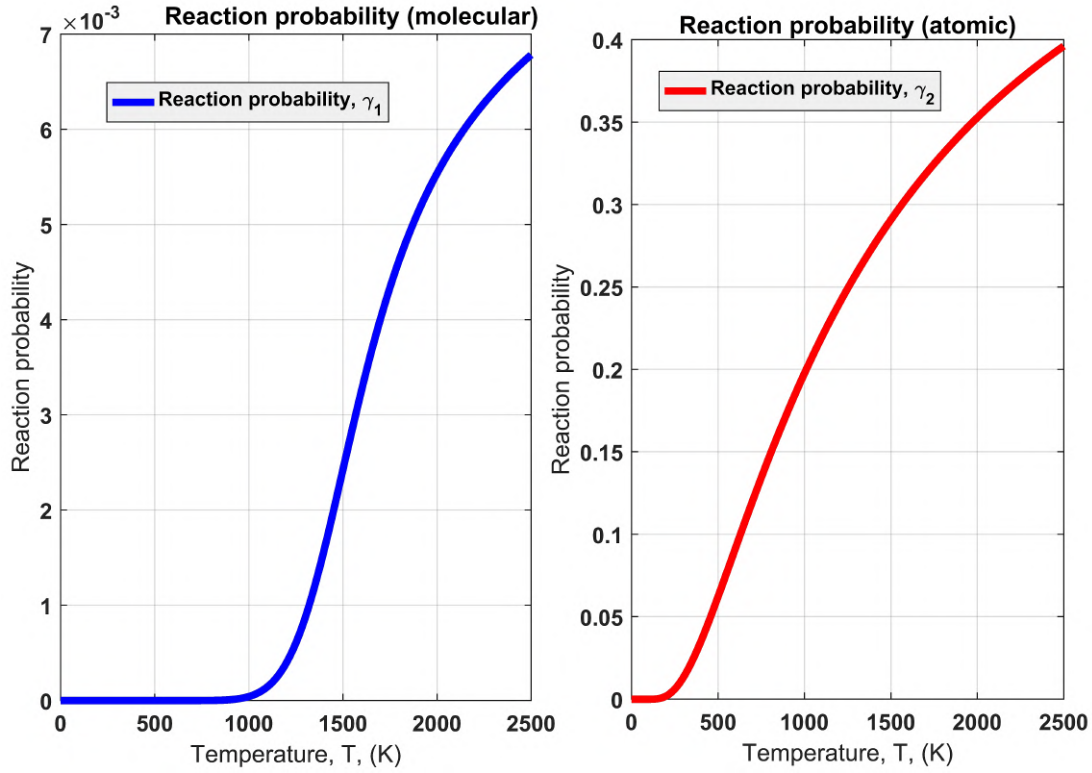


Figure 2.12: Behaviour of the reaction probability curves with temperatures. The calculations were carried out using the $\gamma_1$ and $\gamma_2$ information in Table 2.2.

### 2.3.3 Nitridation

Frequently only atomic nitridation is considered in surface reaction models because molecular nitrogen ($N_2$) does not normally react with graphite surfaces (Helber, Alessandro, Chazot and Thierry, 2015). The experimental study of graphite pieces exposed to pure nitrogen test flow, suggests that nitridation reaction takes the form N + C(s) $\rightarrow$ CN + 0.35 eV (Suzuki, Fujita and Sakai, 2010*b*). Supported by the earlier experimental work involving nitridation reaction occurring at a graphite surface (Suzuki, Fujita, Ando and Sakai, 2008) and the experimental study of graphite ablation in nitrogen flow, using an inductively-coupled plasma-heated wind tunnel (Suzuki, Fujita and Sakai, 2010*a*), the nitridation reaction probability is expressed in Equation 2.1.

$$\gamma_N = 8.441 \times 10^{-3} exp\left(-\frac{2322}{T_w}\right) \tag{2.1}$$

However, there is also evidence that suggests that CN species can be formed even without $N_2$ dissociation from hot carbon subjected to a stream of molecular nitrogen. This can be achieved by first forming a chemical compound called cyanogen from the reaction between graphite and $N_2$ (Brotherton and Lynn, 1959). Cyanogen has a structural formula N≡C-C≡N which is two cyano groups with a single bond between the two adjacent carbon atoms. The cyanogen compound with a molecular formula $(CN)_2$ is highly unstable and undergoes a thermal dissociation process (Natarajan, Thielen, Hermanns and Roth, 1986) to form two CN species. The experimentally determined rate coefficient data for the dissociation of cyanogen, were all seen to closely fit the Arrhenius expression shown in Table 2.3, where $k_{C_2N_2}$ is the dissociation rate coefficient, and $T$ is the shock heated temperature.

Table 2.3: Cyanogen dissociation rate coefficient in $cm^3/s$.

| Temperature | Equation of dissociation rate | Source |
|---|---|---|
| 1900 - 2650 K | $k_{C_2N_2} = 2.97 \times 10^{-7} exp\left(\frac{-53665}{T}\right)$ | (Natarajan et al., 1986) |
| 1700 - 2500 K | $k_{C_2N_2} = 6.64 \times 10^{-8} exp\left(\frac{-48000}{T}\right)$ | (Tsang, Bauer and Cowperthwaite, 1962) |
| 2200 - 3700 K | $k_{C_2N_2} = 1.11 \times 10^{-7} exp\left(\frac{-49600}{T}\right)$ | (Fueno, Tabayashi and Kajimoto, 1973) |
| 2200 - 2800 K | $k_{C_2N_2} = 6.82 \times 10^{-8} exp\left(\frac{-47070}{T}\right)$ | (Colket III, 1984) |
| 2500 - 3450 K | $k_{C_2N_2} = 1.05 \times 10^{-7} exp\left(\frac{-50040}{T}\right)$ | (Szekely, Hanson and Bowman, 1984) |

Figure 2.13 shows a summary of rate coefficients in $cm^3/s$ over a general temperature range of 1700 - 3650 K (upper and lower temperature limits for all experimental data in Table 2.3), reflecting the degree of uncertainty in the rate coefficient data.

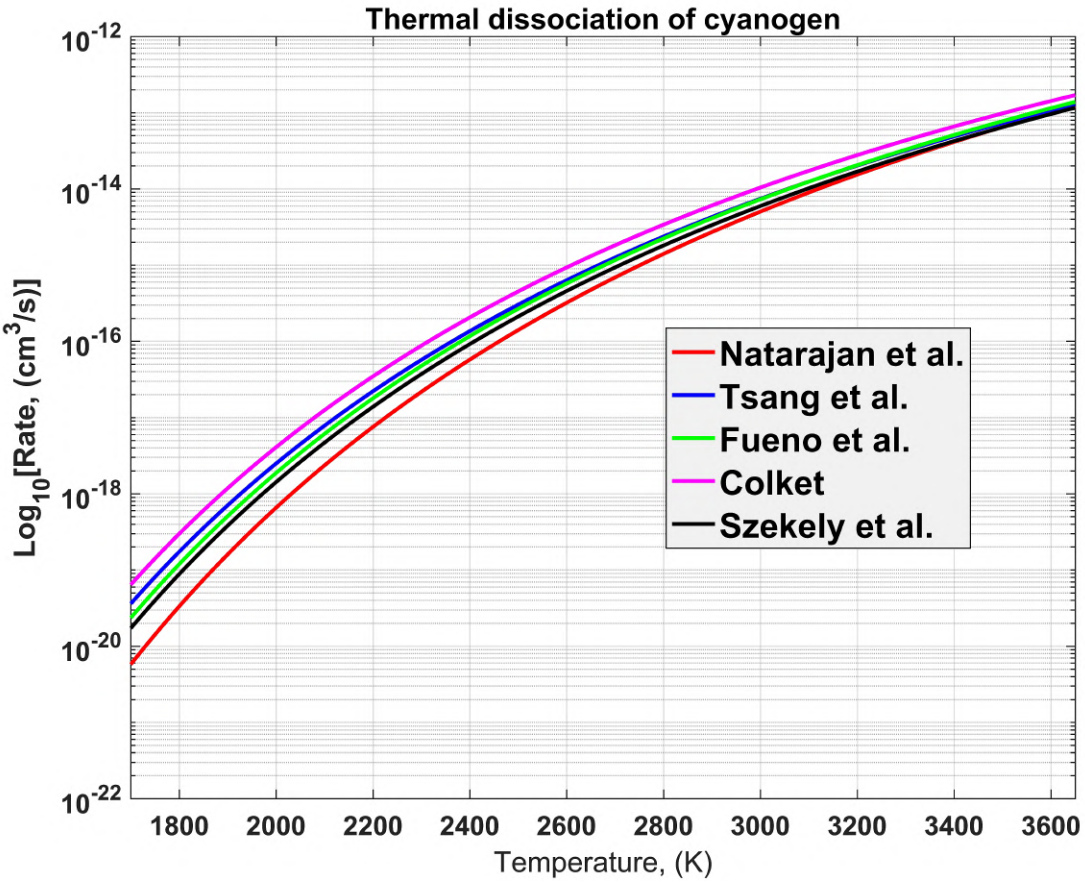


Figure 2.13: Dissociation rate coefficient of cyanogen in $cm^3/s$ using Table 2.3.

### 2.3.4 Sublimation

Disagreement still exists about the actual sublimation rate producing $C_3$. The experimental work involving thermochemical ablation of heat shields for earth atmospheric entry (Turchi, Congedo and Magin, 2017), ablation simulation in Earth atmospheric entry (Keenan and Candler, 1993), numerical solution of laminar boundary layer and thin shock layer equations predicting electron density around re-entry vehicle (Blottner, 1971), and the stagnation point heat transfer rates for Pioneer-Venus probes (Park and Ahn, 1999), suggest $C_3$ reaction probability at equilibrium with some significant differences (Suzuki, Furudate and Sawada, 2002). Three different equations from three different sources have been reviewed to describe the reaction probability of $C_3$ species which are represented in Equation 2.2, Equation 2.3, and Equation 2.4 from the

work of Keenan, Blottner and Park respectively.

$$\gamma_{C_3K} = 2.47 \times 10^{10} exp\left(-\frac{93227}{T_w}\right) \tag{2.2}$$

$$\gamma_{C_3B} = 4.3 \times 10^{15} \times T_w^{-1.5} exp\left(-\frac{97597}{T_w}\right) \tag{2.3}$$

$$\gamma_{C_3P} = 1.56 \times 10^{5} exp\left(-\frac{59410}{T_w}\right) \tag{2.4}$$

Table 2.4 shows the experimentally determined and simplified reaction probabilities for sublimation species C, $C_2$ and $C_3$ (Dolton, Goldstein and Maurer, 1968), where $\gamma_s$ is the experimentally determined reaction probability for each carbon species.

Table 2.4: Reaction probabilities (Mortensen and Zhong, 2012).

| Species | $\gamma_s$ | Simplified reaction probability |
|---|---|---|
| C | 0.14 | $\gamma_C = \exp\left(\frac{-85715}{T_w} + 18.69\right)$ |
| $C_2$ | 0.26 | $\gamma_{C_2} = \exp\left(\frac{-98363}{T_w} + 22.20\right)$ |
| $C_3$ | 0.03 | $\gamma_{C_3} = \exp\left(\frac{-93227}{T_w} + 23.93\right)$ |

### 2.3.5 Reaction Probability Summary

The chemistry of mass recession rate of graphite at the surface within the temperature range of 1000 - 2500 K is a combination of surface oxidation, sublimation, and the possibility of nitridation. Figure 2.14 shows the generalised reaction probability summary of graphite oxidation, nitridation and sublimation for all species considered in the present work. The atomic oxidation remains the primary mechanism of the oxidation process with the highest reaction probability. The $\gamma_{C_3K}$ curve is essentially that of $C_3$ in Table 2.4.

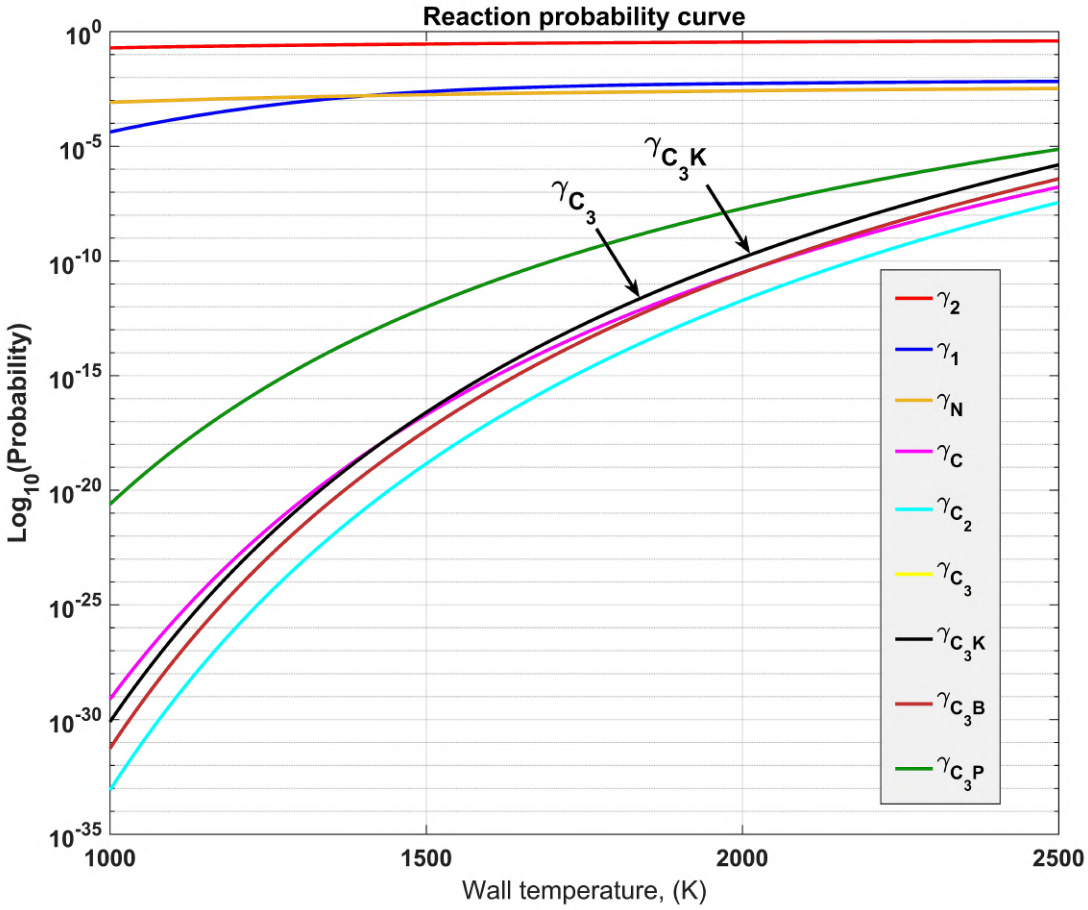


Figure 2.14: The summary of surface reaction probabilities. The values of oxidation species $\gamma_2$ and $\gamma_1$ are computed using the information in Table 2.2. The value of nitridation species $\gamma_N$ is computed using Equation 2.1. Sublimation species C, $C_2$ and $C_3$ are computed using the simplified reaction probabilities in Table 2.4. The values of $\gamma_{C3K}$, $\gamma_{C3B}$ and $\gamma_{C3P}$ are computed using Equation 2.2, Equation 2.3 and Equation 2.4 from the work of Keenan, Blottner and Park respectively.

The reaction review has shown that despite considerable past efforts, the reaction probabilities and the physical mechanisms applied in the study of carbon reaction are disputed to some extent. The non-Arrhenius oxidation behaviour, large variations in the predicted reaction probabilities, and lack of precise measuring techniques to accurately quantify the unstable nitridation at high temperatures make the general ablation process not-well understood.

### 2.3.6 Dissociation and Volumetric Exchange

The reactions and rate coefficients for the gas-phase chemistry model of graphite has a general form of the Arrhenius equation given in Equation 2.5 (Alba, Greendyke, Lewis, Morgan and McIntyre, 2015), where $k_f$ is the temperature dependent forward reaction rate coefficient, $A_r$ is the pre-exponential frequency factor in $m^3/(mol.s)$, $T$ is the Kelvin temperature, $n$ is the temperature exponent, $E_a$ is the activation energy or energy threshold (defined as the minimum amount of energy required to initiate a chemical reaction), and $R$ is the universal gas constant with a value of 8.314 $Jmol^{-1}K^{-1}$. The reaction mechanism is presented in Table 2.5 using the standard interpretation (Farbar, Boyd and Martin, 2012) from Equation 2.5.

$$k_f = A_r T^n exp(-E_a/RT) \tag{2.5}$$

The oxidation reaction in the Hot surface reactions - Heterogeneous Kinetics section in Table 2.5, where C(s) + $CO_2$ $\Rightarrow$ 2CO, suggests oxidation contribution from the diffusion of $CO_2$ to the surface. There are also three possibilities for sublimation.

Table 2.5: Reaction mechanism for non-porous graphite ablation model

| Reaction | Rate coefficient ($m^3$/mole/s) | Reference |
|---|---|---|
| Dissociation of molecular air species (M) at the hot surface | | |
| * $N_2 + M \underset{k_b}{\overset{k_f}{\rightleftharpoons}} N + N + M$ | $3.70\times10^{15}T^{-1.6}\exp(-113\ 200/T)$ | (Park, 1985) |
| * All atomic species ($k_b$) | $1.11\times10^{16}T^{-1.6}\exp(-113\ 200/T)$ | (Park, 1985) |
| * $O_2 + M \underset{k_b}{\overset{k_f}{\rightleftharpoons}} O + O + M$ | $2.75\times10^{13}T^{-1.0}\exp(-59\ 500/T)$ | (Park, 1985) |
| * All atomic species ($k_b$) | $8.25\times10^{13}T^{-1.0}\exp(-59\ 500/T)$ | (Park, 1985) |
| * $NO + M \underset{k_b}{\overset{k_f}{\rightleftharpoons}} N + O + M$ | $2.30\times10^{11}T^{-0.5}\exp(-75\ 500/T)$ | (Park, 1985) |
| * All atomic species ($k_b$) | $4.60\times10^{11}T^{-0.5}\exp(-75\ 500/T)$ | (Park, 1985) |
| Volumetric exchange reaction rates | | |
| * $N_2 + O_2 \underset{k_b}{\overset{k_f}{\rightleftharpoons}} NO + NO$ | $6.69\times10^{3}T^{-2.54}\exp(-64\ 639/T)$ | (Park, 1985) |
| * $N_2 + O \underset{k_b}{\overset{k_f}{\rightleftharpoons}} NO + N$ | $3.18\times10^{7}T^{0.10}\exp(-37\ 700/T)$ | (Park, 1985) |
| * $N + O_2 \underset{k_b}{\overset{k_f}{\rightleftharpoons}} NO + O$ | $2.16\times10^{2}T^{1.29}\exp(-19\ 220/T)$ | (Park, 1985) |
| * $CO + O_2 \underset{k_b}{\overset{k_f}{\rightleftharpoons}} CO_2 + O$ | $3.0\times10^{2}T^{1.0}\exp(-18\ 210/T)$ | (Bhutta and Lewis, 1993) |
| * $N_2 + C \underset{k_b}{\overset{k_f}{\rightleftharpoons}} CN + N$ | $2.0\times10^{8}T^{0.00}\exp(-23\ 200/T)$ | (Bhutta and Lewis, 1993) |
| * $CN + C \underset{k_b}{\overset{k_f}{\rightleftharpoons}} C_2 + N$ | $5.0\times10^{7}T^{0.00}\exp(-13\ 000/T)$ | (Park, Howe, Jaffe and Candler, 1991) |
| * $C_3 + C \underset{k_b}{\overset{k_f}{\rightleftharpoons}} C_2 + C_2$ | $1.70\times10^{3}T^{1.5}\exp(-19\ 580/T)$ | (Park et al., 1991) |
| * $CO + N \underset{k_b}{\overset{k_f}{\rightleftharpoons}} CN + O$ | $2.0\times10^{8}T^{0.00}\exp(-38\ 600/T)$ | (Bhutta and Lewis, 1993) |
| * $CO + N \underset{k_b}{\overset{k_f}{\rightleftharpoons}} NO + C$ | $9.0\times10^{10}T^{-1.0}\exp(-53\ 200/T)$ | (Bhutta and Lewis, 1993) |
| * $CO_2 + N \underset{k_b}{\overset{k_f}{\rightleftharpoons}} CO + NO$ | $1.0\times10^{-3}T^{2.00}\exp(-20\ 980/T)$ | (Bhutta and Lewis, 1993) |
| Hot surface reactions - Heterogeneous Kinetics | | |
| Oxidation at hot surfaces | Nitridation at hot surfaces | Sublimation at hot surfaces |
| 1. C(s) + O ⇒ CO | 1. C(s) + N ⇒ CN | 1. C(s) ⇒ $C_{(vapour)}$ |
| 2. C(s) + $O_2$ ⇒ CO + O | 2. C(s) + NO ⇒ CN + O | 2. 2C(s) ⇒ $C_{2(vapour)}$ |
| 3. C(s) + $CO_2$ ⇒ 2CO | | 3. 3C(s) ⇒ $C_{3(vapour)}$ |

* Refers to the reversible reactions based on the thermodynamic equilibrium boundary-layer assumptions (Denbigh, 1981) where the reverse reaction rate coefficient $k_b$ is also computed from a chemical equilibrium assumption (Turns et al., 1996). The hot surface reaction rates are computed using the reaction probabilities shown in Figure 2.14.

## 2.4 Computational Simulations

### 2.4.1 Low Speed

Figure 2.15 shows OpenFOAM simulations for two fundamental flow configurations: (1) stagnation plane and (2) flat plate generated from a heated graphite surface. The arrows represent fluid streamlines while the vectors along the surface represent boundary-layer mass additions. Species transport and wall-surface reactions of the blunt carbon body was examined at 1600 K and 2400 K subjected to stagnation and flat plate flows with a free-stream velocity of 40 m/s. The figure shows that oxygen species from free-stream air decreases across the boundary layer to almost zero at the wall as it is being consumed in the reactions.

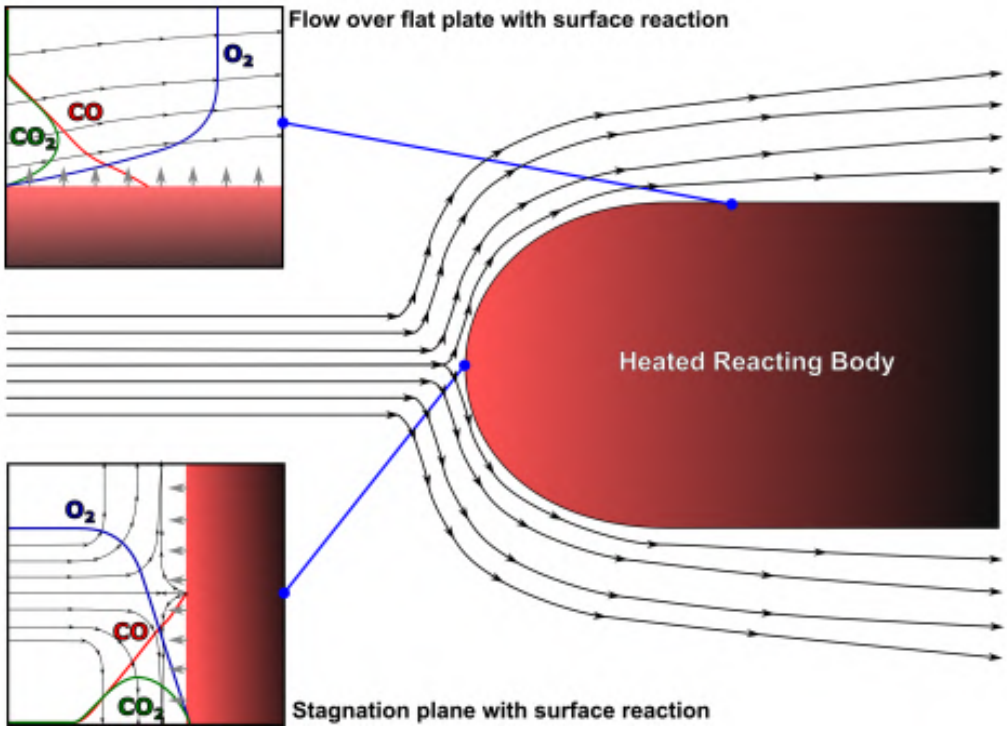


Figure 2.15: Species transport and wall-surface reactions of blunt carbon body subjected to stagnation and flat plate flows with a flow velocity of 40 m/s (Johnson and Chelliah, 2013).

### 2.4.2 High Speed

Simulations were performed on a configuration involving a sphere of 1 metre radius with graphite heat shields of variable thickness set to 0.05 m, 0.1 m, and 0.2 m, at a free-stream speed of 10 km/s and an altitude of 65 km (Zeng et al., 2014). The aim was to examine the transient characteristics of the re-entry flow field during the unsteady ablation of the attached graphite heat shield. The results showed that six carbonaceous species namely CO, $CO_2$, CN, C, $C_2$, and $C_3$ were the products of surface reactions from the thermo-chemical ablation process due to oxidation, nitridation, and sublimation. These carbonaceous species were found to exist mainly in the boundary layer with the mass fractions of CO and C species shown in Figure 2.16. The CO and C species took more than one minute to reach their steady state profiles within the shock and boundary layer region, and peak concentrations for CO and C species were 32 % and 4 % respectively.

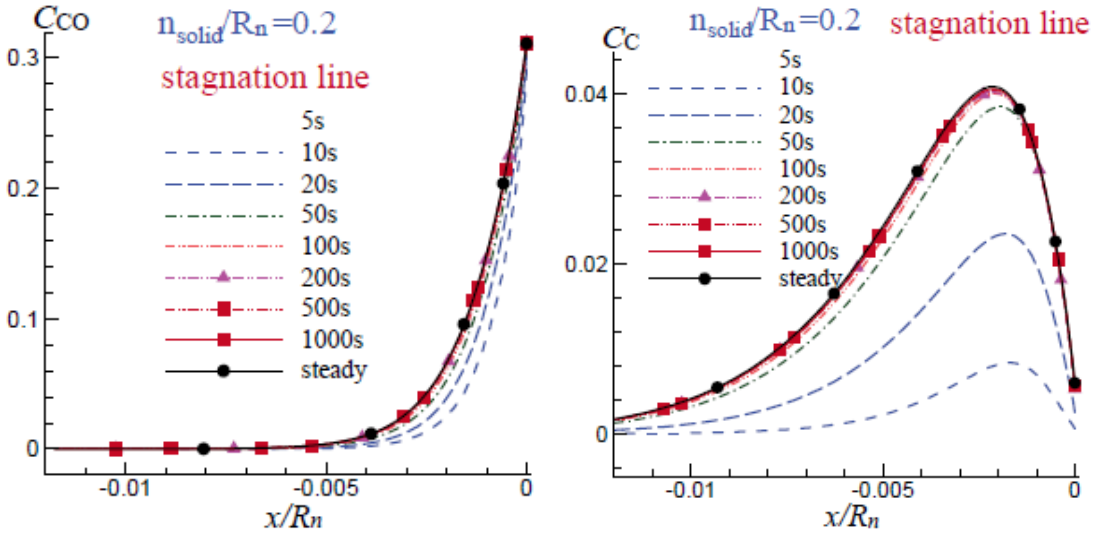


(a) Time evolution of CO.

(b) Time evolution of C.

Figure 2.16: The time evolution of CO and C along the stagnation line was investigated through numerical simulation. Where $n_{solid}$ is the heat shield thickness (0.2 m), $R_n$ is the nose radius of 1 m, and x is the distance to the surface (Zeng et al., 2014).

Figure 2.17a shows the thermal conduction through the heat shield of 0.05 m thickness. The simulation also shown that the time required to reach steady-state became longer

as the heat shield thickness increased as shown in Figure 2.17b. It was also concluded that the heat shield thickness minimally effected the transient processes of the species mass fraction generation at the surface (Zeng et al., 2014).

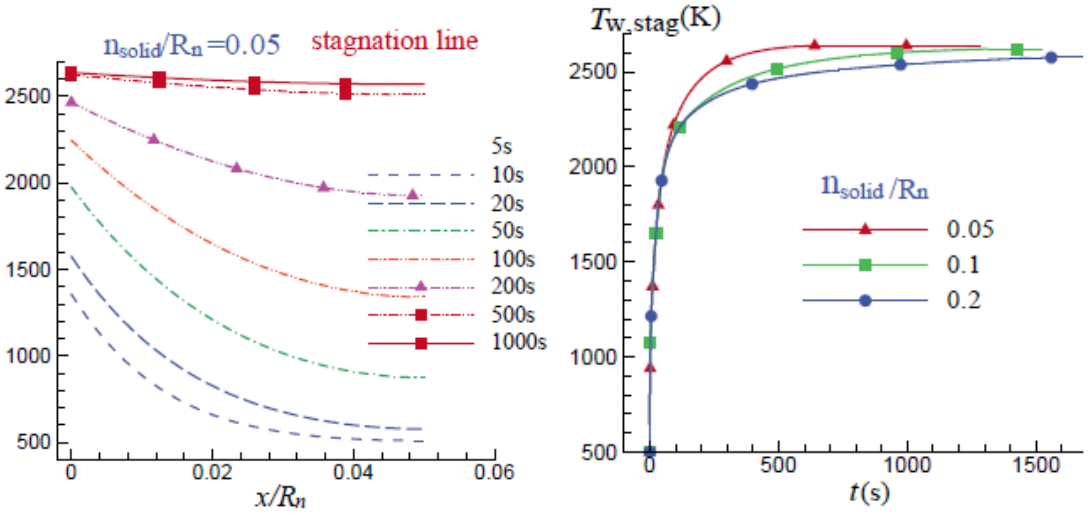


(a) Temperature profile into 0.05 m thickness.

(b) Thickness of 0.05 m, 0.1 m, and 0.2 m.

Figure 2.17: Time evolution of heat shields thickness along the stagnation line was investigated through numerical simulation. Where $n_{solid}$ is the heat shield thickness (0.05, 0.1 and 0.2 m), $R_n$ is the nose radius of 1 m, x is the thickness from the surface and t is the heating time in seconds (Zeng et al., 2014).

## 2.5 Conclusions

Studies involving wind tunnel experiments using heat shield materials have been reviewed. Test samples used in plasma wind tunnels do not require pre-heating, but models for shock/expansion tunnels and other short duration facilities do. Resistive heating, where an electric current is passed through a graphite element, has been the pre-heating method of choice for shock/expansion tunnels. This method is restricted to pre-heating graphite samples with a shape that allows electrical connections at the ends of uniform width profiles. No literature was encountered that preheated circular discs. Models for carbon surface chemistry were reviewed including oxidation, nitridation and sublimation of graphite. Computational simulations have revealed that CO species is the dominant reaction product.

The use of an axisymmetric model is common in simulations, and flat disc probes are used in plasma wind tunnels, which have longer duration flows, but do not replicate shock layers well for hypersonic flow. The combination of a preheated disc in a short duration hypersonic flow has not previously been reported and has potential to make a contribution in the area of heat shield ablation. Chapter 3 describes the development of an experiment and the associated development of a heating technique to allow experiments in this new concept.

# Chapter 3

# Apparatus Development

## 3.1 Introduction

This chapter presents the development of physical hardware and measurement techniques used in the present work. Also presented in this chapter is the rationale for the plasma pre-heating technique, including the difficulty of the electrical resistive pre-heating method for an axisymmetric disc model. All previous pre-heating techniques that have been used in shock and expansion tunnels utilise the conventional resistive heating where an electric current was applied to a graphite specimen. None of the conventional pre-heating techniques is feasible for probe models. A new pre-heating technique which utilises plasma heating has been introduced.

## 3.2 Pre-heating Technique For Axisymmetric Models

### 3.2.1 Rationale For Axisymmetric Models

The axisymmetric configuration was adopted in the present work because: (1) the axisymmetric configuration lends itself to simplified computational simulation without edge effects that are encountered in planar configurations when tested in wind tunnels, and which also necessitate the application of 3D simulations; and (2) the axisymmetric

configuration also makes experimental analysis easier, for example the application of inverse Abel transforms can be used to deduce radial distributions from line-of-sight integrated properties (Dribinski, Ossadtchi, Mandelshtam and Reisler, 2002).

### 3.2.2 Electrical Heating of Graphite - Axisymmetric Disc Problem

The arrangement shown in Figure 3.1 with the idea that electric current flows from the electrode to the edges of graphite disc, is not feasible for pre-heating probe models in the available laboratory environment. This is illustrated through the following analysis.

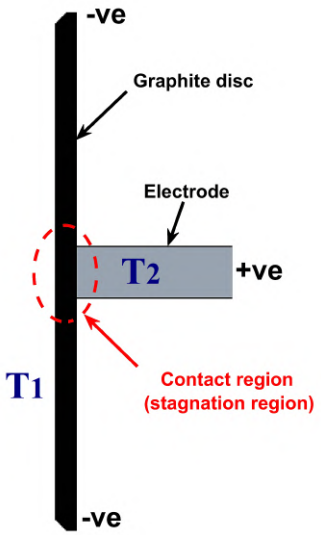


Figure 3.1: A graphite disc contacted by a centralised metallic electrode.

The resistance $R$ ($\Omega$) of any given material can generally be expressed in Equation 3.1,

$$R = \frac{\rho_R}{A}\Delta l \tag{3.1}$$

where $A$ is the cross sectional area through which the current is passing, and $\rho_R$ is the resistivity ($\Omega$.m) of the material, and $\Delta l$ is the length of the material in the direction in which the current is flowing.

In the case of an axisymmetric disc of graphite with a radial flow of current, the resistance of a segment of radial dimension $\Delta r$ is expressed in Equation 3.2, where $t$ is

the local thickness of the disc at radius $r$.

$$R = \frac{\rho_R \Delta r}{(2\pi r)t} \tag{3.2}$$

The rate of electrical heating energy (Watts) delivered to a volume of radial width $\Delta r$ at a radius of $r$ is expressed in Equation 3.3.

$$P_{elec} = I^2 R = \frac{I^2 \rho_R \Delta r}{(2\pi r)t} \tag{3.3}$$

The rate of radiative heat loss from this same element will be given by Equation 3.4,

$$P_{rad} = \epsilon \sigma A_{surf}(T^4 - T_{amb}^4) \tag{3.4}$$

where $\epsilon$ is the emissivity of the graphite, $\sigma$ is the Stefan-Boltzmann constant, $A_{surf}$ is the surface area from which the radiative heat loss occurs, $T$ is the local temperature of the disc, and $T_{amb}$ is the ambient temperature.

Assuming the radiative heat loss occurs from both front and back sides of the disc, the radiative heat loss from a segment of radial width $\Delta r$ at a radius of $r$ can be written as Equation 3.5.

$$P_{rad} = \epsilon \sigma (4\pi r \Delta r)(T^4 - T_{amb}^4) \tag{3.5}$$

Neglecting any conduction or convection effects, at equilibrium, when the electrical heating energy input to the disc segment equals the radiation heat loss from the segment we have Equation 3.6.

$$P_{elec} = P_{rad} \Rightarrow \frac{I^2 \rho_R \Delta r}{(2\pi r)t} = \epsilon \sigma (4\pi r \Delta r)(T^4 - T_{amb}^4) \tag{3.6}$$

Rearranging Equation 3.6 and making the thickness $t$ the subject formula will produce

Equation 3.7.

$$t = \frac{I^2 \rho_R}{8\pi^2 \epsilon \sigma r^2 (T^4 - T_{amb}^4)} \tag{3.7}$$

The current supply in the laboratory is limited to a maximum value of 700 A, and taking the resistivity of a typical graphite material as $\rho_R = 10 \times 10^{-6}$ Ω.m, along with a representative emissivity value for graphite of $\epsilon = 0.95$, and the Stefan-Boltzmann constant of $\sigma = 5.667 \times 10^{-8}$ W/(m$^2$K$^4$), the disc thickness $t$ can be plotted as a function of radius $r$, as shown in Figure 3.2.

Figure 3.2 demonstrates that for a reasonably-sized model, comparable to those used in other facilities, with a radius of, say 25 mm, an impractically thin disc at the outer radius is required to achieve a constant temperature. The target minimum temperature needed for the ablation studies in the present work is about 2000 K, because at this temperature, other studies have indicated that the surface ablation of graphite in a hypersonic flowing air becomes significant (Alba et al., 2015). While it may be possible to machine a disc with the required profile, the aerodynamic loading on the disc supported around the edge with a very small thickness will likely be too high, and the sample will break. Thermal expansion, load needed to maintain electrical conductivity between the disc and electrode, and other constraints results from holding the disc will exacerbate any potential for failure of the disc.

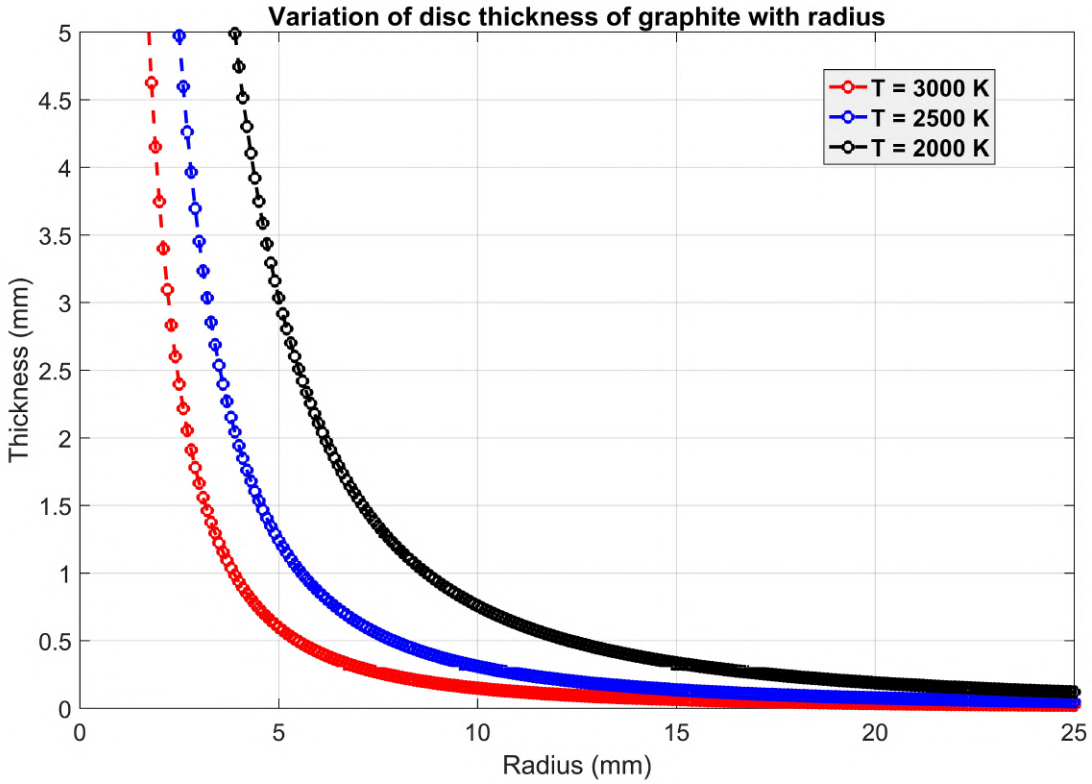


Figure 3.2: Variation of disc thickness of graphite with radius to maintain a constant surface temperature in the case of electrical pre-heating.

### 3.2.3 Developing the New Pre-heating Technique

The pre-heating technique used in the present work is a plasma-based method for pre-heating on the reverse side of the sample. This methodology utilises Tungsten Inert Gas (TIG) plasma in a low pressure environment. In a conventional TIG welding process, there are three possible polarity choices: (1) Direct Current Straight Polarity (DCSP), (2) Direct Current Reverse Polarity (DCRP), and (3) Alternating Current with or without High Frequency stabilisation (ACHF). The heat penetration pattern into the work-piece depends on the choice of polarity and the magnitude of the applied current (Haidar, 1998). Table 3.1 summarises the characteristics of the different options; the DCSP polarity type was adopted in the present work due to its heating efficiency: according to the information presented, DCSP was able to direct most (about 70%) of the generated heat into the graphite disc.

A long series of tests was completed to identify a functional arrangement for the disc heating. In the low pressure of the test section which was initially around 500 Pa (required for the hypersonic nozzle to perform), in combination with the electrical characteristics of the graphite disc, the plasma was very temperamental. The separation of the tungsten electrode from the disc surface and the length that the electrode protruded from the shroud had influences on the ability to start a plasma.

Table 3.1: Comparison of different electrode polarity characteristics in TIG welding (Ding et al., 2014).

| Characteristics | DCSP | DCRP | ACHF |
|---|---|---|---|
| Electrode polarity | negative | positive | alternating |
| Heat-flux balance in the arc | 70% at work end and 30% at electrode end | 30% at work end and 70% at electrode end | 50% at work end and 50% at electrode end |
| Penetration profile | deep and narrow | shallow and wide | medium |
| Electrode capacity | Excellent | Poor | Good |
| Oxide cleaning action | No | Yes | Yes (once every half cycle) |

Figure 3.3 shows the early arrangements of the experiment while exploring heating options. Consistency of starting the plasma was improved with the addition of springs (positioned at both sides of the probe) which helped to create a better electrical contact between the disc and steel probe support structure, and at the same time allowing for material expansions.

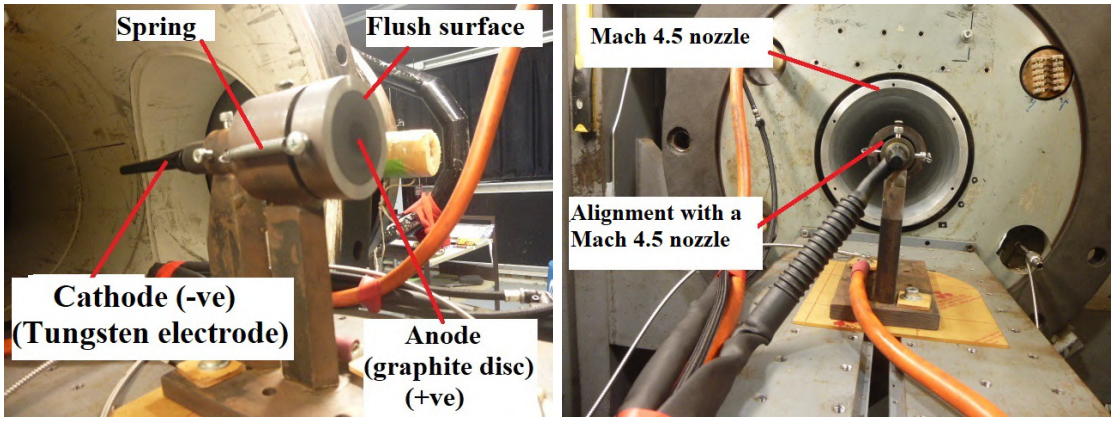


(a) General setup (b) Model aligned to nozzle

Figure 3.3: Early arrangements of the experiment while exploring heating options.

A flush surface between the disc and the holding ring shown in Figure 3.3a was used to prevent flow disturbances at the extremity of the disc. Figure 3.4 shows the detail of how the disc was mounted in the probe creating a flush surface at the contact between the holding ring and the disc. This was achieved by machining a 1 mm by 45 degree chamfer on the disc and the equivalent shape on the internal edge of the holding ring. Also shown in Figure 3.4 is the positioning of the TIG torch into the probe model; the tungsten electrode and the ceramic shroud around the electrode are part of the TIG torch. The heating process is very similar to the well-established TIG process (Traidia, 2011). The separation between the welding electrode and work-piece forms the electrode gap which is occupied by the plasma. The shielding gas flow helps to direct the plasma to the disc.

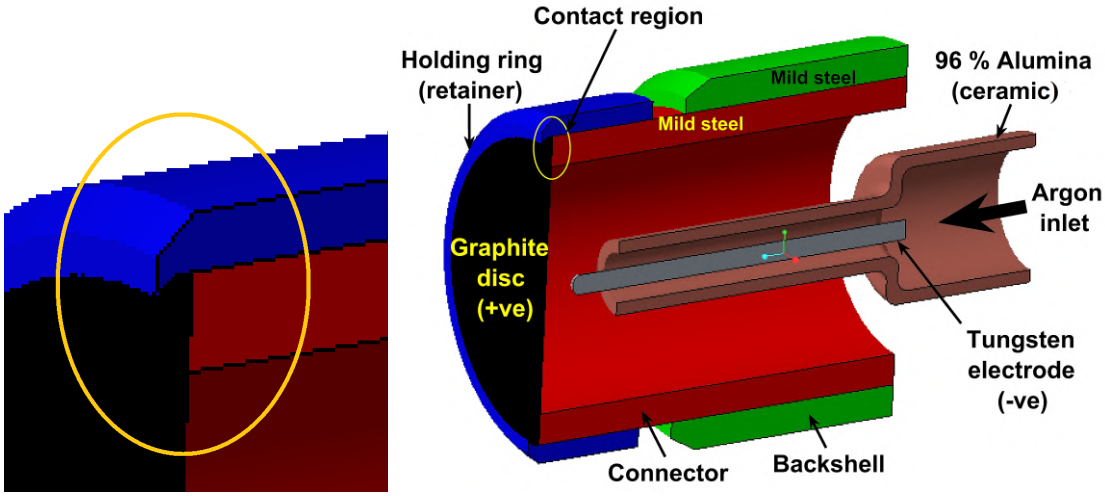


(a) Contact region (b) Sectional view

Figure 3.4: Sectional view of the plasma-generating arrangement for pre-heating on the reverse side of the graphite disc.

The two most important geometric parameters controlling the heat flux to the graphite disc are the electrode gap and the protrusion as shown in Figure 3.5. The figure shows a solid model of the TIG torch used in the present work. The TIG torch is centralised in the model to maintain the axisymmetric nature of the arrangement. Figure 3.6 shows the Miller Dynasty 700 TIG welder which was used for the DC power supply to the model.

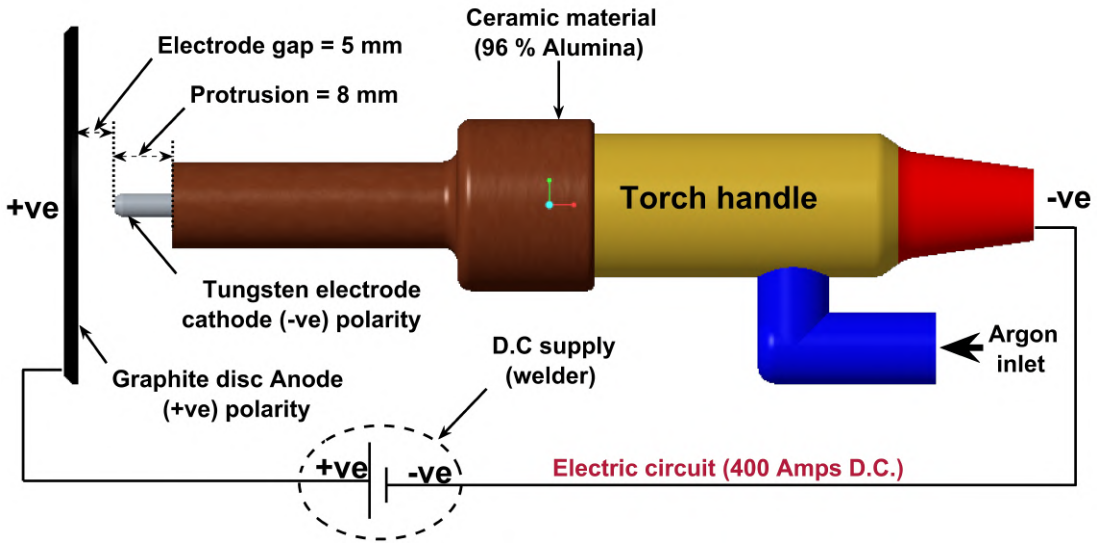


Figure 3.5: A side view of the solid model of the plasma-generating configuration.

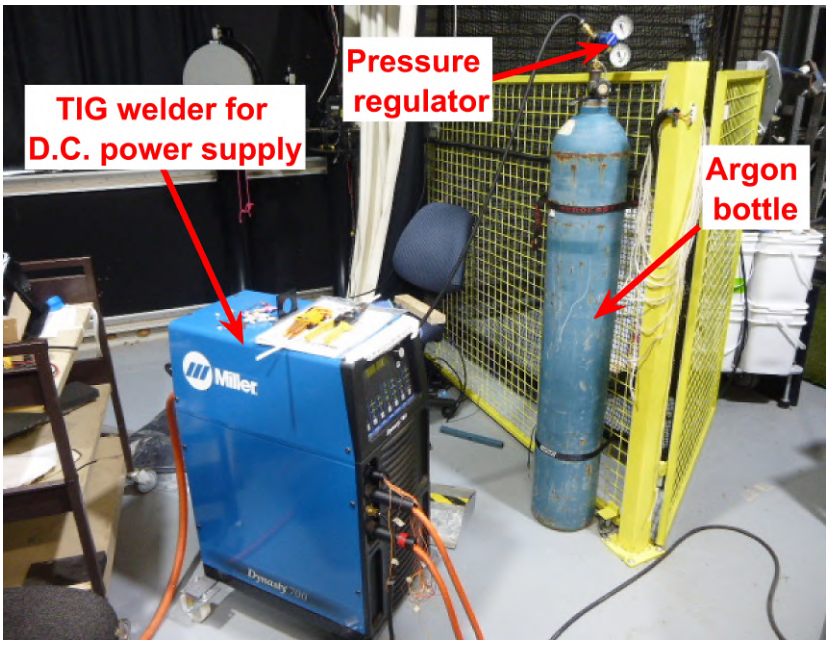


Figure 3.6: Miller Dynasty 700 TIG welder used for the DC power supply to the model.

The tungsten electrode was machined to the required tip shape as shown in Figure 3.7. The geometry of 8 mm protrusion and 5 mm electrode gap was determined through trial and error to be the most effective arrangement. An argon flow rate of 20 L/min was used.

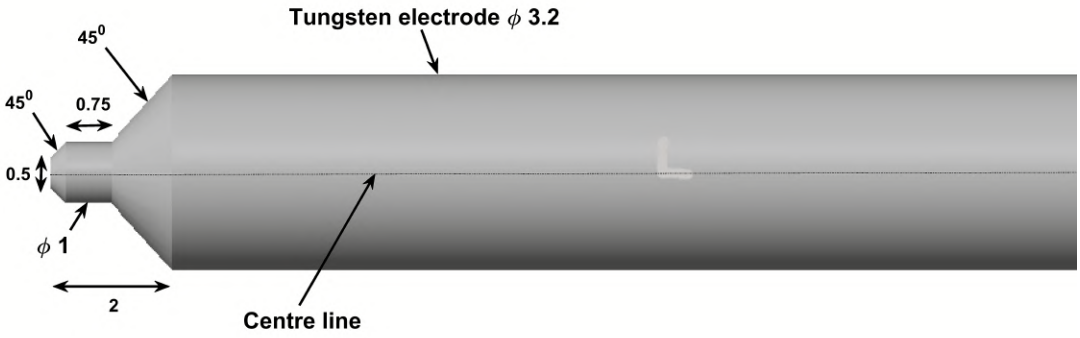


Figure 3.7: Shape of electrode tip (all dimensions in mm).

Unlike the standard European probes which are specially designed for long duration, high enthalpy flows (Herdrich, Dropmann, Marynowski, Löhle and Fasoulas, 2010), the probe in the present work has no water cooling systems because it is used in a short-

duration test. The design of the experimental probe is shown in Figure 3.8 with all dimensions in millimetres.

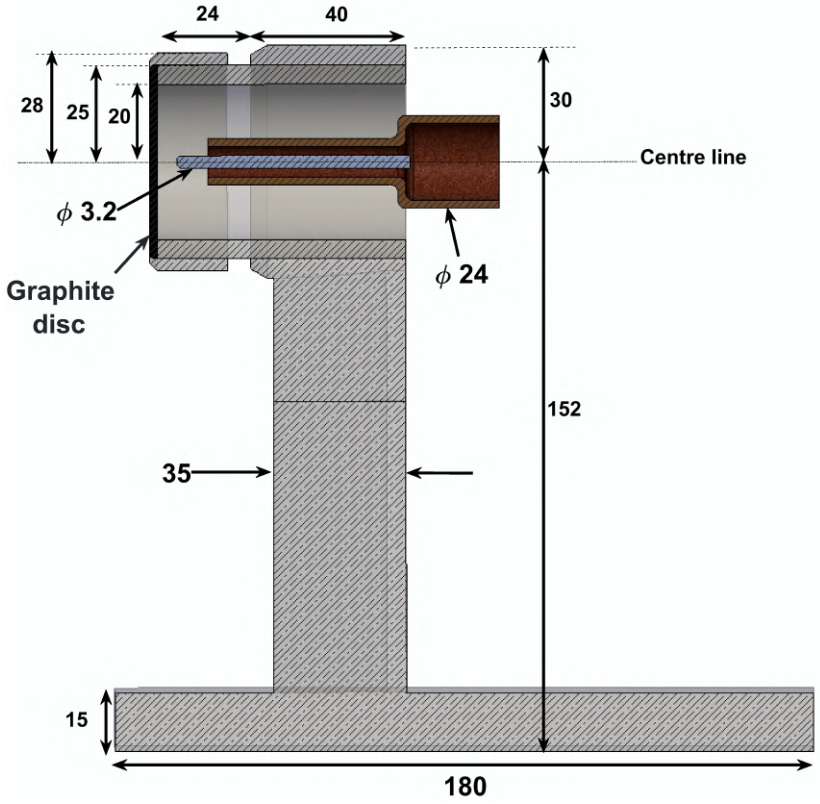


Figure 3.8: Dimensions of experimental probe with a 50 mm diameter carbon disc.

Potential exists for the disc to fail in the arrangement planned, due to the thermal expansion differential between the heated disc and the holding ring. If the disc is constrained to not allow expansion at the outer edge, Figure 3.9 shows an FEA analysis of what shape would result for the disc. The disc constraint setting in the FEA model is a compression only constraint of the 1 mm wide cylindrical surface, which represents the effective constraint on the disc, as the holding ring is free to move axially and therefore only frictional force would result in any loads on the chamfer. The FEA model is simplified to only use constraint on the 1 mm wide cylindrical surface. The proposed minimum 2000 K temperature was applied as a uniform temperature in the disc and standard graphite material properties applied, including a coefficient of thermal expansion of $2.7 \times 10^{-6}$ $K^{-1}$.

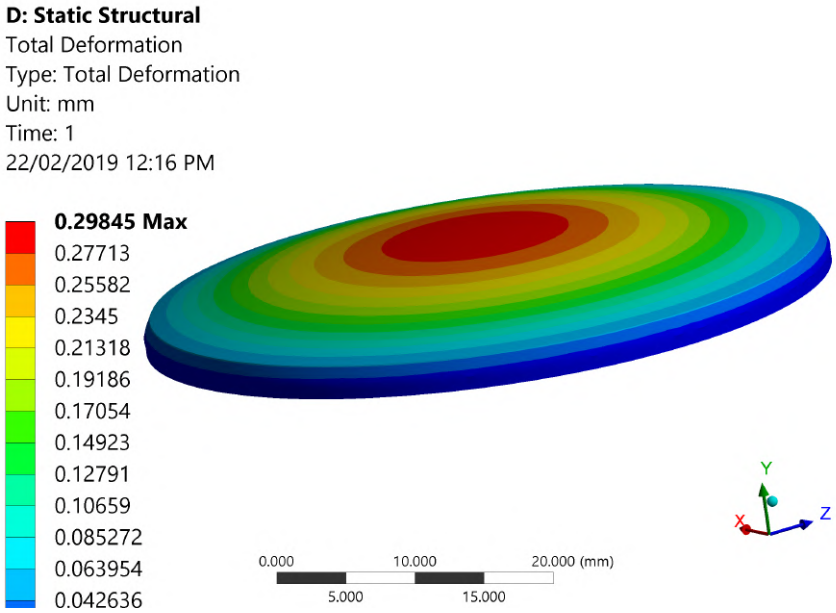


Figure 3.9: Result showing deformation of graphite disc using static structural FEA.

The FEA simulation calculated that the disc would deform to be convex towards the flow, with a maximum deflection (based on a uniform 2000 K disc temperature) of approximately 0.3 mm. The normal stress at the surface on the convex side is predicted as a uniform 15 MPa compression and 23 MPa compression on the concave side.

The deflection may have some influence on the flow characteristics relative to a flat disc, but the amplitude of the deflection is considered small enough to be acceptable. The compressive stresses in the disc are well below the material's compressive strength and are also considered acceptable.

## 3.3 Surface Temperature Measurement Technique

Figure 3.10 shows the response curve for red, green, and blue wavelengths at around 630, 540, and 460 nm respectively of the Olympus High-Speed camera (i-Speed3) used in the experiments. The camera uses a colour filter array (CFA) that filters light impinging on each pixel into the given wavelengths. These colour filter arrays are known as Bayer filters. The CCD sensors under Bayer filter arrays are arranged such

that green contributes 50%, red is 25%, and blue is 25% (Zhen and Stevenson, 2015). The green colour takes twice the proportion of the other two colours in the filter because the filters are designed to mimic the human eye which is most sensitive to green.

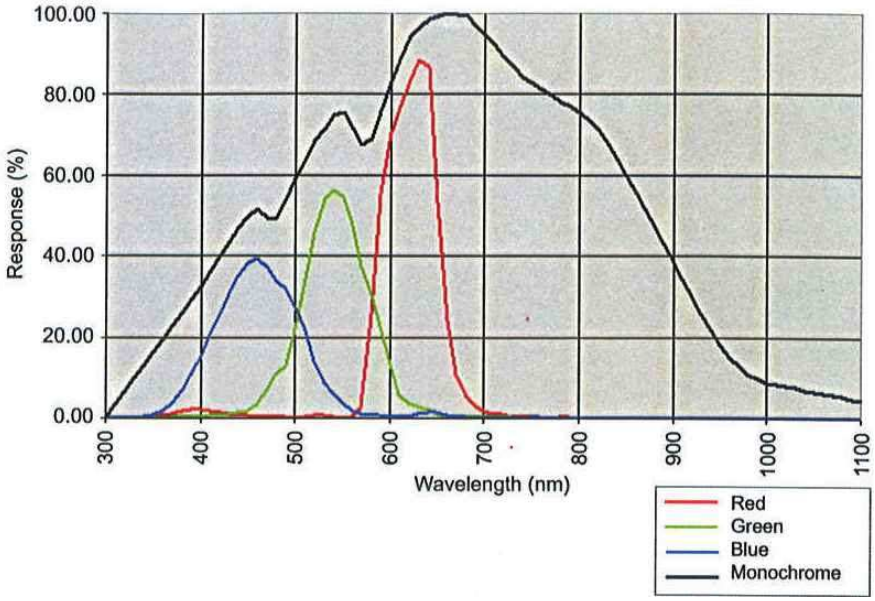


Figure 3.10: Signal sensitivity of the high speed Olympus camera (Thorlabs instruments).

In order to obtain a good reproducibility of temperature data, the same camera settings were adopted for all measurements. The settings used for the Olympus camera are presented in Table 3.2.

Table 3.2: The camera settings applied to present work

| Camera settings | |
|---|---|
| White balance | None |
| Frame speed | 2500 fps |
| Shutter speed | ×100 |
| Aperture | 22 |
| Zoom | full zoom (×210) |

The red, green, and blue signals from the high speed Olympus camera showed a non-linear increase with increasing surface temperatures as shown in Figure 3.11. The red pixel sensitivity was used for the hot-wall temperature measurements because it had the highest value of pixel counts that could be correlated with changing temperatures.

The method of Least Square fitting using a second order polynomial was the approach used to extrapolate temperatures beyond 2500 K. The reference temperature for the Olympus calibration was obtained from a spectrometer optically viewing the heated disc surface through a lens connected by an optical fibre, as discussed in relation to Figure 3.13.

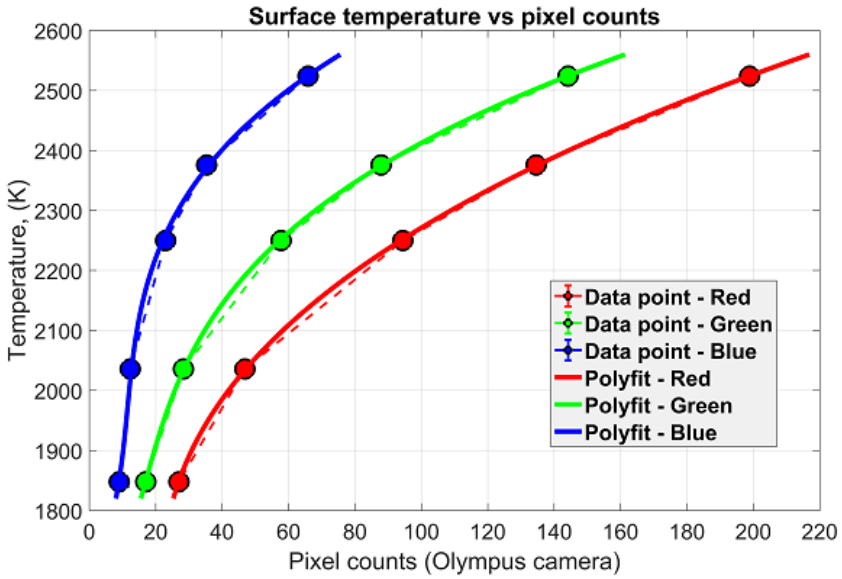


Figure 3.11: Relationship between the hot wall temperatures and pixel counts for camera settings described in Table 3.2.

The technique of measuring temperature using the red count from the high-speed camera requires that the calibration be undertaken without changing the camera's settings such as frame rate, exposure time, field of view and aperture between the calibration and the measurements of the temperature during the experiments. If the camera pixel count suggested that the sensor approached saturation, a new calibration was required by reducing camera aperture or exposure time. If the count was very low, the sensitivity of the measurement was lost, again requiring a new calibration. Photographs of a graphite disc, supported in the probe, after pre-heating for 15 seconds is shown in Figure 3.12. All temperature measurements were carried out using no-flow conditions unless otherwise stated.

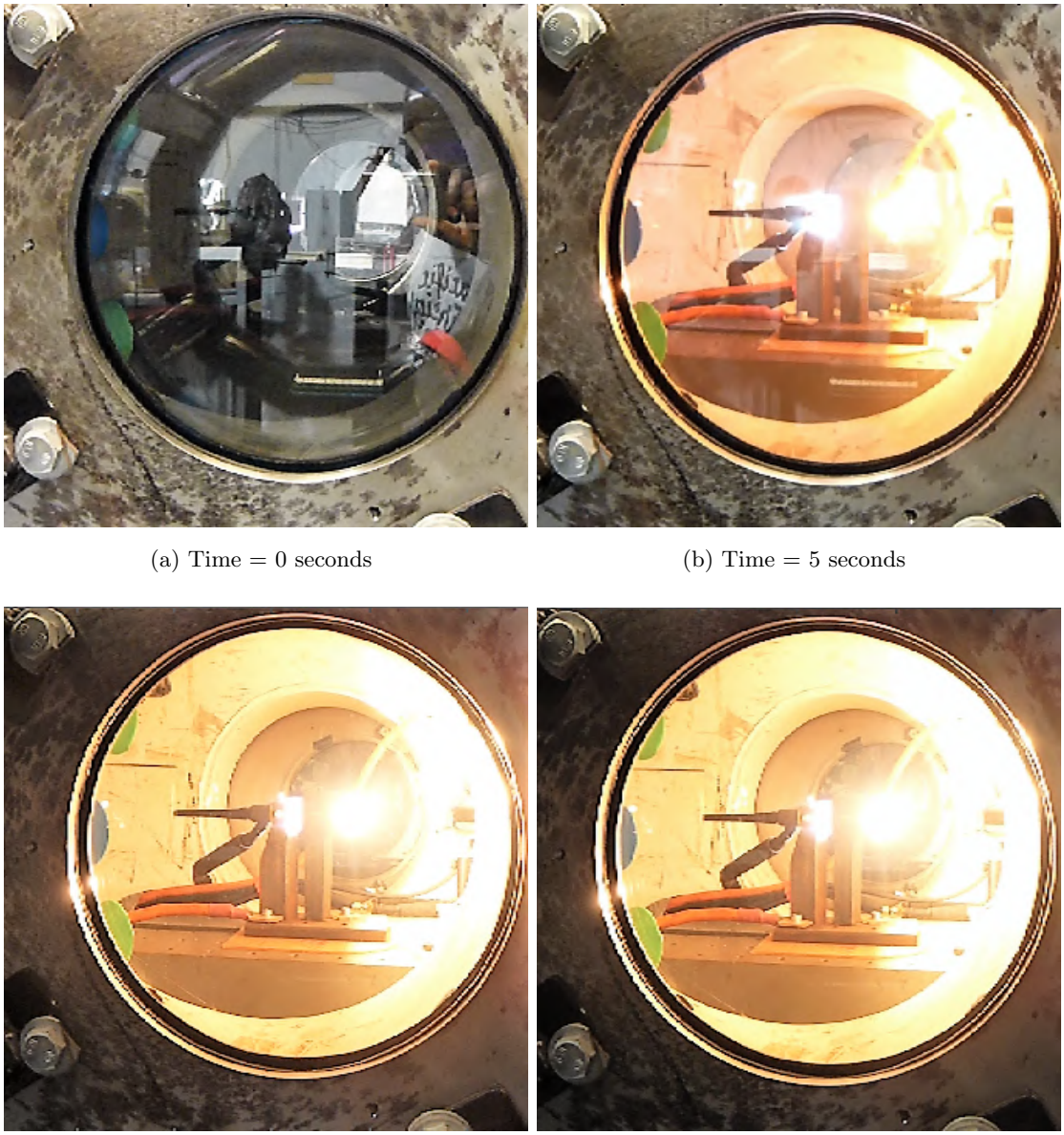

(a) Time = 0 seconds

(b) Time = 5 seconds

(c) Time = 10 seconds

(d) Time = 15 seconds

Figure 3.12: Experimental heating conducted at 500 Pa for 15 seconds using the TIG pre-heating technique. The brightness of the disc is not accurately indicated in the images because an auto-iris was used on the camera used for these images, to keep the images from over-exposure. Some sense of the light intensity emitted from the disc is evident in the contrast within each image.

Figure 3.13 shows the arrangement for using the high speed Olympus camera for temperature measurement. The spectrometer was first calibrated using the integrating sphere. Then an in-situ temperature measurement using the calibrated spectrometer

was used to obtain a temperature correlation on the red pixel intensity of the High Speed Olympus Camera. The mirror shown in Figure 3.13a, is used to allow the camera to see a reflected image as depicted in Figure 3.14. The mirror was required to allow as full a frontal view of the graphite disc as possible accounting for the requirement to not have any obstacle in the flow and positioning the probe within the core flow of the nozzle. Figure 3.14 shows the mirror arrangement in the present work, allowing the high speed Olympus camera to acquire images for temperature analysis. An optical fibre transmit the signals from the hot model to the spectrometer.

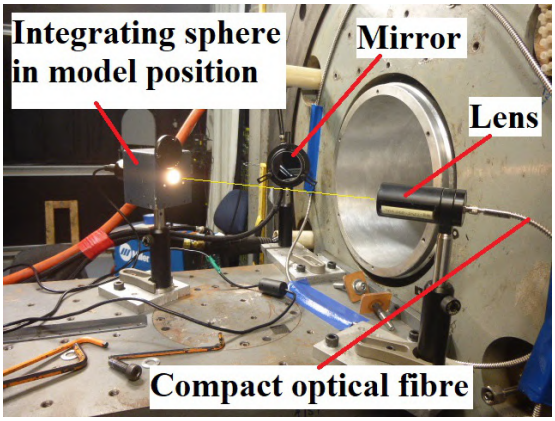


(a) LabSphere in the place of model.

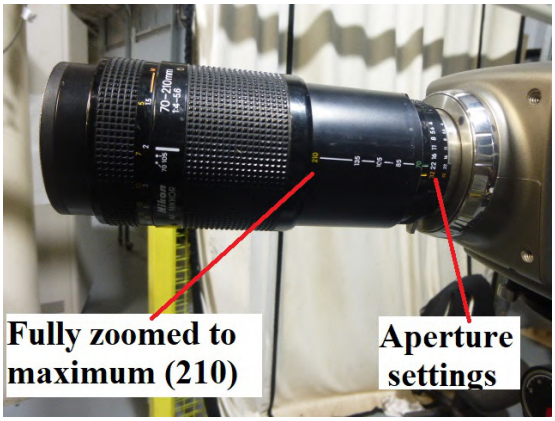


(b) Upgraded focus for better capability.

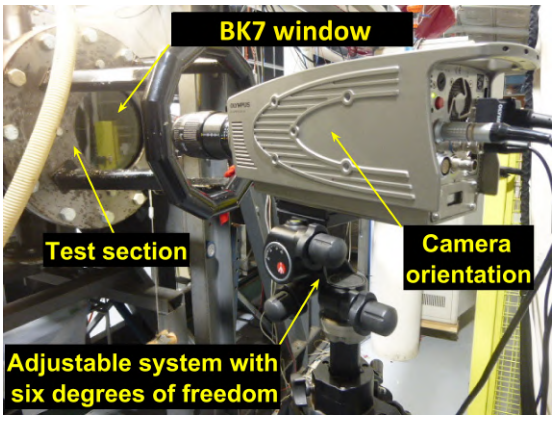


(c) Upgraded optical setup at TUSQ.

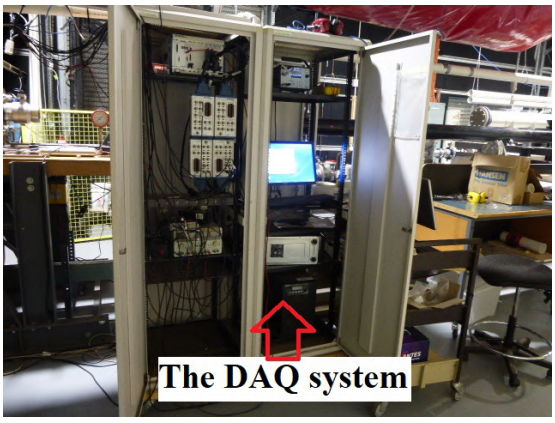


(d) Data acquisition system (DAQ).

Figure 3.13: Set-up used for in-situ calibration of the camera red pixel count (Figure 3.18) and the associated data acquisition for the calibration and the spectrometer output for cross-checking the temperature determined from the camera during the experiments.

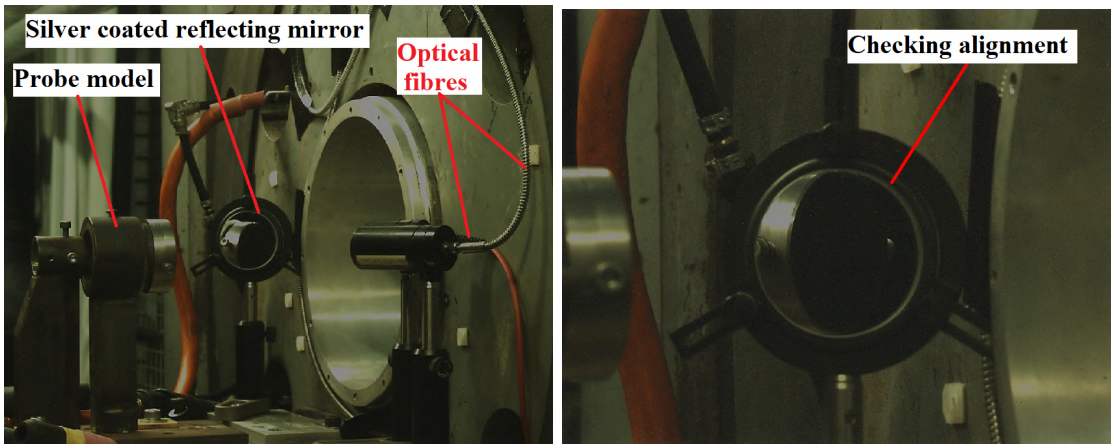


(a) Position of the mirror and spectrometer lens for access to the graphite disc, while keeping the flow path clear.

(b) What the camera sees of the probe reflected in the mirror.

Figure 3.14: Set-ups of probe, mirror, spectrometer lens and optical fibres.

The camera sees a hot surface image like the one shown in Figure 3.15. The geometry of the hot-spot is actually axisymmetric unlike the elliptical image seen by the camera. This results from the viewing angle. The image in Figure 3.15 is a combined image of the hotspot seen at the camera settings that keep the image below saturation and used for temperature analysis, overlaid on the visible image of the mirror with the probe visible as a reflection.

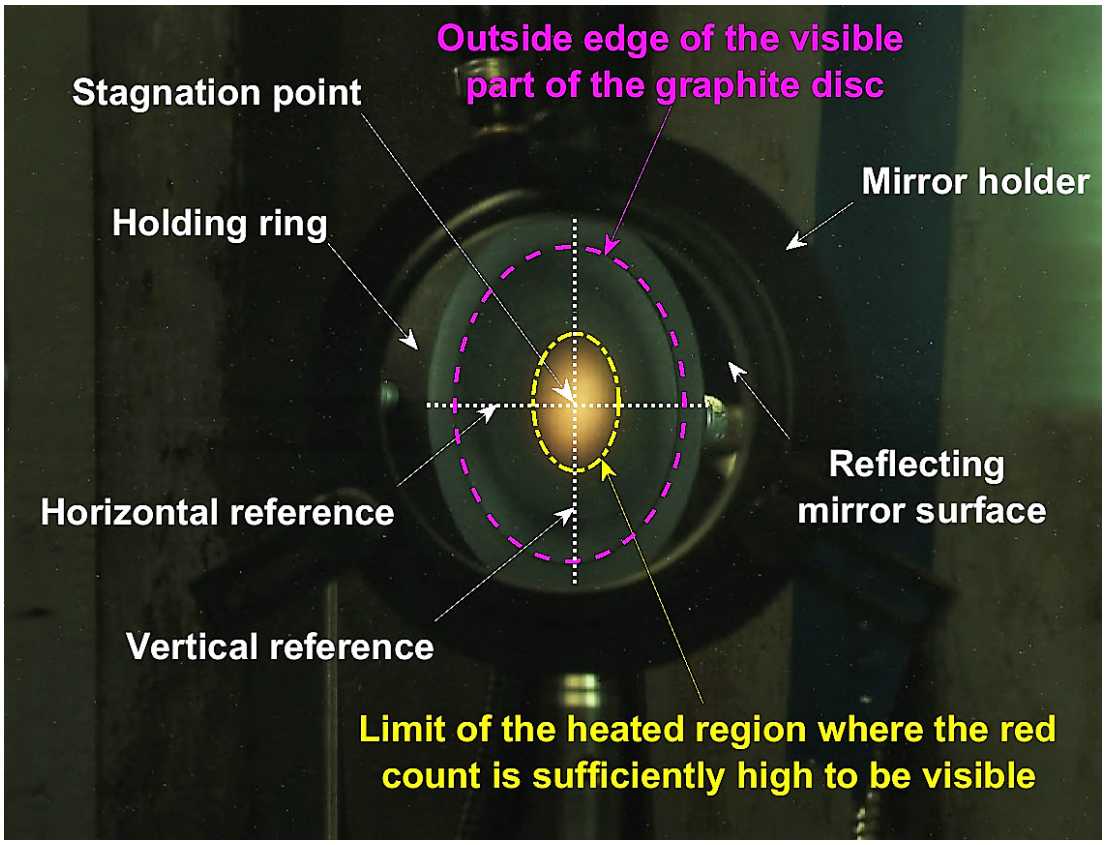


Figure 3.15: Image of the heated disc superimposed on a photograph of the probe seen by the Olympus camera used to measure the graphite disc surface temperatures.

To measure the hot-wall temperature, a temperature reference was determined from wavelength and intensity calibration of the Thorlabs instrument (shown in Figure 3.16) through the fitting of a Planck curve. The spectrometer has a wavelength range of 500 to 1000 $\mu$m and the spectrometer was calibrated with a Lab-Sphere source (illustrated in Figure 3.13a). Sample intensity was then converted to temperature using Planck curve fitting; details are presented in Appendix A. This reference temperature was correlated with the red-pixel of the Olympus camera as shown in Figure 3.11 in order to specify the surface temperature. The Olympus camera complemented the spectrometer by producing spatial temperature profiles across the heated surface at the high frame rate.

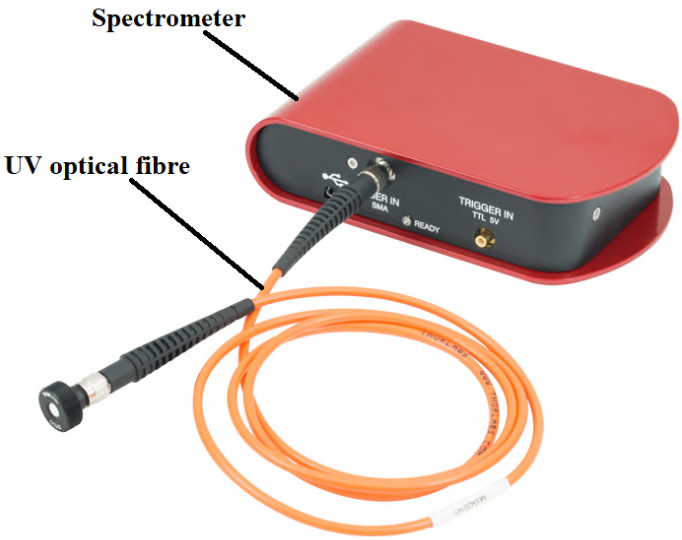


Figure 3.16: The UV spectrometer (Thorlabs instruments).

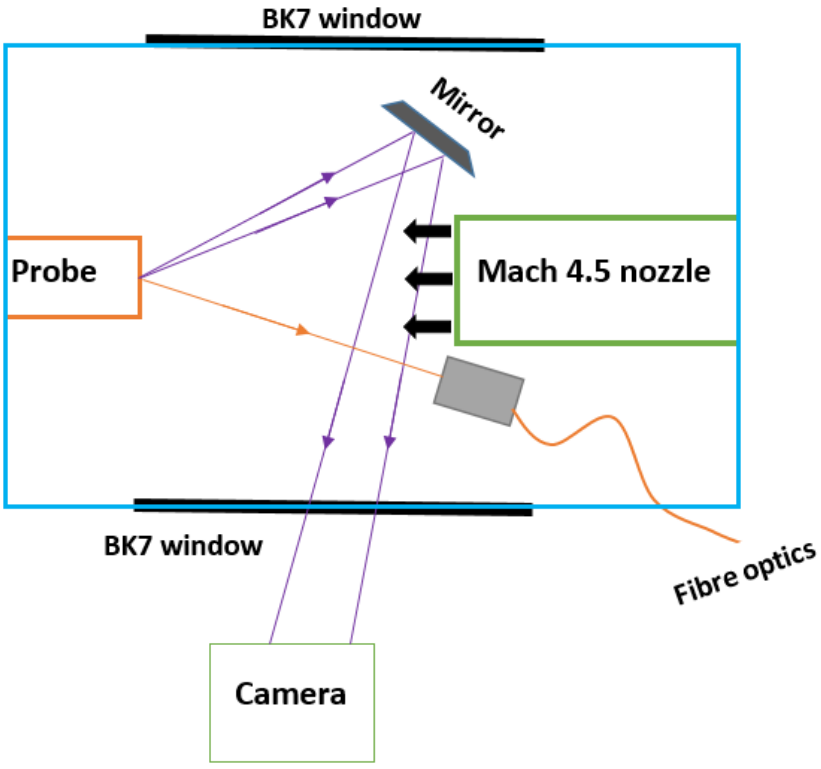


Figure 3.17: Illustration showing top view of optical arrangement.

The surface temperature of the graphite disc was found to increase with increasing

current as shown in Figure 3.18. Currents of 200 A, 250 A, 300 A, 350 A, and 400A were used. The DC supply from the welder was limited to 400 A in the present work, due to the physical capability of the electrode and shroud to tolerate the generated heat.

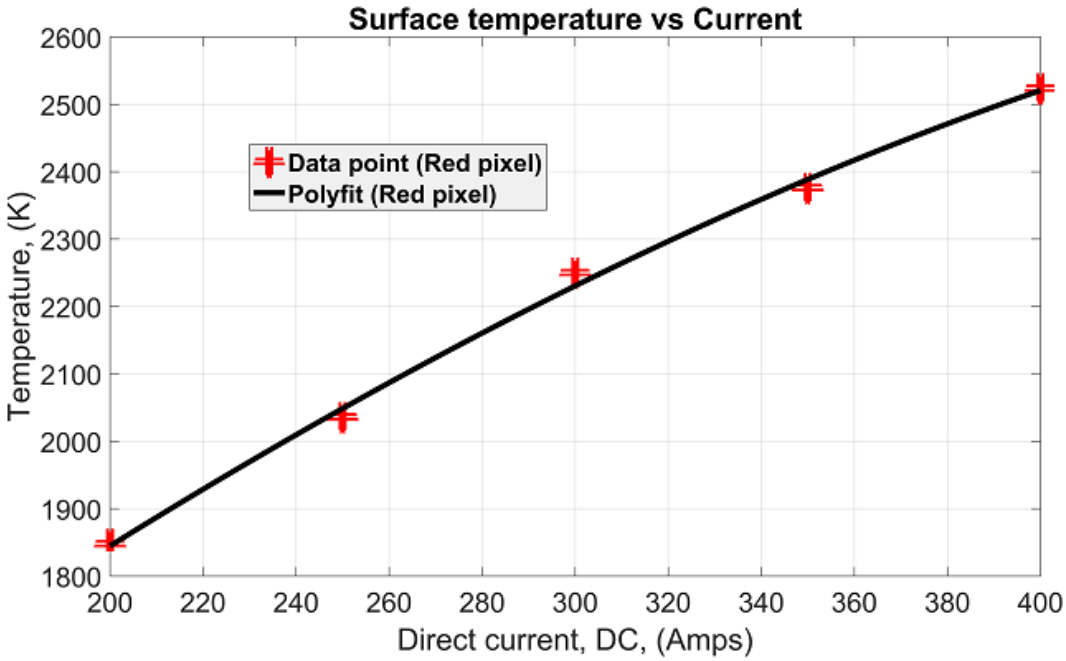


Figure 3.18: Relationship between maximum temperature on the upstream side of the graphite disc (at the stagnation point) after 15 seconds of heating, versus plasma current.

## 3.4 Optimisation of Plasma Heating

A series of experiments were conducted using different currents and different electrode gaps to ascertain the optimum combinations that will generate the best temperature profile on the front surface of the graphite; the results are shown in Figure 3.19. Various attempts were made to flatten the temperature profile, by adjusting argon flow rate, electrode gap, electrode protrusion from the shroud, the shroud shape and position. Moving the electrode gap to 18 mm produced a significant drop in the surface temperature which is represented by the broken blue line. The broken red line reached a temperature of 2950 K with an electrode protrusion of 3.5 mm but the end of the shroud could not tolerate the locally very high temperatures.

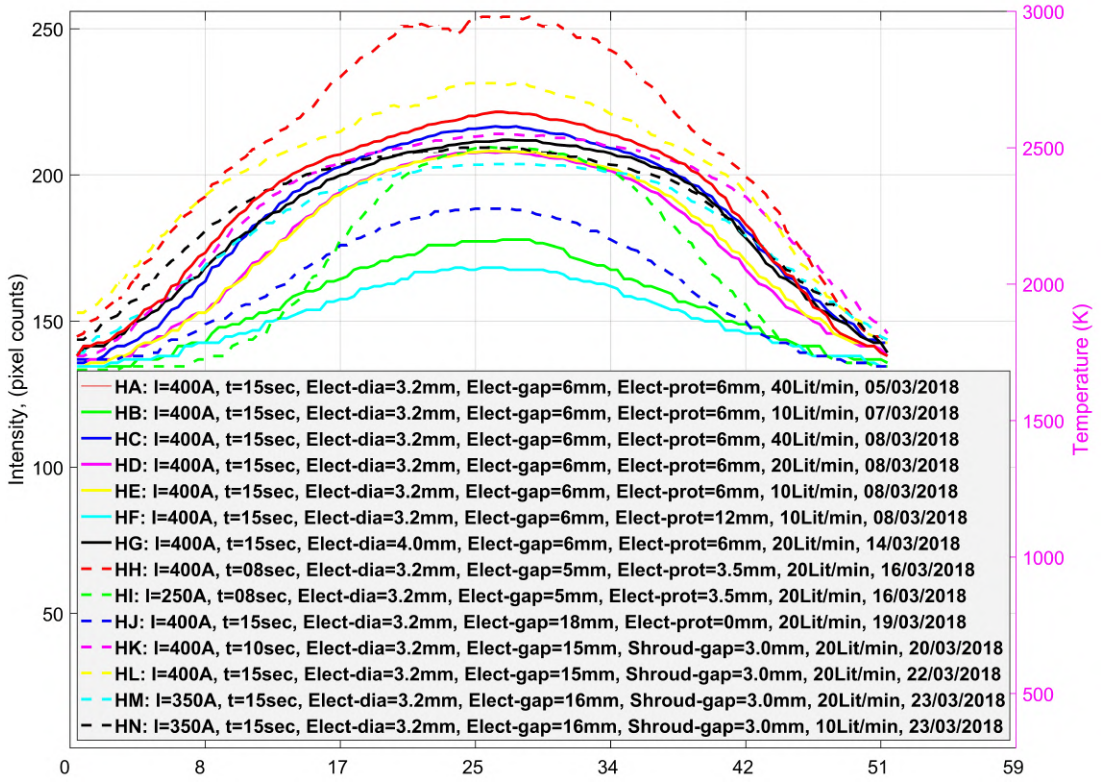


Figure 3.19: Preliminary pre-heating by combining different current, heating time, electrode diameter, electrode gap, electrode protrusion, additional shroud and argon flow.

Figure 3.20 shows the improved flatter temperature profile across the disc at an argon flow rate of 20 L/min. Aiming for a flatter and consistent temperature profile will reduce the complexity of analysis of the results from the experiments. The results shows a good agreement at a maximum surface temperature of about 2500 K for ten different runs at 400 Amps. No-flow conditions were used for all preheating tests. The legend in (Figure 3.20) is the set of conditions used for the ten pre-heating experiments completed on the same day.

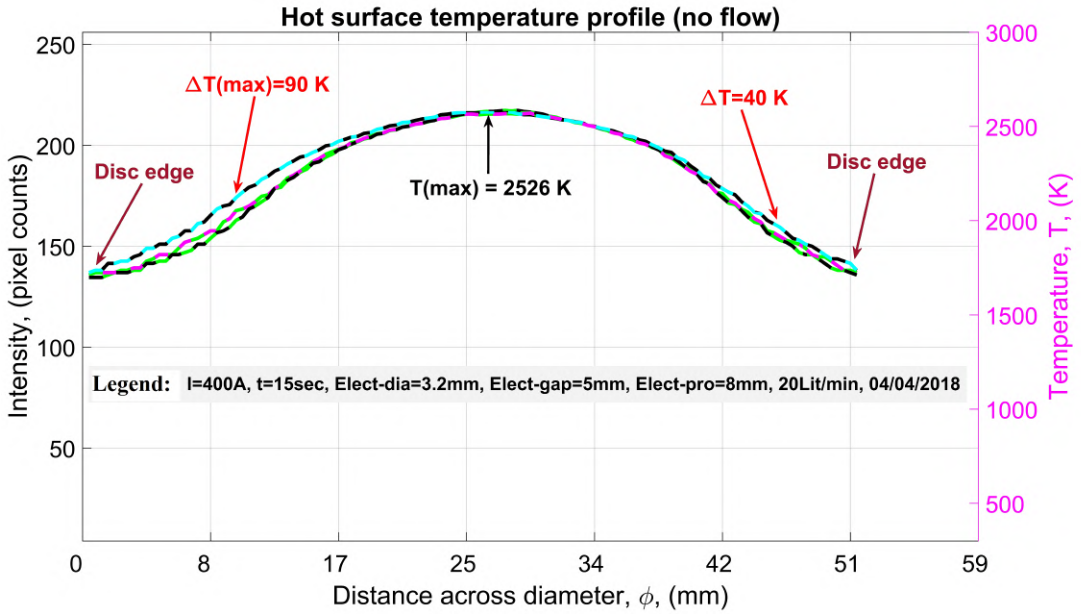


Figure 3.20: Repeatability of pre-heating tests at 400 Amps current, 15 seconds heating time, 3.2 mm electrode diameter, 5 mm electrode gap, 8 mm electrode protrusion, and 20 L/min argon flow rate. All plots are under the same conditions described.

The results in Figure 3.20 show a general consistency between the various pre-heating tests, around the stagnation region. A consistent maximum temperature of around 2526 ± 2 K was achieved. Significant temperature differences between the runs was only experienced at about 12 mm from the outer edges, with a maximum difference of about 90 K.

## 3.5 Simulation of Graphite Pre-heating

### 3.5.1 Overview and Purpose

Pre-heating of the graphite disc was achieved with plasma generated by a DC current between a tungsten electrode and the back (downstream) side of the disc. Figure 3.21 is a sectional view of the model which illustrates the heat transfer processes from the hot plasma to the disc. The plasma was formed when the current flowed from the electrode to the graphite disc through the argon gas at low pressure. The disc was heated through

convection from the plasma, energy delivered when the plasma interacted on the back of the disc and radiated heat from the plasma and the other heated components in contact with the plasma. The disc acted as an electrode for the plasma, so the current creating the plasma flowed through the disc to the connector, generating some resistive heating in the disc. The relatively high thermal conductivity of the graphite generated the high temperatures on the front of the disc while allowing the disc to maintain its structure.

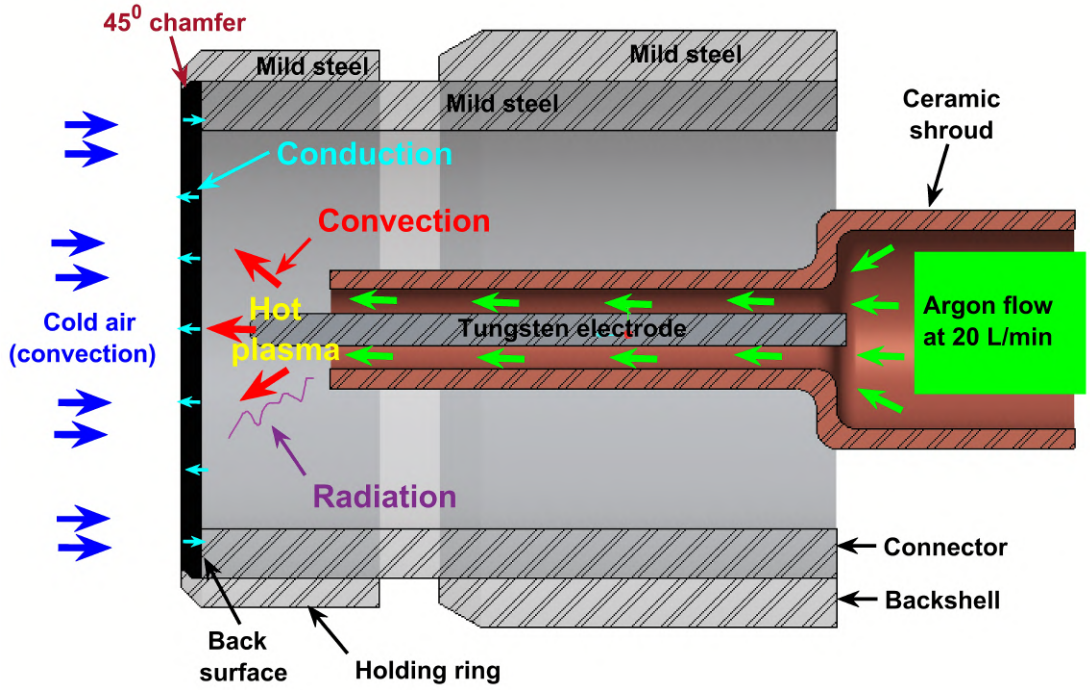


Figure 3.21: Illustration of heat transfer processes from hot plasma to the graphite disc.

### 3.5.2 Materials Properties Used in Simulations

Carbon is the basic ingredient for the majority of ablative heat shield materials (Lachaud, Aspa and Vignoles, 2008). Graphite is considered as the basic carbon material (Eswein et al., 2011) for assessing ablation properties. Graphite remains a class of superior carbonaceous material because it possesses refractory ability, high thermal shock resistance, good mechanical strength at high temperatures, excellent machinability, high thermal conductivity, high sublimation temperature, a relatively low oxidation rate, and low material cost (Scala, 1962). This supports the choice of graphite as a representative ablative material in the present work.

Table 3.3: Properties of graphite used in the present work. A product of Graphite Australia.

| Physical properties of PCC-X2 graphite | | | | |
|---|---|---|---|---|
| Bulk density | Maximum particle size | Rockwell hardness | Compressive strength | Flexural strength |
| 1.78 g/cm$^3$ | 0.045 mm | 85 | 60 MPa | 30 MPa |
| **Other properties of PCC-X2 graphite** | | | | |
| Porosity | Specific resistance | Ash content | Thermal conductivity | CTE |
| 12 - 14 % | 8.0 $\mu\Omega$m | 0.05 % | 95 W/(mK) | 2.7 $\times$ 10$^{-6}$ (K$^{-1}$) |

CTE refers to Coefficient of Thermal Expansion.

The graphite used in the present work is an iso-statically pressed graphite with grade PCC-X2 from Graphite Australia with the properties listed in Table 3.3. Oxidation analysis of other materials can be made by simply reproducing the methodology and replacing the disc material properties in the simulation.

#### 3.5.2.1 Boundary Conditions for Simulation

The procedure started by using a transient thermal simulation coupled with an engineering data source containing graphite and mild-steel materials. Heat flux was applied to the back of the disc as shown in Figure 3.22. Only 40 mm of the disc diameter was directly in contact with the plasma at the back of the disc. This was divided into ten segments with diameters from 4 mm to 40 mm with successive diameter increments of 4 mm from the stagnation point to the edges. Pre-heating time was 15 seconds. Radiation was applied. The connection type adopted at the contact regions were 'rough' with manually imputed values of thermal conductance. A more complete description of the simulation settings is given in Section 5.2.

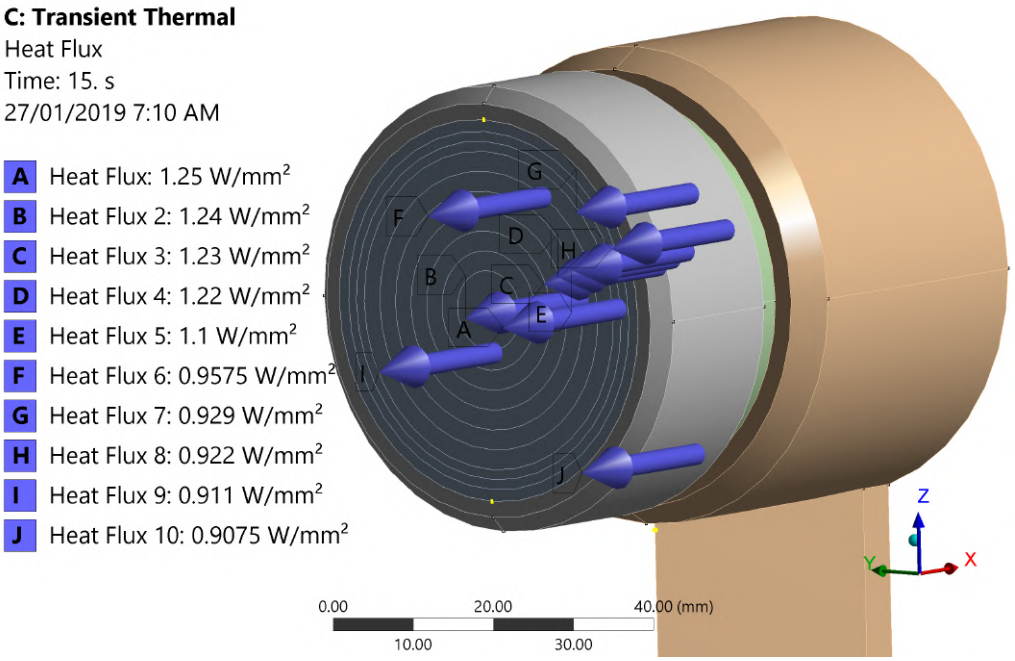


Figure 3.22: Set-up showing boundary conditions for heat flux.

### 3.5.3 Simulation Results for Heating Analysis

The temperature distribution of the experimental probe was simulated using a 3D Finite Element Analysis (FEA) with Ansys. The simulation is for no flow and the heat flux inputs (Figure 3.22) were tuned to produce the measured surface temperature of the experimental set up. Figure 3.23 shows the temperature contours across the centre plane using a transient thermal simulation for a heating duration of 15 seconds. The graphite disc reached a maximum temperature of about 2530 K at the stagnation point, and decreased non-linearly from the stagnation point to about 1800 K at the edges. The tuned heat flux inputs produced a reasonable agreement between the experimental temperature profile and the simulated temperature profile.

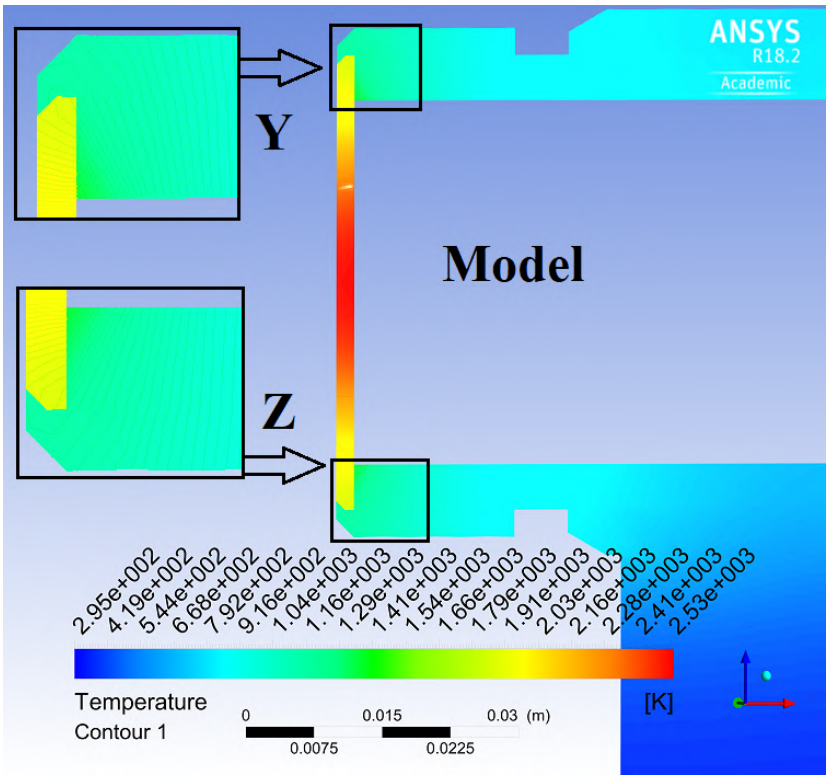


Figure 3.23: Temperature contours across the centre plane through simulation tuned to produce the measured probe temperature profile without flow, where Y and Z are the contact regions between the disc and its retainer.

Three reference lines A, B, and C positioned on both sides and midway through the disc, as shown in Figure 3.24, were used to evaluate the temperature gradient through the graphite disc.

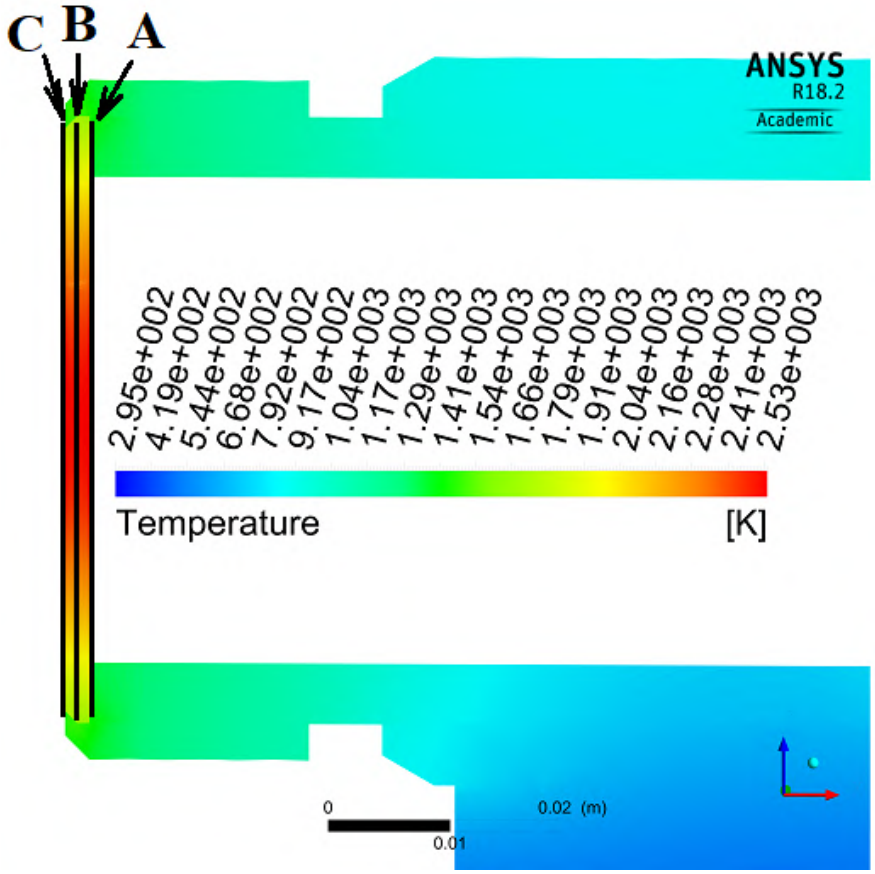


Figure 3.24: Thermal analysis of the experimental probe using three reference lines.

Figure 3.25 shows results from the transient thermal simulation of the probe during heating. The temperature rise was fastest at the onset of the heating, gradually decreased as time progressed, and approaching a steady state condition at the end of 15 seconds.

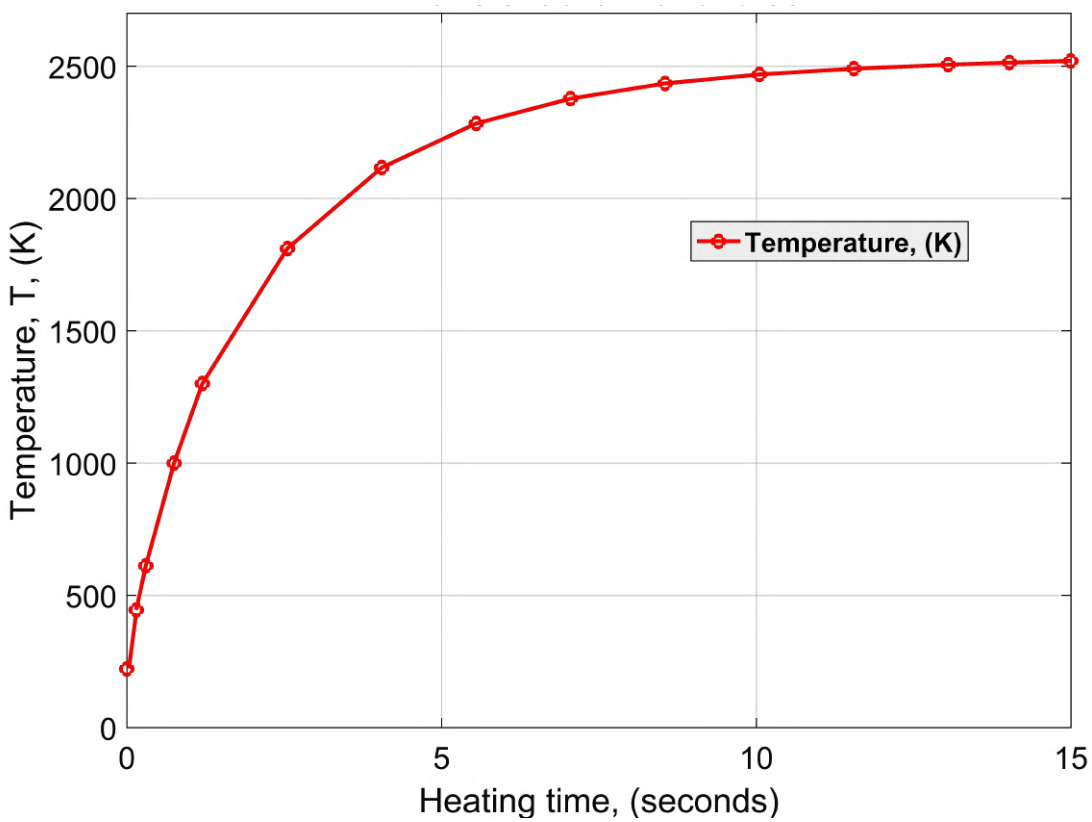


Figure 3.25: Simulated stagnation point temperature rise for 15 seconds of heating using no-flow conditions.

Figure 3.26 shows the temperature profile of the three reference lines, A, B and C, with maximum values at or adjacent to the stagnation point. Moving away from the stagnation point to the disc edges (just before the contact regions Y and Z), the temperature decreased along paths A, B, and C. Path A is on the disc surface on the plasma side. The ends of path A pass through the contact between the holding ring and the steel body of the probe. Path B is within the disc and its ends pass through the contact with the holding ring. Path C is on the side of the disc that will be exposed to the flow; the last 1 mm at each end of path C are at the surface of the holding ring. At the contact regions Y and Z in Figure 3.26, the temperatures drops sharply due to the low conductivity across the contact and the high thermal diffusivity of mild steel. By setting the contact region conductivity to produce the experimentally measured disc temperature and comparing the temperatures at the disc edges (zone Y and Z) to the surrounding mild steel (zone 1 and 2), a step in temperature of about 570 K results. The thermal diffusivity of a material is represented in Equation 3.8, where k is the

thermal conductivity constant (W/(m.K)), $\rho$ is density (kg/m$^3$), and $c_p$ is the specific heat capacity (J/(kg.K)).

$$\alpha = \frac{k}{\rho C_p} \tag{3.8}$$

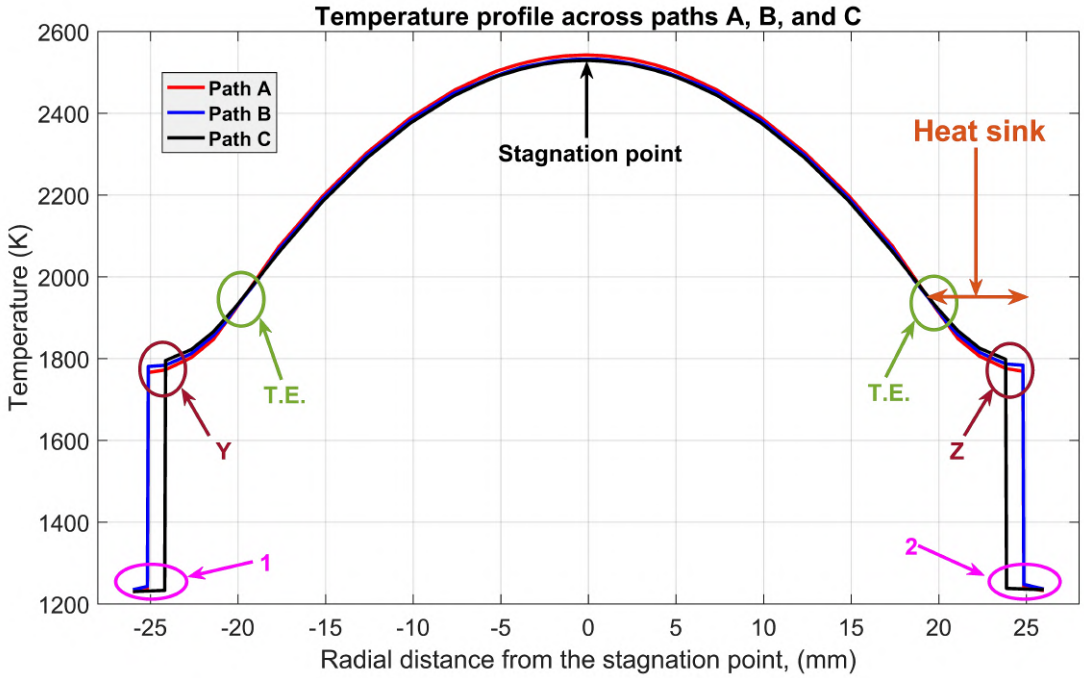


Figure 3.26: Temperature profiles from simulation showing along three reference lines A, B, and C. The zones marked Y and Z are the contact regions at the disc while the zones marked 1 and 2 are the corresponding contact regions at the holding ring. T.E represents thermal equilibrium zone. The thermal equilibrium zone is the region where the three reference lines A, B, and C have the same temperature values.

The simulation suggests that the steel should tolerate pre-heating for the 15 seconds used in the experiments.

The simulation to replicate the experimentally measured temperature profile was created to obtain a suitable heat flux input to use in a fully coupled transient simulation of the experiments. This coupled CFD and thermal transient simulation was not completed.

### 3.5.4 Establishing Temperature Profiles for Input into Simulations

#### 3.5.4.1 Approaching a Steady State Temperature Profile

Figure 3.27 shows the degree of conformity between simulation and experimental temperature profiles. In the simulation, only the temperature profile along path C was used because the Olympus camera only sees the surface facing the flow. Although the measured temperature distribution from experiment matches with simulation, a comparison of the heat-up time is needed to complement this steady state result.

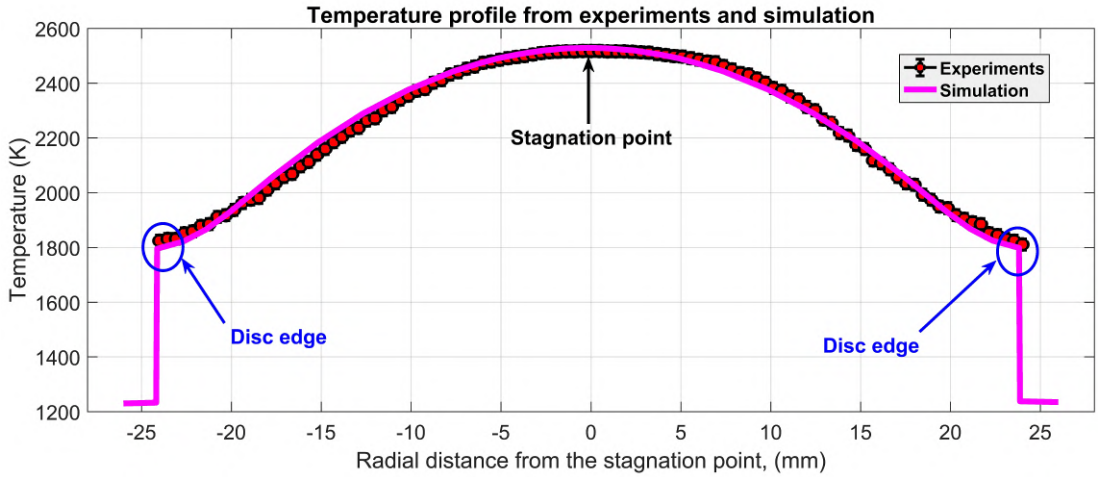


Figure 3.27: Temperature profiles showing the degree of conformity of simulation with experiments.

#### 3.5.4.2 Transient Temperature Profile

The spatial distribution during heat-up time is an independent validation of the simulation results. It compares the heat-up time from the simulations with experiments by indicating the rates of temperature rise in the stagnation point of the sample. Figure 3.28 shows the heat-up time from simulation and experiments. It was difficult to measure temperatures below 1000 K because of the camera settings. The pre-heating starts from 0 and ends at 15 seconds while the cold flow was immediately released at 15 seconds. The heating stops at about 16 seconds and the temperature profile after 16 seconds shows the rate of cooling.

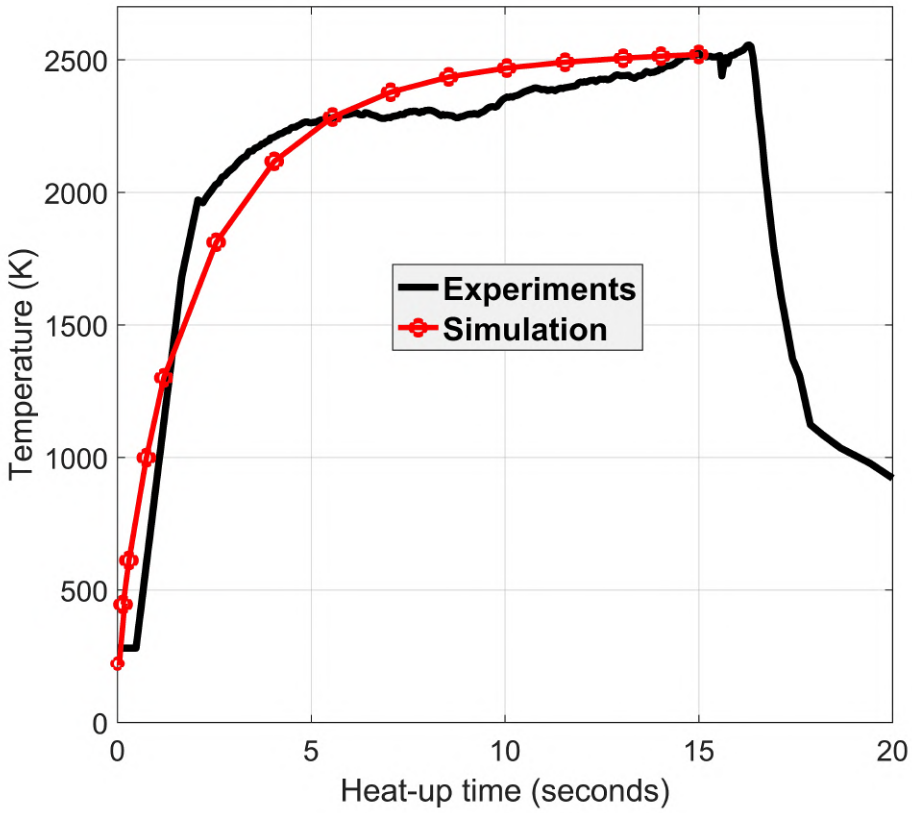


Figure 3.28: Temperature profiles showing the heat-up time from simulation and experiments. The Mach 4.5 flow started at 15 seconds and ended at about 15.5 seconds in the experiment.

## 3.6 Thermal Damage During Pre-heating

Various attempts to direct the plasma flow to increase heating at the outer diameter of the disc were unsuccessful. Figure 3.29d shows the resulting failure of one of the shroud combinations used for this purpose. The use of a sacrificial wire enabled good plasma start repeatability but created problems associated with the deposition of the molten metal from the wire on the disc surface leading to weighing errors. Although an effective improver to starting the plasma, the use of sacrificial wire was discontinued. The long series of trials of various arrangements concluded that a 5 mm gap with 8 mm electrode protrusion from the standard shroud was the best combination for reliability and good temperature profile. An electrode gap of 5 mm, resulted in a Pressure/(Electrode-spacing) in the range of 1.5 - 2.1 mmHg.cm which has a good agreement with the

Paschen's minimum breakdown voltage for the argon gas.

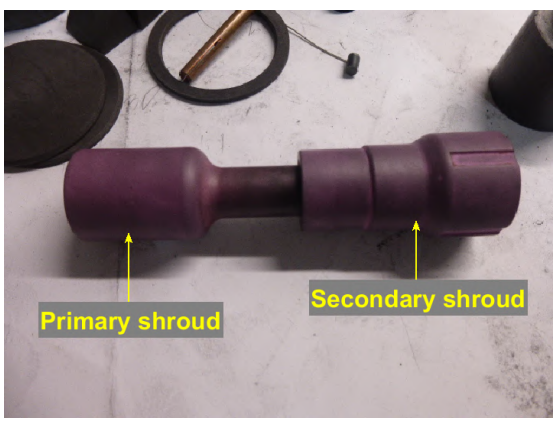


(a) Adding a secondary shroud.

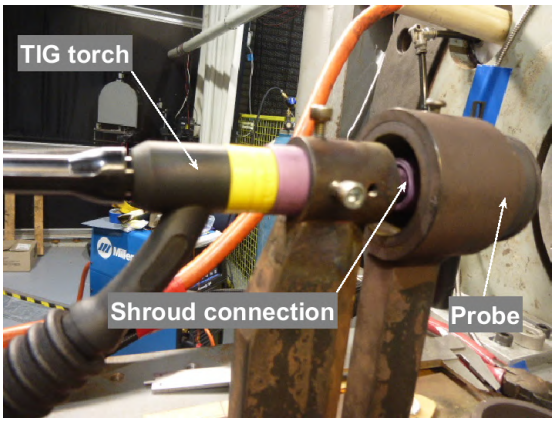


(b) Connecting shrouds to TIG torch.

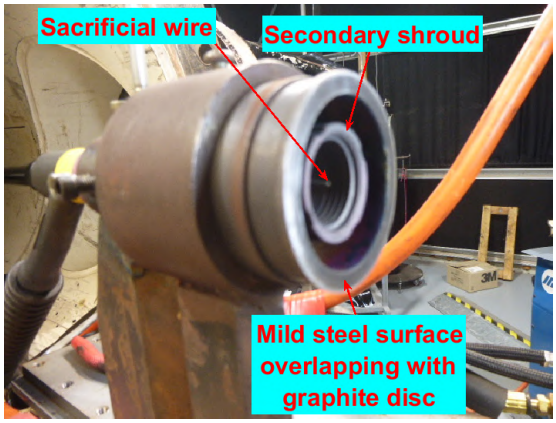


(c) Face of secondary shroud.

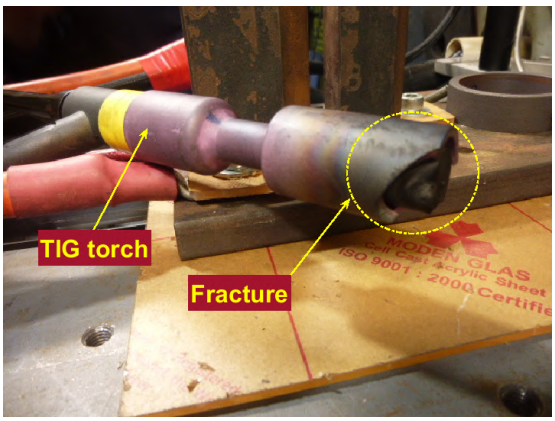


(d) Thermal fracture of secondary shroud.

Figure 3.29: Aspects of the TIG torch used to create the plasma and the failure of one of the secondary shrouds used in trials in attempts to improve the temperature profile across the disc.

Many trials were conducted in attempts to improve the temperature profile across the disc. Various techniques were employed in efforts to reduce the temperature difference between the centre and edge of the disc. Most attempts were motivated by the evident localised grounding of the plasma on the back of the disc. Attempts to distribute this to a larger proportion of the disc or to deflect the plasma to increase heating at the outer regions of the discs proved unsuccessful. Figure 3.30 shows some of the arrangements explored.

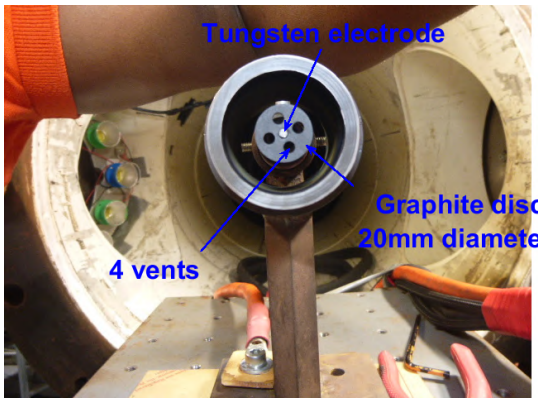


(a) A circular graphite disc was added at the end of the electrode. Holes were included to maintain argon gas supply to the plasma.

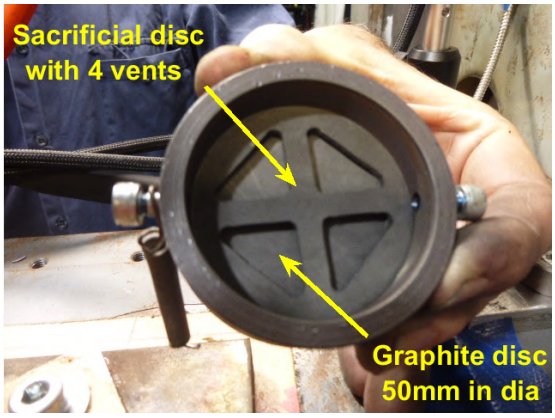


(b) A graphite disc was machined to increase the material thickness near the centre of the disc, hoping to shift the majority of heating towards the outer edges.

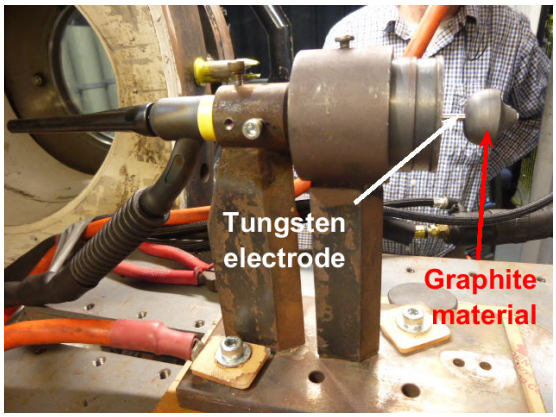


(c) This image shows one of various axisymmetric graphite tips trialled to investigate changing the shape of the plasma.

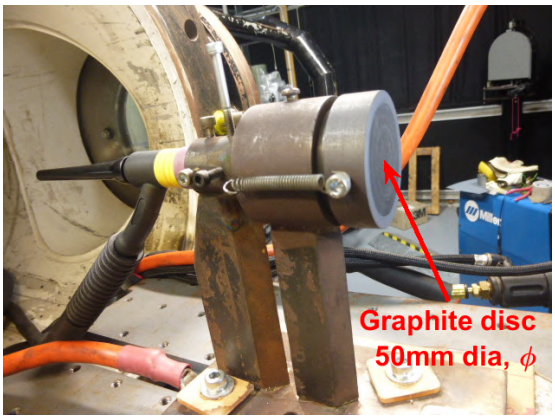


(d) All changes wre made within the probe so that the heated disc remained in the same position in the Mach 4.5 flow.

Figure 3.30: Various attempts to modify the plasma and argon flow to flatten the temperature profile across the disc. None proved successful enough to use and the experiments proceeded with the temperature profile shown in Figure 3.27.

Increasing the surface roughness could potentially contribute to an unsteady shear layer (Combs, Clemens and Danehy, 2014). This requires that new graphite samples should be prepared in a reproducible way. The images in Figure 3.31 shows a used disc after one heated-with-flow run while Figure 3.32 shows some preparations of graphite discs before use.

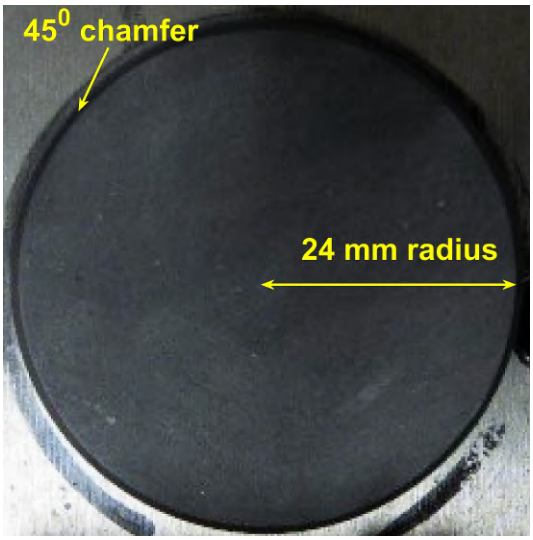


(a) Front of graphite disc (new).

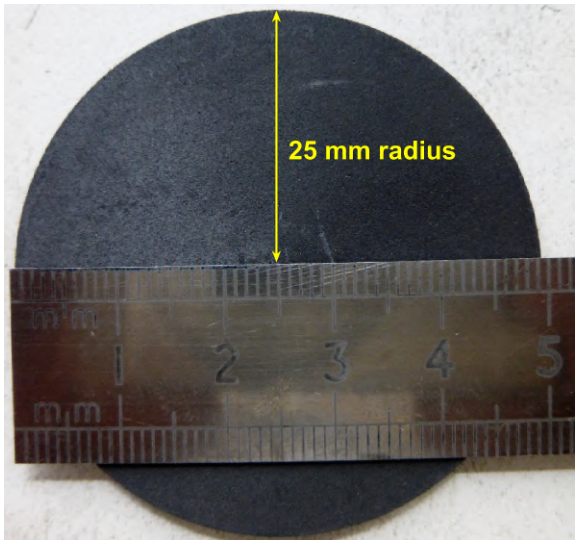


(b) Back of graphite disc (new).

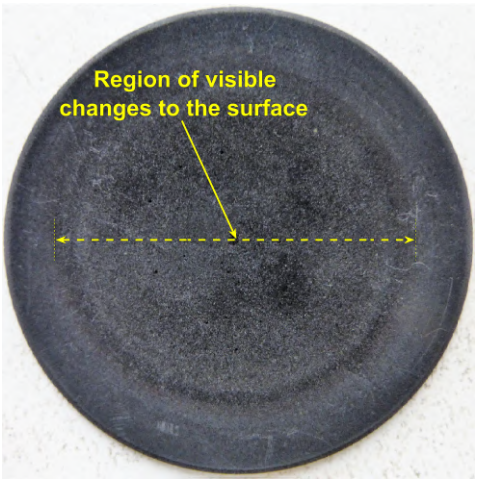


(c) Front of graphite disc (used).

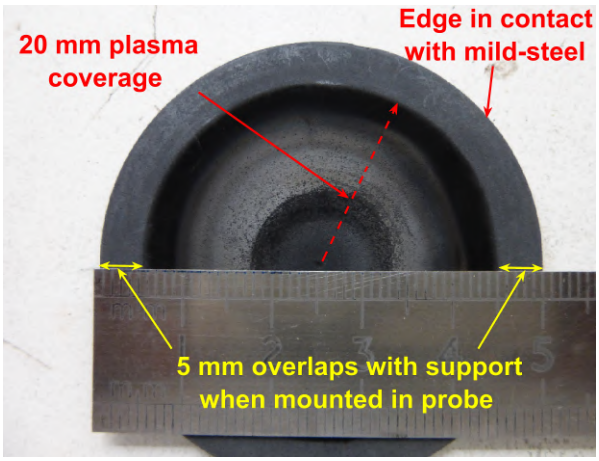


(d) Back of graphite disc (used).

Figure 3.31: Graphite disc showing the effect of the plasma on the back of the disc and indication on the side exposed to flow, where a region of higher temperature together with the Mach 4.5 flow has made visible changes to the surface.

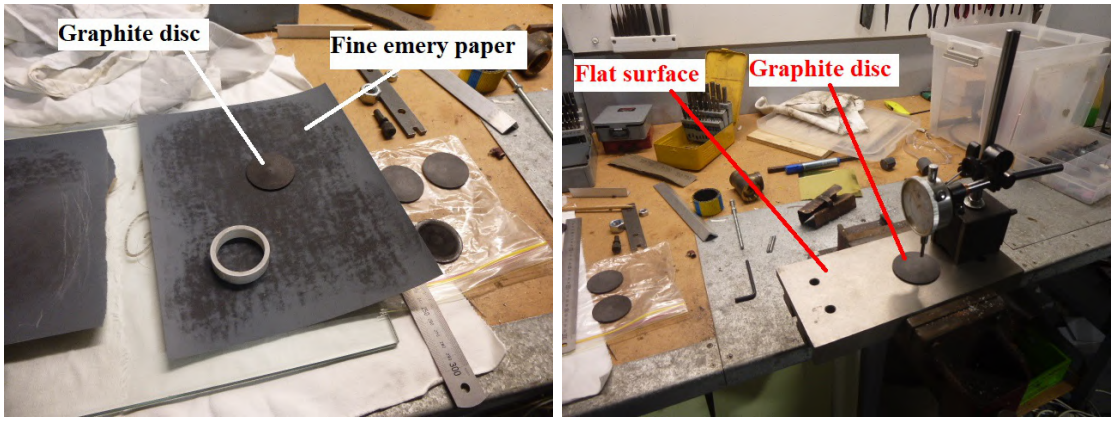


(a) Smoothing with fine emery paper. (b) Surface check using surface gauge.

Figure 3.32: Preparing new discs for experiments including surface flatness checks.

## 3.7 Mach 4.5 Facility

### 3.7.1 Configuration

The TUSQ facility was configured in an atmospheric blow-down arrangement with a Mach 4.5 nozzle. This provided a suitable hypersonic flow environment and offered the advantage of longer flow durationsof approximately 0.5 s, which was very useful for the mass-loss assessments. Unlike hypersonic aerodynamic heating where the heat flux is from hot flow to cold model, the direction of heat flux at TUSQ is from the hot model to cold flow. Figure 3.33 shows the general set-up of the experimental probe in the atmospheric blow-down configuration at TUSQ wind tunnel facility.

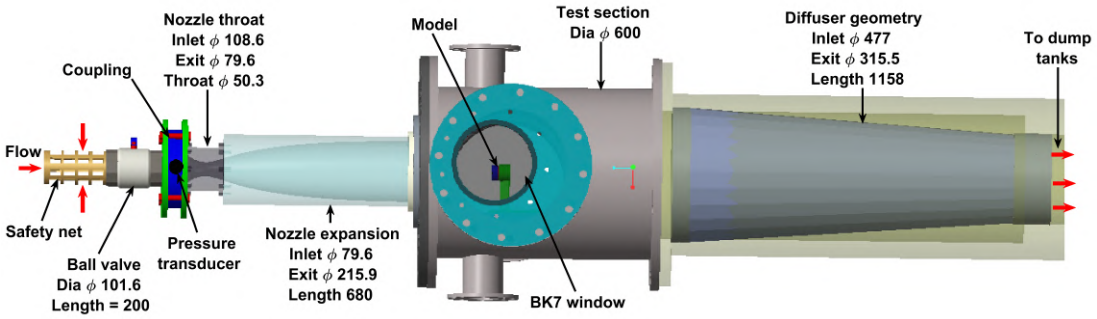


Figure 3.33: Atmospheric blow-down configuration of TUSQ wind tunnel facility.

Figure 3.34 shows the solid model of the atmospheric blow-down configuration at TUSQ. A 4 inch ball valve was used to control the inlet flow, and was manually operated.

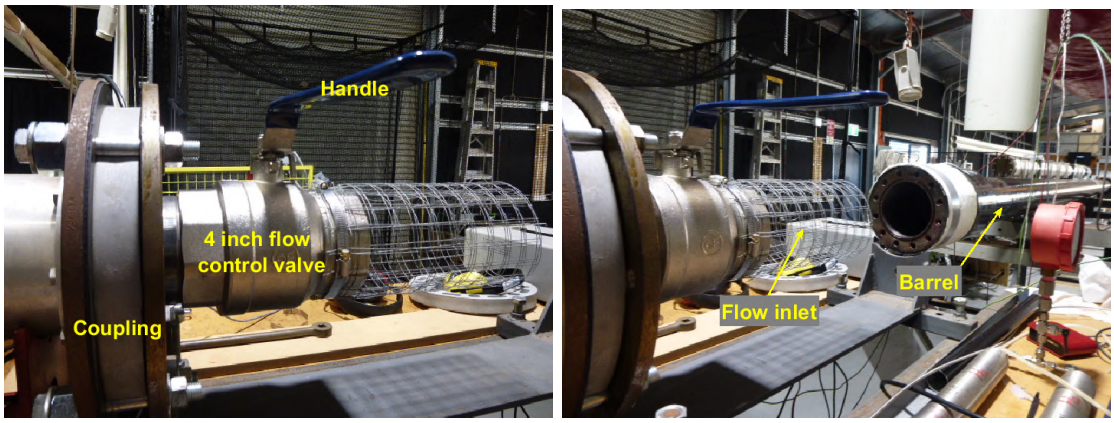


(a) Mach 4.5 atmospheric blow-down. (b) Barrel disassembled for blow-down.

Figure 3.34: The barrel required for higher mach numvber flows is disconnected for the Mach 4.5 atmospheric blow-down configuration.

### 3.7.2 Definition of Flow Conditions

Characterisation of the flow in the test section for the experiments was essential to quantify flow conditions for simulations. Flow conditions were assessed with an array of pitot pressure transducers as shown in Figure 3.35.

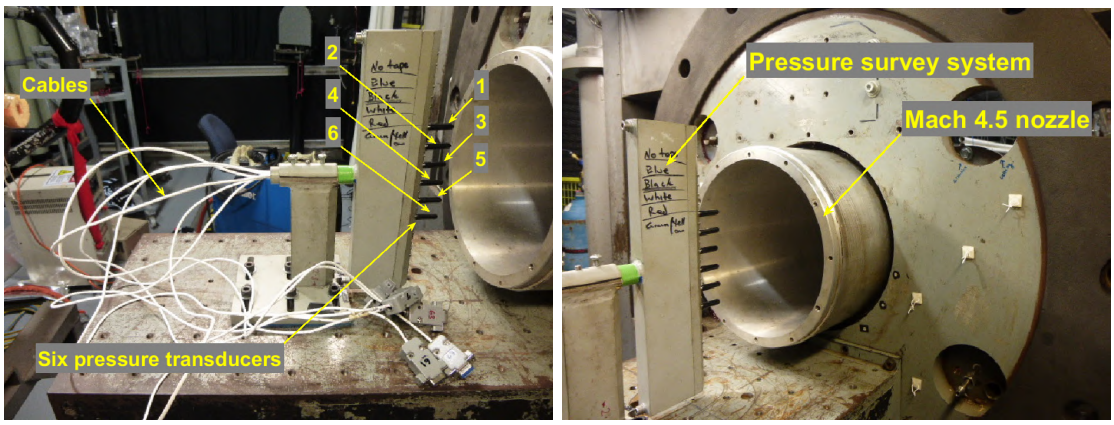


(a) Six transducers used in pitot rake. (b) Pitot pressure rake at Mach 4.5 nozzle exit.

Figure 3.35: Mounting of pitot pressure rake in the TUSQ test section.

The pitot pressure survey data was collected through the main Data Acquisition system (DAQ), as shown in Figure 3.36 The main components of the DAQ and the control systems used during operation of the experiments are the test section pressure indicator, trigger board and power supply, pulse generator for the Schlieren camera, and the computer components.

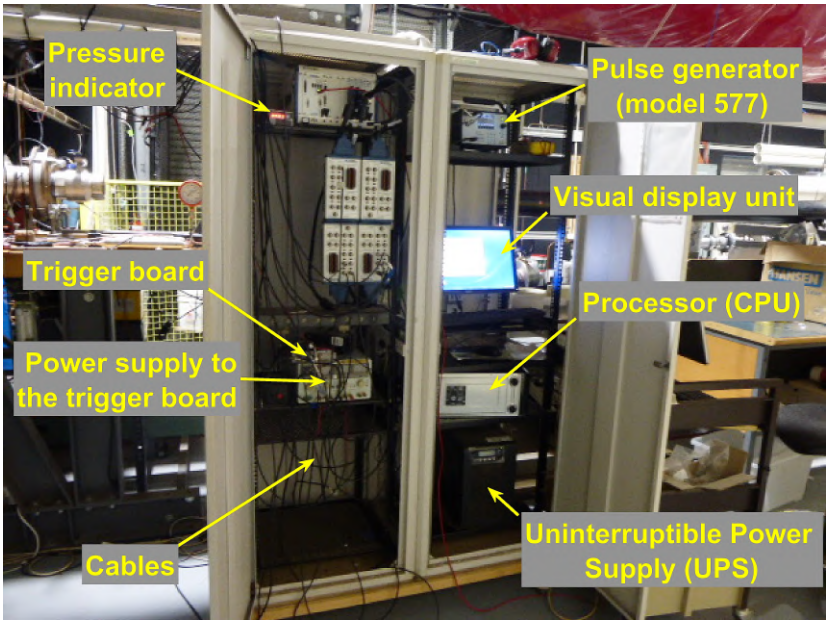


Figure 3.36: The TUSQ data acquisition system (DAQ) used for the experiments.

As shown in Figure 3.37, during a calibrating run, the Test Section Pressure, the Pitot Pressure and the Plenum Pressure were all constant while the nozzle operated in a started condition during a run from approximately 0.7 seconds at point B to 1.2 seconds at point C. The various plots of the Pitot Pressure are for all the transducers in the array. The transducers in the core flow show the steady flow condition while the nozzle is in the started condition. The annotations show the useful experimental run time starts at point B and ends at point C, points D and E are after the flow control valve is closed. The test section pressure is held at minimum during the run from points B to C. The steps after point C at about 1.2 seconds is because the ejector characteristic of the diffuser downstream of the test section could no longer hold the test section pressure low. So at about 1.2 seconds (point C), the nozzle unstarted and the test section pressure progressively increased, the Pitot pressure fluctuated due to turbulent flow leaving the unstarted nozzle, and the Plenum pressure approached a constant for

another 1.5 seconds indicating a relatively constant flow rate. This suggests that the nozzle unstarted due to rising back-pressure in the test section.

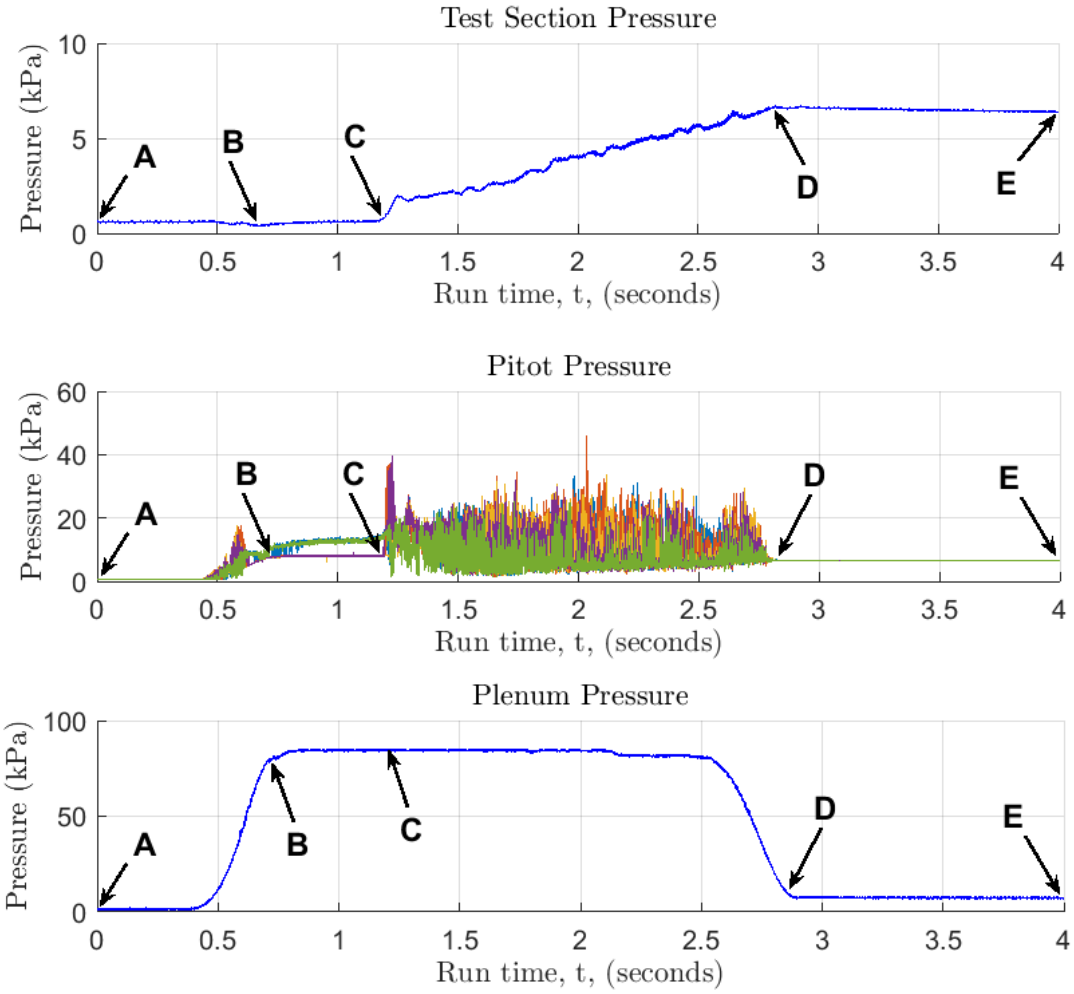


Figure 3.37: Pressure survey array, plenum and test section pressure during a calibration run. The green and blue traces of the Pitot array are not in the core flow of the nozzle, so they do not see core flow Pitot pressure.

Confirmation of similar performance during experiments with the graphite disc was based on the comparison of the pressure in the plenum, immediately upstream of the nozzle inlet and the test section pressure during the run. Confirmation of the flow characteristic of the nozzle (nozzle start) was supported by Schlieren high speed video images. The flow Mach number results derived from the Pitot Pressure and Plenum Pressure are shown in Figure 3.38. The Mach number of almost 4.5 lasted for about 0.5 seconds (from time 0.7 - 1.2 approximately).

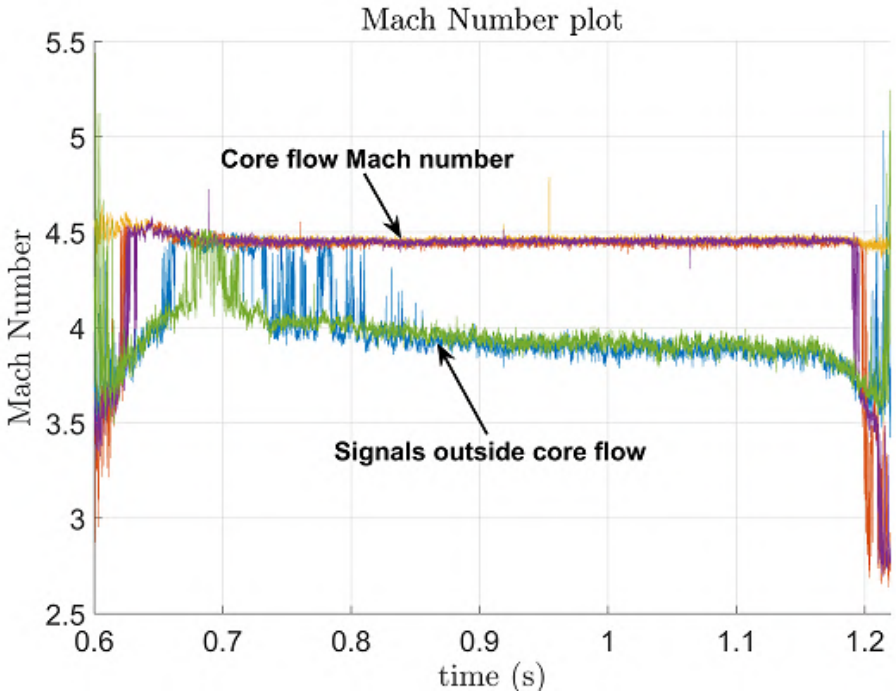


Figure 3.38: Mach number plot using the data from pressure survey system. Each line has a different Kulite sensor, with different radial location, and different axial position. The blue and green traces of the Pitot array were not in the core flow of the nozzle, and so they did not see core flow Mach number.

The Schlieren images in Figure 3.39 show the orientation of the experimental model with the bow shock easily identifiable.

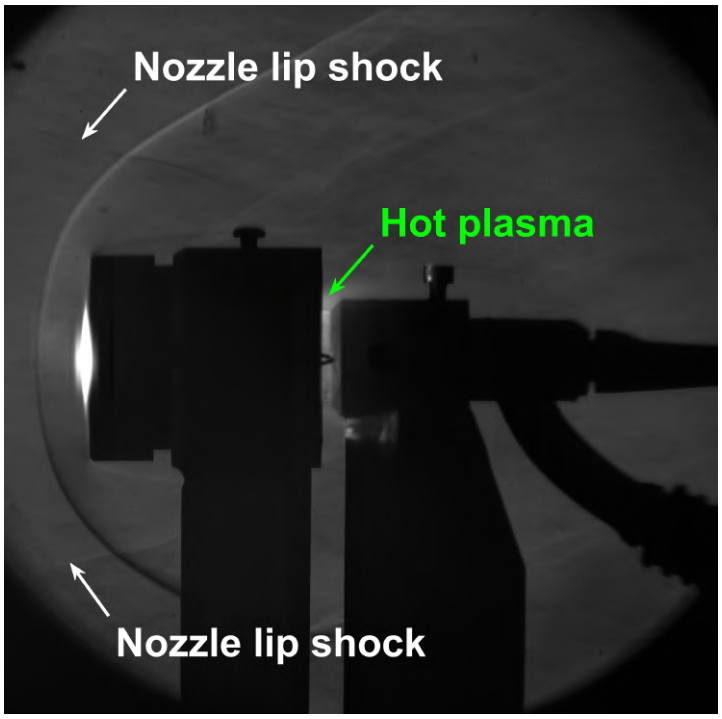


Figure 3.39: High speed camera Schlieren imaging for a heated-with-flow at Mach 4.5 at TUSQ at about the time flow would normally be started.

### 3.7.3 Facility Operation for Pre-heated Sample Experiments

An accurate assessment of the duration of the flow in the experiments is essential for accurate evaluation of the mass loss rate. The TUSQ data acquisition system (DAQ), automatically saves the run times which allows the duration of each run to be determined. Knowing the mass losses and using the run times from the DAQ, the average material loss rate was determined.

Figure 3.40 shows the Schlieren arrangement used during the experiments. The Schlieren technique based on the principle of changing densities in the gas was used to identify the establishment of the bow shock and therefore the commencement of Mach 4.5 flow. The high speed camera was set at a frame-rate of 2500 fps and frames at the specific points during the flow are shown in Figure 3.41.

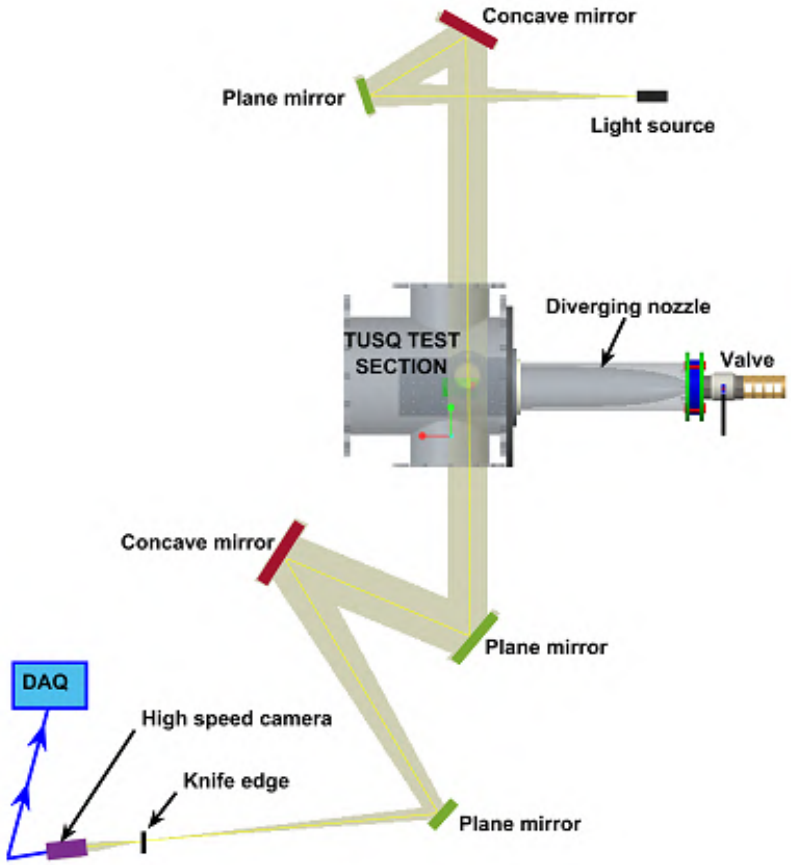


Figure 3.40: The arrangement of Schlieren video for the experiments.

Figure 3.41 and Figure 3.42 show the run durations of five experiments conducted prior to the sixteen runs of the main experiment. The duration varied between runs due to human factors associated with manual opening and closing of the valve. The start and end times were taken as the times the flows produce a clearly define bow shock. The rapid rise in plenum pressure (the pressure upstream of the nozzle inlet) shows that transition from valve closed to open and open to closed was relatively fast, typically less than 0.05 seconds.

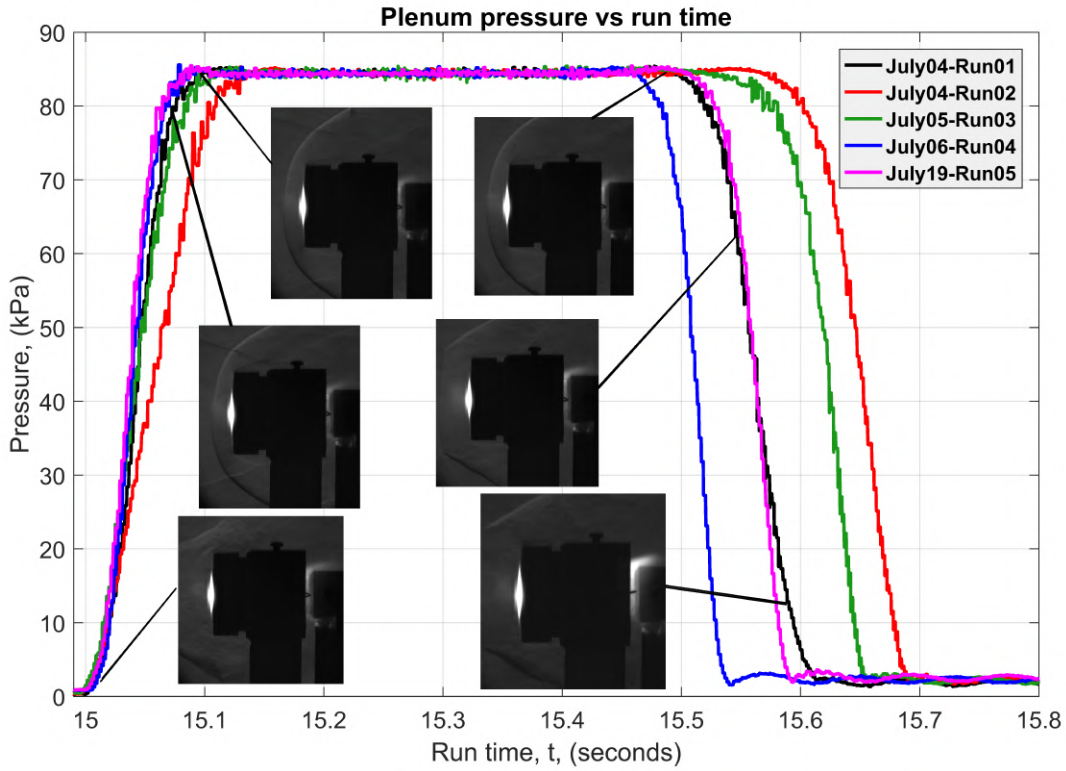


Figure 3.41: Matching run times with Schlieren images to identify when flow starts.

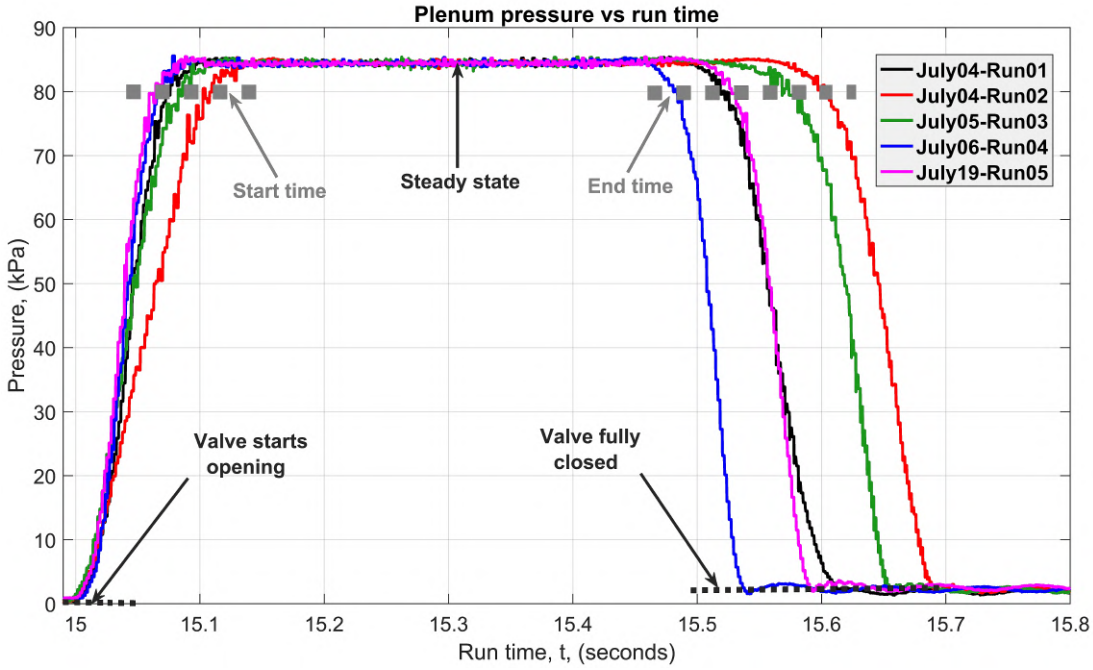


Figure 3.42: The start and end times from runs prior to the 16 runs of the main mass loss experiments. Same data as Figure 3.41.

The start and end times for the sixteen heated-with-flow runs are shown in Figure 3.43. The shortest run time was 0.45 seconds while the longest was 0.64 seconds. This gives an average run time of 0.54 seconds for a 16 heated-with-flow run.

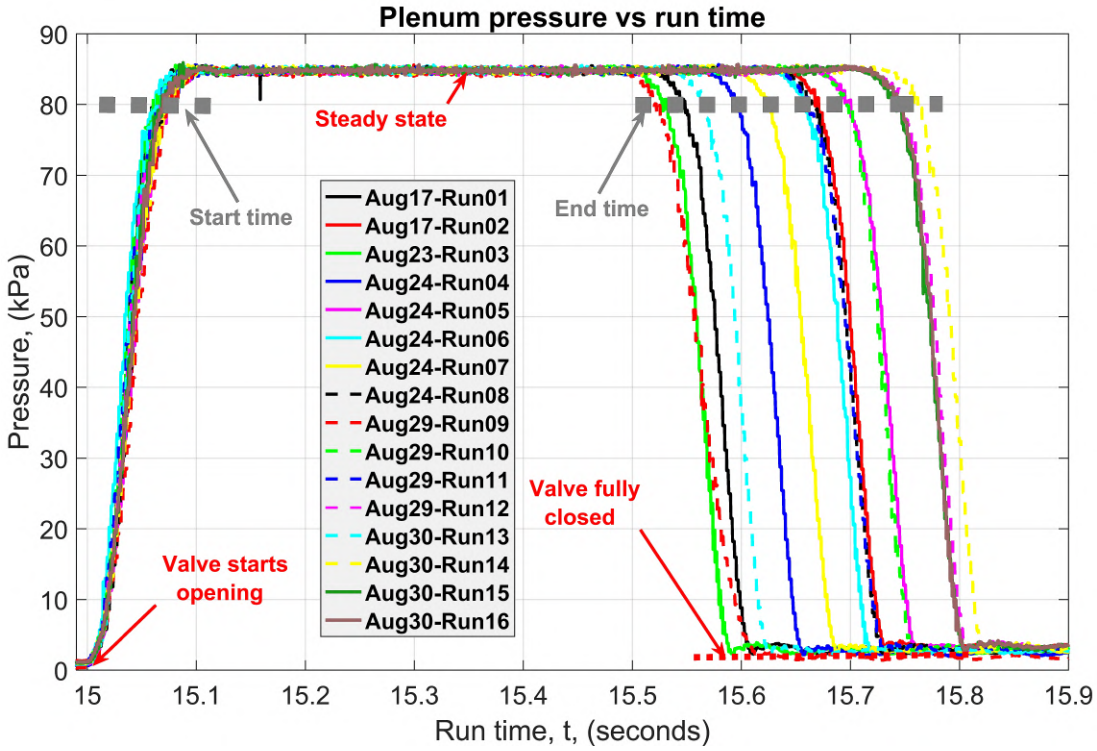


Figure 3.43: The start and end times from the 16 heated-with-flow run of the experiments used to determine material loss rates. Mass loss was measured for each of runs 1 and 2, then at the end of runs 4, 8, 12 and 16. For each of these sets of runs, the total duration and total mass loss were used to determine the mass loss rate reported in Figure 4.3.

## 3.8 Conclusions

Apparatus development for the new preheating methodology, calibration of camera and spectrometer, and FEA simulations have shown that the determined temperature profile of the heated disc is suitable to continue with mass loss assessments with heated-with-flow runs.

It was shown that it is not possible to proceed with a resistive heating approach, using a central electrode contacting the graphite disc, as the required disc thickness profile would be structurally prone to failure. Plasma heating is confirmed to be suitable for

the goals of the ablation experiments. An electrode gap of 5 mm and a protrusion of 8 mm has been adopted for the plasma set-up in the present work because it created the best temperature profile across the disc. A method of temperature measurement using the red pixel count of a high-speed camera, correlated with a calibrated spectrometer, was determined to be effective for this current work. Preparation and assessment of the experimental set up encourages completing ablation experiments as presented in Chapter 4.

# Chapter 4

# Experimental Results

## 4.1 Introduction

Presented here are the results for the material loss and surface recession for the experiments. Two methods were utilised in the ablation measurements: (1) a weighing method, and (2) a volume-based method. Tools such as the Romer Multi-Gage 6-axis Coordinate Measuring Arm, the laser beam technique, and the Scanning Electron Microscope (SEM) were used.

## 4.2 Mass Loss Measurements

### 4.2.1 Methods

Using the arrangement of the experiment described in Section 3.2.3, a sequence of eighteen runs were conducted in three different cases. The same disc was used for all eighteen runs. Each run required the disc to be removed for measurement and/or cleaning of the holder. This required the test section to be opened after each run.

#### 4.2.1.1 Flow-Only Case

The disc used in the flow-only case was placed in the holder as described in Section 3.2.3. The test section was sealed and the vacuum pump operated for approximately 20 minutes to reduce the test section pressure to approximately 500 Pa. No pre-heating was applied before the main valve was operated to produce the flow. Flow durations were typically 0.5 seconds (see Section 3.7).

#### 4.2.1.2 Heated-Only Case

The disc holder surfaces were cleaned and the disc installed. A new electrode was placed in the TIG torch and the TIG settings required for the plasma were applied. The test section was sealed and vacuum pumps operated and after the 20 minutes required to reduce the test section pressure to approximately 500 Pa, the run was commenced by initiating the plasma. The plasma heated the disc for 15 seconds, manually timed. No flow was used in this case.

#### 4.2.1.3 Heated-With-Flow Case

The disc was set up and heated for 15 seconds as per heated-only case. The flow was initiated after 15 seconds of heating, manually timed. The heating remained on during the flow and for about 0.5 seconds after the flow stopped.

### 4.2.2 Procedures for Final Experiments

The process involved the following steps. These steps were followed chronologically during the eighteen runs of the final experiments.

1. Graphite disc was prepared using a centre lathe by parting from a 50 mm diameter bar. Only one disc was used during the final experiments of eighteen runs.
2. The disc was sanded by hand on emery paper against a machined flat surface to

remove machining marks.

3. The disc was weighed using a mass balance (see Section 4.2.3).
4. The disc thickness at various positions was measured using a micrometer gauge.
5. A visualisation technique using a laser sheet (see Section 4.5) produced an image representing the profile of the surface.
6. A Scanning Electron Microscope was used to show the surface texture at various positions on the disc.
7. The measured disc was subjected to one flow-only case (see Section 4.2.1.1) and processes 3 to 6 were repeated.
8. The same disc was subjected to one heated-only case (see Section 4.2.1.2) and processes 3 to 6 were repeated.
9. The same disc was subjected to the first of sixteen heated-with-flow runs (see Section 4.2.1.3) and processes 3 to 6 were repeated.
10. The same disc was subjected to a second heated-with-flow run and processes 3 to 6 were repeated.
11. The same disc was subjected to another two heated-with-flow run after which, processes 3 to 6 were repeated.
12. The same disc was subjected to three series, each of four heated-with-flow runs and after each series, processes 3 to 6 were repeated.

### 4.2.3 Mass Weighing Method

To measure the degree of ablation losses, the mass loss during the experiments (flow only, heated-only and heated-with-flow) were measured using a Kern ABT mass balance. The balance displays at an increment of 0.00001 g and reproduces a weighed mass at a resolution of 0.0001 g. The mass loss during each test was the difference in readings before and after the tests. At each weighing, the disc is placed on the balance and the machine automatically detects when the reading is stable, at which time the

weight was recorded. The disc was removed from the balance, then replaced and a new weight recorded. This was repeated to record a total of three weights, which were averaged with an attributed uncertainty specified as the maximum difference between the average and any of the three recorded weights. Table 4.1 shows the disc mass loss for all the 18 runs of the final experiments and mass loss for various pre-tests undertaken during the research. Pre-tests data were included in order to obtain a general comparison of all experimental data for same set of conditions at different times.

Table 4.1: Raw mass data for each weighing event.

| **Flow-only** | | **Heated-only** | | **Heated-with-flow** | |
|---|---|---|---|---|---|
| Mass loss (g) | Run time (s) | Mass loss (g) | Heating time (s) | Mass loss (g) | Run time (s) |
| **Experiments during the final 18 runs** | | | | | |
| 0.00050 | 0.495 | 0.00790 | 15 | 0.0138 | 0.450 |
| - | - | - | - | 0.0167 | 0.460 |
| - | - | - | - | 0.0373/ 2 runs | 0.960/ 2 runs |
| - | - | - | - | 0.0746/ 4 runs | 2.200/ 4 runs |
| - | - | - | - | 0.0811/ 4 runs | 2.240/ 4 runs |
| - | - | - | - | 0.0831/ 4 runs | 2.240/ 4 runs |
| **Pre-tests conducted at various times before the final 18 runs** | | | | | |
| 0.000544 | 0.58 | 0.00816 | 15 | 0.0164 | 0.458 |
| 0.000475 | 0.51 | 0.00820 | 15 | 0.01735 | 0.480 |
| 0.000583 | 0.55 | 0.00812 | 15 | 0.01766 | 0.495 |
| 0.000525 | 0.53 | 0.00792 | 15 | 0.01767 | 0.520 |
| 0.00051 | 0.50 | 0.00803 | 15 | 0.01802 | 0.530 |
| - | - | 0.00806 | 15 | 0.019221 | 0.540 |
| - | - | 0.00810 | 15 | 0.01933 | 0.540 |
| - | - | 0.00799 | 15 | 0.01984 | 0.550 |
| - | - | 0.00802 | 15 | 0.02002 | 0.560 |
| - | - | 0.00830 | 15 | 0.02042 | 0.569 |
| - | - | 0.00822 | 15 | 0.02065 | 0.570 |
| - | - | - | - | 0.02083 | 0.580 |

From Table 4.1, the average mass losses for flow-only, heated-only and heated-with-flow cases are 0.000527, 0.0082, and 0.0190 g respectively. The average mass loss $\overline{m}_{loss}$ for the flow period of a heated-with-flow run is represented by Equation 4.1, where $\Delta\overline{m}$ is the difference between the average mass loss from heated-only and the average mass loss from heated-with-flow runs. The parameter $\Delta\overline{m}$ accounts for the actual mass loss during the real flow period from the heated-with-flow runs with an average run time $\Delta\bar{t}$ of 0.54 seconds for this flow period. This actual mass loss during the flow period is reasonable because all heated-with-flow cases had undergone the heated-only stage before the flow was initiated.

$$\overline{m}_{loss} = \frac{\Delta\overline{m}}{\Delta\bar{t}} = \frac{0.0190 - 0.0082}{0.54} = 0.020\ g/s \tag{4.1}$$

Figure 4.1 presents the experimental results for the flow-only cases. The average mass loss rate for flow-only is on average 0.0010 g/s. The mass loss for flow-only was an average of 0.000527 g, which represents about 2.8 % to the overall ablation for the heated-with-flow runs. It represents 4.9 % of the ablation that occurs during the flow in a heated-with-flow run. This flow-only mass loss resulted without any chemical reactions, thus suggesting that mechanical actions were not insignificant, but only a minor contributor.

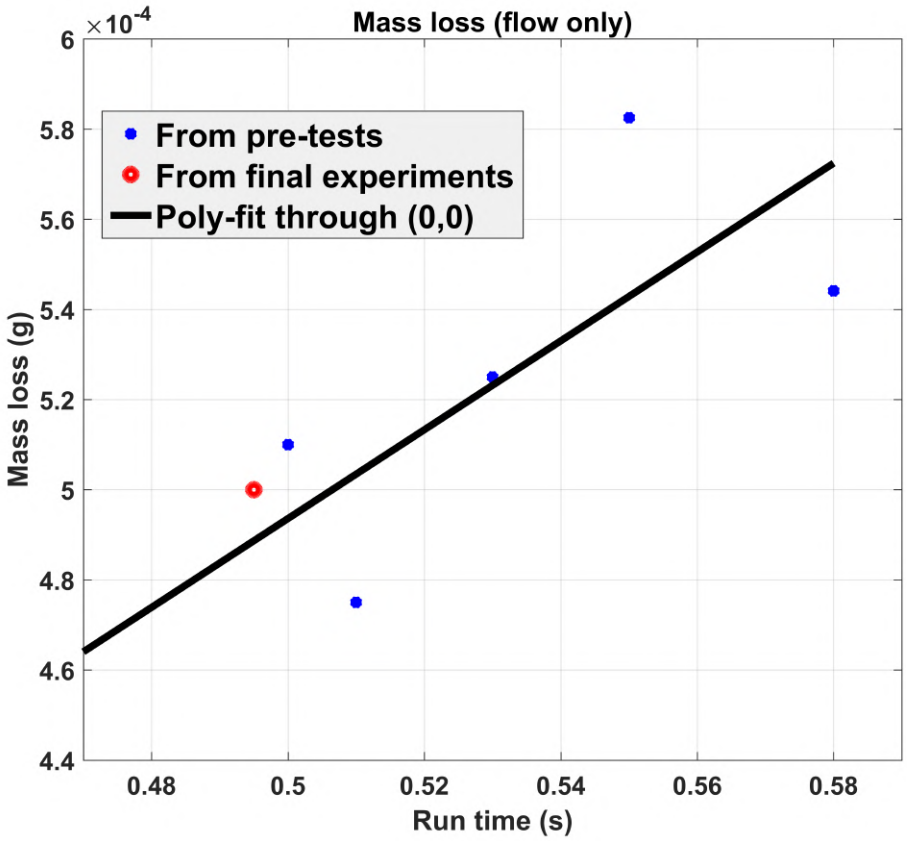


Figure 4.1: Plots of mass losses for flow-only cases. The datum point for the flow-only case at the start of the final 18 runs is depicted with a red-dot marker type. The mass lost rate is depicted by the slope of a linear best fit line forced through the origin, giving a mass loss rate of 0.00099 g/s.

For the heated-only experiments, dividing the accumulated mass losses from the twelve different heated-only runs by the total time of heating, produces a mass loss rate. This assumes a constant mass loss rate during the heating cycle, but the temperature increased during a cycle as displayed in Figure 3.28. The mass loss rate will be dependent on temperature, so a mass loss rate as a function of temperature is not obtainable from the heating only data. The average mass loss rate during a heating only run was 0.00055 g/s. A more useful value is the average mass loss per heating cycle, as the heating cycles were consistently of the same duration of 15 seconds. The average mass loss per heating cycle was 0.0082 g. The average mass loss due to the heating cycle was about 43 % (0.0082/0.0190) of the overall ablation for the heated-with-flow run.

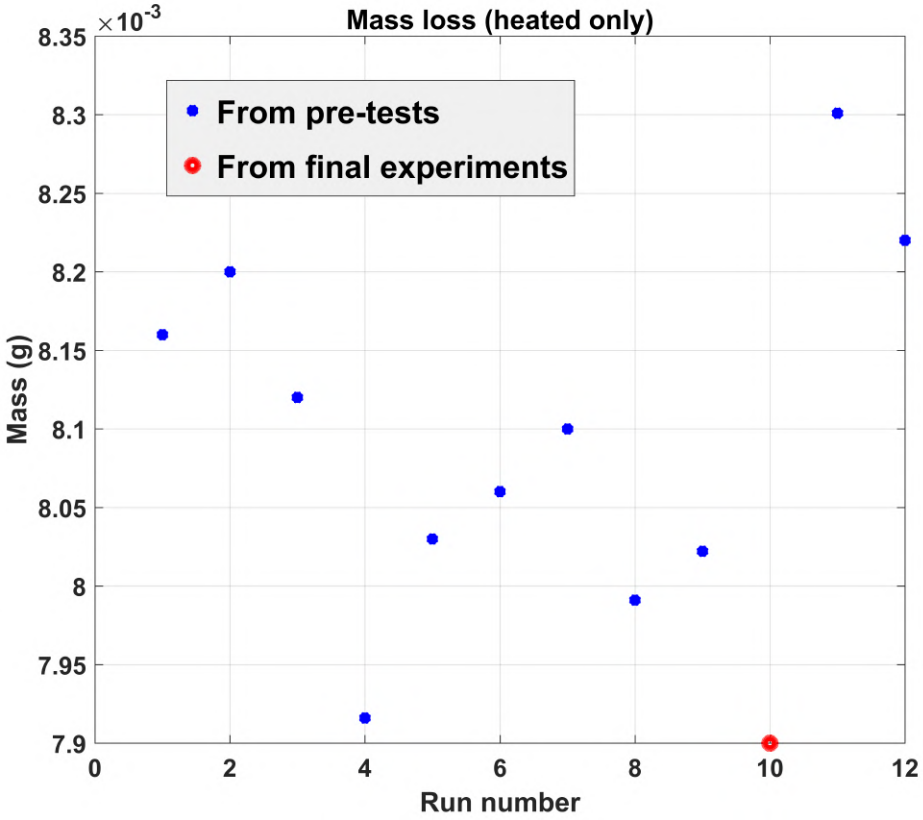


Figure 4.2: The results for heated-only mass loss during 15 second heating cycles. A separate graphite disc was used to produce eleven pre-tests data to the one heated-only case of the final experiments.

Figure 4.3 shows the mass losses from sixteen heated-with-flow runs, completed as six stages (see experimental procedures 8 to 12 in Section 4.2.2). The flow run time varied from 0.45 seconds to about 0.56 seconds, with a target of 0.5 seconds. The time variation was due to the manual opening and closing of the flow control valve. The mass loss shows a general increase with increasing run time. The result from step 6 shows an increase in mass loss over that of step 5 despite the same run time. This difference might be attributed to the crack, which potentially exposed more graphite material to ablation, although the difference is not outside the range of the error indicated by the best fit shown in Figure 4.3. The red line shows the best-fit (linear fit) of which the slope is about 0.020 g/s running through point (0,0.0082), as there is already a mass loss of about 0.0082 g when the flow started. The value 0.0082 g was obtained from the average of the heated-only experiments. It is reasonable to apply this average as

the heating time was consistently the same. The displayed flow durations for the series of heated-with-flow runs (see Section 4.2.2) are the averages for those series.

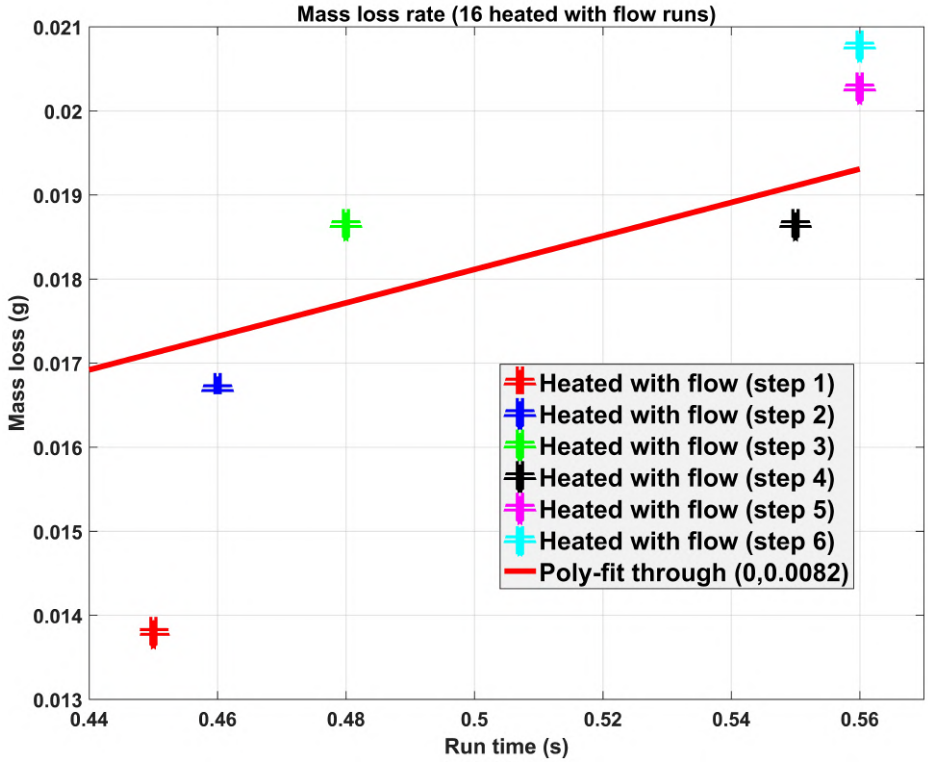


Figure 4.3: Result showing the mass losses for the flow period from sixteen heated-with-flow runs (see experimental procedures 8 to 12 in Section 4.2.2 to explain the data points). The slope of the poly-fit line represents to average mass loss rate of 0.020 g/s.

As a check of the data reproducibility of the sixteen heated-with-flow runs, analysis of earlier heated-with-flow runs was carried out. Figure 4.4 also shows the results of the mass losses from other heated-with-flow runs from earlier experiments. The mass loss rates ranged from 0.034 g/s to 0.036 g/s with an average of about 0.035 g/s. It was calculated based on the slope of a linear best fit of the plot in Figure 4.4, again going through the point (0,0.0082) as applied for the final 16 runs.

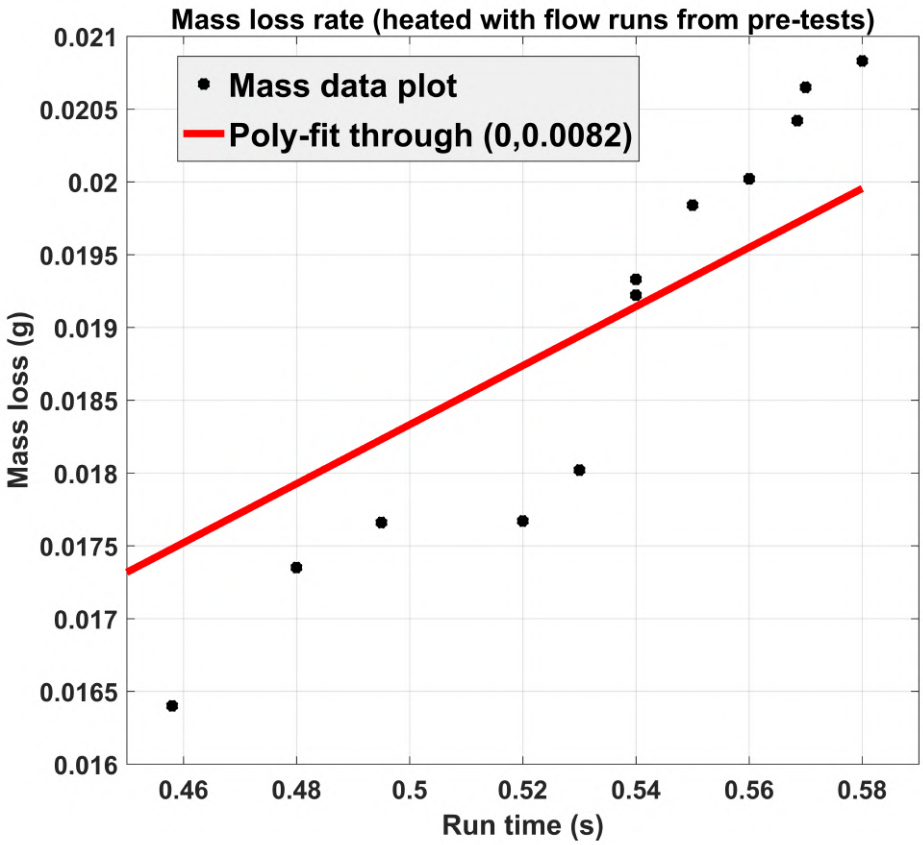


Figure 4.4: Result showing the mass losses from the heated-with-flow runs during pre-tests. The slope of the poly-fit line represents to average mass loss rate of 0.020 g/s.

## 4.3 Characteristics on the Heated Graphite Surface

### 4.3.1 Results from the Scanning Electron Microscope (SEM)

The surface texture of the graphite disc was investigated using images produced by the SEM. Figure 4.5 shows the set-up for the surface analysis using the SEM.

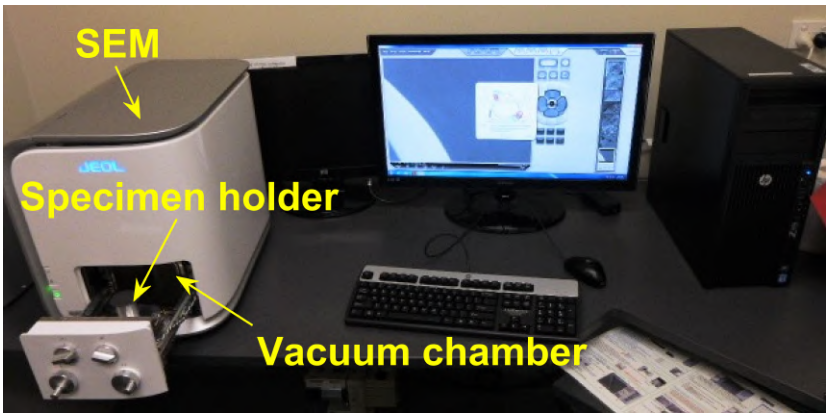


(a) SEM arrangement.

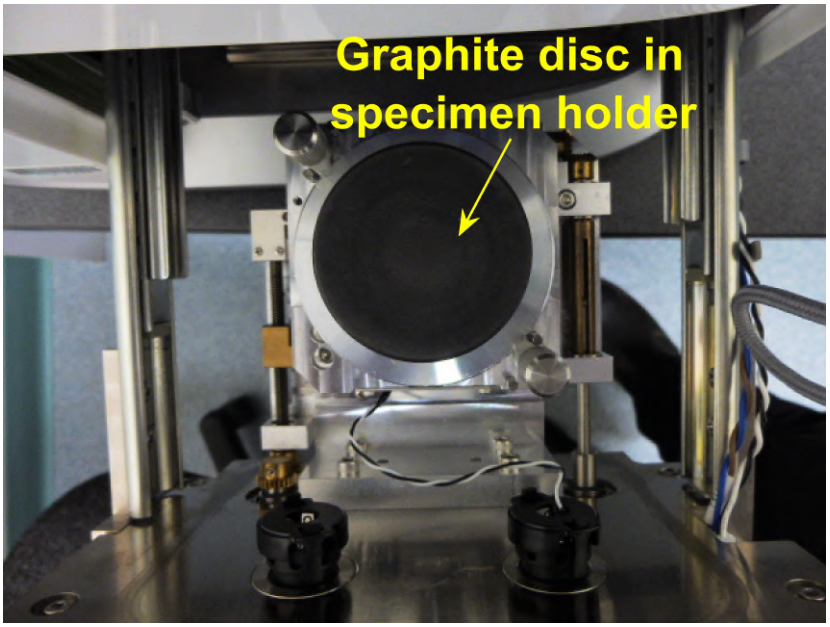


(b) Mounting and centralising the disc sample in the holder, before closing the vacuum chamber.

Figure 4.5: Setting up and mounting graphite disc in the SEM for surface analysis.

The total area able to be scanned by the SEM was limited: the maximum field of view at the amplification used, was 500 $\mu$m. The maximum travel of the specimen holder was 36 mm (18 mm $\times$ 2). Five positions were chosen and used for analysis after each series of runs. The disc was placed in the holder in the same orientation for each set of scans. The centre of the disc was determined by traversing the holder to view the edges of the disc with the y-axis displaced so the extent of travel viewed the edges of the disc, then centering the disc based in these limits. This identified position A in

Figure 4.6 and allowed for 18 mm of travel along the radius of the disc. Five positions in total were chosen at 4.5 mm increments, shown as A, B, C, D, and E in Figure 4.6. This resulted in position E being 7 mm from the outside edge of the disc (6 mm from the chamfer used to retain the disc), see Section 3.2.3 and Appendix C for how the disc was retained.

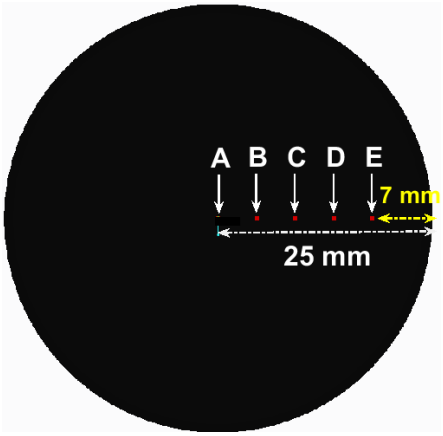


(a) Graphite specimen (top view).

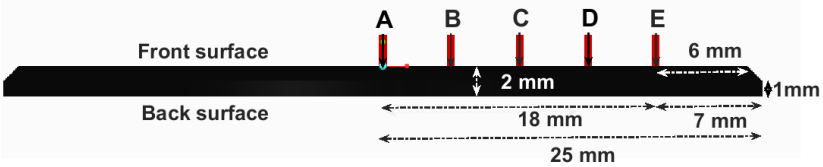


(b) Graphite specimen (side view not to scale).

Figure 4.6: Scanning locations on graphite surface. During experiments, the actual points scanned in the SEM were not exactly the same; each scan was a representative area in close proximity to the points described by A, B, C, D and E.

The images in Figure 4.7 show the SEM results for a newly prepared disc and one each from flow-only, heated-only, and heated-with-flow run. The mechanical actions associated with erosion are the main driving forces which acted on the disc to produce the surface textures shown in the image in Figure 4.7b. Figure 4.7c shows little change from Figure 4.7b, but after flow is added, Figure 4.7d shows that the proportion of smooth areas resulting from contact with the sanding surface during disc preparation has been reduced. Regions in the top left and bottom centre of Figure 4.7d suggests that small fragments of carbon are potentially lost under the action of heat and flow, which were not lost under the independent action of heat or flow.

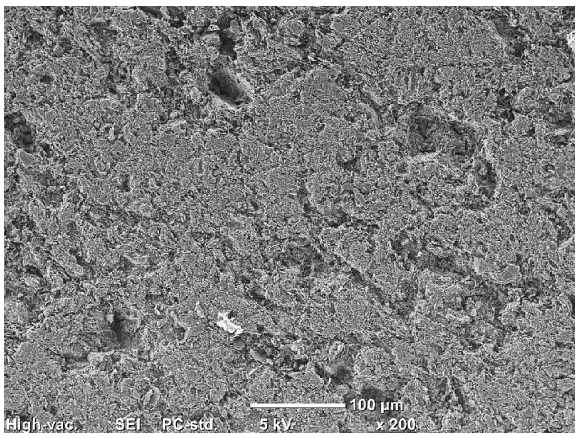


(a) Newly prepared disc in the proximity of point A

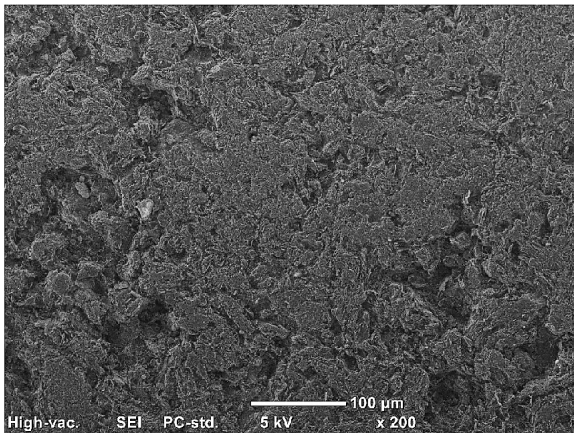


(b) Disc after one flow-only run in the proximity of point A

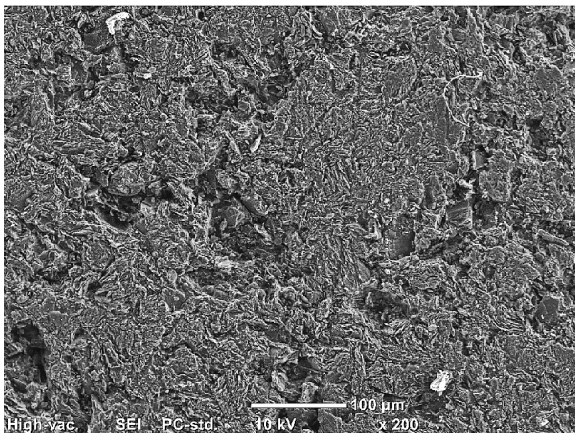


(c) Disc after one heated-only run in the proximity of point A

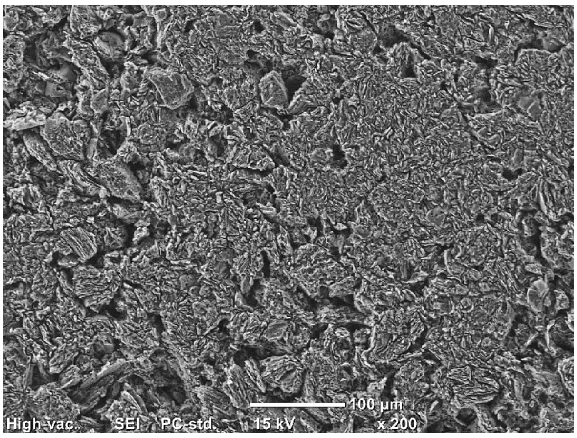


(d) Disc after one heated-with-flow run in the proximity of point A

Figure 4.7: SEM images for the new disc, the same disc subjected to one flow-only, the same disc subjected to an additional one heated-only run, and the same disc subjected to an additional one heated-with-flow run.

The images in Figure 4.8 show the SEM results after the second heated-with-flow run. A crack is seen to have developed near the stagnation point in the proximity of point A. Convex deformation facing the flow as described in Section 3.2.3, Figure 3.9, seems likely to have caused the crack. Figure 4.9 shows the accumulated deterioration of the surface of the disc resulting from the sequence of runs up to the end of the second heated-with-flow run.

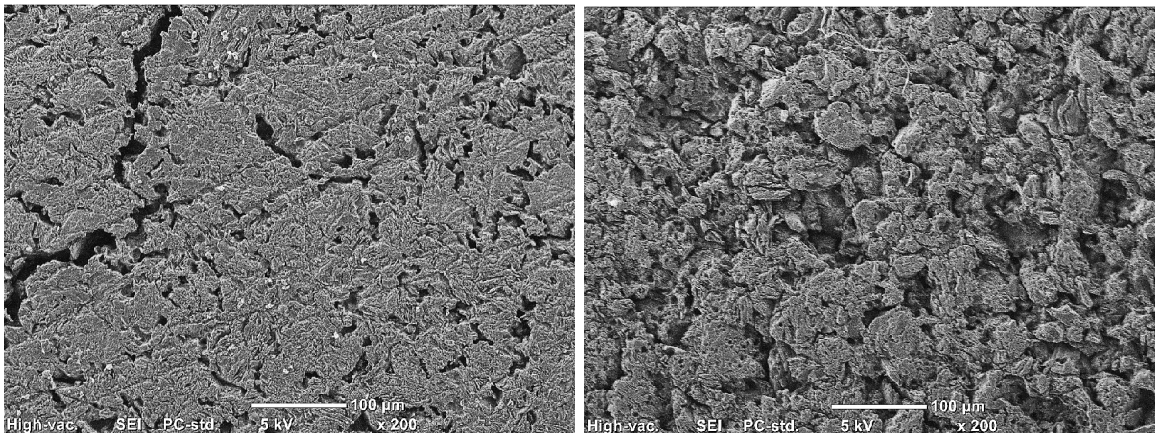


(a) In the proximity of point A (b) In the proximity of point C

Figure 4.8: SEM images after the second heated with flow run in proximity of two points A and C. More details of the disc surface are shown in Appendix E, Figure E.1.

The images in Figure 4.9 show the SEM results after the fourth heated-with-flow run. The crack at the stagnation region widened. Significant changes in the surface texture are evident. Interestingly, the surface near the stagnation point is least effected (apart from the crack). This region had the highest surface temperature, but the lowest flow speed. Assessment of the causes are discussed in Section 6.4.

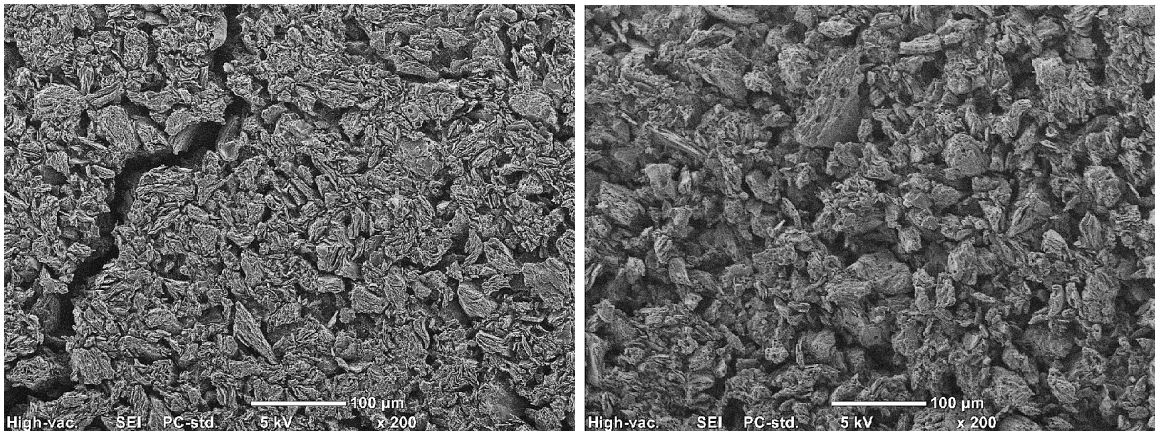


(a) In the proximity of point A (b) In the proximity of point C

Figure 4.9: SEM images after the fourth heated-with-flow run in proximity of two points A and C. More details are shown in Appendix E, Figure E.2.

The images in Figure 4.10 show the SEM results after the eighth heated-with-flow run.

The crack near the stagnation region continued to widen. The increasing convex shape of the disc over successive runs is likely to be responsible for widening the crack.

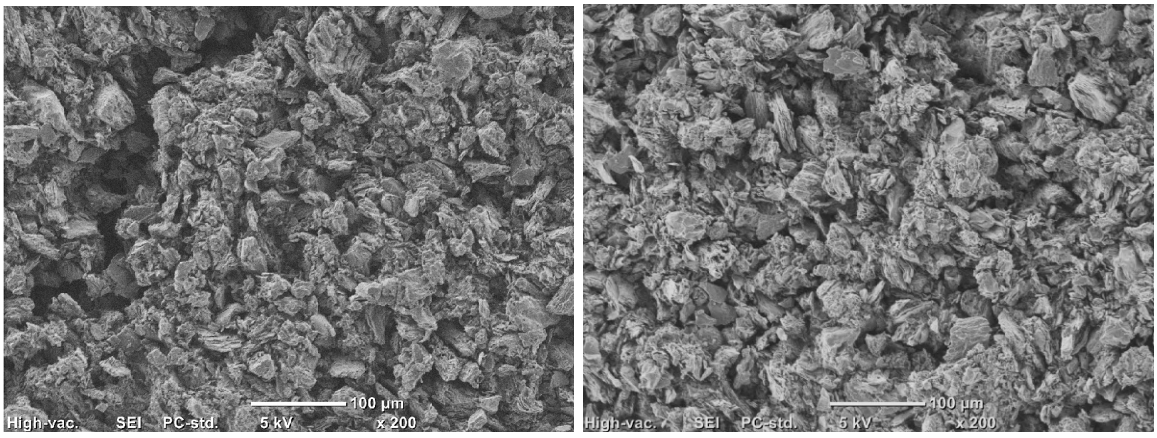


(a) In the proximity of point A (b) In the proximity of point C

Figure 4.10: SEM images after the eighth heated-with-flow run in proximity of two points A and C. More details are shown in Appendix E, Figure E.3.

The images in Figure 4.11 show the SEM results for the front surface after the twelfth heated-with-flow run. The width of the crack near the stagnation region kept increasing or perhaps the edges of the crack are more prone to erosion leading to the perception that the crack is widening.

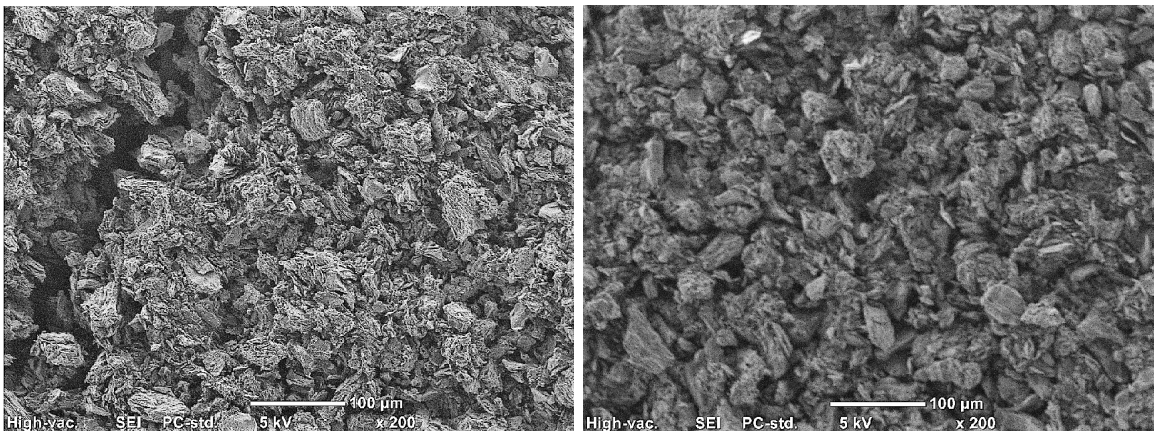


(a) In the proximity of point A (b) In the proximity of point C

Figure 4.11: SEM images after the 12th heated-with-flow run in proximity of two points A and C. More details are shown in Appendix E, Figure E.4.

At about the twelfth run, a crack became visible to the naked eyes. The scan in the proximity of Point A captured a portion of the crack showing that it widened, but no indication that it penetrated full depth. The trend of deterioration over the various points on the disc continued. Large fragments from the edges of the crack have been removed. The surface texture at the stagnation point and the points analysed away from the stagnation point in the radial direction, show less difference than in the images from the previous runs. The image in Figure 4.12 shows the SEM result at the front of the carbon disc after the sixteenth heated-with-flow run. During the sixteenth run, this crack widened substantially and a reduction of accuracy of mass loss measurement was expected to result and this prevented further runs.

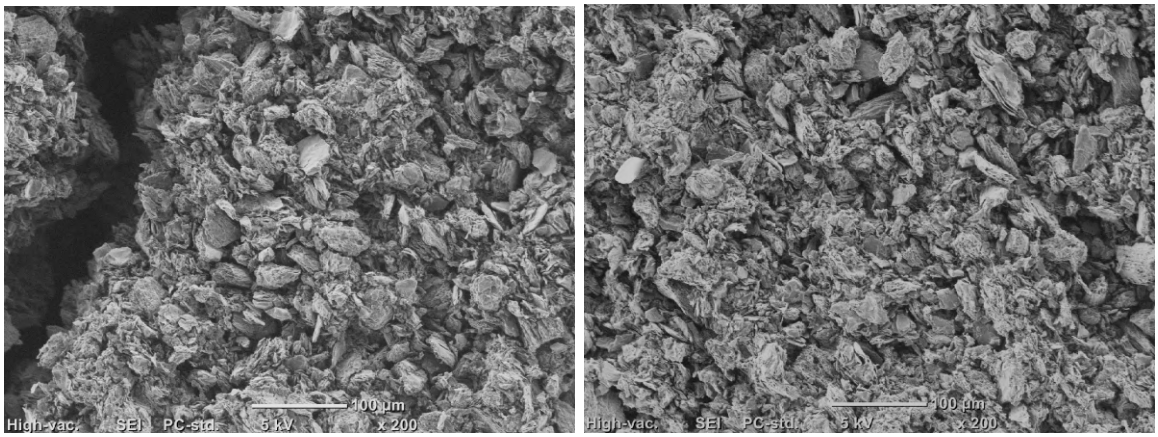


(a) In the proximity of point A (b) In the proximity of point C

Figure 4.12: SEM image after the 16th heated-with-flow run in proximity of points A and C. More details are shown in Appendix E, Figure E.5.

The images in Figure 4.13 show the SEM results at the back of the carbon disc after the sixteenth heated-with-flow run. The crack evident here was the reason that the experiment was terminated at sixteen heated and flow runs. The deterioration of the surface exposed to the flow over the last four runs was extreme. The disc was assessed to be unlikely to survive another series of runs. The edges of the crack on the back of the disc in Figure 4.13 seem relatively sharp, in combination with no sign of a crack at the back after 12 runs, suggests that the full-depth crack formed suddenly on cooling after the sixteenth run.

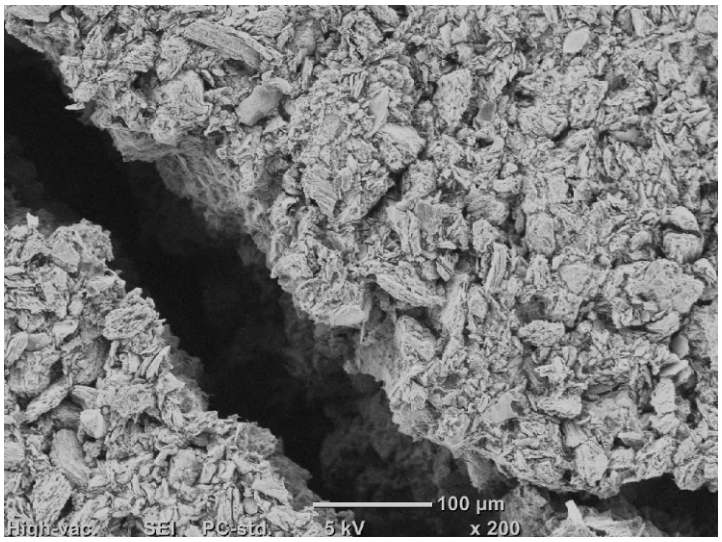


Figure 4.13: SEM image (on the back of the disc) after 16th heated-with-flow run in proximity of point A. More details are shown in Appendix E, Figure E.7.

Characteristics consistent with the disc preparation process and the deterioration resulting from successive runs were evident in the SEM images. The position of the crack in the different images that contain the crack (Images for the proximity of point A) is representative of the variation of the disc position for each image shown. At the end of the sixteenth heated-with-flow run, there was a step height difference across the crack near the stagnation region, indicating that the crack finally penetrated the full thickness of the disc. This is evident in the laser sheet image to be discussed in Section 4.5 and the image of the back of the disc in Figure 4.13.

### 4.3.2 Surface Roughness of the Disc

The SEM system has the capability of producing data which describes the degree of surface roughness. The SEM machine could analyse the relative height across a reference line. The SEM data for the surfaces were extracted and plotted as summarised in Figure 4.14 and Figure 4.15.

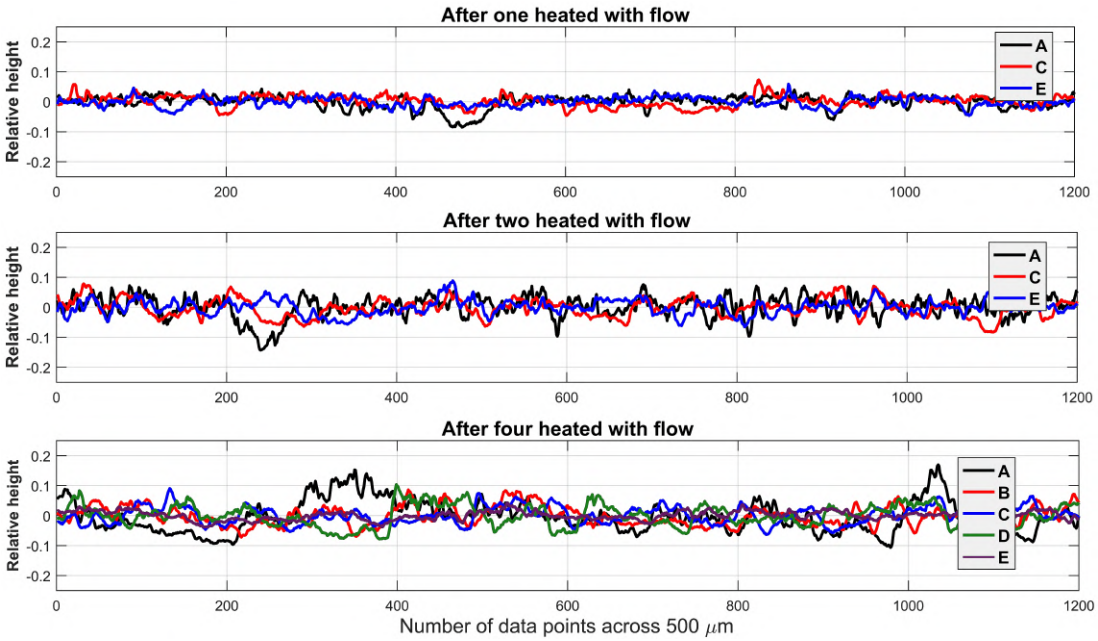


Figure 4.14: Surface texture relative height summary after 1, 2 and 4 heated-with-flow runs.

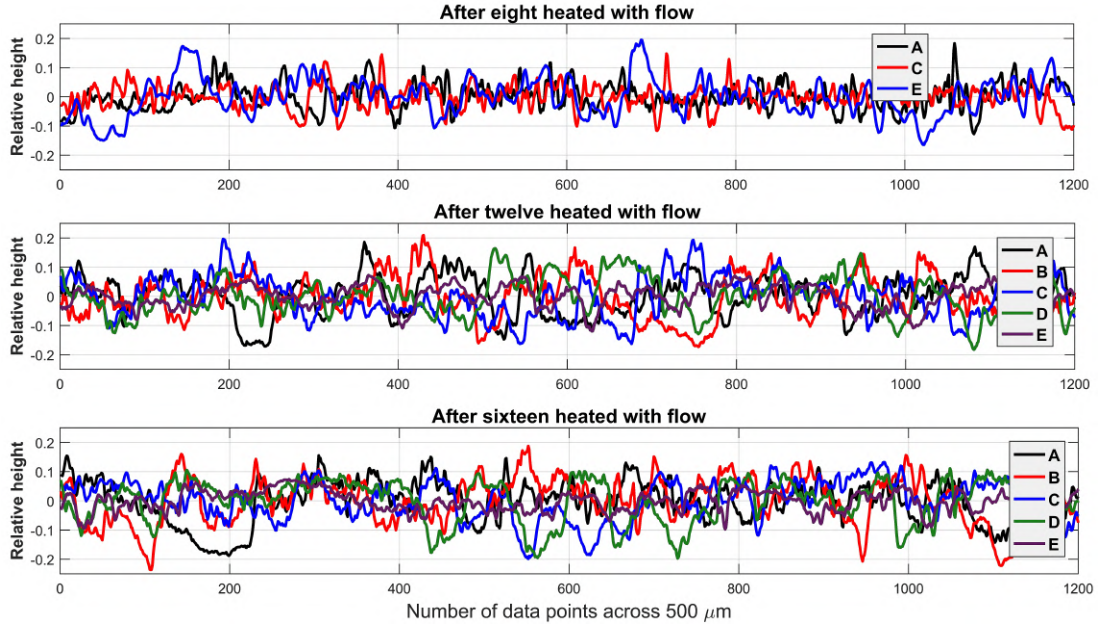


Figure 4.15: Surface texture relative height summary after 8, 12 and 16 heated-with-flow runs.

Arithmetic average height parameter was used to estimate the surface roughness of the disc. Two basic parameters defining the surface roughness are: (1) maximum height of

peaks which defines the maximum height of the profile above the mean line within the assessment length, and (2) maximum depth of valleys which defines the maximum depth of the profile below the mean line within the assessment length (Gadelmawla, Koura, Maksoud, Elewa and Soliman, 2002). Determination of roughness using the arithmetic average $R_a$ defines the deviation of roughness irregularities from the mean line over a sample length $n$ as shown in Equation 4.2 (Smith, Breakspear and Campbell, 2003), where $y_i$ is the height at each pixel position along the line profile and $\overline{y}$ is the mean height.

$$R_a = \frac{1}{n}\sum_{i=1}^{n} |y_i - \overline{y}| \tag{4.2}$$

The degree of surface roughness increases with increasing number of runs, suggesting that potentially larger fragments of carbon are being removed, or the surfaces at the bottom of the valleys are more prone to the ablative actions than those at the peaks. In addition to reducing thickness (increased total material removal), if the increased removal of material from the valleys is occurring, this suggests that chemical reactions are more involved than mechanical erosion. There appears to be a general correlation between the number of runs and the degree of surface roughness as shown in Figure 4.16. Each point of surface roughness was obtained by averaging the relative heights at each at point C at each SEM measurement. Point C is shown as it is indicative of the ablation changes to the surface involving heating and flow effects.

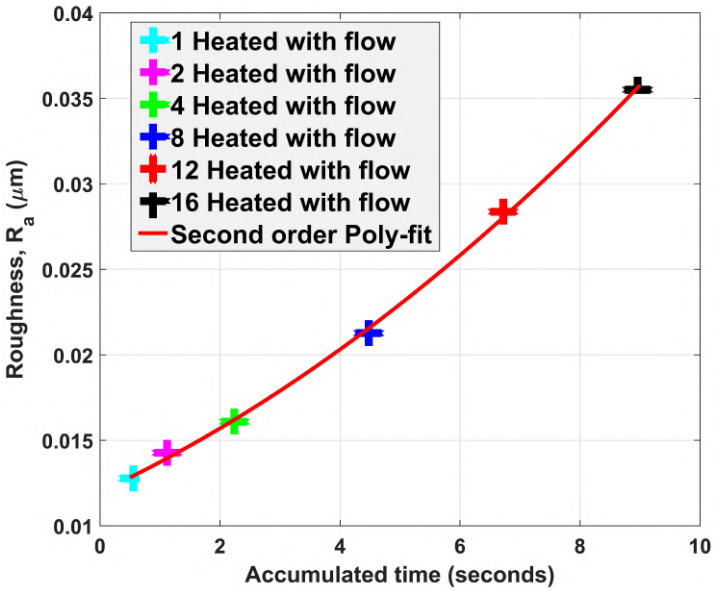


Figure 4.16: Surface roughness summary from SEM measurements after 1, 2, 4, 8, 12 and 16 heated-with-flow.

## 4.4 Surface Characteristics using the Measuring Arm

### 4.4.1 Overview

The measurements with the measuring arm (see Appendix B) proved effective in determining the shape of the surface of the disc. The measurements were taken along three radii, R1, R2 and R3. Where R1 and R2 were taken along a diameter, and R3 was taken in the direction that is perpendicular to the diameter as shown in Figure 4.17.

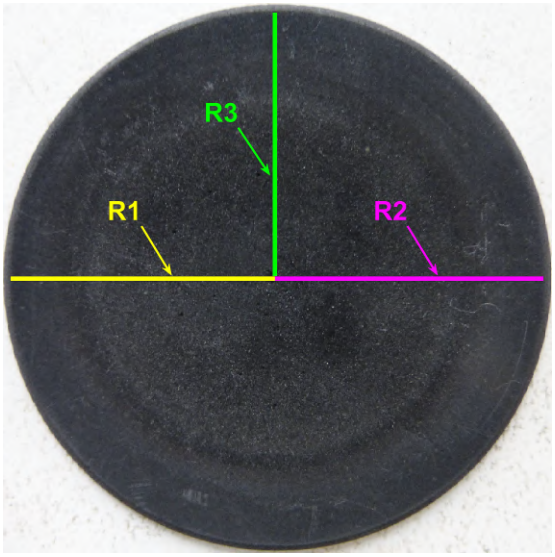


Figure 4.17: The image of disc is defined by three radii R1, R2 and R3. An average of nine measurements were taken along each radius.

Referencing the back surface as facing the plasma and the front surface facing the flow, the thickness of the disc was determined from data obtained on various paths as shown in Figure 4.17. The measurements from the measuring arm were restricted to one half of the disc because the developed crack had a significant influence over the shape of the other half of the disc. Disc thickness was defined by the measurements along the three radii on the front of the disc in relation to measurements at the same positions on the back side of the disc. The advantage of using three radii was to get data to identify the precision with which the shape was measured and therefore give data to provide an estimate of the uncertainty with which the shape and mass loss were measured. The measuring arm was not used after each run because the required contact to take the measurements would damage the surface and effect the subsequent ablation.

### 4.4.2 Carbon Mass Loss from Measuring Arm

Figure 4.18 shows the relative heights of positions along R1, R2, and R3 at the back and front of the disc. The paths along the back appears to be more consistent when comparing the three radii than the paths along the front. The change in height on the back surface, due to the heating (see Figure 3.9), produces a smoother profile than is

evident on the front surface subjected to ablation.

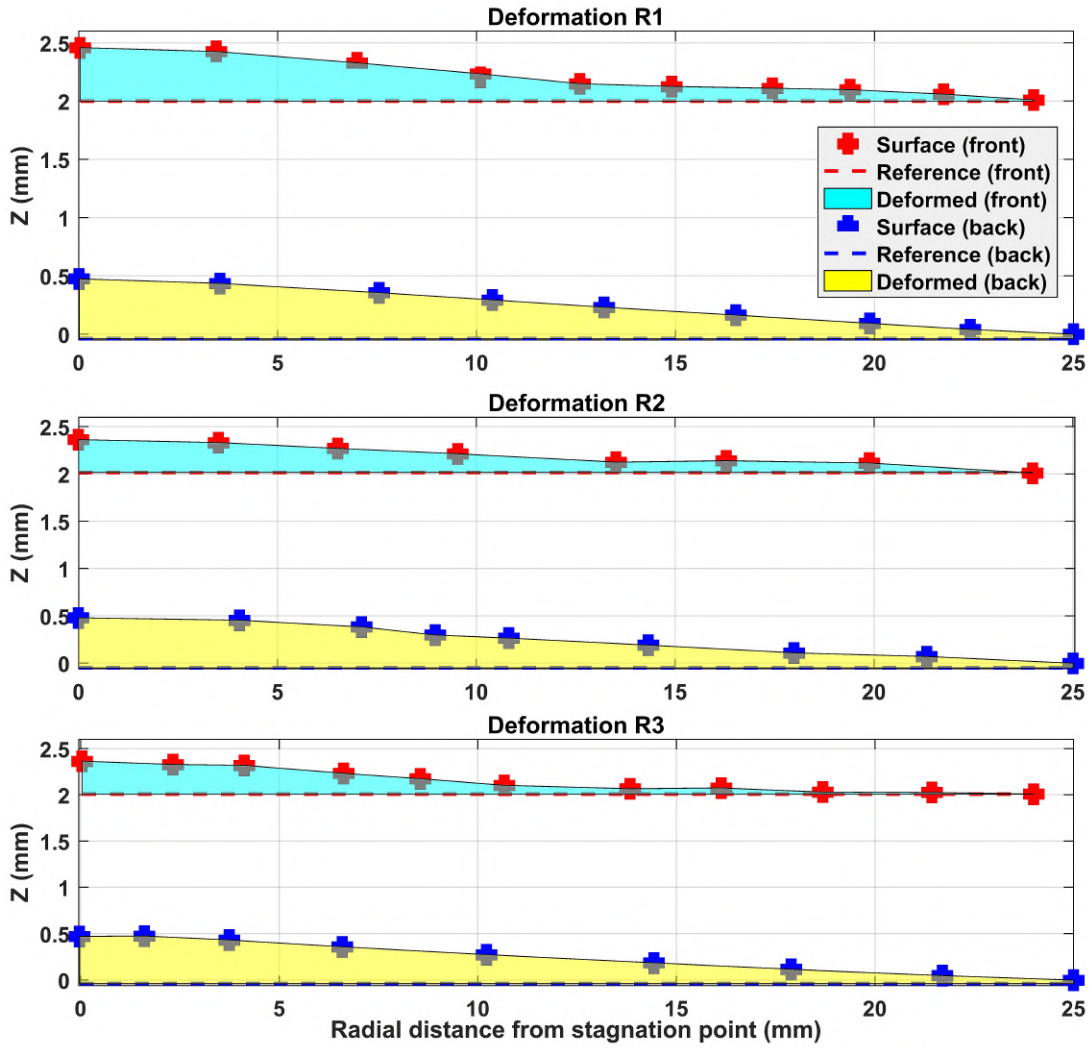


Figure 4.18: Measurements of the front and back of the disc along paths R1, R2, and R3 after sixteen heated-with-flow runs.

Using Figure 4.18, an average of the thickness at positions along the three radii was calculated and the value was used for calculation of thickness reduction based on an axisymmetric assumption. One end of each radius was the stagnation point; measurements at this common point were necessarily the same. The ends of the radii at the outer edge of the disc were not relative to any particular reference in the raw data taken from the measuring arm. The thickness at these points was obtained from the micrometer measurements (see Figure 4.6) and the relative positions along each radius were respectively adjusted. The data in Figure 4.19 shows the loss in thickness of the

disc along R1, R2 and R3. Starting from the edges, the thickness reduction progressively increases to about 12 mm from the stagnation point. The thickness reduction along R1, R2 and R3 was highest between 0 to 12 mm from the stagnation point. The average thickness reduction was about 0.045 mm at the edges and 0.147 mm at the stagnation point. The shaded area shows the profile of material lost from ablation effects. The data points indicate that there was variation between measurements at the various radial positions along the three radii. The trends are similar along each path, with most deviation from the average occurring in the regions of maximum material loss.

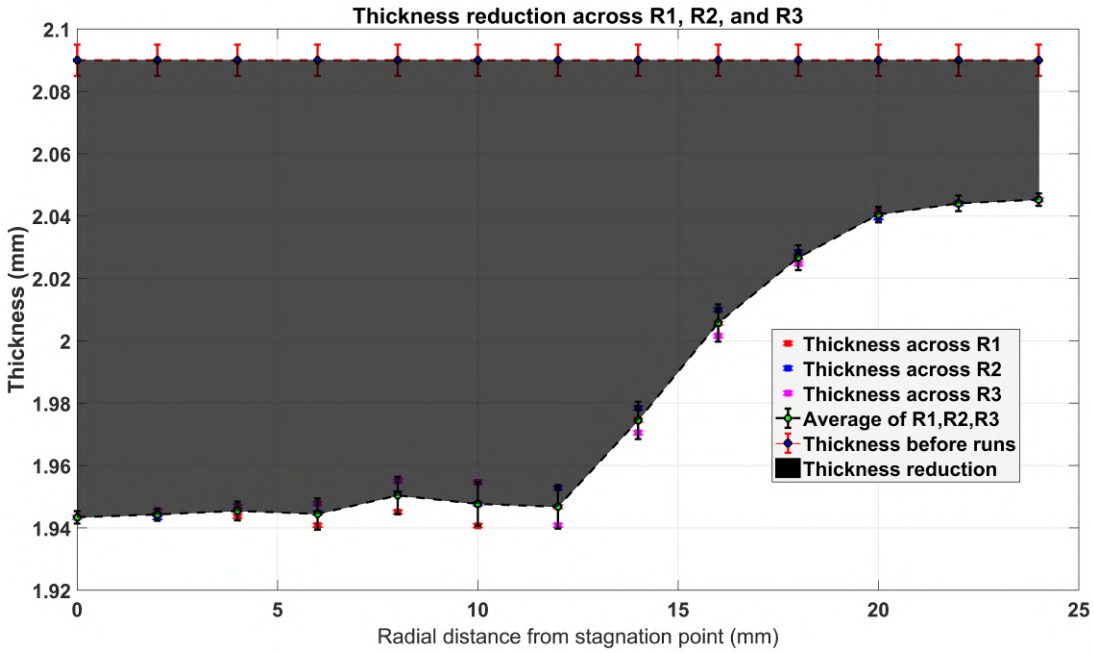


Figure 4.19: Thickness along paths R1, R2, and R3 after sixteen heated-with-flow runs. The error bars were calculated using the maximum deviation from an average of data at the various radial positions along the three paths.

## 4.5 Surface Characteristics using the Laser Beam Techniques

Figure 4.20 shows a schematic diagram of a laser beam refracted in a convex lens to form a flat sheet of light used to determine the surface shape of the experimental disc. The laser technique used in the present work was supportive of the details obtained

from the measuring arm, but did not provide sufficient accuracy to determine material loss; the technique was oriented towards visualisation of the surface shape change. The intersection between the laser sheet and the disc produces a shape that is able to be converted into a variation in depth via the angle of the laser sheet, but only at the positions where the laser sheet illuminated the disc. The overall deformation of disc due to heating constrained the angle of incidence used for the beam, which in turn restricted the sensitivity with which the technique could determine the material loss. Generally, the laser visualisation supported the shape determined from the measuring arm.

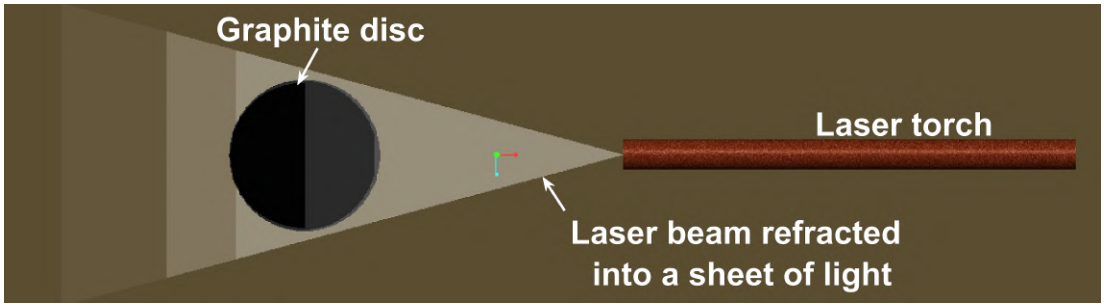


(a) Laser beam (top view)

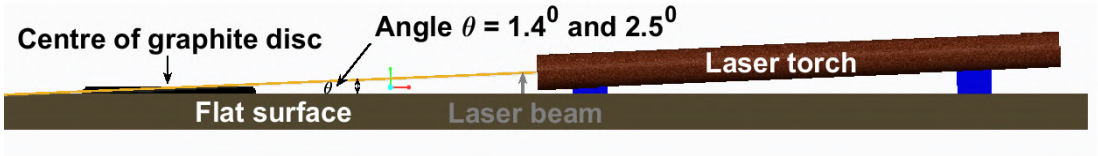


(b) Laser beam (side view)

Figure 4.20: Applying the laser beam technique to view the surface characteristics.

The disc used for the sixteen runs of the experiment, was measured prior to use as shown in Figure 4.21. The laser sheet is oriented at an angle of $1.4^0$ to the surface. The laser sheet was passed over a knife edge to produce a good planar sheet. This also created interference lines as Figure 4.21 shows. The repositioning of the disc for the laser sheet visualisation after each set of runs, required manipulation of the laser sheet, knife edge and graphite disc position to produce the most effective contrast between the edges of the interference lines and the graphite disc features. Figure 4.21 shows a typically optimised position of the set-up, depicting the technique showing the flat surface of the disc at a diameter labelled AB.

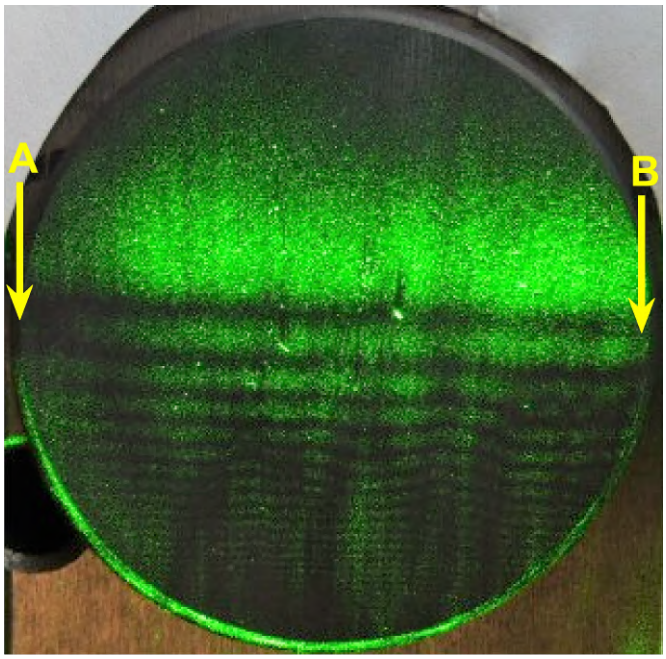


Figure 4.21: New graphite disc.

The surface was monitored using the laser sheet after the first, second, fourth, eighth, twelfth and sixteenth heated-with-flow runs. The trigonometry used to calculate shape is shown in Figure 4.22, where $\theta$ is the angle that the incident sheet makes with the flat surface.

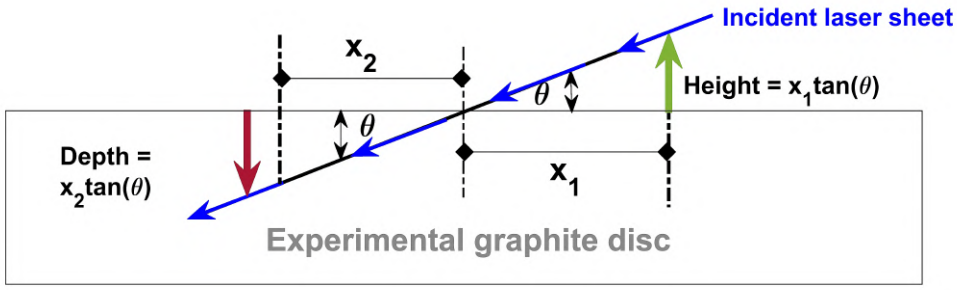


Figure 4.22: Trigonometry used to calculate the depth and height using angle of incident beam, $\theta$.

Figure 4.23 shows the front and back surfaces after one heated-with-flow run at $\theta = 1.4^0$. The disc had previously been subjected to one heated-only run and one flow-only run. The height at the front of the disc appeared closer to the laser source while the depth at the back of the disc appeared further away from the laser source.

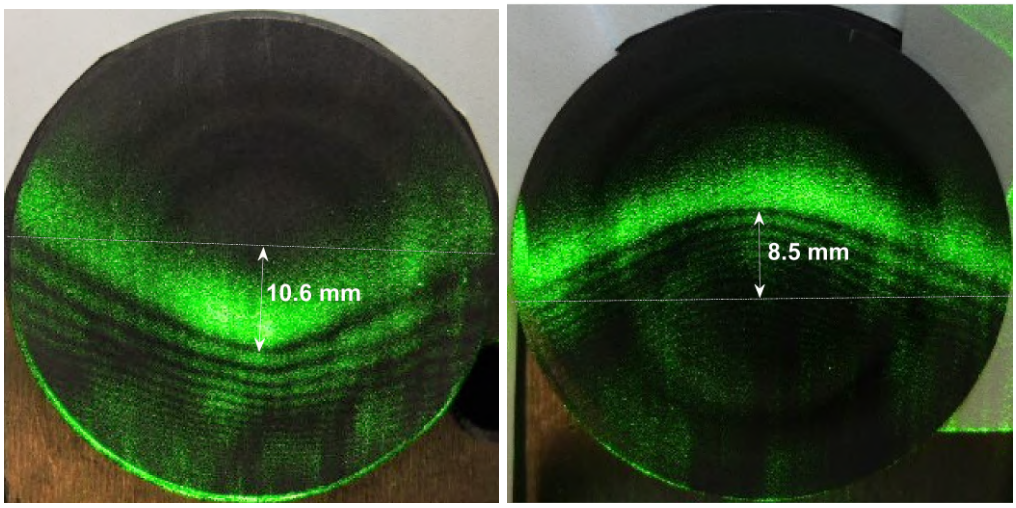


(a) Disc (front) where $x_1 = 10.6$ mm (b) Disc (back) where $x_2 = 8.5$ mm

Figure 4.23: Surface characteristics after one heated-with-flow run with the incident laser sheet at an angle of $1.4^0$. The light source is from below in these images.

After the second heated-with-flow run, the values of $x_1$ and $x_2$ increased to 12.7 and 12.0 mm respectively. The surface profile is shown in Figure 4.24.

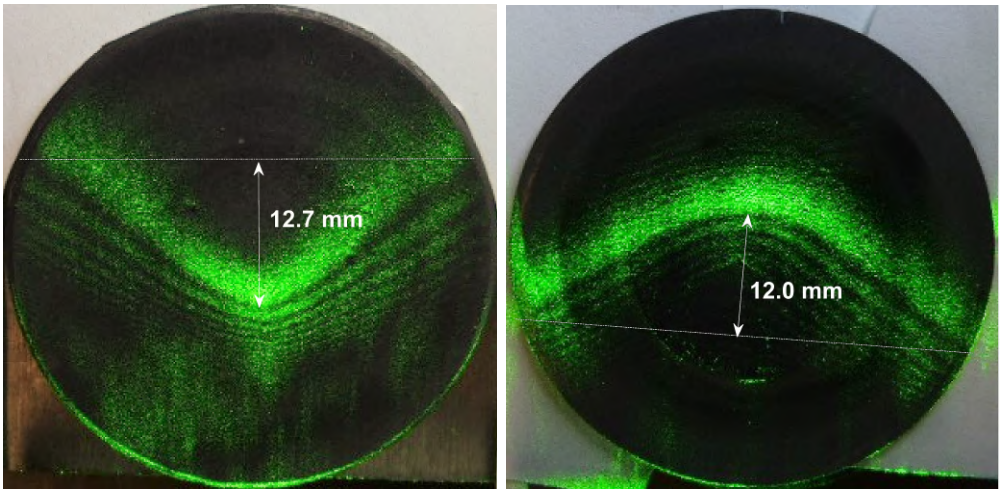


(a) Disc (front) (b) Disc (back)

Figure 4.24: Surface characteristics after two heated-with-flow runs with the incident laser sheet at an angle of $1.4^0$. The light source is from below in these images.

The disc deformation increased with further runs as shown in Figure 4.25. Figure 4.26 also shows the surface deformation after the eighth heated-with-flow run.

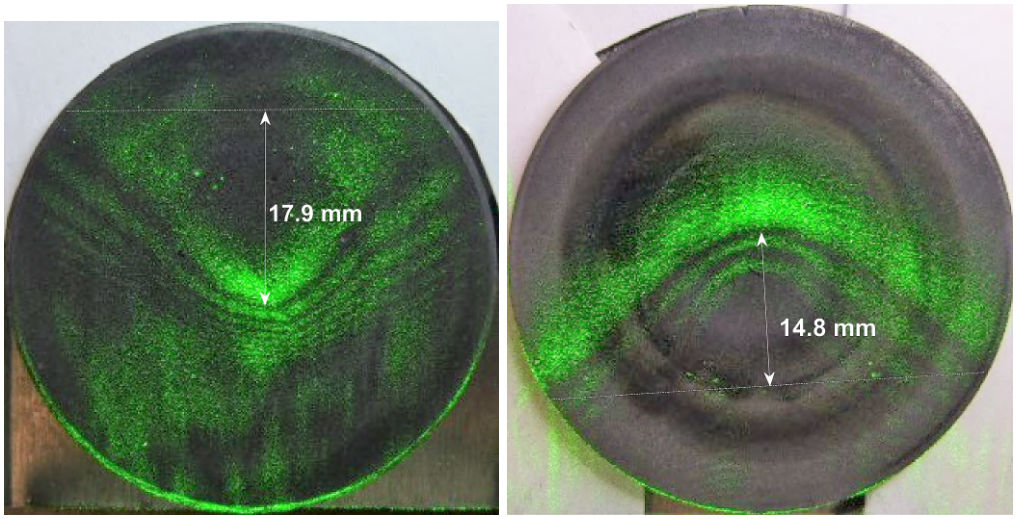


(a) Disc (front) (b) Disc (back)

Figure 4.25: Surface characteristics after fourth heated-with-flow run with the incident laser sheet at an angle of $1.4^0$. The light source is from below in these images.

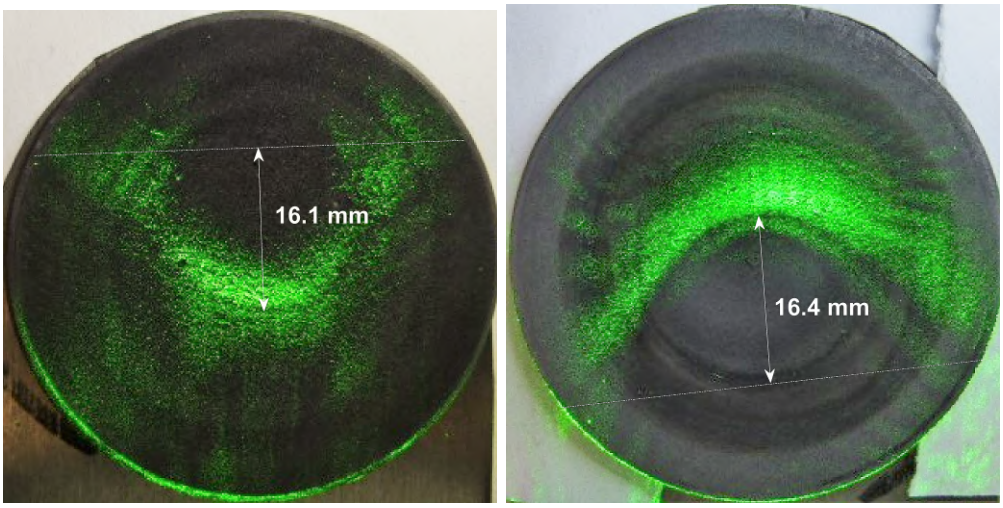


(a) Disc (front) (b) Disc (back)

Figure 4.26: Surface characteristics after eighth heated-with-flow run with the incident laser sheet at an angle of $1.4^0$. The light source is from below in these images.

For the twelfth and sixteenth heated-with-flow runs, the angle of incident was increased from $1.4^0$ to $2.5^0$ in order to accommodate the magnitude of the deformation of the disc resulting from the heating.

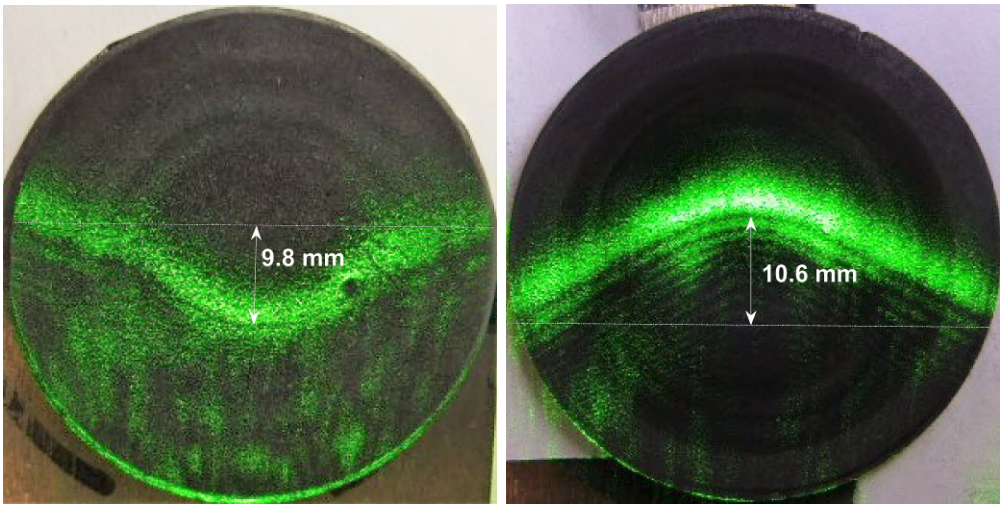


(a) Disc (front) (b) Disc (back)

Figure 4.27: Surface characteristics after twelve heated-with-flow runs with the incident laser sheet at an angle of $2.5^0$. The light source is from below in these images.

The sixteenth heated-with-flow run images shown in Figure 4.28 indicates the amplitude of the deformations resulting as the successive run, continued to increase. After sixteen runs, the disc displayed the first notable signs of asymmetry.

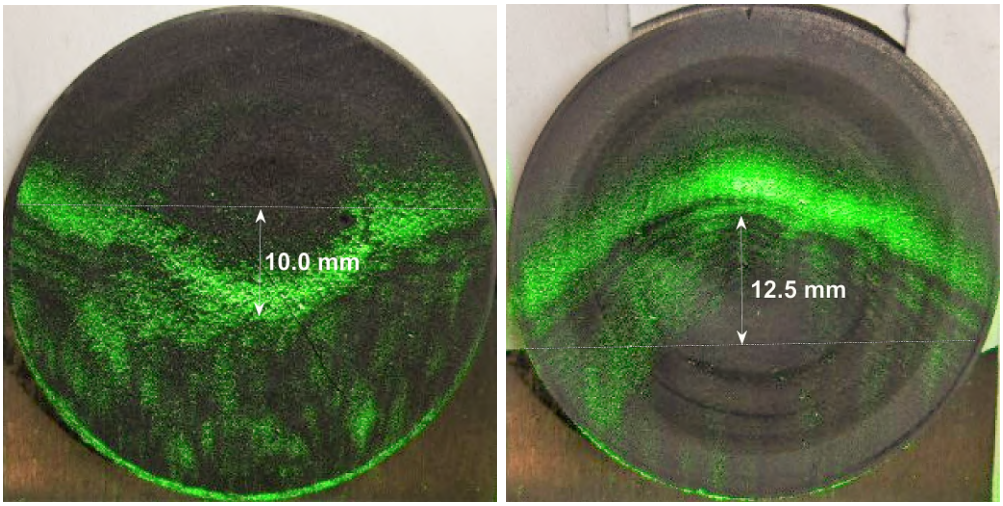


(a) Disc (front) (b) Disc (back)

Figure 4.28: Surface characteristics after sixteen heated-with-flow runs with the incident laser sheet at an angle of $2.5^0$. The light source is from below in these images.

When the disc was inspected after the sixteenth run, a large crack was discovered on the disc. This prevented continuation of the experiments. Figure 4.29 is the disc image after sixteen heated-with-flow runs with the disc rotated so the crack is visible in the laser sheet. The general changes indicate that the surface deformation was continuous.

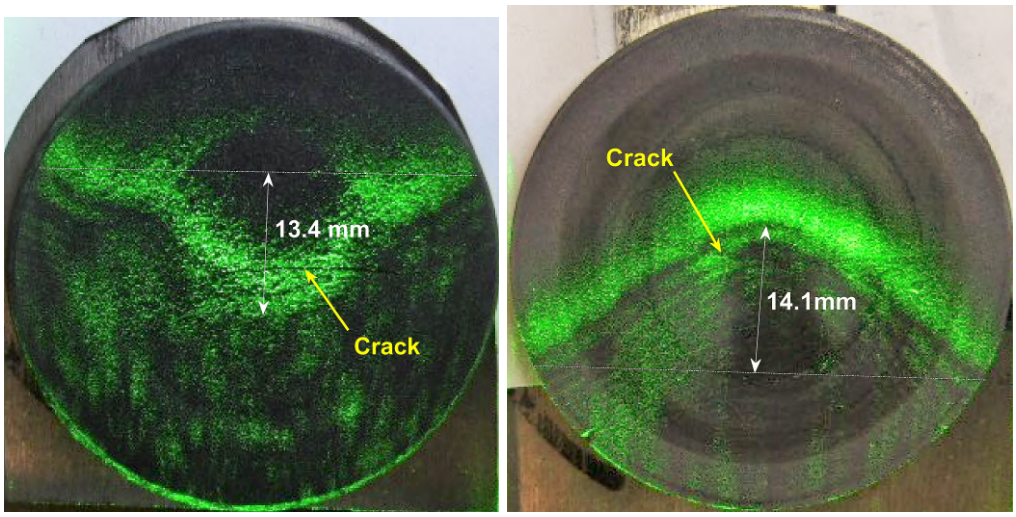


(a) Disc (front) (b) Disc (back)

Figure 4.29: Surface characteristics after sixteen heated-with-flow runs adjacent to the crack, with the incident laser sheet at an angle of $2.5^0$. The light source is from below in these images.

From the laser sheet investigations, it was evident that convex and concave shapes developed on the front and back of the disc respectively. The distances between the front and back surfaces were measured at various radial positions along the disc surface using the laser beam calculation in Figure 4.22 in order to estimate the final thickness of the disc. This final thickness was then subtracted from the original thickness in order to access the thickness reduction along the surface as shown in Figure 4.30. The results show that disc thickness continues to reduce with increasing numbers of heated with flow runs. The thickness reduction across the surface (from the edges to the stagnation region) has a non-linear distribution, which is maximum at the stagnation region and minimum at the edges.

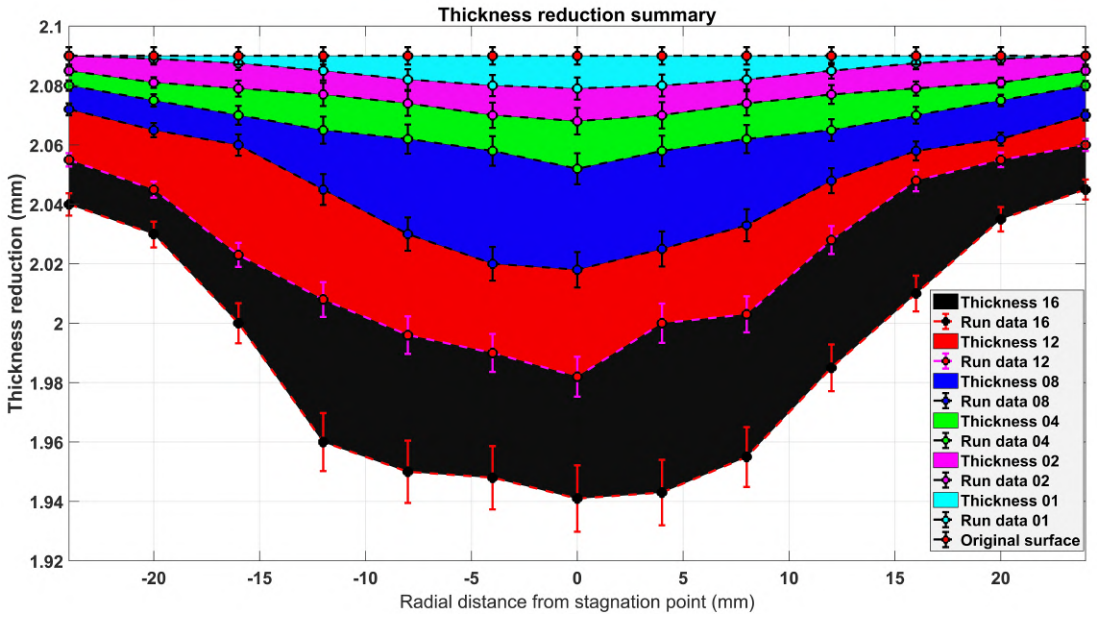


Figure 4.30: Surface deformation summary from laser sheet measurements after 1, 2, 4, 8, 12 and 16 heated-with-flow runs.

## 4.6 Surface Characteristics using the Micrometre Gauge

The micrometre measurements also recorded losses in thickness over successive runs. Four points were used across the disc at 0 mm, 8 mm, 16 mm, and 24 mm from the centre. The measured thickness across the four locations is shown in Figure 4.31. The anvil and spindle of the micrometer (where the micrometer contacted the disc) were 6.5 mm in diameter. The disc deformation and the ablating surface meant that the contact from the micrometer was unlikely to accurately measure the local thickness at each point, but more likely measured a general thickness at the location in the vicinity of each point. Figure 4.31 shows the general trend resulting from the ablation of the disc, where the top image is a magnified view and bottom image is the view relative to the whole thickness.

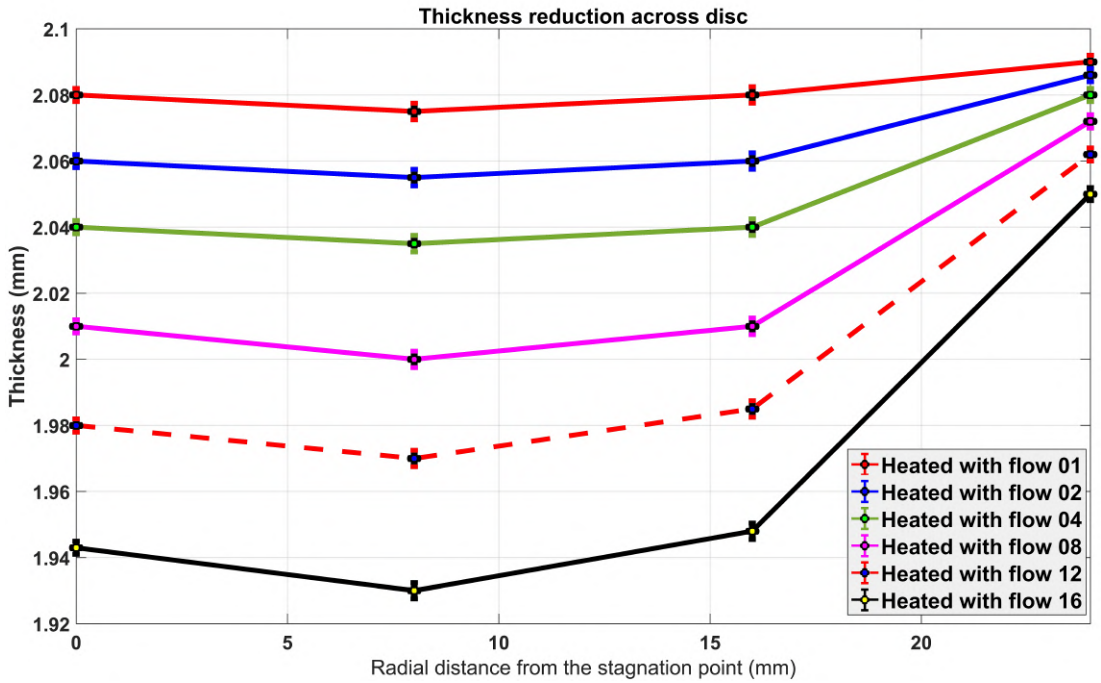


Figure 4.31: Variation in thickness across disc along paths perpendicular to the surface at various radial positions using the micrometre gauge after 1, 2, 4, 8, 12 and 16 heated with flow runs.

The thickness from the micrometer measurements in Figure 4.31 shows a general agreement with that obtained from the measuring arm in Figure 4.19. The laser sheet visualisation confidently identifies that the material loss is not at a consistent rate along a radius of the disc, but that the trend of the material loss rate is relatively consistent over the duration of the experiments.

## 4.7 Conclusions

The weighing method concluded that the average mass loss rate was 0.020 g/s for the flow period during sixteen heated-with-flow runs, 0.001 g/s for flow-only and 0.00055 g/s on average for heated-only. Flow-only mass loss rate is about 4.9 % of the average mass loss rate during the flow of heated-with-flow runs. An average mass loss rate during the heated-only runs (and therefore during the heating phase of a heated-with-flow run) is not particularly useful to report.

The Scanning Electron Microscope (SEM), the Laser beam visualisations, micrometer gauge, and measurements using the measuring arm were used to identify the shape changes due to ablation. The comparison with the shape change predicted from the mass loss is informed by the simulation of Chapter 5. Chapter 6 reports the techniques and outcomes for the volume based calculation of mass loss. Changing surface characteristics resulting from flow were identified by using the Scanning Electron Microscope (SEM). The results from SEM and laser sheet experiments reveal continuous thickness reduction with increasing number of runs. The CFD analysis will be explored in Chapter 5 to understand the mechanism of material loss identified in the experiments.

# Chapter 5

# Simulation Results

## 5.1 Introduction

This chapter presents the simulation results; how well the experimental results are able to be duplicated by simulation are addressed in Chapter 6. The surface reactions were simulated using Ansys Fluent CFD, modelled in a 2D axisymmetric mode. Schlieren images from the experiments were used to measure the position of the bow shock, as an indicator that the simulation is replicating the inviscid stagnation region flow. No direct measurements were achieved that could be compared with the simulation's chemistry, but a technique was employed in the analysis of the simulations to compare with the mass loss of carbon from the surface measured in the experiments. The mass of carbon contained in the reaction products calculated by the simulations was used for this purpose. This allowed a degree of comparison between the experiments and the simulation to be presented in Chapter 6.

## 5.2 Simulating Surface Chemistry

### 5.2.1 Overview

An academic version of the commercial software Ansys 18.2 was used to simulate the reactions at the surface. A 2D axisymmetric geometry was used in the model with meshing, set-up, solutions and results. The surface reaction chemistry was modelled to include site species. The simulations were run with laminar reacting flow and including reactions at the walls. The simulation employed a density-based solver.

### 5.2.2 Geometry and Meshing

The Ansys Design Modeller was used to define the shape of the model and subsequently design the fluid domain. The meshing was achieved using the programme controlled element order, adaptive size function, slow transition and span angle centre set to fine. Smoothing was set to high quality and the inflation growth rate of 1.2 applied. This resulted in 20845 nodes and 6852 elements. Named selections were created by dividing the surfaces of the disc, the holding ring and the surrounding mild steel into partitions in order to be able to input separate surface temperatures in different areas of the model. The meshing used for the fluid domain in the simulation is shown in Figure 5.1.

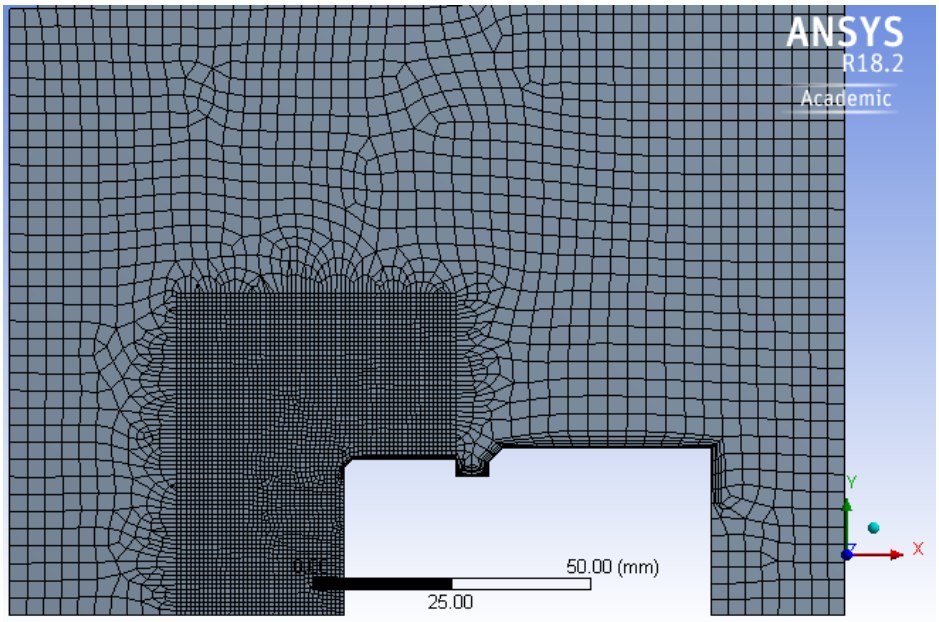


Figure 5.1: Mesh refinement resulting from application of various meshing tools to improve simulation accuracy.

### 5.2.3 Set-up

The set-up was a double precision, parallel solver with four processes. Steady state simulations were performed, as the software could not achieve transient simulations in 2D axisymmetric mode. The model was configured with energy on and viscous laminar conditions applied. The species transport was set-up by activating volume and wall surface reactions, heat of surface reactions, diffusion energy source and full multicomponent diffusion. A finite rate chemistry model was used. Import Chemkin mechanism was not used but the reacting species were manually set-up using the mixture-template as shown in Table 5.1.

Table 5.1: Reaction mechanism in the mixture-template

| Mixture-template | |
|---|---|
| Reaction type | Chemical reaction |
| Wall surface | $C + O \rightarrow CO$ |
| Wall surface | $C + O_2 \rightarrow CO + O$ |
| Wall surface | $C + CO_2 \rightarrow 2CO$ |
| Wall surface | $C + N \rightarrow CN$ |
| Wall surface | $C \rightarrow C$ |
| Wall surface | $2C \rightarrow C_2$ |
| Wall surface | $3C \rightarrow C_3$ |
| Volumetric | $C + O_2 \rightarrow CO_2$ |
| Volumetric | $N_2 \rightarrow N_2$ (non-reacting portion) |
| Volumetric | $O_2 \rightarrow O_2$ (non-reacting portion) |
| Site species | C and $O_2$ |

The reacting species consist of volumetric, surface and site species. The nozzle geometry position relative to the probe was also simulated. The finite rate wall-surface reactions were carried out by setting up the reactants and products and inputting stoichiometric coefficients to balance the reactions based on the Park model of Section 2.3.6. The surface coverage-dependent reaction was activated in order to account for the site species, although activating this feature only had a negligible effect on the simulation results. Attempts to input user-defined temperature profiles to replicate the spatially varying temperature were not successful. A technique was employed which divided the disc into twelve concentric areas and each area was assigned with a temperature value (constant) representing an average temperature in that area. The surface temperatures were extracted from data used to create the plot in Figure 3.27. Necessarily, chemical reactions was activated. The simulation was initiated by flow speed at the inlet to the simulation, which was the geometry of the outlet from the nozzle in the experiments. The simulation used air at the conditions known to exist at the outlet of the nozzle. The summary for the reaction set-up is shown in Figure 5.2 and Figure 5.3. The number of Volumetric Species was ten, number of solid species was one (carbon solid) and the number of active site species was two.

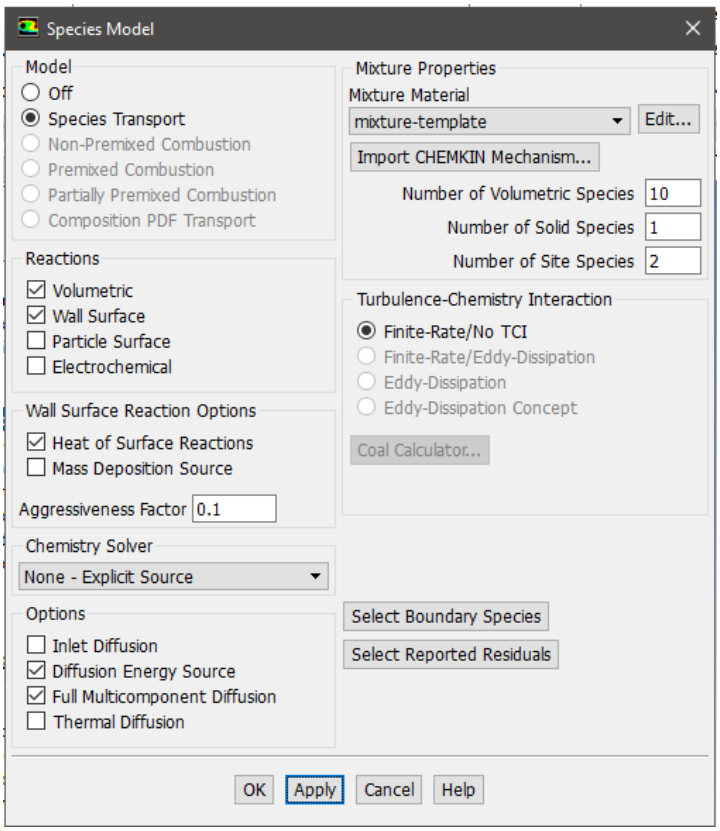


Figure 5.2: Summary of set-ups for the surface reactions.

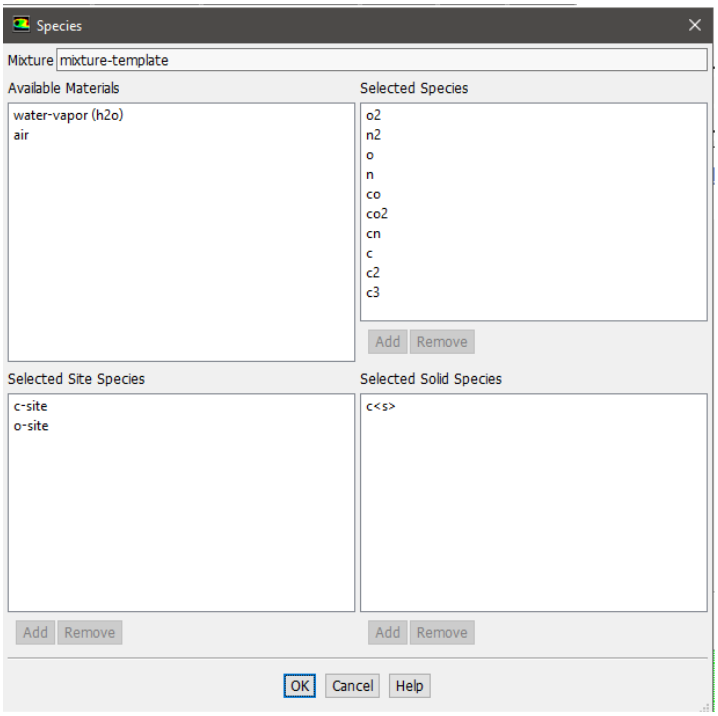


Figure 5.3: Set-ups for species, where selected species are the Volumetric Species.

### 5.2.4 Solutions and Results

The selection of spatial discretisation was by default and second order solutions were chosen to maximise accuracy as recommended by ANSYS Manual (Guide, 2011). Gradient was set as least square cell based, pressure set as second order. Density, momentum, turbulent kinetic energy, specific dissipation rate, species and energy were all set as second order upwind. Pseudo-transient was activated to help with solution convergence and a standard initialisation was used. The simulation boundary conditions were established including surface temperatures, flow velocity and pressure, and the simulation run to establish flow. Chemical reactions were then activated. Each step required iterations ranging from 400,000 to 850,000 depending on the convergence. The contours for image results were interpreted graphically and files were exported for further processing in MATLAB.

## 5.3 Simulation Results from CFD

The chemistry at the graphite surface is significantly influenced by the flow characteristics. Combustion species are only evident in the boundary layer. Reactions require temperatures that only exist in the boundary layer. Figure 5.4 shows the front surface of a 3D representation of the graphite disc. The images in Figure 5.5 show the anticipated effect of ablation on the graphite specimen as identified in the experiments. The height above the disc surface is represented by $y$ while the radial direction away from the axis of symmetry is represented by $R$. The cylindrical area annotated in Figure 5.4 is normal to the flow and represents the area through which all the reaction species must flow. This area was used within the simulation results to specify the mass fraction, density and velocity from which the mass flow rates of various species were calculated.

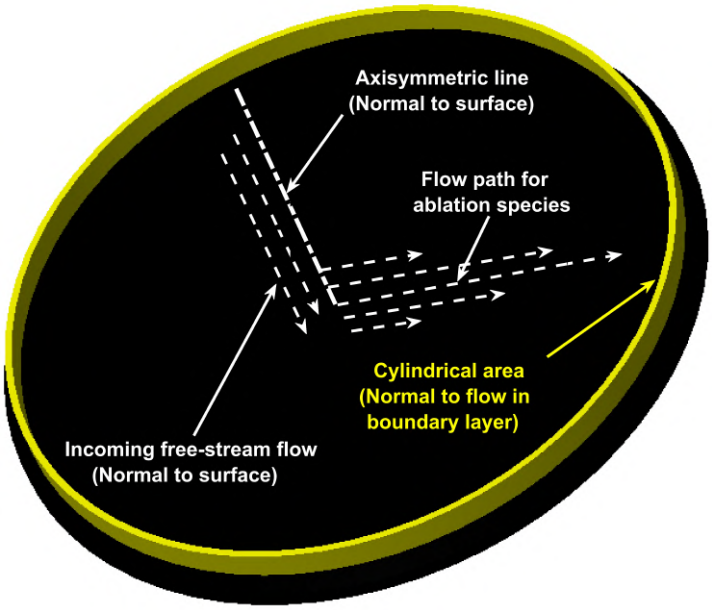


Figure 5.4: 3D representation of the flow in the simulations and the region through which the flow was assessed to calculate species leaving the carbon surface.

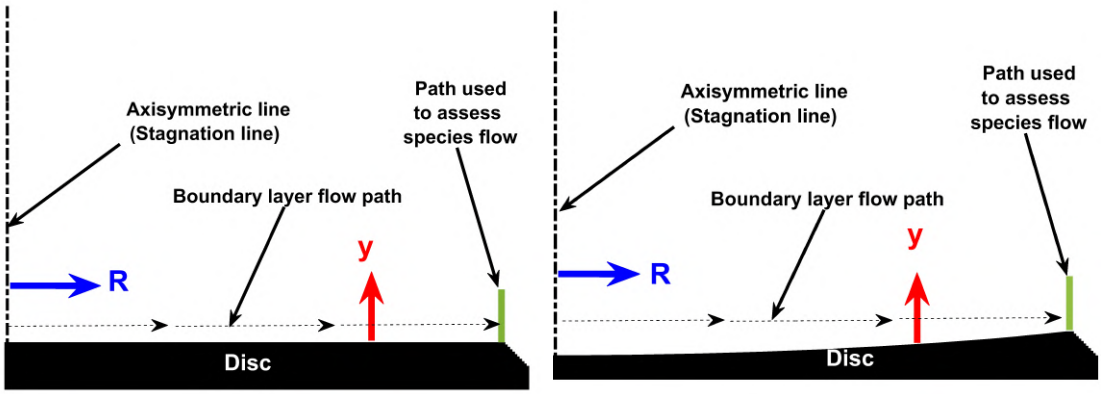


(a) New graphite disc

(b) Ablated graphite disc

Figure 5.5: Sectional representation of the 3D image in Figure 5.4 showing flow effect on the disc material and the path representing the cylindrical area used to assess species mass flow rates.

Figure 5.6 shows the set-up used to define the hot surface temperature distribution. Lines A and B (R02 and R24) are named selections used to define temperatures at the stagnation and edge regions respectively along a radius on the front surface of the disc. The points in Figure 5.6 define the ends of the various line segments with a length

of 2 mm that were used to create the required named selections. The resulting 12 different partitions along the 24 mm radius have temperatures allocated based on the temperature profile of Figure 3.27. The temperature used was the temperature at the midpoint of each segment.

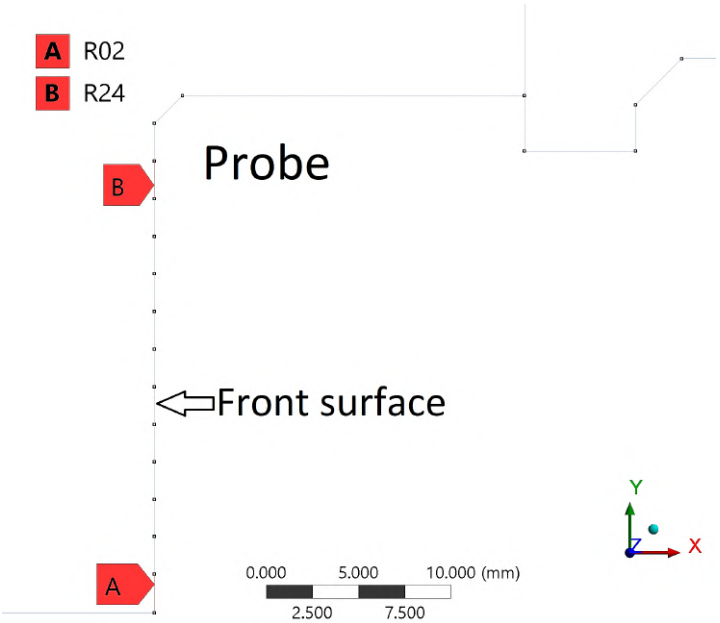


Figure 5.6: The geometric set-up for defining the named selections for spatially varying temperature on the hot graphite surface.

Figure 5.7 shows properties calculated in the simulation. During the flow, the experiments identified that the maximum surface temperature of the graphite fell by about 20 K. The properties shown in Figure 5.7 are for a steady state simulation based on a temperature profile of the disc surface at the start of flow.

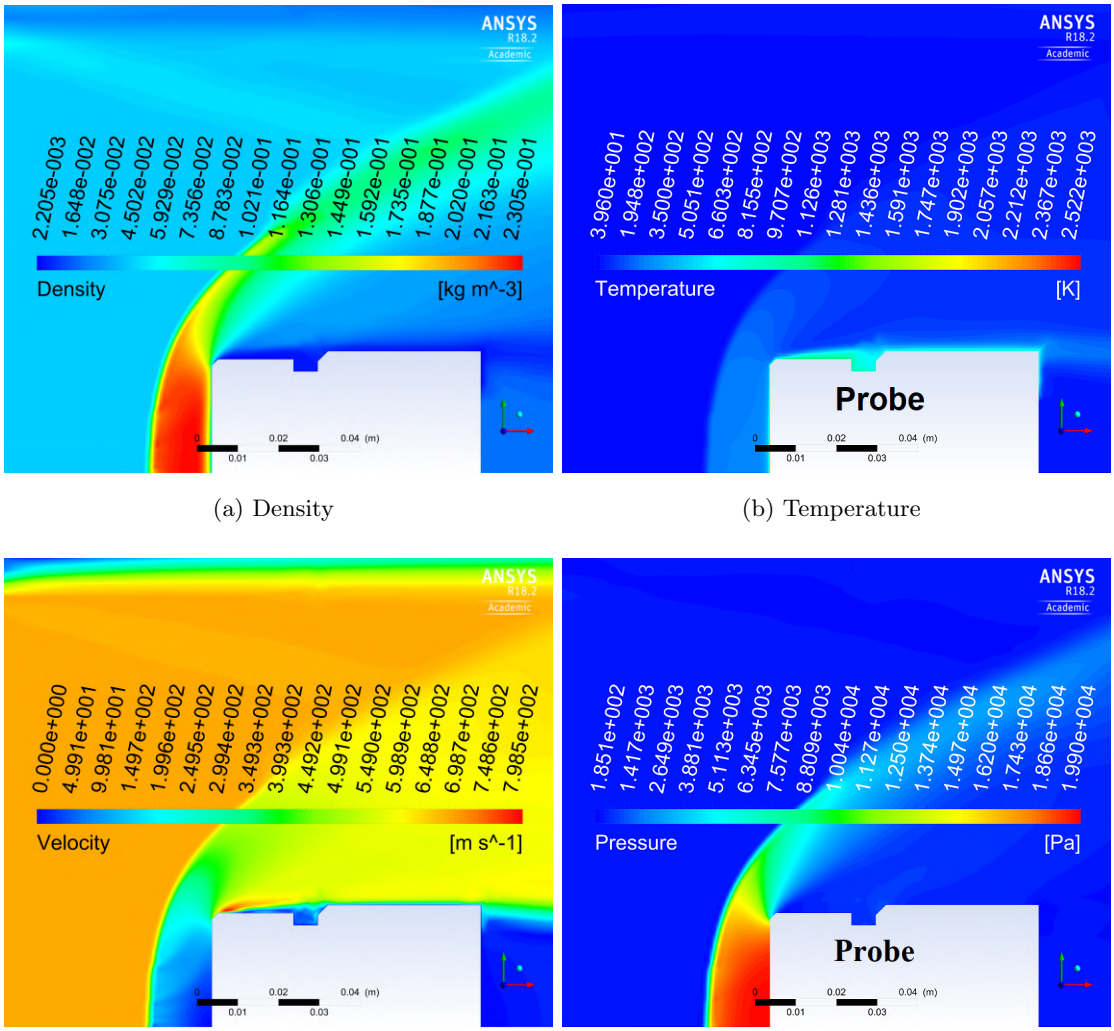


(a) Density (b) Temperature

(c) Velocity (d) Pressure

Figure 5.7: Contour maps of various properties of simulated flow generated in the simulation from the same boundary conditions of the experiments.

Figure 5.8 shows the contour plot for the pressure gradient which identified the bow shock stand-off position. On the centreline, the upstream edge of the bow shock was about 15 mm from the surface, very similar to the bow shock position in the experiments as shown in Figure 5.9.

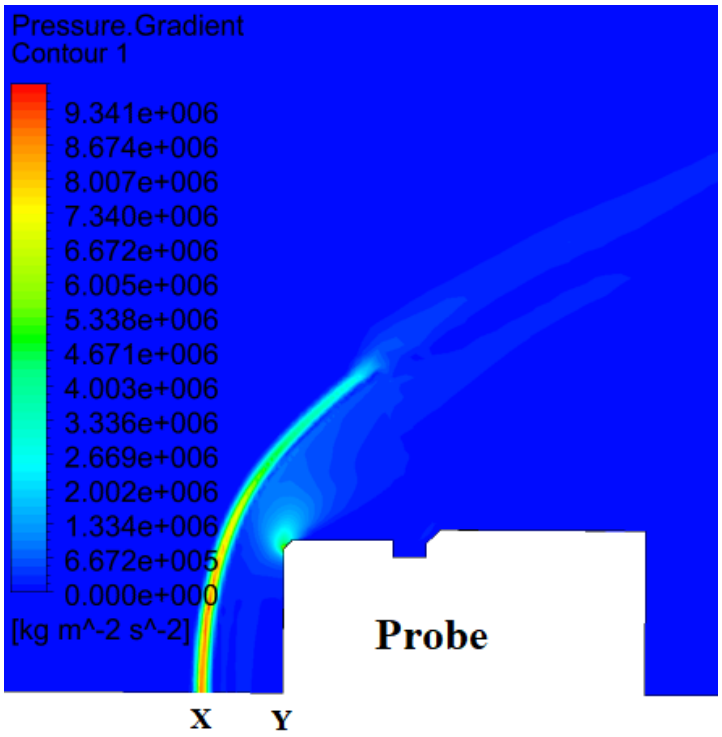


Figure 5.8: Contour map of pressure gradient, where XY = 15 mm along the axis.

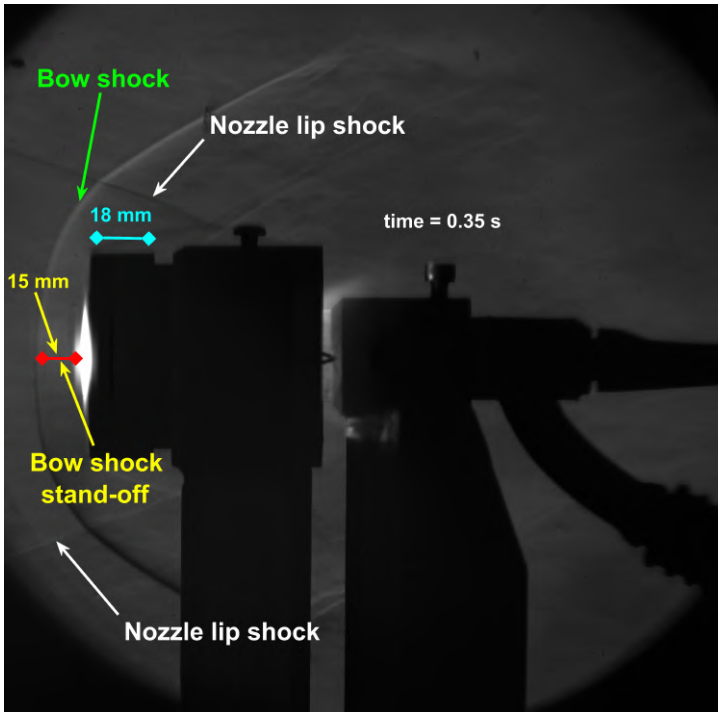


Figure 5.9: Schlieren image showing bow shock stand-off distance in the experiments, calculated from scaling of known probe dimensions.

Simulated properties of the flow are shown in Figure 5.10. The x-axes in these figures are along the axis of the probe in the simulation; the origin is at the surface of the disc. The pressure increased from 400 Pa to 18.6 kPa across the shock in the flow direction. The gas density increases from 0.045 $kgm^{-3}$ to 0.22 $kgm^{-3}$ across the shock, and continues to rise to a maximum value of 0.23 $kgm^{-3}$ at about 4 mm from the wall, and finally dropping to a minimum value of 0.033 $kgm^{-3}$ at the wall. The static temperature rises from 60 K to 272 K across the shock, maintaining this relatively constant value to about 4 mm from the hot surface, then rises to a maximum value of about 2500 K at the wall, which explains the density change. The turbulence kinetic energy is greatest at the shock and falls to almost zero at the stagnation point, suggesting a laminar boundary layer. The gas velocity also decreased across the shock from about 700 m/s to about 51 m/s, and then experiencing a small rise immediately after the shock and gradually falling to zero at the stagnation point.

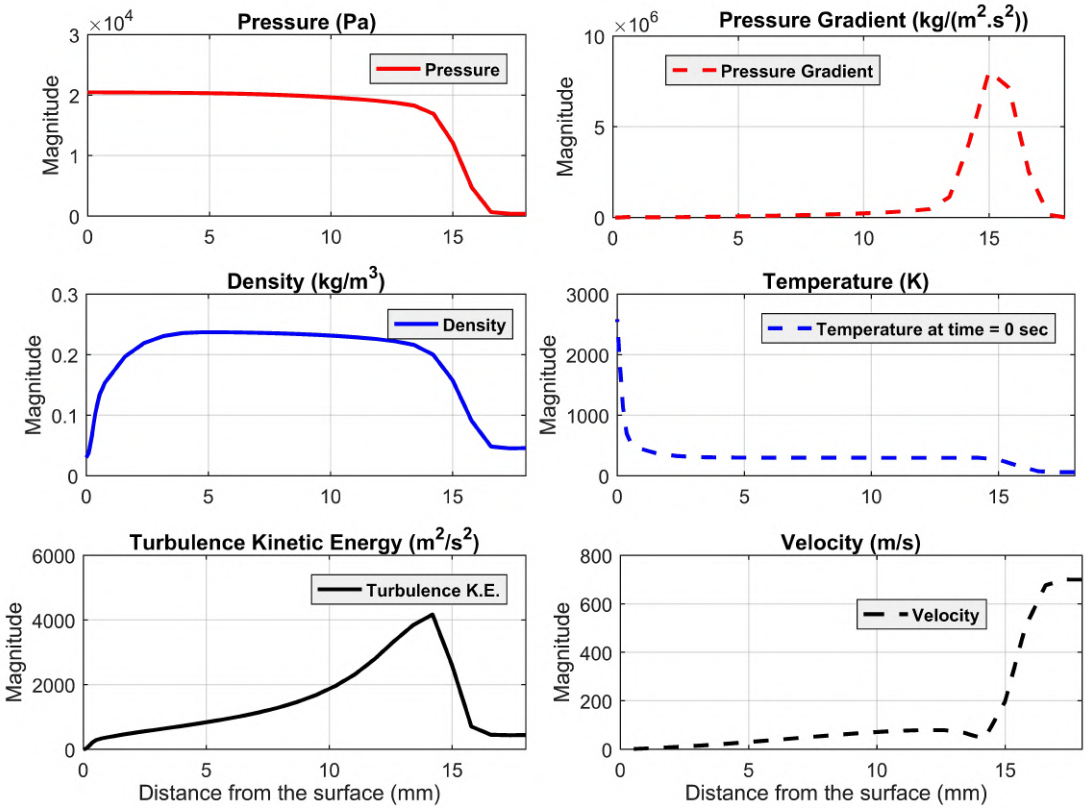


Figure 5.10: Flow properties along the probe axis from the simulation. The simulation replicated the bow shock stand-off distance.

The air in the simulation is prescribed as a mixture of 21 % oxygen and 79 % nitrogen.

No changes in the gas properties are evident until approximately 4 mm from the wall. The mass fraction of $N_2$ behaves in a similar way to that of $O_2$ with a sharp drop near the surface as shown in Figure 5.11 as a result of the increase in mass fraction of reaction products entering the flow from the surface. The mass fraction of molecular oxygen dropped from 21% to about 8% at the wall while that of molecular nitrogen dropped from 79% to about 67% at the wall. Neither the molecular oxygen nor nitrogen concentration dropped to zero at the wall as the temperature reached by the gas is not sufficient for complete dissociation. This indicates that a mixture of $N_2$ and $O_2$ was still present in the reacting boundary layer. A contribution to the reduced concentration of molecular oxygen results from its consumption in combustion. The molecular oxygen was only dissociated in very close proximity to the surface as the gas temperature only reached the dissociation temperature within 0.0025 mm from the wall.

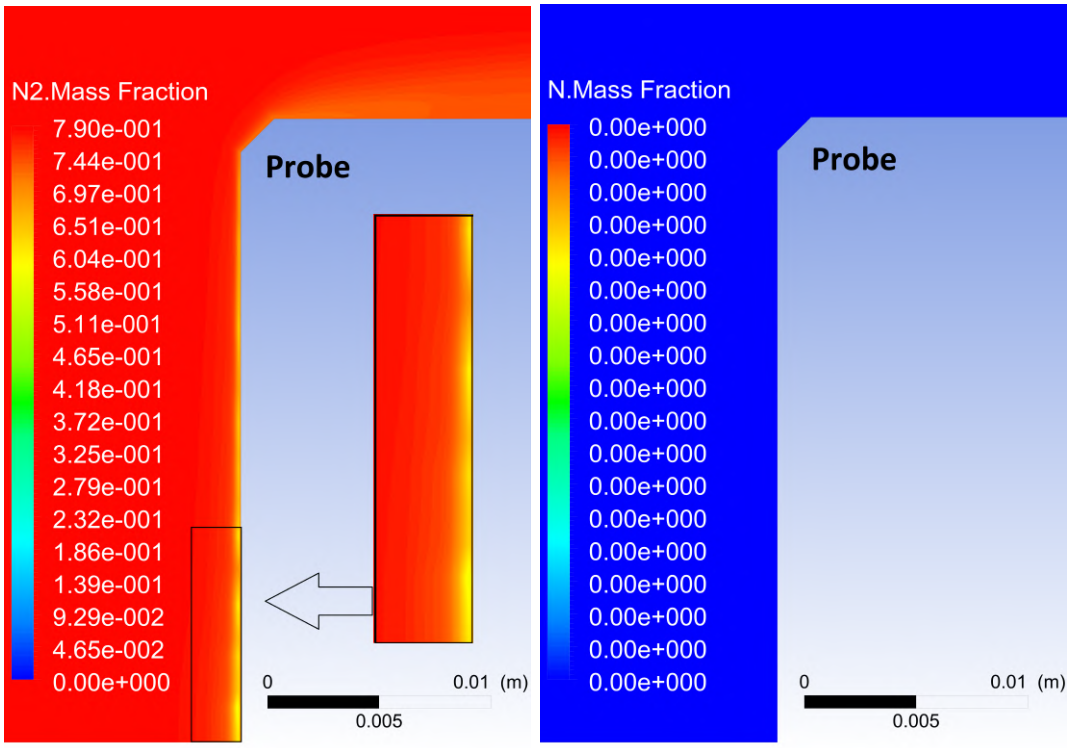


(a) Molecular nitrogen

(b) Atomic nitrogen

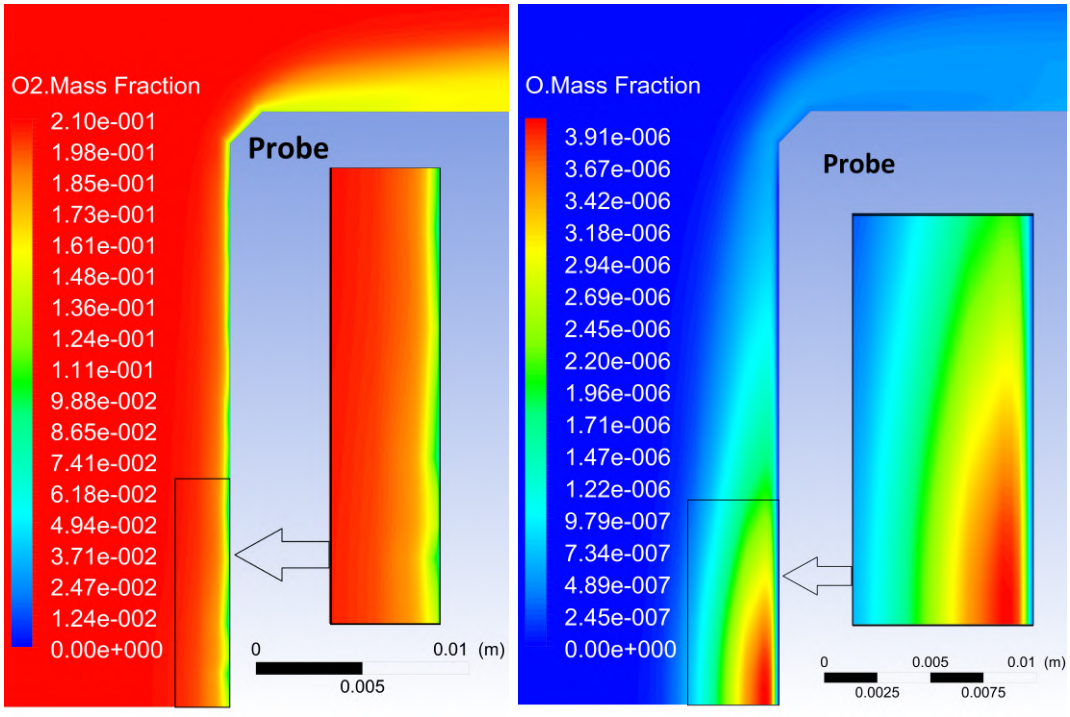


(c) Molecular oxygen

(d) Atomic oxygen

Figure 5.11: Mass fractions of gases using steady state CFD simulation with spatially varying wall temperatures.

The simulation did not predict atomic nitrogen in the present work. This is because the temperature needed to cause $N_2$ dissociation was not achieved in the present work. Contour plots showing the results of mass fractions of the six carbonaceous species are shown in Figure 5.12, Figure 5.13 and Figure 5.14. The CO formation was the major contributor to graphite mass loss and contributions from all other carbonaceous species were insignificant. The peak values for the mass fractions of CO, $CO_2$, CN, C, $C_2$ and $C_3$ are 0.079, $1.18 \times 10^{-7}$, $1.48 \times 10^{-17}$, $1.58 \times 10^{-12}$, $1.92 \times 10^{-12}$ and $2.44 \times 10^{-11}$ respectively. All carbonaceous species have their peak values around the stagnation region at the wall. The mass fraction of CO species rises to a maximum value at the wall. Mass fraction of $CO_2$ increases to a maximum near the wall and then drops closer to the wall.

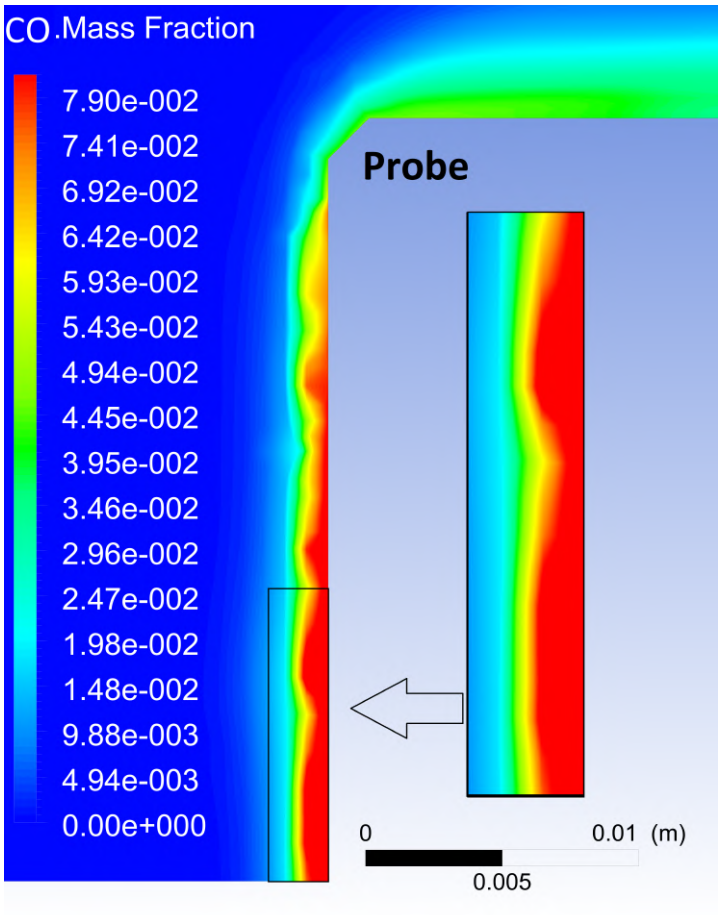


Figure 5.12: Simulation result for CO mass fraction in the boundary layer.

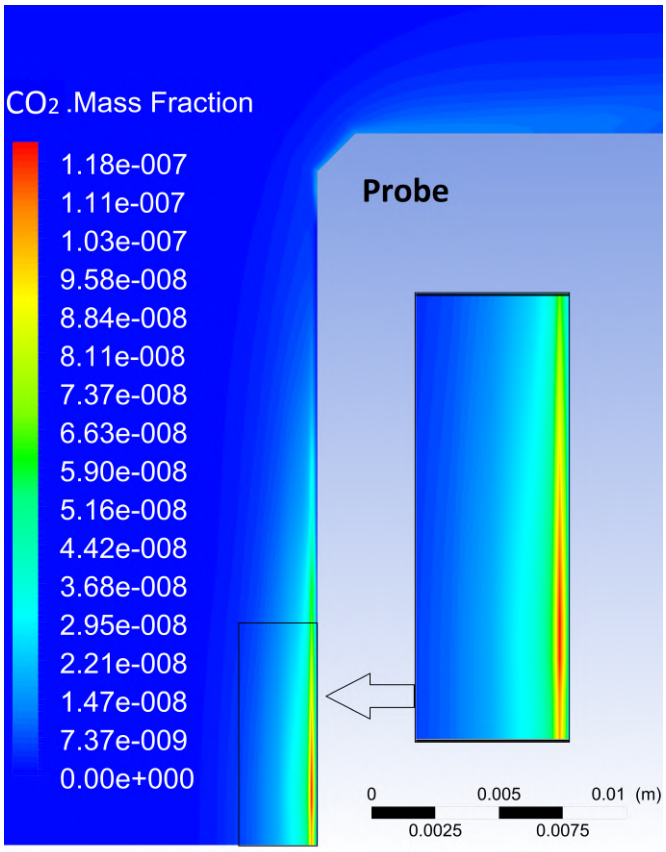


(a) Mass fraction of $CO_2$ species

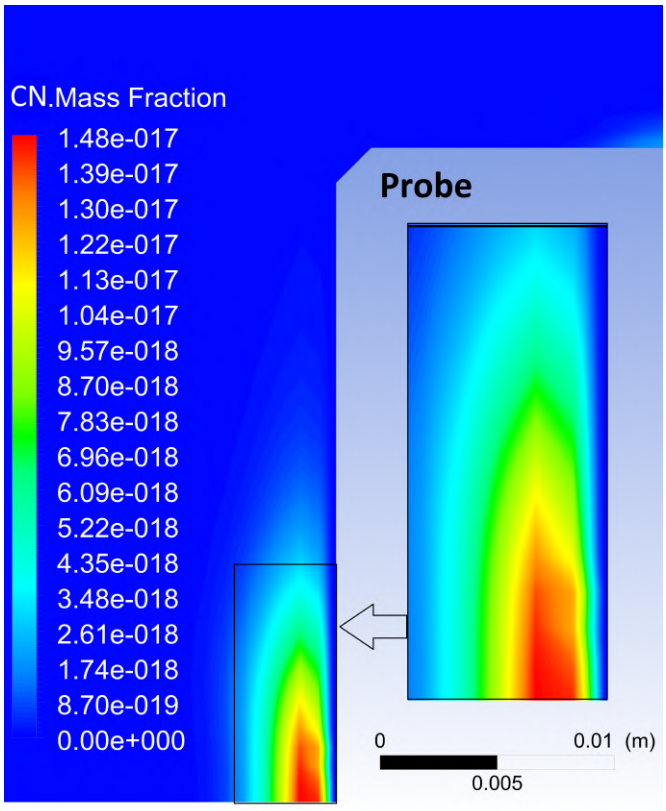


(b) Mass fraction of CN species

Figure 5.13: Species mass fractions for $CO_2$ and CN in the boundary layer.

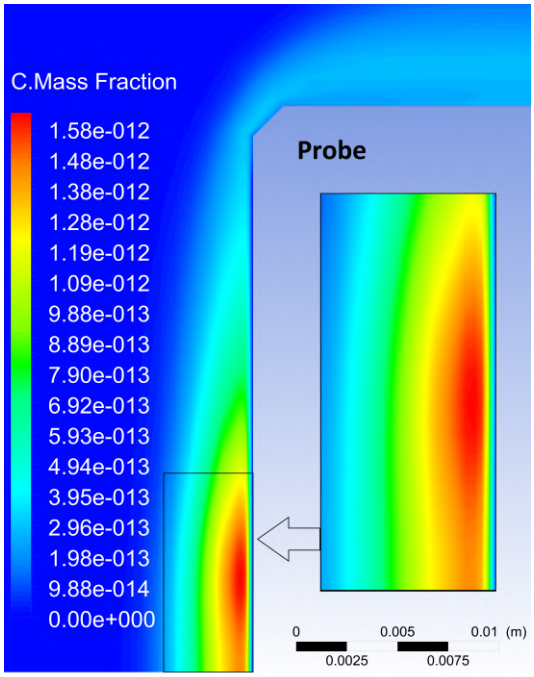


(a) Mass fraction of C species

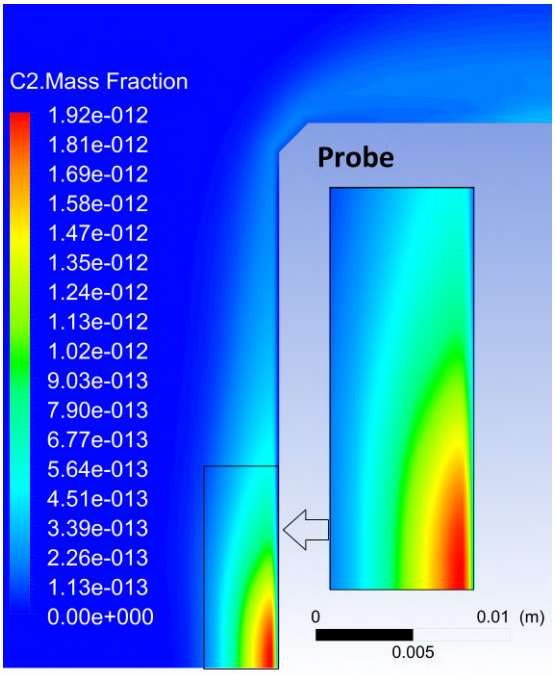


(b) Mass fraction of $C_2$ species

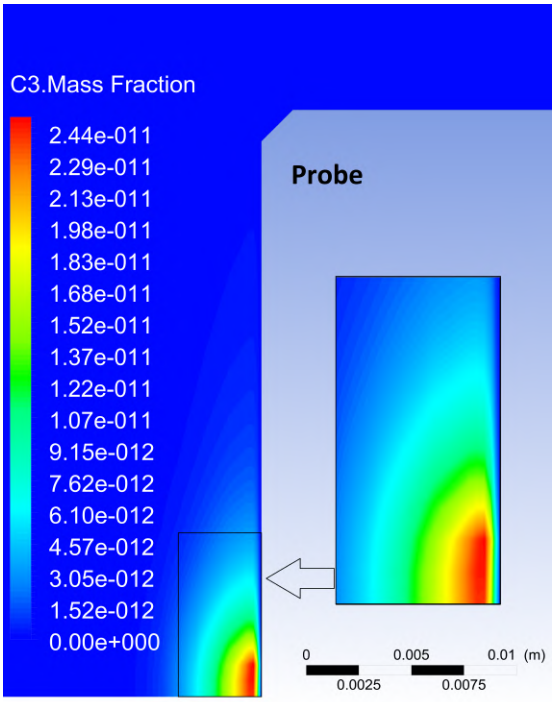


(c) Mass fraction of $C_3$ species

Figure 5.14: The mass fractions for sublimation species, C, $C_2$ and $C_3$ in the boundary layer.

Simulation results from CFD show that the peak mass fraction of CO at the surface was about 7.9 %. At about 1 mm from the surface, Figure 5.15 shows the concentration of products peak. But Figure 5.10 indicates that the temperature has not changed significantly until within 1 mm from the wall, so the concentration of products is not entirely driven by temperature alone. The $CO_2$ mass fraction is about six orders of magnitude lower than that of CO.

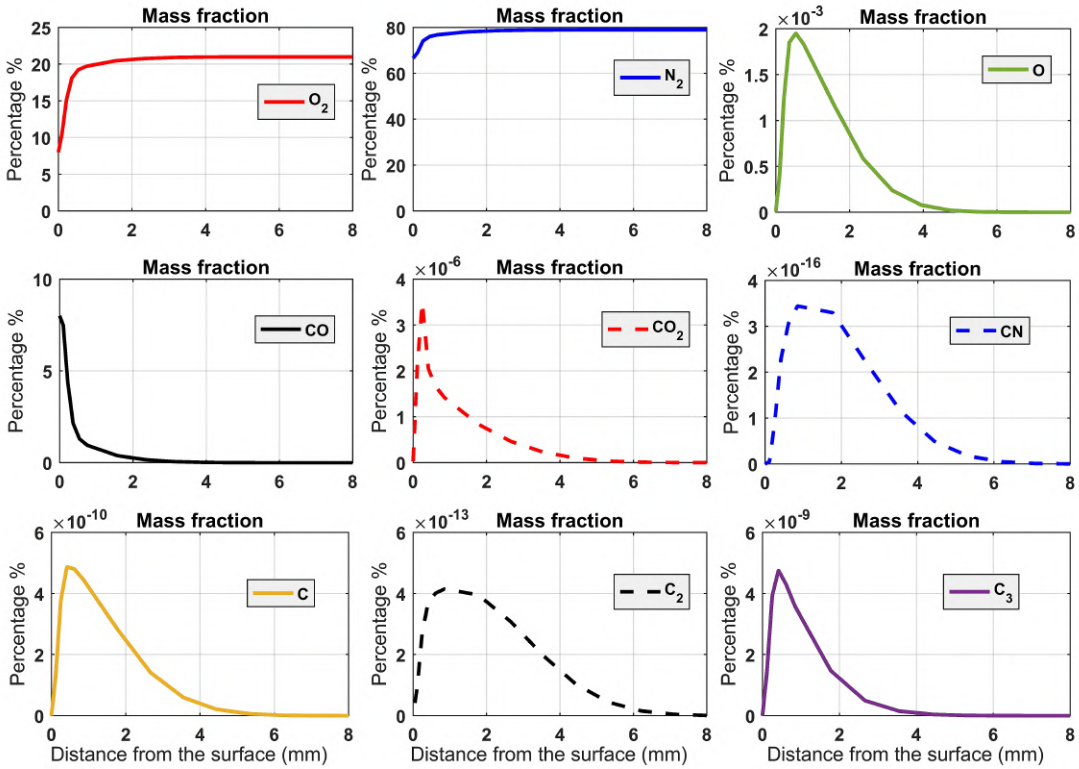


Figure 5.15: The species mass fractions along the probe axis from the simulations. The atomic nitrogen was not included in the results because it was calculated to be effectively zero.

Thermally initiated chemical reactions are the formation process of all carbonaceous species in Figure 5.15, except for the carbon sublimation species, C, $C_2$, $C_3$. The $CO_2$ species are formed from further oxidation of CO species, thus making $CO_2$ a secondary reaction. The $CO_2$ concentration shows a maximum at the stagnation flow region where the O species are maximum, which suggests the requirement of O species for $CO_2$ formation. The result also shows that $CO_2$ has a sharp drop from the peak value to almost zero at the surface within the experimental temperature limit of 2530 K.

The CN species distribution also show a similar pattern to that of $CO_2$. This also suggests that CN is not a product of direct surface reaction within the experimental temperature limit. This further supports the absence of dissociated nitrogen atoms which would otherwise aid direct formation of CN at the surface. The sublimation species C, $C_2$, and $C_3$ are almost zero.

## 5.4 Mass Loss Rate

### 5.4.1 Bulk Flow Properties

The procedure for analysis of the carbon mass transport involves dividing the surface radius of 24 mm into twelve different partitions of 2 mm increments as shown in Figure 5.16, which is a schematic representation of the detail shown in Figure 5.6. The software reported the mass fractions of reaction products flowing through each of the partitions. Density and velocity were also obtained for the flow through these partitions, and used to calculate the mass flow rate of each reactant as per Equation 5.1.

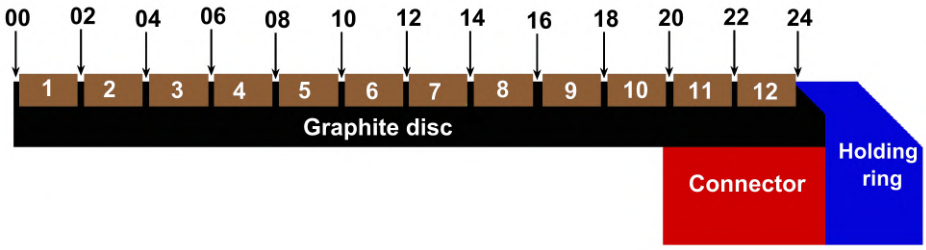


Figure 5.16: The disc was partitioned into 12 parts to access mass flow rates of reaction products to enable calculation of carbon mass loss from each partitioned section. This is achieved by extracting the total mass of carbon from all carbonaceous species calculated in the simulation in the flow at each of the 12 positions depicted.

The estimation of mass flow rate $\dot{m}$, based on simulation, is given by Equation 5.1, where $\rho$, $v$ and $A_{cyl}$ respectively represent density, velocity, and the cylindrical area

normal to the flow (defined by the location of partitions in Figure 5.16).

$$\dot{m} = \frac{mass}{time} = \rho \times \frac{Volume}{time} = \rho \times v \times A_{cyl} \tag{5.1}$$

The simulation result from Figure 5.17 shows the density and velocity within 4 mm height above the disc. The density at different radial positions ($R$), was reasonably constant at the various positions along the radius, and starts to drop from about 0.23 kg/m$^3$ at 2.5 mm from the surface to a minimum of about 0.04 kg/m$^3$ at the surface. The velocity at different radial positions ($R$) also varied and the magnitudes dropped from the outer edge to the line of symmetry, $R = 0$ mm. All velocities dropped to zero at the surface irrespective of the radial position (no slip condition in the simulation).

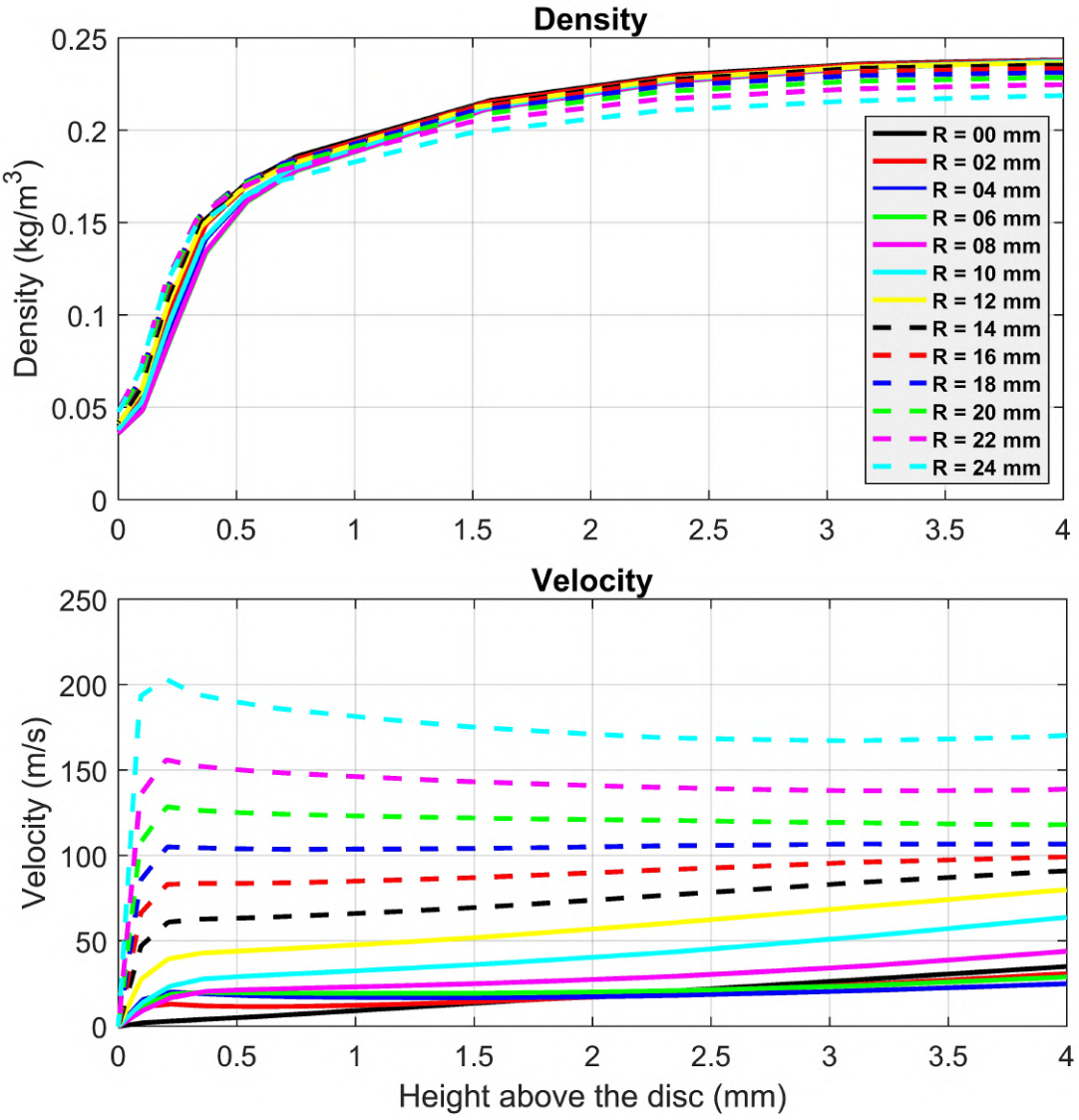


Figure 5.17: Bulk flow parameters (showing the variation of air density and velocity) along paths perpendicular to the surface at various radial locations.

The cylindrical area $\Delta A$ normal to the flow (see Figure 5.4) was calculated (using $2\pi Rh$) at various radial locations, where $h$ is the height above the surface. The value $R$ increases in the radial direction from the stagnation point ($R = 0$ mm) to the edges ($R = 24$ mm). The maximum height above the disc surface was restricted to 4 mm in the plots because all species formation occurred within 4 mm from the surface. The data sourced from the simulation was to a height of 8 mm above the surface. The top plot of Figure 5.18 shows the cylindrical area for each incremental step height, $\Delta h$ at various radial distances. The data from the simulation was exported as 1000 points

over the 8 mm height considered, giving $\Delta h$ to be 0.008 mm. The value of $\Delta A$ has a linear relationship with $R$ for an elemental height above the surface. The bottom plot of Figure 5.18 shows the mass flow rate of all gaseous species leaving the flow at successive radial locations for each $\Delta h$ using Equation 5.1.

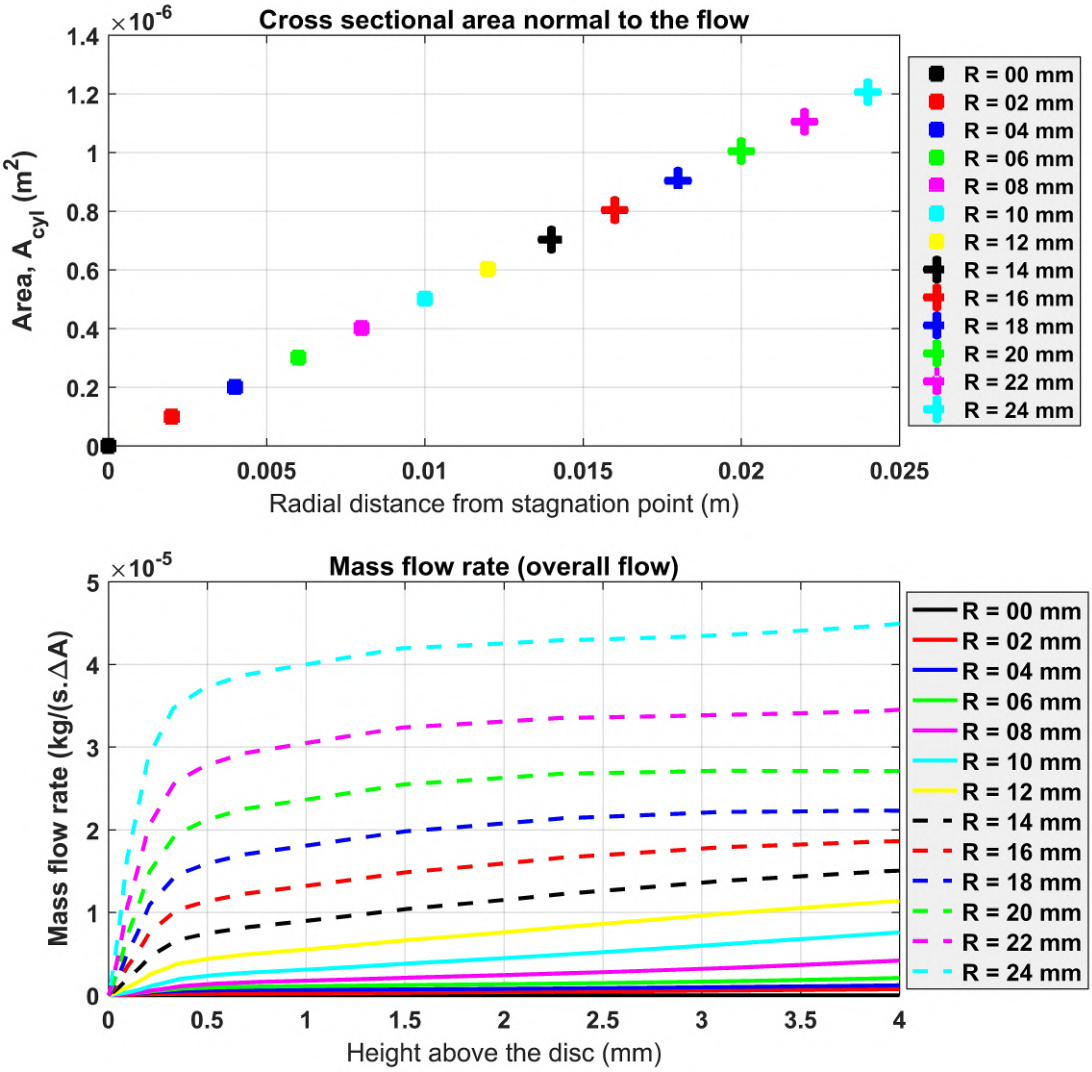


Figure 5.18: Bulk flow parameters showing the variation of cross sectional area and mass flow rate through paths perpendicular to the surface at various radial locations. The mass flow rate is specified to be the total flow of all gaseous species through the small incremental areas, $\Delta A$ of height $\Delta h$, for each of the 1000 step height increments over the 8 mm height considered (plots are restricted to the 4 mm height representing the region of interest for reaction species)

### 5.4.2 Mass Fraction of Species

Figure 5.19 and Figure 5.20 show the mass fractions at various heights above the disc, for the six carbonaceous species in the present work, CO, $CO_2$, CN, C, $C_2$, and $C_3$. All species plots are raw data exported from CFD simulations under the conditions of the experiments. The results show that CO is the major contributor to the carbon mass loss. The contributions from all other carbonaceous species were insignificant.

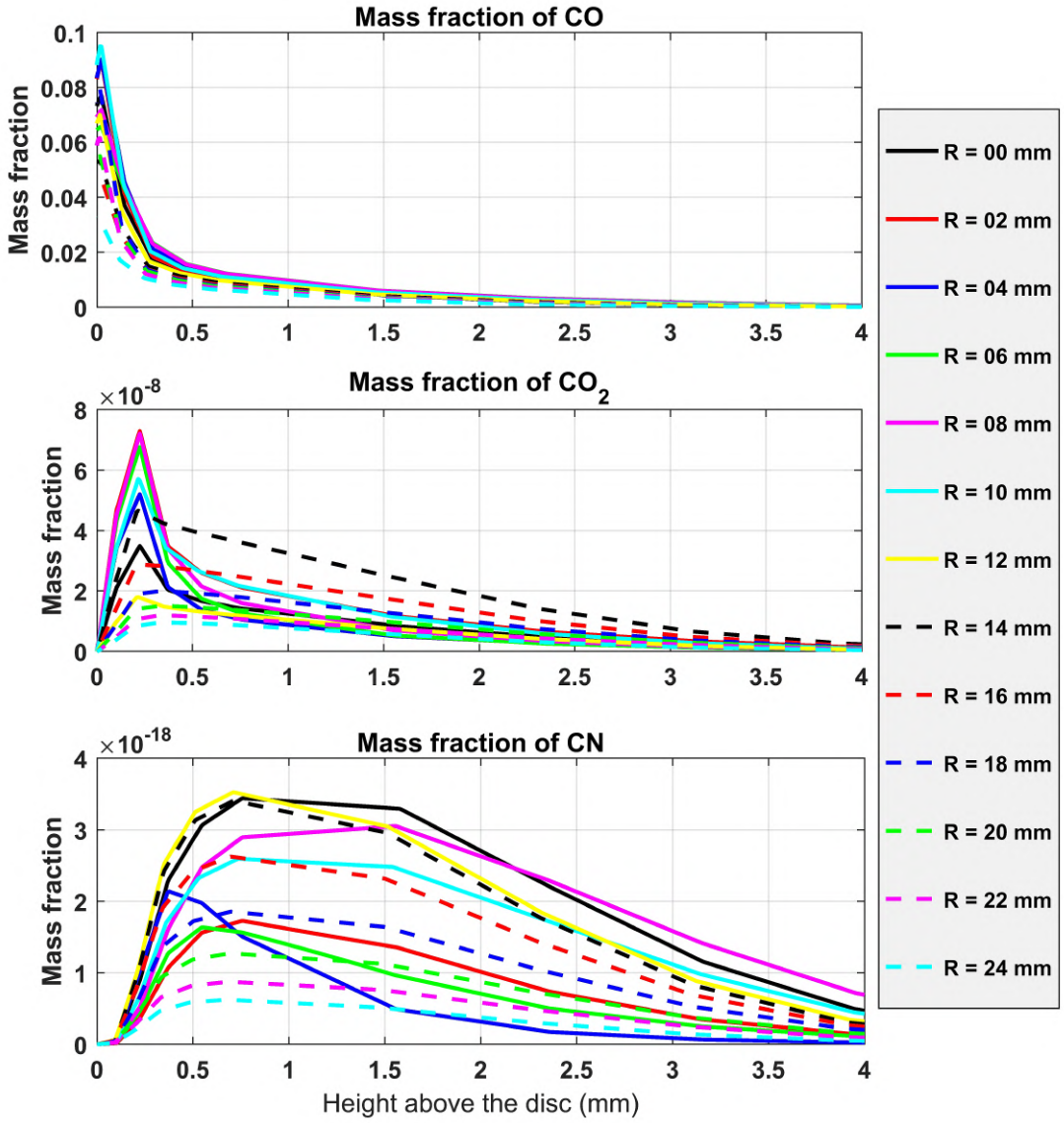


Figure 5.19: Mass fractions of CO, $CO_2$, and CN species through paths perpendicular to the surface at various radial locations.

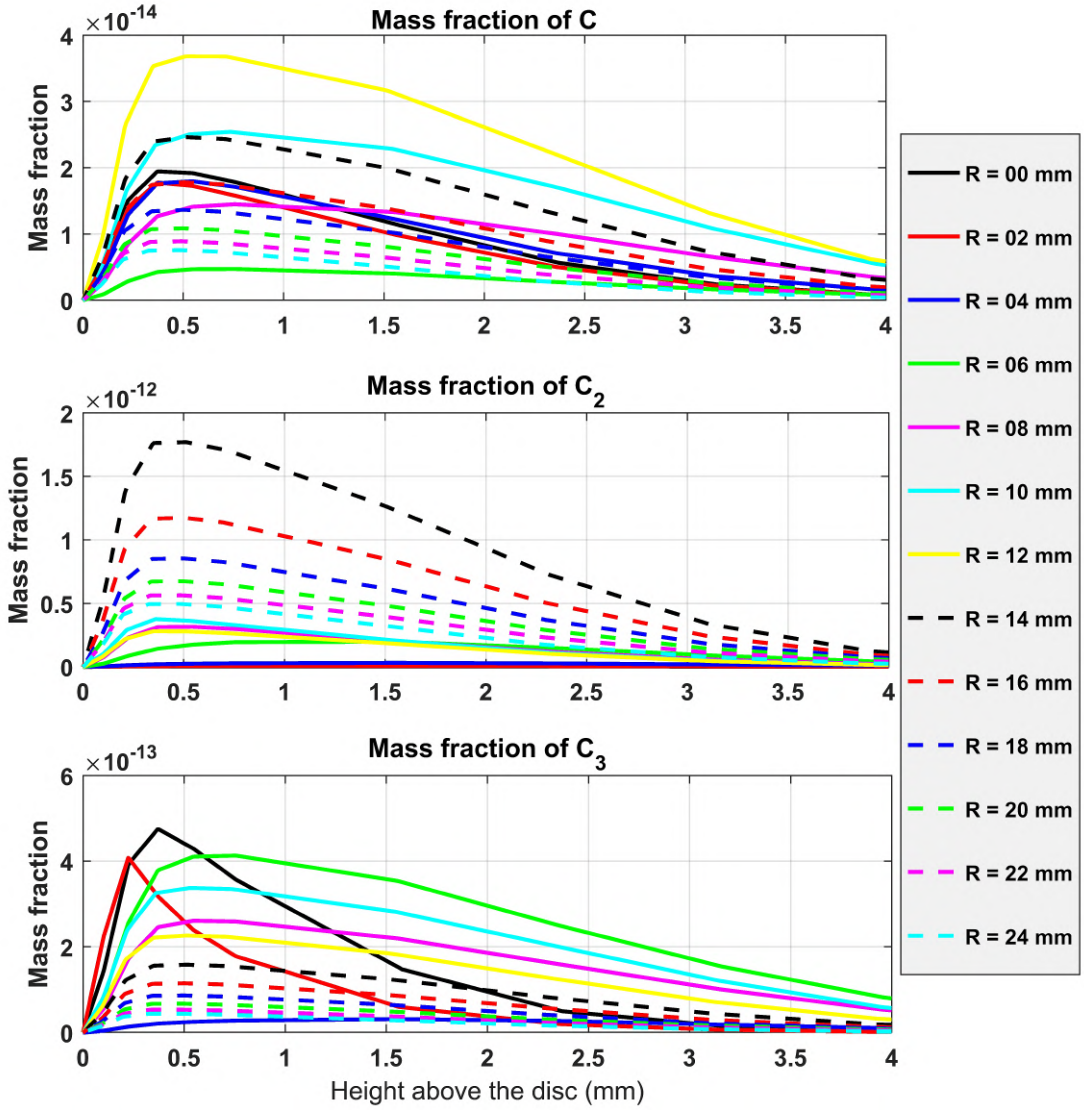


Figure 5.20: Mass fractions of C, $C_2$, and $C_3$ species through paths perpendicular to the surface at various radial locations.

The total amount of carbon lost from the disc, necessarily leaves as carbonaceous species in the flow that leaves the edge of the disc. The atomic weight of elements in grams per mole used to calculate the mass of carbon in the flow is provided in Table 5.2.

Table 5.2: Estimating the mass of carbon loss from chemical species.

| Elements | Atomic mass of element | Species | Weight of carbon ratios ($W_i$) |
|---|---|---|---|
| C | $C_{wt}$ = 12.0107 g/mol | CO | $C_{wt}/(C_{wt} + O_{wt}) = 0.4288$ |
| O | $O_{wt}$ = 15.9994 g/mol | $CO_2$ | $C_{wt}/(C_{wt} + 2O_{wt}) = 0.2729$ |
| N | $N_{wt}$ = 14.0067 g/mol | CN | $C_{wt}/(C_{wt} + N_{wt}) = 0.4616$ |
| - | - | C | $C_{wt}/C_{wt} = 1$ |
| - | - | $C_2$ | $2C_{wt}/2C_{wt} = 1$ |
| - | - | $C_3$ | $3C_{wt}/3C_{wt} = 1$ |

The mass loss of each carbon species was calculated by multiplying the respective weight of carbon ratio in Table 5.2 by the overall mass flow rate and mass fraction for each of the twelve partitions in the radial direction as shown in Equation 5.2. Where $C_i$ (kg/(s.m$^2$)) is the carbon mass leaving each cylindrical partition, $Y_i$ is the mass fraction of each of the six carbonaceous species (CO, $CO_2$ CN, C, $C_2$ and $C_3$ ), $W_i$ is the weight of carbon ratio, $\dot{m}$ (kg/s) is the mass flow rate from Equation 5.1 and $n$ is the number of carbonaceous species ($n = 6$).

$$C_i = \sum_{i=1}^{n} (Y_i \times W_i \times \dot{m}) \tag{5.2}$$

Using Equation 5.2, the mass removal rate of carbon from each of the twelve partitions, to the height of 4 mm is presented in Figure 5.21.

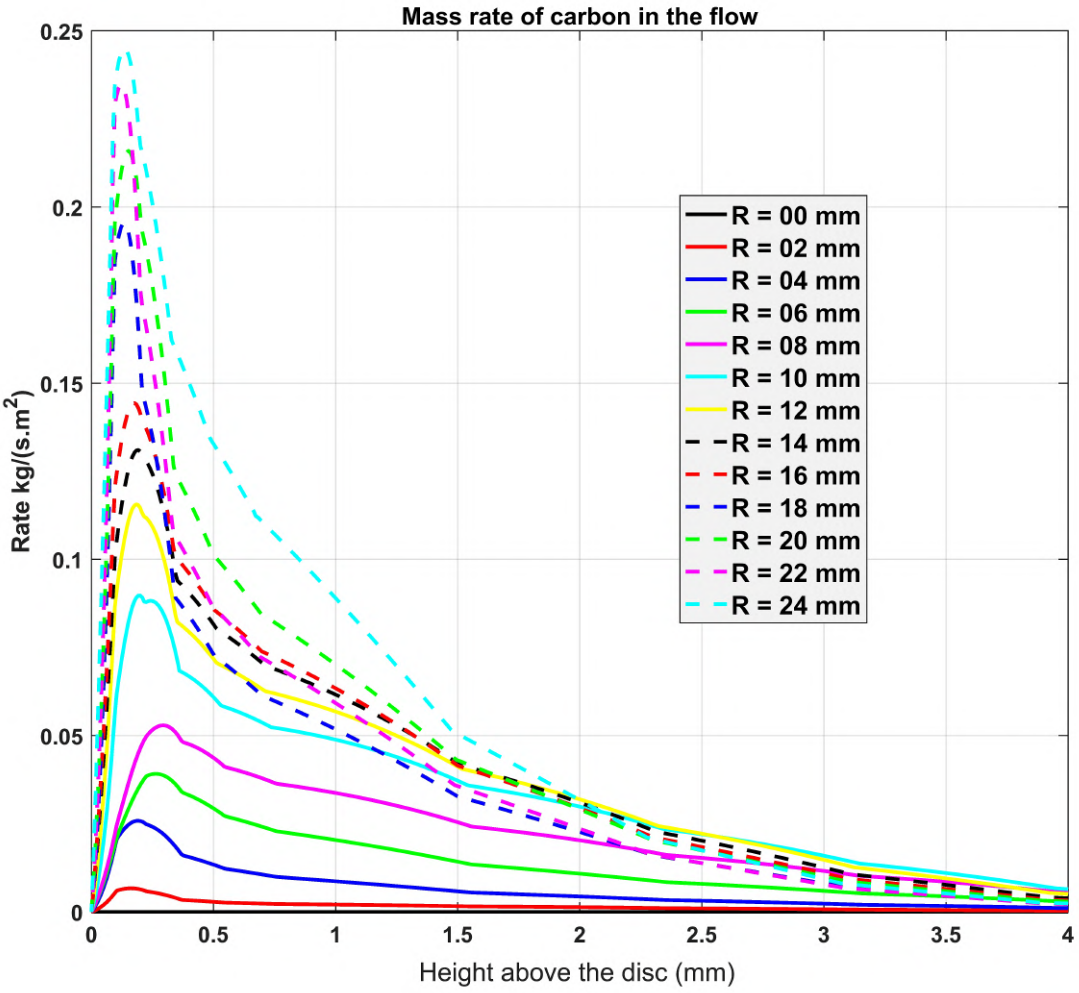


Figure 5.21: Mass flow rate of carbon at various radial positions. The mass flow rate is specified to be the flow through the small incremental areas $\Delta A$, of height $\Delta h$, for each of the 1000 step height increments over the 8 mm height considered (plots are restricted to the 4 mm height representing the region of interest for reaction species).

### 5.4.3 Calculation of Mass Loss

The simulation results for the total mass of carbon flowing in the gas at various locations are shown in Figure 5.22. The plot shows the carbon mass flow rate $\dot{m}_p$ (g/s), where each point is the total for all the flow through the cylindrical partition at each location. The simulated total mass flow rate of carbon for the whole disc is displayed for the edge partition at 24 mm of about 0.023 g/s. Equation 5.3 was used to calculate the

carbon mass flow rate in each of the twelve cylindrical partitions used in Figure 5.22.

$$\dot{m}_p = \sum_{i=1}^{n} (C_i \times A_{cyl} i) \tag{5.3}$$

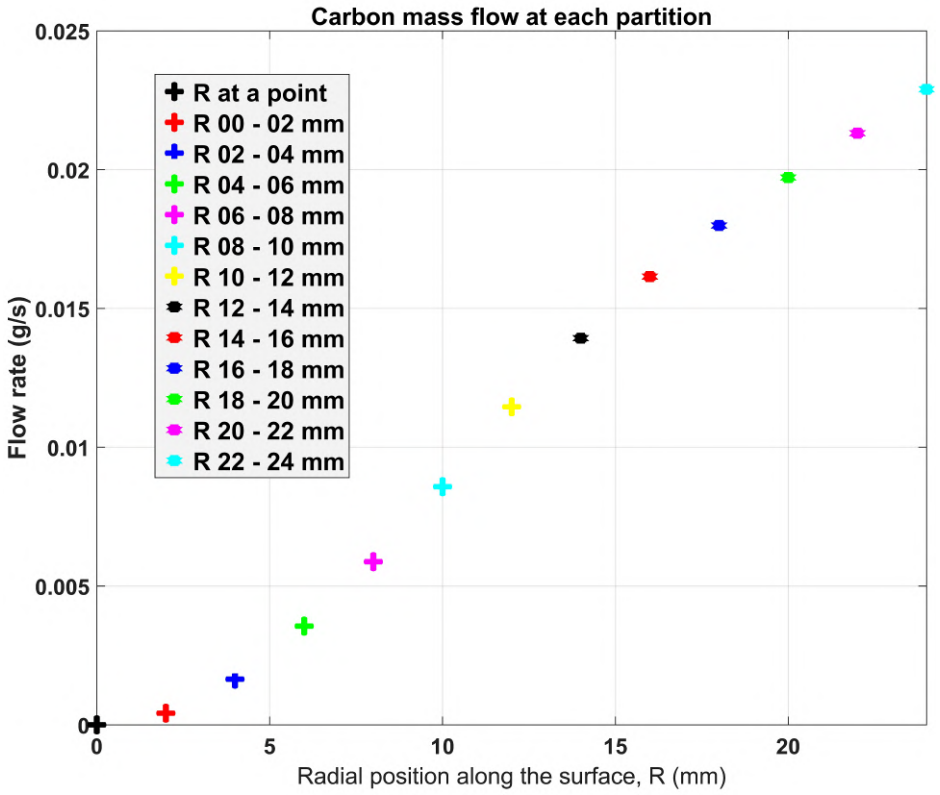


Figure 5.22: Total mass flow rate of carbon at various radial positions.

The mass flow rates in Figure 5.22 are the mass loss rates from the surface upstream of each partition. The mass of carbon passing through each cylindrical partition was calculated by integrating the plots in Figure 5.21, for each of the twelve cylindrical partition. Each mass flow rate is used to determine the mass change that would be required in the disc for these carbon flow rates to exist in the flow at these various positions.

The carbon mass flow rate through each cylindrical partition is equal to the rate of carbon removal from the disc surface as represented by Equation 5.4. The disc surface between each partition has an annular area with the outer and inner radii $R_p$ and $R_{(p-2)}$ respectively. The difference between the mass flow rate at any partition and

the next partition upstream will represent the mass lost from the surface between the two partitions. The mass of carbon lost from the surface per unit area is shown in Figure 5.23.

$$m_p = \frac{\sum_{p=1}^{12}(\dot{m}_p)}{\sum_{p=1}^{12}\pi(R_p^2 - R_{(p-2)}^2)} \tag{5.4}$$

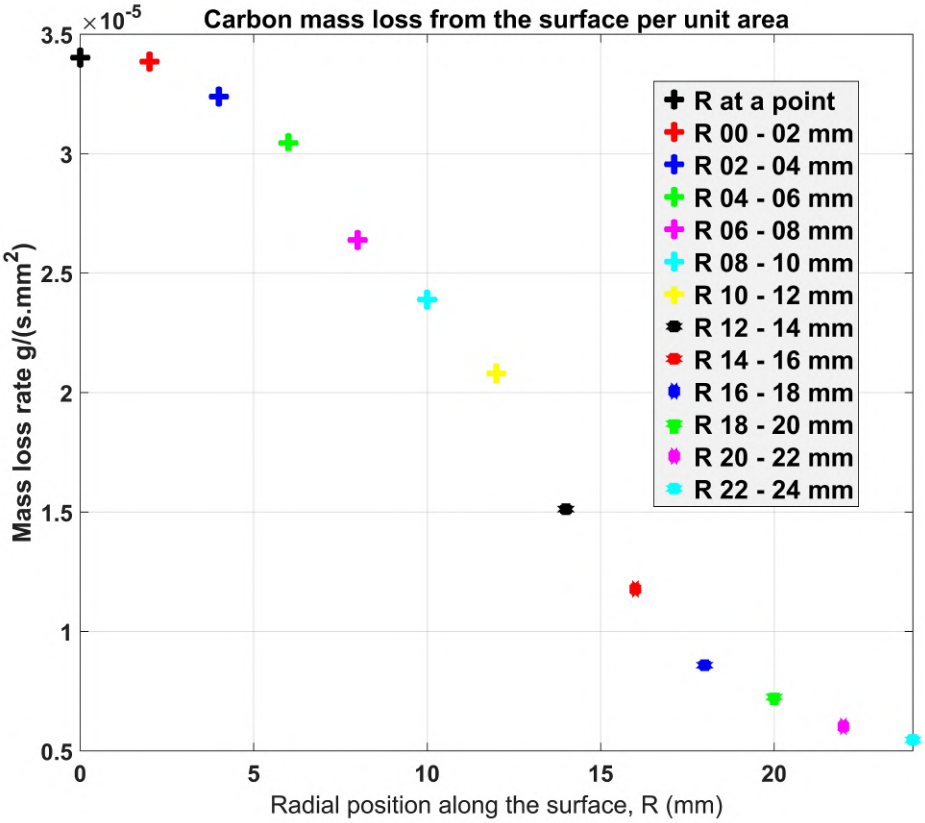


Figure 5.23: Mass loss rate of carbon from the surface at various radial positions.

The thickness loss per unit time $t_p$ (mm/s) can then be estimated using Equation 5.5, where $m_p$ is in g/(s.mm$^2$) and $\rho_p$ is graphite density in g/mm$^3$. Graphite density used in the present work was 0.00176 g/mm$^3$. Dividing the value of $\dot{m}_p$ by $\rho_p$ gives the rate of thickness reduction per second due to ablation as shown in top plot of Figure 5.24. The bottom plot shows the thickness reduction: 0.123 mm at the stagnation point and 0.020 mm at the edges over 8.64 s of the total flow time of the sixteen heated-with-flow

runs of the final experiments.

$$t_p = \frac{\sum_{p=1}^{12} m_p}{\rho_p} \tag{5.5}$$

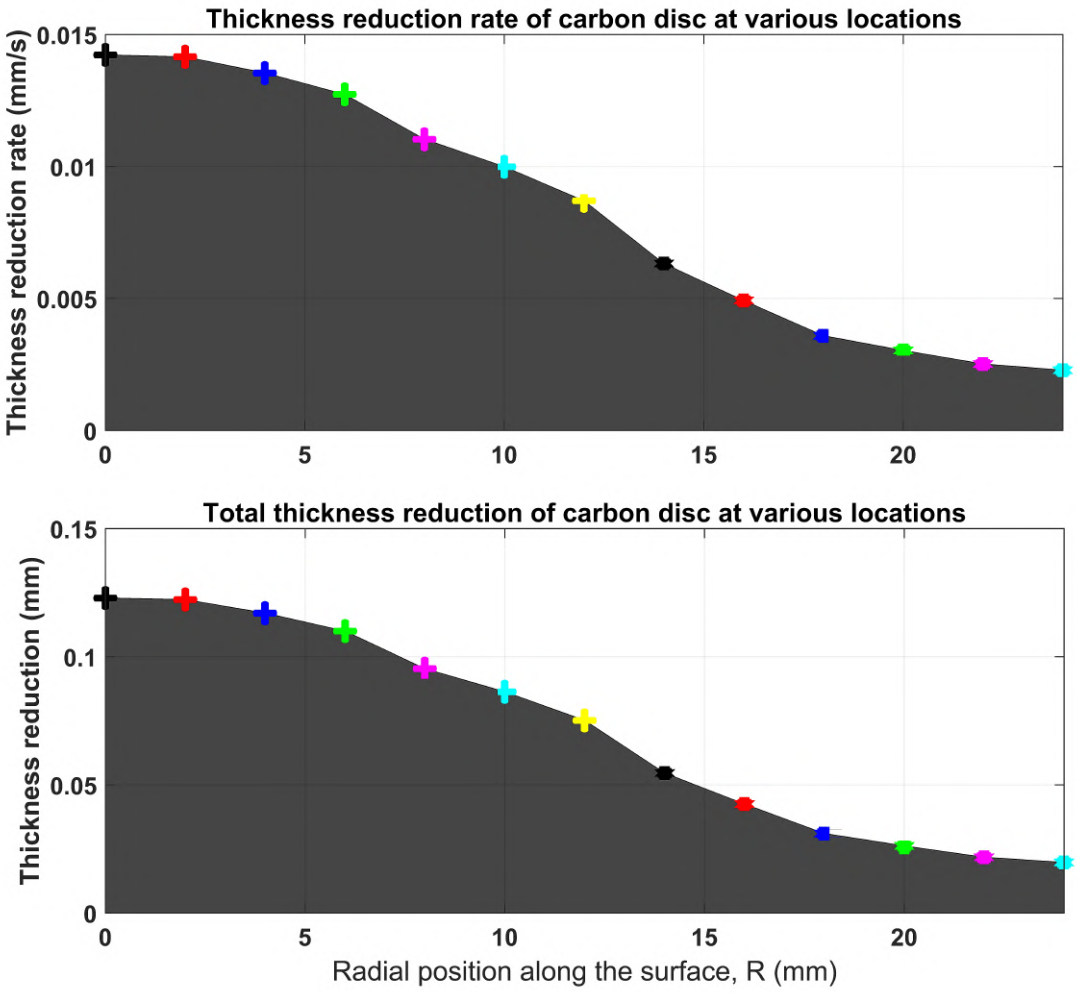


Figure 5.24: Thickness reduction of carbon disc at various radial positions, calculated from the simulated carbon mass flow rate over the same duration as the experiments total flow time, for the heated-with-flow runs (8.64 s).

## 5.5 Conclusions

The simulation results have been used to calculate a mass loss rate of 0.023 g/s during the flow period of the heated-with-flow runs. This calculation was achieved by using

the simulations' mass flow rates and applying ratios of atomic weights to calculate the carbon leaving in the gaseous flow. This carbon mass loss was used to calculate a thickness reduction of 0.123 mm at the stagnation point and 0.020 mm at the edges for the total flow period of 8.64 s for the sixteen heated-with-flow runs of the final experiments. The simulations include the chemistry and the formation of gaseous carbon species in the heated conditions, but do not include the mechanical actions of erosion.

Some confidence in the simulation capability was evident in the simulation's calculated bow shock stand-off distance.

The simulations indicate that essentially all the carbon ablated from the surface leaves in the reaction product CO, with very little resulting from sublimation or reactions resulting in $CO_2$.

The simulations give a good basis for analysis that can now be compared to the carbon mass loss measured in the experiments in Chapter 6.

# Chapter 6

# Analysis of Results

## 6.1 Introduction

This chapter presents the analyses of results, investigating material loss characteristics, and considers the discrepancy between experimental and CFD determination of the ablation rates. The CFD results only included the reaction chemistry during flow over the heated disc and did not consider the mechanical actions, such as erosion and spallations. The experimental material loss included losses while the heating cycle occurred for the heated-only, and heated-with-flow runs. This pre-heating part of the heating cycle was taken into account for the comparison with simulation. Experimentally measured mass loss for the heating cycles were averaged and assumed to apply for the mass loss during the heating phase of the heated-with-flow runs. The potential for mechanical actions to explain the difference between simulation and experimental results is investigated.

## 6.2 Calculation of Mass Loss Based on Volume Loss

Before the experiments, the original density of the disc was calculated by dividing the mass by the original volume. Just after disc preparation for experiments, the original mass was 7.1116 $\pm$ 0.0001 g, thickness was a uniform 2.09 $\pm$ 0.01 mm and a diameter of 50.0 $\pm$ 0.1 mm with a 1 mm chamfer which resulted in a volume of 4046.4 $\pm$ 36 $mm^3$

and a density of $0.00176 \pm 0.000015$ g/mm$^3$. The density from the manufacturer's published properties was 0.00178 g/mm$^3$, about 1.1 % higher than measured/calculated density. Uncertainty in the measurements produced a calculated error in the density of 0.8 %. This suggests that the difference between the manufacturer's published density and the density of the graphite used in the experiments is small and that the manufacturer's published density is probably slightly high. A density of 0.00176 g/mm$^3$ is used throughout this analysis. The heating simulation of Figure 3.9 shows that the disc was placed into compression during heating and may have resulted in the density increase, although the disc was not constrained on the front or back. The heating cycles could produce changes in the disc material micro-structure, which could cause a density change. The material manufacturer's properties describe the disc material as iso-statically pressed graphite. Perhaps some form of sintering occurs during the heating process, which may contribute to a density change. Overall, additional uncertainty exists in the results based on density variation.

The volume was calculated numerically, based on 1000 points of a spline fit through the 12 points of Figure 4.19. $\Delta R$ is $\frac{24}{1000} = 0.024$ mm/increment. The thickness reduction produces a material volume loss in the 18 runs of the final experiments as shown in Figure 6.1. The bottom plot of Figure 6.1 shows the total volume loss (numerical integration of the upper plot) during the experiments to be 159.1 mm$^3$.

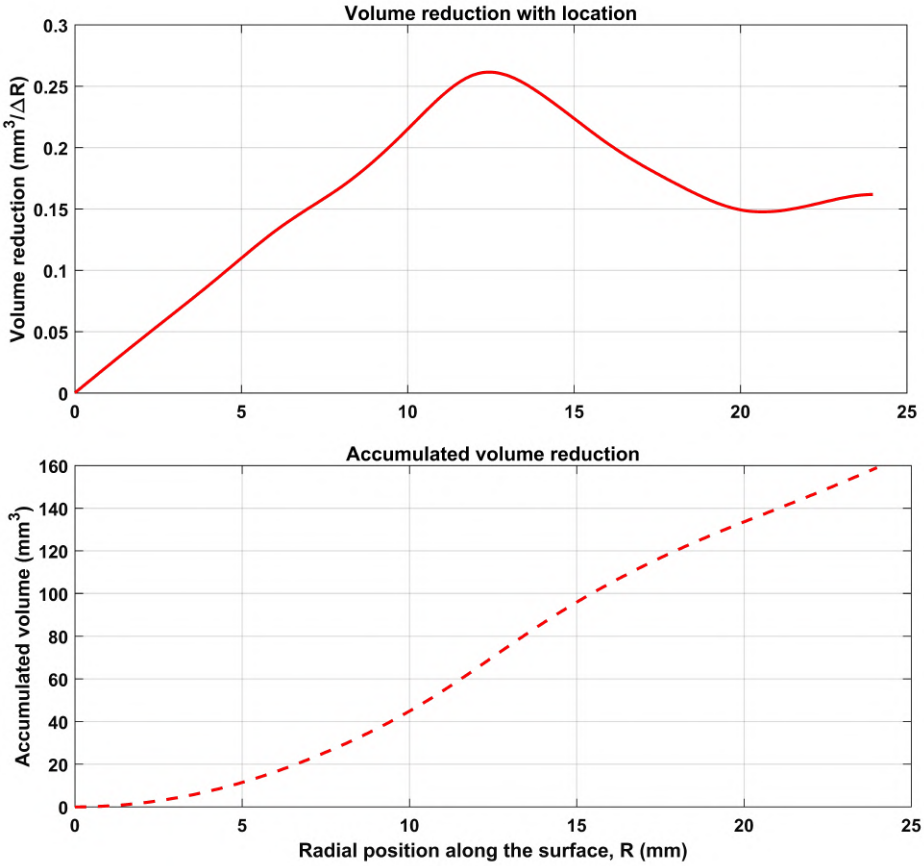


Figure 6.1: The volume loss from experiments, where the upper plot displays the volume loss per $\Delta R$ and the lower plot is a numerical integration of the upper plot giving accumulated volume loss.

On a per second basis and displayed as the mass loss per $\Delta R$, Figure 6.2 shows the data from the lower plot of Figure 6.1 multiplied by density to allow a cross-check total mass lost. This total mass loss is displayed as the cumulative sum. The total mass loss during the 18 runs experiments is numerically determined to be 0.280 g, whereas the measured mass loss was 0.3176 g. The major contributor to this 12 % error is probably the result of the assumption to use an axisymmetric profile for the final disc shape, based on the average radius profile from the measuring arm data of Section 4.4. Density variation may also have an influence.

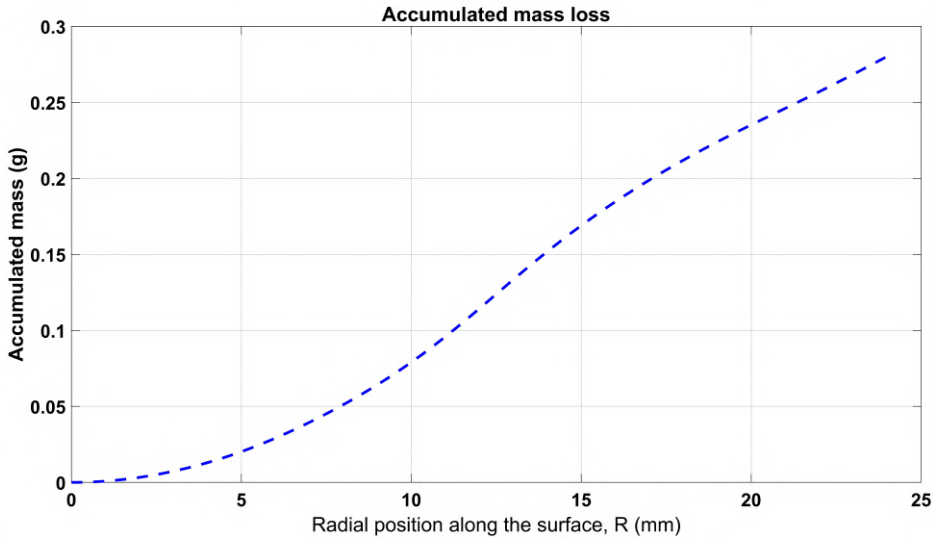


Figure 6.2: Accumulated mass loss from experiments. The total mass loss is the value displayed for the outside radius of 24 mm.

## 6.3 Comparison of Simulations to Experiments

### 6.3.1 Comparison of Methods

The top image of Figure 6.3 shows the mass fraction of CO species at the edge of the disc, from simulations at three different maximum surface temperatures reflecting the temperature change that occurred during the flow of heated-with-flow runs as described in Section 3.5.4. The simulations were steady state at fixed surface temperatures (spatially varying). The temperature change experienced by the disc during the flow had a notable effect on the simulated mass loss rate. The plots in Figure 6.3 suggest there is varying CO concentration and potentially significant sensitivity to temperature in the simulation. At the start of flow in a typical heated-with-flow run, the maximum surface temperature was about 2528 K, producing 0.079 mass fraction of CO species in the flow at the edge of the disc. At midway through the flow, the maximum temperature dropped to about 2518 K producing 0.077 mass fraction of CO. At the end of run, the maximum temperature was about 2508 K producing 0.073 mass fraction of CO. The mass loss rate of carbon from the surface, calculated from the simulation were 0.023 g/s, 0.020 g/s, and 0.018 g/s at 2528 K, 2518 K, and 2508 K maximum surface

temperature respectively, as shown in the bottom image of Figure 6.3.

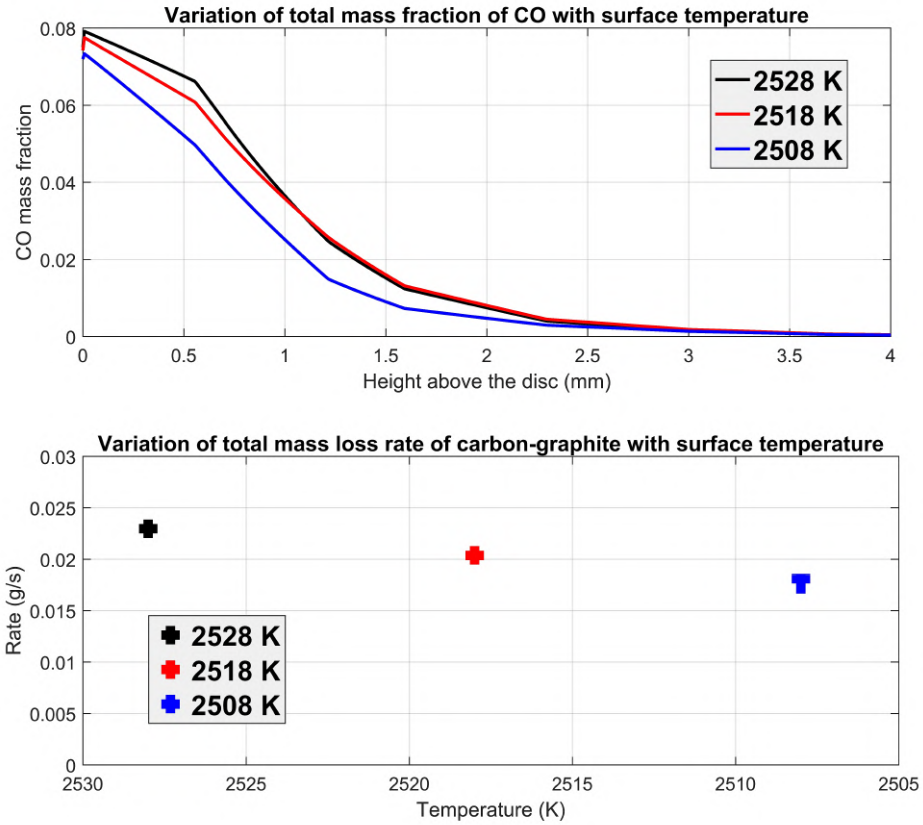


Figure 6.3: Simulation results for the variations of mass fraction CO species at the edge of the disc and total mass loss rate of graphite from the disc surface for conditions experienced in the heated-with-flow runs.

The simulation data reported in Figure 6.3 is based on the numerical application of the data from the three simulations using the three different maximum temperatures of 2528 K, 2518 K, and 2508 K. Numerical calculation applied to the results from the simulation for the relative proportion of the flow time at which they applied, resulted in a total mass flow rate of carbon of 0.020 g/s.

### 6.3.2 Comparison of Simulated to Measured Volume Loss

The experiments only measured the thickness of the disc accurately at the end of the 18 runs of the final experiments. To determine the material thickness loss during the flow of the heated-with-flow runs, there needs to be an assessment of the thickness loss

during the heated phase of the heated-with-flow runs. This thickness loss in the heating phase was not possible to measure during a heated-with-flow run in the experimental arrangement used. Experimental data on mass loss from heated-only runs, including the heated-only run in the final experiments and runs at the same settings prior to the final experiments, indicates that thickness loss was reasonably constant at about 0.0082 g per run. The actions of the plasma on the back of the disc evidently removed some material as seen in Figure 4.13. Oxidation on the front of the disc is expected to be responsible for most of the material lost. Since the outer 5 mm of the back of the disc was in contact with the connector (see Figure 3.4), any action of the plasma was masked in this region. No step in thickness is evident at this position of the disc. This suggests that the plasma was not responsible for significant material loss, or at least not near the connector. A speculative profile of material loss required to produce the mass loss measured for the heated-only runs is displayed in Figure 6.4. For the 17 runs with heating in the final experiments, this produces a total thickness loss of 0.07 mm at the centre of the disc and 0.03 mm at the edge. Because total mass loss is more significant for thickness loss at the edges of the disc, little variation in the thickness loss applied at the edges was possible to maintain the known measured total mass loss. Variation in the profile is certainly a viable option, but the assumption that mass loss was a function of temperature led to the selected profile for thickness loss for the heating only runs.

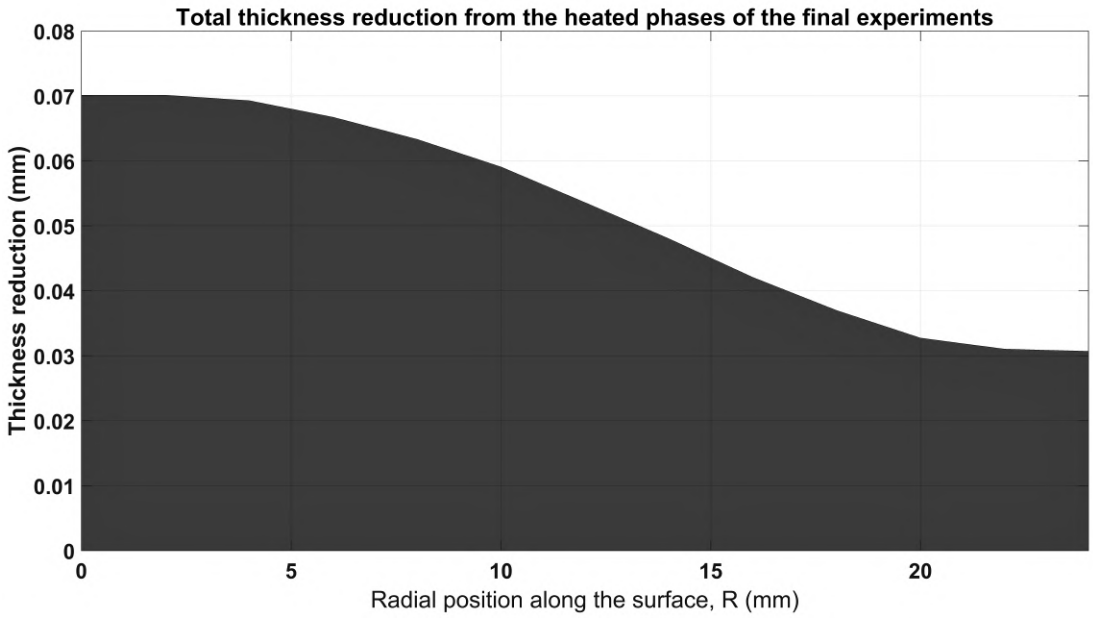


Figure 6.4: Thickness loss profile applied that produces the measured mass loss for heated-only runs.

The experiments produced a mass loss rate of 0.020 g/s during the flow period of the heated-with-flow runs. Including losses from the heating cycles during the 18 runs of the final experiments (17 with heating), a total thickness reduction of approximately 0.147 mm at the stagnation point and 0.045 mm at the edges was measured in the experiments as shown in Figure 6.5. The material volume loss was calculated using an assumption that the material loss was axisymmetric based on the radial profile of Figure 6.4. The mass loss attributed to the flow phase of the heated-with-flow runs is displayed as the grey zone in Figure 6.5 (the total material loss from the experiments minus the heating phase losses of Figure 6.4). The figure also shows the calculated thickness loss from the simulations of 0.123 mm at the stagnation point and 0.020 mm at the edges (see Section 5.4.3).

The results displayed in Figure 6.5 suggests that ablation producing thickness loss during the flow phase of heated-with-flow runs is relatively constant up to about 10 mm from the stagnation point, then shows a small spike then reduces towards the edge of the disc. The simulation does not predict material loss well. The red zone in Figure 6.5 shows the difference between the simulation and experiments for flow over a heated surface. Considering that the experimental losses include the mechanical actions

of ablation and the simulations do not, the results probably under-estimate the total difference between the simulations and experiments. The overall results also suggest that mechanical actions are possibly not a significant contributor to material loss in ablation processes under the conditions of the experiments, if any confidence is to be attributed to the simulation results.

## 6.4 Surface Sensitivity to Temperature

The material loss shown in Figure 6.5 suggest that the simulations are more sensitive to surface temperature than the experiment results indicate. Figure 6.5, showing a portion of the data in Figure 3.27, shows that the temperature conditions experience in the experiments are closely matched by the simulation. Because the simulation calculates a significantly higher rate of material loss at the higher temperatures of the surface than the experiment indicates, the mechanisms employed in the simulation which rely on temperature are probably not accurate.

Figure 5.17 shows that the flow speeds increase significantly over the radius of the disc (based on simulation). High speed flows along the surface reduce the residence time of species within the reaction layers. Surface sensitivity to flow conditions can be attributed to diffusion and convection transport effects, and local temperatures of the surface and within the flow. The effects of the various inputs into reaction rates is complex. Surface reactions and subsequent species concentrations in the boundary layer interact and no particular aspect of the conditions can be readily identified that cause the difference between the experiments and the simulation results.

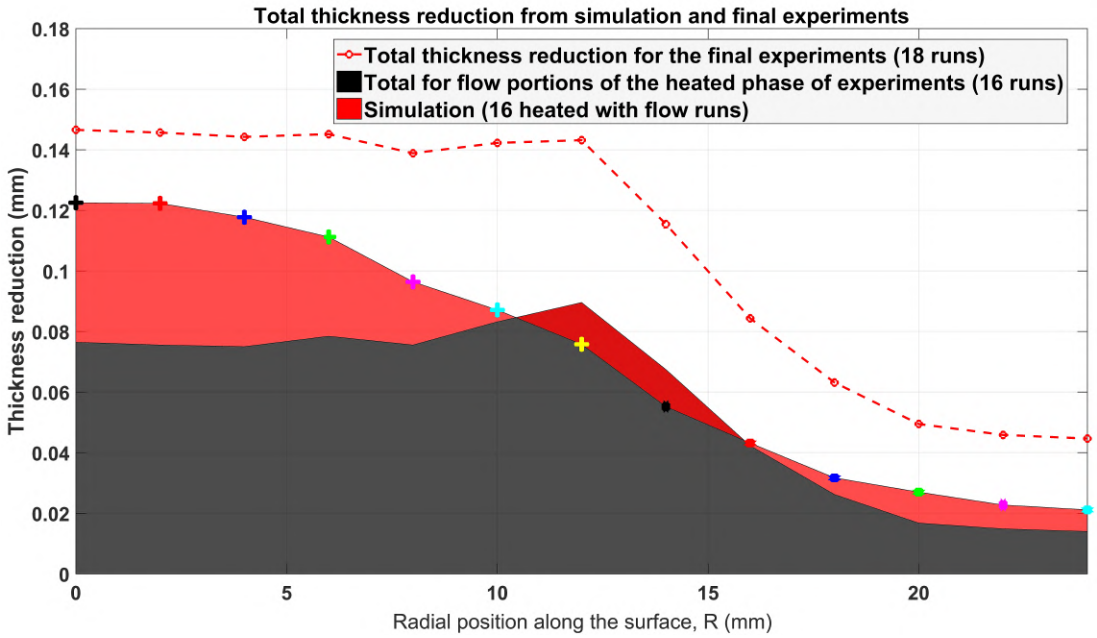


Figure 6.5: The thickness reduction calculated from the experimental data and the simulation results. Only a small region results where the experimental material loss during the flow phase of heated-with-flow runs exceeds the simulation results.

## 6.5 Material Failure

The disc developed a crack from the first heated run in the final experiments. This also occurred in other discs used in other experiments prior to the final 18 runs, but did not always occur. It is not clear why some discs cracked and others did not. If it was the result of material property differences across the disc, then these property differences could effect the material loss from the surfaces in the experiments. Figure 6.6 shows the crack magnified in an SEM image at the end of the final experiments. This crack had an average width of 100 $\mu$m across the disc (front surface). There does not appear to be any substantial local changes to the surface in close proximity to the crack; although the filed of view is small.

In general the carbon discs survived the very high temperatures, the relatively fast temperature changes and the aerodynamic loads of the experiments well.

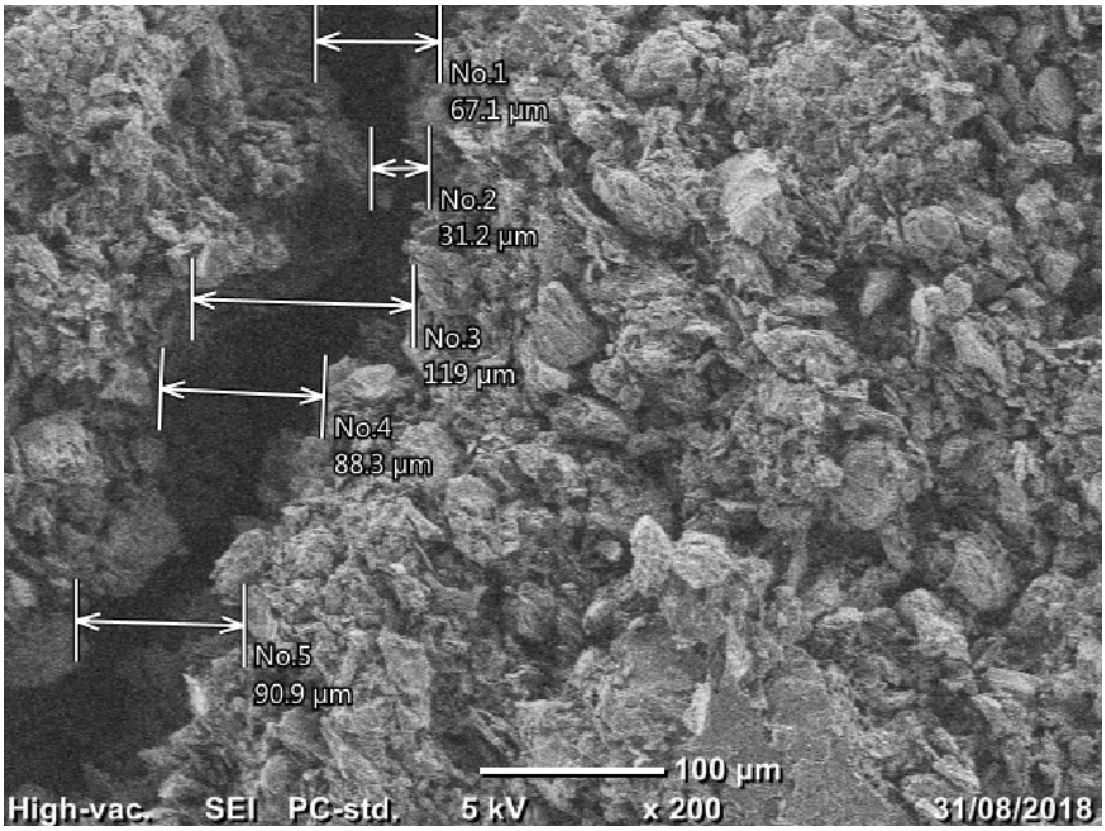


Figure 6.6: Image of the crack that formed on the upstream side of the disc near the stagnation point after 16 heated-with-flow runs. It is likely the crack resulted from expansion of the disc during heating while being constrained in the holder, in combination with the forces resulting from the plasma heating.

## 6.6 Conclusions

Of the three methods used to assess mass loss, the weighing method is significantly more reliable. The volume-based method aids identification of where mass is lost. The comparison of mass loss rate measurements between simulation and experiments reveals that significant uncertainty exists in the outcomes. The assessment undertaken suggests that the simulation did not provide any real indications that the calculation used reflect the conditions of the experiments. The assertions about the mass loss due the action of the plasma on the back of the disc are supported by the fact that the accurately weighed mass loss could not have occurred in significantly different ways, since there was little margin to remove material in other ways and maintain the known

mass loss and oblige the expectation that mass loss was a function of temperature. This edge thickness was also relatively accurately measured.

The analysis demonstrates the value of the general techniques applied in the experiments, but also lead to identifying various aspect of the techniques employed that could be improved. These are discussed in Chapter 7.

# Chapter 7

# Conclusions and Future Work

## 7.1 Introduction

Presented in this chapter is the summary of the research reported in this thesis leading to suggestions for future work. Temperatures in excess of 2500 K have been achieved on a pre-heated graphite surface used for the assessment of mass loss through ablation in a Mach 4.5 flow. The heating process involved using an argon plasma powered by a 400 A DC supply for about 15 seconds to pre-heat the disc before it was exposed to the flow. Recent experiments based on Orion re-entry conditions used a surface temperature of about 2800 K (Glass, 2008) and Apollo 4 lunar return speed of 11 km/s reportedly experienced a surface temperature of about 2400 K (Dec and Braun, 2006), while typical re-entry surface temperatures for Space Shuttles was about 1740 K (Glass, 2008). The use of a plasma as the means of heating the disc was proven to be effective for reaching temperatures of these magnitudes and the process has potential to be more widely used for similar experiments.

## 7.2 Experimental Outcomes

The mass loss data from the experiments of the present work is a notable contribution to knowledge. The measured mass loss indicated a reasonably consistent mass loss rate

of 0.020 g/s during flow under the experimental conditions. The material removed from the surface through ablation was generally axisymmetric about the stagnation point and showed different rates of material removal in the radial direction.

The experiments used the test section of the TUSQ facility, with a Mach 4.5 nozzle operated in the atmospheric blow-down configuration. This arrangement allowed for test durations in excess of 0.5 seconds. The work is based around experiments for a cold flow over a pre-heated disc. The simplest analysis would have been achieved with a uniform temperature across the graphite disc surface but this was not achieved in the experiments. The centre of the disc up to half the disc diameter did achieve a reasonably constant temperature of within 250 K of the maximum temperature at the disc centre. Many attempts to improve the uniformity of temperature were made by combining different currents, different electrode gaps, different lengths of electrode protrusion from the primary shroud, and different argon flow rates. The temperature profile from the best set of combinations which gave the least variation in temperature across the disc has been presented.

After supplying the plasma for about 16 seconds during a single experiment, the electrode's crystal structure was altered significantly, so that the plasma could not be reliably started for the next experiment. Polishing or re-machining the tip did not overcome this issue. Each run required a new electrode with an appropriately shaped tip. Used electrodes were employed on some runs, but required 20 mm to be cut off from the tip end, with the appropriately shaped tip machined. These used electrodes were successful at starting and maintaining a plasma for about 80 % of attempts. New electrodes always started the plasma on first attempt.

The temperature achieved on the surface of the disc in the experiments were not limited by the power available from the DC power supply, but were limited by the physical capability of the materials used. The electrode and the gas shroud both failed at temperatures that produced a maximum surface temperature less than 100 K above the maximum surface temperature used in the experiments. Material failure evidently occurred as a function of temperature, because higher currents were tolerated until the resulting surface temperature of the disc reached about 2600 K.

## 7.3 Surface Characteristics

The SEM data for the surfaces were analysed and the degree of surface roughness increased with increasing number of runs, suggesting material removal process was not time invariant on a microscopic scale.

The data obtained from the measuring arm was used to determine the shape of the surface after the experiments. This shape was used to determine the material volume loss, which allowed for a check of mass loss calculated using the graphite's density. The measuring arm determined the shape of the surface and was supported by the laser sheet visualisation technique.

## 7.4 Mass Loss Rates from CFD Simulations

The simulation indicated there was varying concentrations of the reaction species in the boundary layer close to the surface. These carbonaceous species had their maximum concentrations at about 0.2 mm from the surface. CO was essentially the only carbon-containing species leaving in the flow.

A technique was developed which allowed for calculation of the simulated carbon loss rate from various positions along the radius of the disc. This produced a thickness change, which enabled a comparison with the experiments' results.

Direct measurement of carbon losses during the heating phase of all the experiments was not possible in the experimental arrangement used. An estimate of the material lost in the heating phase allowed for an estimate of the material lost during the flow phase of heated-with-flow runs, and therefore a comparison with the simulation results.

The simulations did not consider the mechanical actions of ablation. Any discrepancies between the experimental results and the simulations could be accounted for by this mechanical action, but in general, the simulation replicated the experiments reasonably well, achieving a result that was within 50% of the measurements at the stagnation point, and with better agreement elsewhere on the disc. Overall material loss rates

from the experiments and the simulations were similar, but localised material loss rates prediction from simulations were most accurate at the edges and least accurate at the stagnation point.

## 7.5 Future Work

### 7.5.1 Modification to Experiments to Overcome Deficiencies

The experiments' processes produce reasonable results for total material removed, shape and surface texture. The lack of precision of the determination of the amount and shape of material lost during the heating, impeded the reliability of comparison with the simulations. A program of heated-only runs with the associated mass changes and shape changes would improve the reliability of the comparison with simulation and consequently improve the determination of the material lost for ablation.

The experiments were conducted with a surface temperature which generated a boundary layer temperature near the threshold for the dissociation of molecular oxygen. Higher temperatures would have increased the concentrations of atomic oxygen and likely increased the rate of formation of CO. This may have allowed for detection of CO by direct techniques such as spectrometry. Higher rates of formation of reaction species would also potentially improve the accuracy of measurement of material loss. Work to improve the set-up for generating the plasma which allowed for the components to tolerate higher temperatures would improve the capability of future experimental programs.

### 7.5.2 Possible Future Experiments with Changes to Experiment Set-up

The TUSQ hypersonic wind tunnel is in the process of being reconfigured to provide up to Mach 7 flow. More experiments at different flow speeds will be possible, but over a shorter run-time, generally less than 200 ms. A program of experiments to compare material loss rates at different flow speeds could be useful for developing insights into

the influence of flow speeds on material loss rates. The performance of simulations may also be improved based on experimental data at different flow speeds.

The USQ facility is capable of producing flows containing gases other than Earth's atmospheric gas mixture. Varying the oxygen concentration could allow improvements in validation of simulations. Experimental data could be obtained from tests using gas concentrations from known atmospheres through which extra-terrestrial flights are planned.

The current experiments used a flat disc in a configuration similar to the standard European probe. Experiments are possible with a heated surface of varying shape and varying orientation to the flow, including on a heated surface arranged to have laminar or turbulent flow well downstream of a stagnation point.

The current technique for generating the plasma allows for arrangements that would produce a lower disc temperature. Development of more durable components used in generating the plasma would allow for higher temperatures. These aspects would allow for studies over a range of temperatures, which would extend the experimental capability and potentially aid simulation validation.

## 7.6 Conclusions

The present work could not replicate the temperatures of heat shields used for re-entry vehicles like Orion, Apollo and Stardust. This was because the TUSQ hypersonic wind tunnel facility could not replicate high enthalpy re-entry flows. However, the present work has created a model of a representative heat shield and given information about how well a simulation can predict the material losses. Experiments could be further developed to potentially replicate heat shield conditions of re-entry missions. The oxidation rate in the present work could be extended to other carbon-based materials like Avcoat, Phenolic Impregnated Carbon Ablator (PICA) and Silicon Impregnated Reusable Ceramic Ablator (SIRCA) for deeper planetary missions.

The main objective of this work was to explore options for techniques to conduct exper-

iments to support research into ablation rates. The experiments conducted, quantified the oxidation species and surface mass-loss rates in a hypersonic boundary layer near the stagnation point. The experimental procedures developed, in particular, the plasma heating technique, have proven effective. Contributions to knowledge about ablation of carbon surfaces was achieved with the approach of using a heated surface in a cold hypersonic flow. Experimental data was compared to CFD simulation results. This will potentially lead to improved simulation capability, once validation is achieved across a wider range of conditions. The present work encourages future work to identify the aspects of CFD simulations which cause the differences between CFD and results measured in experiments such as those conducted in the present work.

# References


Acosta, R. I., Gross, K. C. and Perram, G. P. (2016), 'Combustion kinetics of laser irradiated porous graphite from imaging Fourier transform spectroscopy', *Combustion and Flame* **163**, 90–99.

Alba, C. R., Greendyke, R. B., Lewis, S. W., Morgan, R. G. and McIntyre, T. J. (2015), 'Numerical modelling of earth re-entry flow with surface ablation', *Journal of Spacecraft and Rockets* **53**(1), 84–97.

Allouis, C., Esposito, A., Salatino, P., Savino, R. and Senneca, O. (2014), 'Set up of an experimental protocol for the investigation of graphite combustion in supersonic flow', *Experimental Thermal and Fluid Science* **56**, 9–15.

Berkowitz, J. B. (1966), Research to determine the effects of surface catalyticity on materials behaviour in dissociated gas streams, Technical report, Inc Cambridge.

Bhutta, B. A. and Lewis, C. H. (1993), 'Low-to-high altitude predictions of three-dimensional ablative re-entry flow fields', *Journal of Spacecraft and Rockets* **30**(4), 395–403.

Bianchi, D., Nasuti, F., Paciorri, R. and Onofri, M. (2013), Computational analysis of hypersonic flows including finite rate ablation thermochemistry, *in* 'Proceedings of the 7th European Workshop on Thermal Protection Systems and Hot Structures', ESA–ESTEC, Noordwijk, Netherlands.

Blottner, F. (1971), 'Prediction of electron density in the boundary layer on entry vehicles with ablation', *NASA Special Publication* **252**, 219–232.

Brotherton, T. and Lynn, J. (1959), 'The synthesis and chemistry of cyanogen', *Chemical Reviews* **59**(5), 841–883.

Chazot, O. (2006), Experimental studies on hypersonic stagnation point chemical environment, Technical report, Von Karman Institute for fluid dynamics, Rhode-Saint-Genese (Belgium), RTO-EN-AVT-142, pp. 1–33.

Chelliah, H., Makino, A., Kato, I., Araki, N. and Law, C. (1996), 'Modelling of graphite oxidation in a stagnation-point flow field using detailed homogeneous and semi-global heterogeneous mechanisms with comparisons to experiments', *Combustion and Flame* **104**(4), 469–480.

Colket III, M. (1984), 'Cyanogen pyrolysis, the CN and NO reaction behind incident shock waves', *International Journal of Chemical Kinetics* **16**(4), 353–369.

Combs, C., Clemens, N. T. and Danehy, P. M. (2014), Development of naphthalene PLIF for visualising ablation products from a space capsule heat shield, *in* '52nd Aerospace Sciences Meeting', pp. 1152–1164.

Dec, J. and Braun, R. (2006), An approximate ablative thermal protection system sizing tool for entry system design, *in* '44th AIAA Aerospace Sciences Meeting and Exhibit', pp. 780–794.

Denbigh, K.G. (1981), *The principles of chemical equilibrium: with applications in chemistry and chemical engineering*, Cambridge University Press, fourth edition, pp. 333–459.

Ding, J.K., Wang, D.P., Ying, W. and Hui, D. (2014), 'Effect of post weld heat treatment on properties of variable polarity TIG welded AA2219 aluminium alloy joints', *Transactions of Non-ferrous Metals Society of China* **24**(5), 1307–1316.

Dolton, T., Goldstein, H. and Maurer, R. (1968), Thermodynamic performance of carbon in hyperthermal environments, *in* '3rd Thermophysics Conference', pp. 754–766.

Dribinski, V., Ossadtchi, A., Mandelshtam, V. A. and Reisler, H. (2002), 'Reconstruction of Abel-transformable images: The Gaussian basis-set expansion Abel transform method', *Review of Scientific Instruments* **73**(7), 2634–2642.

Erdos, J., Bakos, R., Castrogiovanni, A. and Rogers (1997), Dual mode shock-expansion/reflected-shock tunnel, *in* '35th Aerospace Sciences Meeting and Exhibit', pp. 560–573.

Eswein, N., Herdrich, G., Fasoulas, S. and Röser, H.P. (2011), Investigation of graphite ablation at IRS, *in* '42nd AIAA Thermophysics Conference', pp. 3615–3633.

Farbar, E., Boyd, I. and Martin, A. (2012), Modelling ablation of charring heat shield materials for non-continuum hypersonic flow, *in* '50th AIAA Aerospace Sciences Meeting Including the New Horizons Forum and Aerospace Exposition', pp. 532–547.

Fueno, T., Tabayashi, K. and Kajimoto, O. (1973), 'Bimolecular dissociation of cyanogen behind incident shock waves', *The Journal of Physical Chemistry* **77**(5), 575–581.

Gadelmawla, E., Koura, M., Maksoud, T., Elewa, I. and Soliman, H. (2002), 'Roughness parameters', *Journal of Materials Processing Technology* **123**(1), 133–145.

Gilbert, L. and Scala, S. (1965), 'Sublimation of graphite at hypersonic speeds', *AIAA Journal* **3**(9), 1635–1644.

Glass, D. (2008), Ceramic matrix composite (CMC) thermal protection systems (TPS) and hot structures for hypersonic vehicles, *in* '15th AIAA International Space Planes and Hypersonic Systems and Technologies Conference', pp. 2682–2718.

González-Madruga, D., Cuesta, E., Barreiro, J. and Fernandez-Abia, A. (2013), 'Application of a force sensor to improve the reliability of measurement with articulated arm coordinate measuring machines', *Sensors* **13**(8), 10430–10448.

Gosse, R., Gogineni, S. and Roy, S. (2012), Graphite ablation experiments in the IH-MEL laser facility, *in* '43rd AIAA Thermophysics Conference', PP. 2745–2764.

Guide, A. F. U. (2011), 'Release 14.0, Ansys', *Inc., USA, November*.

Haidar, J. (1998), 'A theoretical model for gas metal arc welding and gas tungsten arc welding', *Journal of Applied Physics* **84**(7), 3518–3529.

Hayhurst, A. and Parmar, M. (1998), 'Does solid carbon burn in oxygen to give the gaseous intermediate CO or produce $CO_2$ directly? Some experiments in a hot bed of sand fluidised by air', *Chemical Engineering Science* **53**(3), 427–438.

Helber, B., Alessandro, T., Chazot, O. and Thierry, M. (2015), Physico-chemistry of CN in the boundary layer of graphite in nitrogen plasmas, *in* '45th AIAA Thermophysics Conference', pp. 2668–2685.

Helber, B., Asma, C. O., Babou, Y., Hubin, A., Chazot, O. and Magin, T. E. (2014), 'Material response characterisation of a low-density carbon composite ablators in high-enthalpy plasma flows', *Journal of Materials Science* **49**(13), 4530–4543.

Herdrich, G., Dropmann, M., Marynowski, T., Löhle, S. and Fasoulas, S. (2010), Atmospheric entry simulation capabilities of the IRS plasma wind tunnel PWK3 for Mars and Venus, *in* '7th International Planetary Probe Workshop', pp. 1–8.

Johnson, R. F. and Chelliah, H. (2013), Laminar reactive boundary layer simulation of an ablating heated carbon surface, *in* '51st AIAA Aerospace Sciences Meeting including the New Horizons Forum and Aerospace Exposition', pp. 184–195.

Keenan, J. and Candler, G. (1993), Simulation of ablation in earth atmospheric entry, *in* '28th Thermophysics Conference', pp. 2789–2803.

Lachaud, J., Aspa, Y. and Vignoles, G. L. (2008), 'Analytical modelling of the steady state ablation of a 3D C/C composite', *International Journal of Heat and Mass Transfer* **51**(9), 2614–2627.

Lachaud, J., Cozmuta, I. and Mansour, N. N. (2010), 'Multi-scale approach to ablation modelling of phenolic impregnated carbon ablators', *Journal of Spacecraft and Rockets* **47**(6), 910–921.

Lewis, S. W. (2017), 'Hypervelocity shock-layer emission spectroscopy with high temperature ablating models', *PhD thesis*, University of Queensland.

Luo, L., Wang, Y., Liu, L., Duan, L., Wang, G. and Lu, Y. (2016), 'Ablation behaviour of C/SiC composites in plasma wind tunnel', *Carbon Volume 103,* **103**, 73–83.

Luo, X. and Jean-Charles, R. (2003), 'Research of oxidation properties of graphite

used in HTR-10', Institute of Nuclear and New Energy Technology, Tsinghua University, Beijing 100084 China, pp. 20–45.

Marschall, J. and Fletcher, D. G. (2010), 'High-enthalpy test environments, flow modelling and in-situ diagnostics for characterising ultra-high temperature ceramics', *Journal of the European Ceramic Society* **30**(11), 2323–2336.

Martin, A. and Boyd, I. D. (2015), 'Modelling of heat transfer attenuation by ablative gases during the stardust re-entry', *Journal of Thermophysics and Heat Transfer* **29**(3), 450–466.

Massuti-Ballester, B., Pidan, S., Herdrich, G. and Fertig, M. (2015), 'Recent catalysis measurements at IRS', *Advances in Space Research* **56**(4), 742–765.

Miller, C. G. (1978), 'Operational experience in the Langley expansion tube with various test gases', *AIAA Journal* **16**(3), 195–196.

Miller, I. M. and Sutton, K. (1966), 'An experimental study of the oxidation of graphite in high-temperature supersonic and hypersonic environments', pp. 1–45.

Mirels, H. (1964), 'Shock tube test time limitation due to turbulent wall boundary layer', *AIAA Journal* **2**(1), 84–93.

Monteverde, F., Savino, R., Fumo, M. D. S. and Di Maso, A. (2010), 'Plasma wind tunnel testing of ultra-high temperature $ZrB_2$–SiC composites under hypersonic re-entry conditions', *Journal of the European Ceramic Society* **30**(11), 2313–2321.

Mortensen, C. and Zhong, X. (2012), High-order shock-fitting method for hypersonic flow with graphite ablation and boundary layer stability, *in* '42nd AIAA Fluid Dynamics Conference and Exhibit', pp. 3150–3176.

Natarajan, K., Thielen, K., Hermanns, H. and Roth, P. (1986), 'Thermal decomposition of cyanogen measured in $C_2N_2/O_2$ and $C_2N_2/H_2$ reaction systems by atomic resonance absorption', *Berichte der Bunsengesellschaft für physikalische Chemie* **90**(6), 533–539.

Pagan, A. S., Zuber, C., Massuti-Ballester, B., Herdrich, G., Hald, H. and Fasoulas, S. (2017), The ablation performance and dynamics of the heat shield material

zuram®, *in* '31st International Symposium on Space Technology and Science' pp. 1–10.

Panerai, F., Mansour, N. N., Lachaud, J. and Martin, A. (2014), 'Experimental and numerical study of carbon fibre oxidation', pp. 1–15.

Park, C. (1976), 'Effects of atomic oxygen on graphite ablation', *AIAA Journal* **14**(11), 1640–1642.

Park, C. (1985), On convergence of computation of chemically reacting flows, *in* '23rd Aerospace Sciences Meeting', pp. 247–265.

Park, C. and Ahn, H.-K. (1999), 'Stagnation-point heat transfer rates for pioneer-Venus probes', *Journal of Thermophysics and Heat Transfer* **13**(1), 33–41.

Park, C., Howe, J., Jaffe, R. and Candler, G. (1991), Chemical-kinetic problems of future NASA missions, *in* '29th Aerospace Sciences Meeting', pp. 464–497.

Park, C., Howe, J. T., Jaffe, R. L. and Candler, G. V. (1994), 'Review of chemical-kinetic problems of future NASA missions. II-Mars entries', *Journal of Thermophysics and Heat Transfer* **8**(1), 9–23.

Porter, L. (2007), NASA new aeronautics research program, *in* 'Presentation at the 45th AIAA Aerospace Science Meeting & Exhibit', pp. 1–49.

Potter, D. F. (2011), 'Modelling of radiating shock layers for atmospheric entry at Earth and Mars', *PhD thesis*, University of Queensland.

Savino, R., Fumo, M. D. S., Paterna, D., Di Maso, A. and Monteverde, F. (2010), 'Arc-jet testing of ultra-high-temperature-ceramics', *Aerospace Science and Technology* **14**(3), 178–187.

Scala, S. M. (1962), *The Ablation of Graphite in Dissociated Air: Theory*, Missile and Space Division, General Electric, pp. 1–94.

Shaddix, C. R., Holzleithner, F., Geier, M. and Haynes, B. S. (2013), 'Numerical assessment of Tognotti determination of $CO_2/CO$ production ratio during char oxidation', *Combustion and Flame* **160**(9), 1827–1834.

Smith, J. R., Breakspear, S. and Campbell, S. A. (2003), 'AFM in surface finishing: Part II. surface roughness', *Transactions of the IMF* **81**(3), B55–B58.

Suzuki, T., Fujita, K., Ando, K. and Sakai, T. (2008), 'Experimental study of graphite ablation in nitrogen flow', *Journal of Thermophysics and Heat Transfer* **22**(3), 382–389.

Suzuki, T., Fujita, K. and Sakai, T. (2010*a*), 'Experimental study of graphite ablation in nitrogen flow, part II: Further numerical analysis', *Journal of Thermophysics and Heat Transfer* **24**(3), 589–597.

Suzuki, T., Fujita, K. and Sakai, T. (2010*b*), 'Graphite nitridation in lower surface temperature regime', *Journal of Thermophysics and Heat Transfer* **24**(1), 212–215.

Suzuki, T., Furudate, M. and Sawada, K. (2002), 'Unified calculation of hypersonic flow-field for a re-entry vehicle', *Journal of Thermophysics and Heat Transfer* **16**(1), 94–100.

Szekely, A., Hanson, R. K. and Bowman, C. T. (1984), 'Shock tube study of the thermal decomposition of cyanogen', *The Journal of Chemical Physics* **80**(10), 4982–4985.

Traidia, A. (2011), Multi-physics modelling and numerical simulation of GTA weld pools, PhD thesis, Ecole Polytechnique.

Tsang, W., Bauer, S. and Cowperthwaite, M. (1962), 'Dissociation energy and rate of decomposition of $C_2N_2$', *The Journal of Chemical Physics* **36**(7), 1768–1775.

Turchi, A., Congedo, P. M. and Magin, T. E. (2017), 'Thermochemical ablation modelling forward uncertainty analysis - part I: Numerical methods and effect of model parameters', *International Journal of Thermal Sciences* **118**, 497–509.

Turns, S. R. et al. (1996), *An Introduction to Combustion, Concepts and Applications*, McGraw-hill New York, Third Edition, pp. 1–24.

Venkatapathy, E. and Reuther, J. (2008), NASA crew exploration vehicle, thermal protection system, lessons learned, Georgia Institute of Technology, pp. 1–38.

Vennik, J., Neely, A. J., Tuttle, S., Choudhury, R. and Buttsworth, D.R. (2017), Reproducing non-uniform surface temperature profiles on hypersonic cruise vehicles in

impulsive wind tunnels, *in* '21st AIAA International Space Planes and Hypersonics Technologies Conference', pp. 2194–2213.

Xiaowei, L., Jean-Charles, R. and Suyuan, Y. (2004), 'Effect of temperature on graphite oxidation behaviour', *Nuclear Engineering and Design* **227**(3), 273–280.

Zander, F., Morgan, R., Sheikh, U., Buttsworth, D. and Teakle, P. (2012), 'Hot-wall re-entry testing in hypersonic impulse facilities', *AIAA Journal* **51**(2), 476–484.

Zeng, M., Liu, J., Xu, D. and Zhang, W. (2014), Numerical study of the transient characteristics of ablative hypersonic flow fields, 10th International Conference on Heat Transfer, Fluid Mechanics and Thermodynamics, pp. 2231–2238.

Zeng, T. and Fu, W. B. (1996), 'The ratio $CO/CO_2$ of oxidation on a burning carbon surface', *Combustion and Flame* **107**(3), 197–210.

Zhen, R. and Stevenson, R.L. (2015), Image demosaicing, *in* 'Colour Image and Video Enhancement', Springer, pp. 13–54.

Zhluktov, S. V. and Abe, T. (1999), 'Viscous shock-layer simulation of airflow past ablating blunt body with carbon surface', *Journal of Thermophysics and Heat Transfer* **13**(1), 50–59.

# Appendix A

# MATLAB Code

A MATLAB code for temperature reference was developed using the wavelength and intensity calibrations as shown in Figure A.1 and Figure A.2. The calibration procedure involves using the manufacturer's data for wavelengths and corresponding emission intensities of the LabSphere to calibrate the actual emissions entering the spectrometer from the LabSphere. Based on the calibrated emissions, a reference temperature was determined which served as a basis for analysing every other experimental signal to produce a measured surface temperature.

```
data = load('HR_Aug10_180810153103_RH.dat');  %output data from
Spectrometer
% CCS175 parameters
npix = 3648;
n = 3;
lam_min =500.8078; %496.92;
dlam = 35/229; %1/6;
lam_max = 1099.05;
lam_CCS = [0:1:npix-1]'*dlam+lam_min;

% LabSphere Calibration data:
lab_sphere_data = [ ...
0.300 5.03e-3
0.310 5.95e-3
0.320 6.25e-3
0.330 9.09e-3
0.340 2.13e-2
0.350 6.30e-2
0.400 2.48e00
0.450 8.26e00
0.500 1.72e+1
0.555 3.05e+1
0.600 4.36e+1
0.655 6.08e+1
0.700 7.49e+1
0.800 1.02e+2
0.900 1.16e+2
1.050 1.25e+2
1.150 1.24e+2
1.200 1.21e+2
1.300 1.15e+2
1.540 8.91e+1
1.600 8.41e+1
1.700 6.94e+1
2.000 3.43e+1
2.100 1.84e+1
2.300 1.73e+1
2.400 1.13e+1];
lam_LS = lab_sphere_data(:,1);
I_LS = lab_sphere_data(:,2);
I_LS_cal = interp1(lam_LS*1e3,I_LS,lam_CCS,'spline');

cal = load('Aug09_180809171956_C01.dat'); %calibration file from
LabSphere
cal_dark = load('T_RM_180604112321_dark.dat'); %dark file from
background

[aa,bb] = size(cal);
for i=5:aa-5
  int_time_cal = cal(i,2);
  W_CCS(i-4,:) = cal(i,n:npix+n-1)./int_time_cal;
end

[cc,dd] = size(cal_dark);
for i=5:cc-5
  int_time_dark = cal_dark(i,2);
```

Figure A.1: Building the MATLAB code for temperature reference.

```
  W_CCS_dark(i-4,:) = cal_dark(i,n:npix+n-1)./int_time_dark;
end

W_CCS_cal =mean(W_CCS)'-mean(W_CCS_dark)';

figure(1)
plot(lam_CCS,I_LS_cal,'o',lam_CCS,W_CCS_cal);
cal_vector = I_LS_cal./W_CCS_cal;  % reversion factor rised by optical
transmission coefficient

figure(2)
plot(lam_CCS,cal_vector,'m');

% temperature calculation by fitting measured radiation to Plank curve
[nt,dummy] = size(data);
exp_time = data(:,2);

%the process of output-time recorded by Spectrometer
measurement(Labview). The start of temperature trace is set from 0s
corresponding to the first record
toffset = fix(data(1,1)/100)*100;
time = data(:,1)-toffset;
nfind = find(time > 100);
time(nfind) = fix(time(nfind)/100)*60 + (time(nfind) -100);
time = time -time(1);

W_CCS_run = zeros(nt,npix);
I_CCS_run = W_CCS_run;
N = [1:3300]';
NN = find((lam_CCS > 650)&(lam_CCS < 930));

figure(3)
for i = 1:nt, % 1:nt,
   W_CCS_run(i,:) = data(i,n:npix+n-1)/exp_time(i);
   I_CCS_run(i,:) = W_CCS_run(i,:).*cal_vector';
   lambda = lam_CCS(NN);
   I_meas = I_CCS_run(i,NN)';
   T_est = [1000:1:3000]';
   r = planck_fit(lambda,I_meas,T_est);
   [val,ifind] = max(real(r));
   T(i) = T_est(ifind);
   title([num2str(T(i)),'  ',int2str(i)])
   i
end

figure(4)
plot(time,T, 'r', 'LineWidth', 4);
title('Temperature profile showing the time of heating and run');
grid on;
legend('HR_Aug10_180810153103_RH');
xlabel('Heating time, (s)');
ylabel('Temperature (K)');
set(gca,'FontSize', 14);
% xlim([15 16.5]);
% ylim([2400 2560]);
```

Figure A.2: MATLAB code continuation.

# Appendix B

# Measuring Arm

The Romer Multi-Gauge 6 Axis Coordinate Measuring Arm (Part Number: NCA7-05-16186) was used in the present work measurement as shown in Figure B.1. The measuring arm can achieve accuracies of up to 0.005mm. The power supply and computer interface are built into the base of the Multi-Gauge. The operator holds the arm at the joint marked F, with their fingers positioned on the buttons at (7), to activate the position recording input. Measurements are obtained by bringing the probe (8) into contact with the disc at various positions and data is saved by a button click. The measurements are recorded in 3D spatial orientation relative to a previously set coordinate system origin.

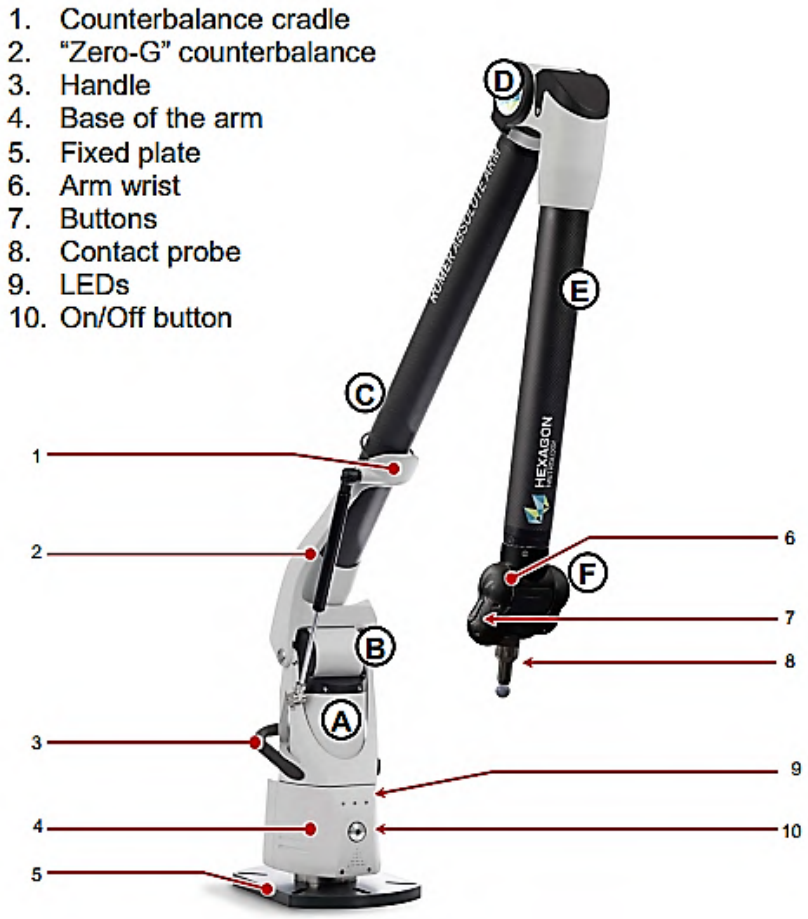


Figure B.1: Romer Multi-Gage Coordinate Measuring Arm. A and B represent the shoulder, C and D represent the elbow, E and F represent the wrist (González-Madruga et al., 2013).

# Appendix C

# The Experimental Probe

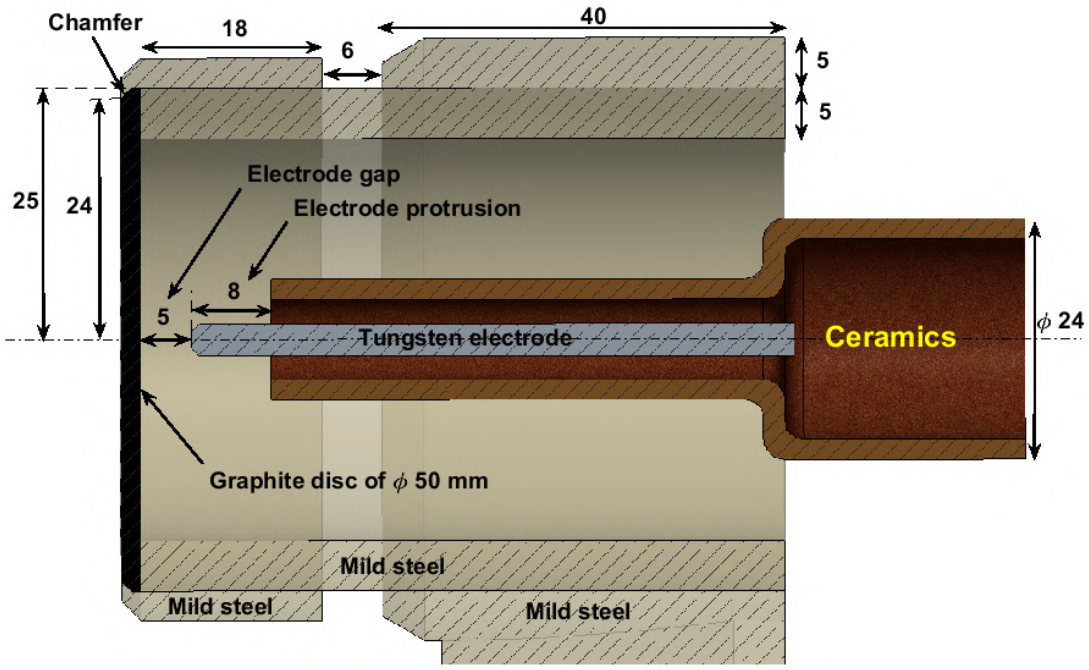


Figure C.1: The probe model for the present work. All dimensions in millimetres.

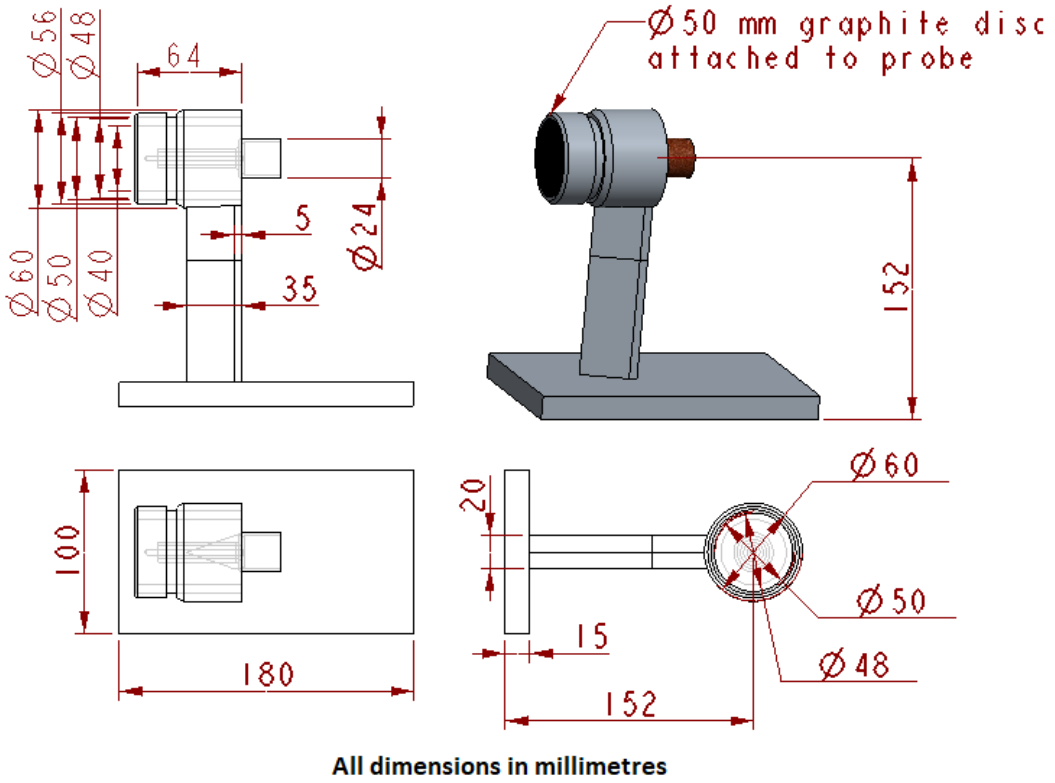


Figure C.2: Conceptual design (orthogonal drawing) of the experimental probe with a 50 mm diameter carbon disc.

# Appendix D

# Setting up the Schlieren Imaging

The working principle of the Schlieren imaging technique is based on changing fuid density. Presented here are details of the high speed imaging and the processing techniques used in the present work. Figure D.1 shows the high speed camera used for the visual imaging.

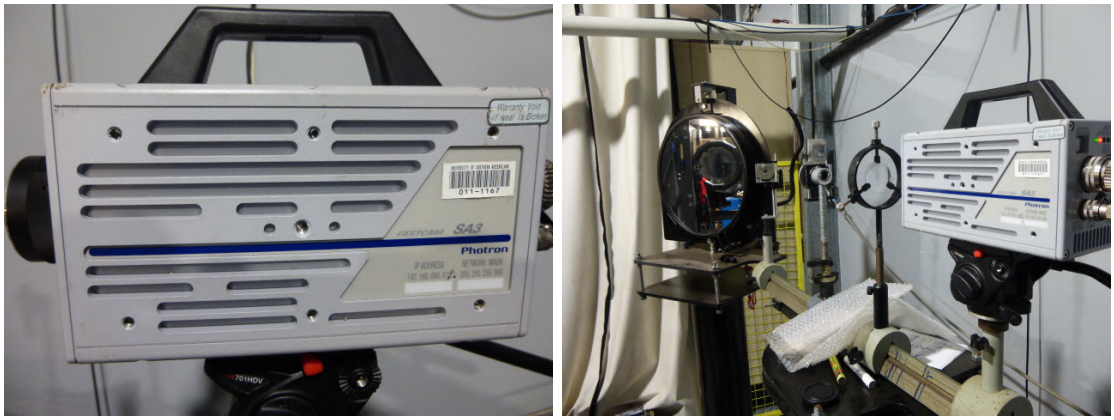


(a) High speed camera (HSC) set to 2000 fps. (b) The HSC looking through the knief edge.

Figure D.1: All signals from Schlieren imaging were connected to the Data Acquisition (DAQ) system, where all data were extracted for further analysis.

Figure D.2 shows the set-up for the Schlieren imaging. The high speed camera was pointing through the knife edge, and the information was extracted through the DAQ system.

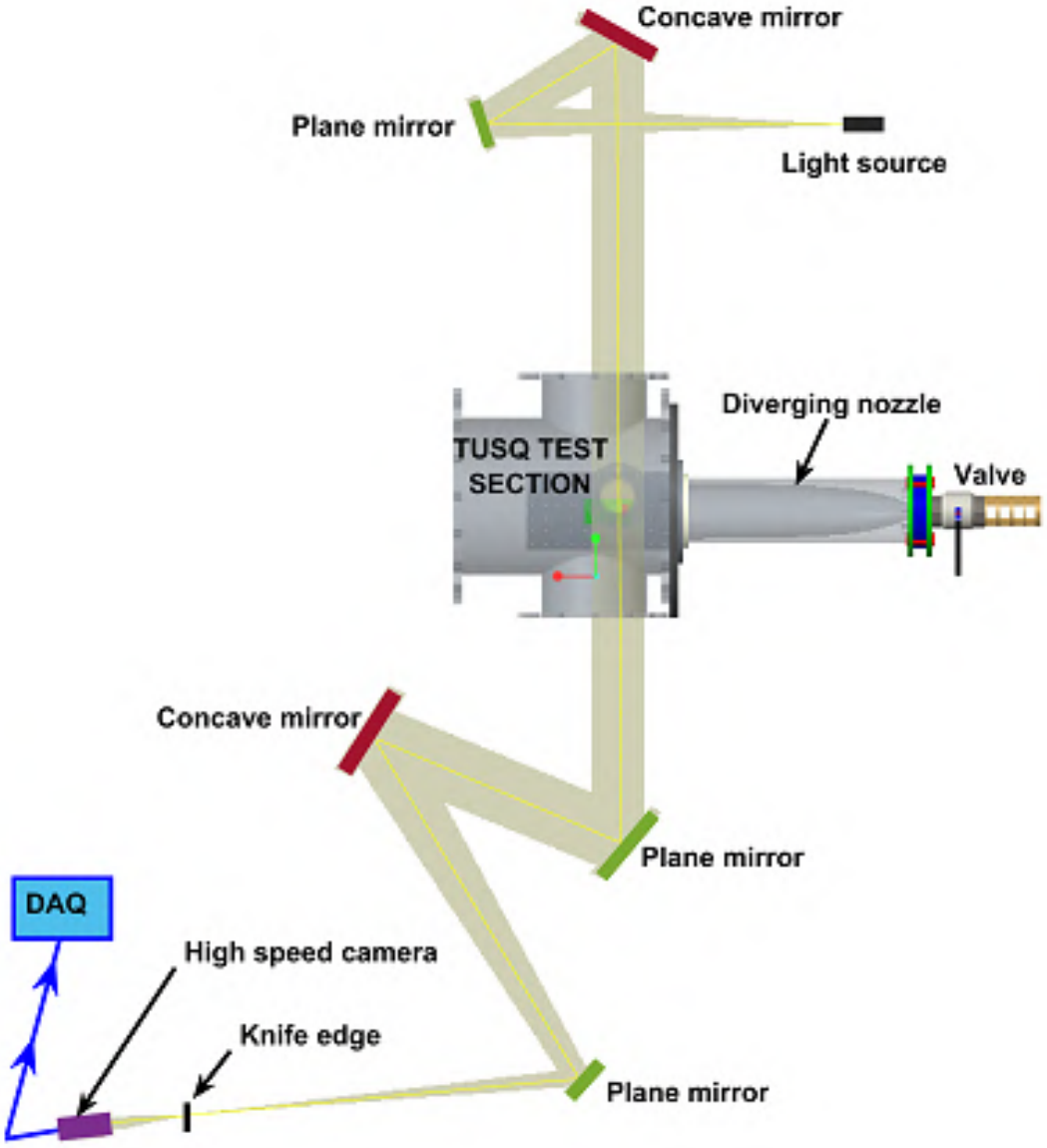


Figure D.2: The Schlieren imaging technique used in the present work.

The high speed video was captured during most of the tests conducted using the Schlieren imaging and the high speed camera. This gave some additional insights about the qualitative analysis of the flow fields as shown in Figure D.3, Figure D.4, and Figure D.5.


(a) Valve opening.

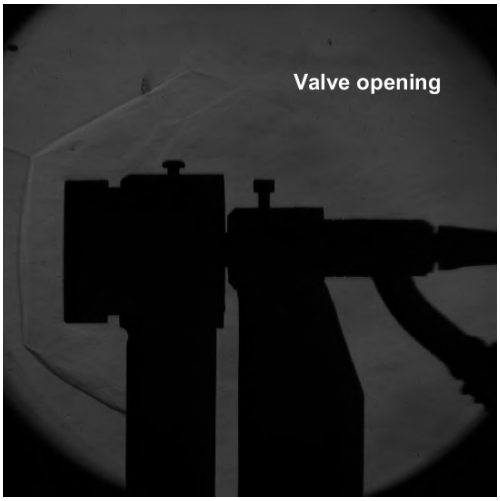


(b) Valve opening.

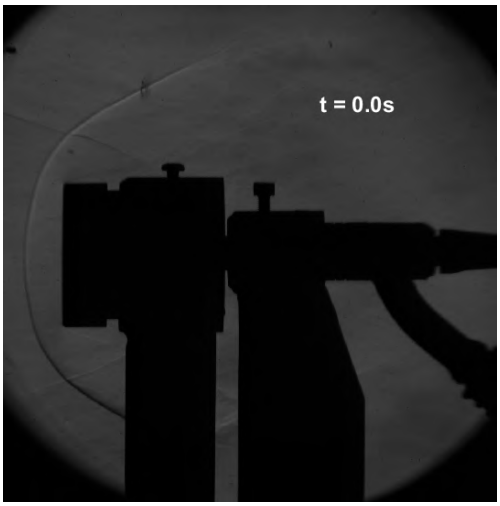


(c) time = 0.0 seconds.

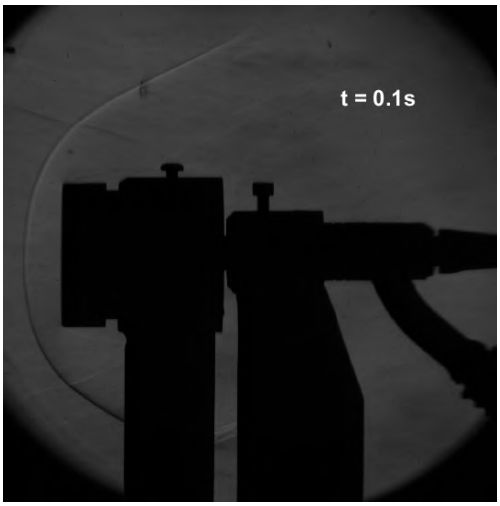


(d) time = 0.1 seconds.

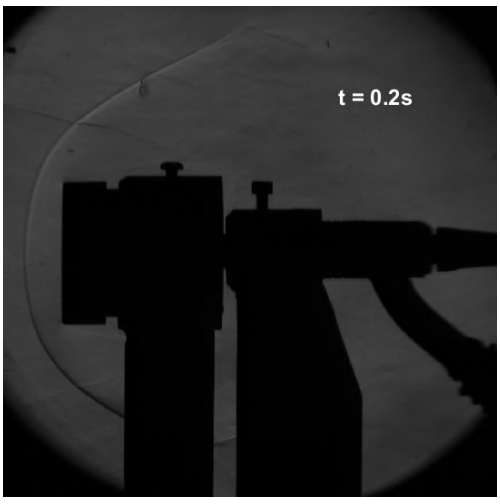


(e) time = 0.2 seconds.

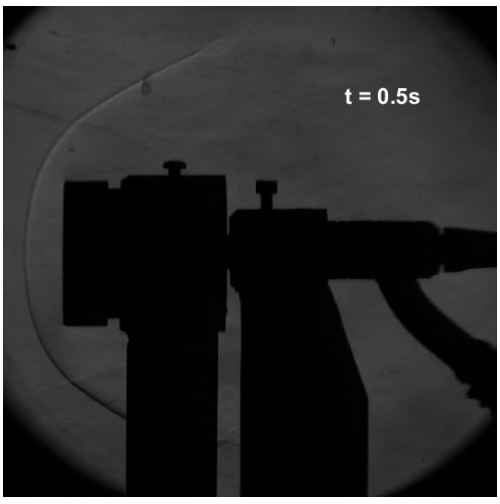


(f) time = 0.5 seconds.

Figure D.3: Schlieren imaging from the high speed camera for flow-only run.

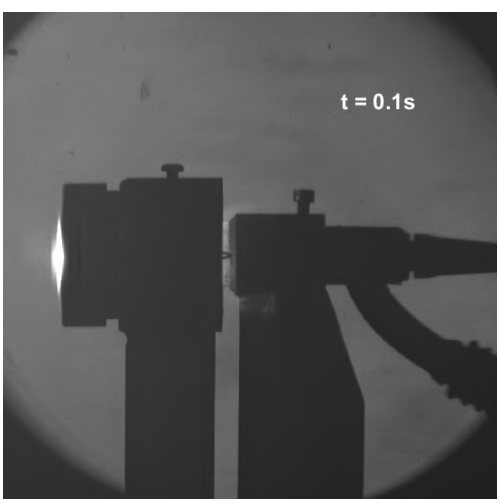


(a) time = 0.1 seconds.

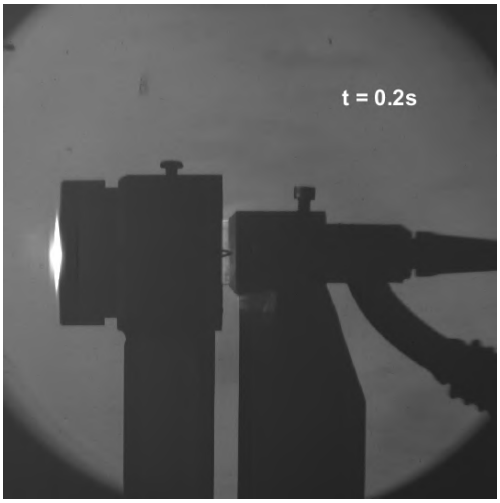


(b) time = 0.2 seconds.

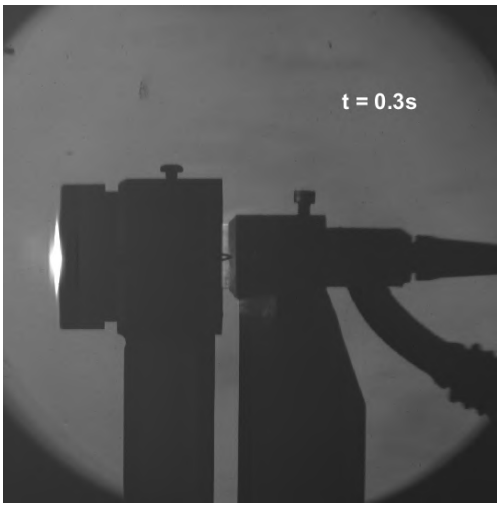


(c) time = 0.3 seconds.

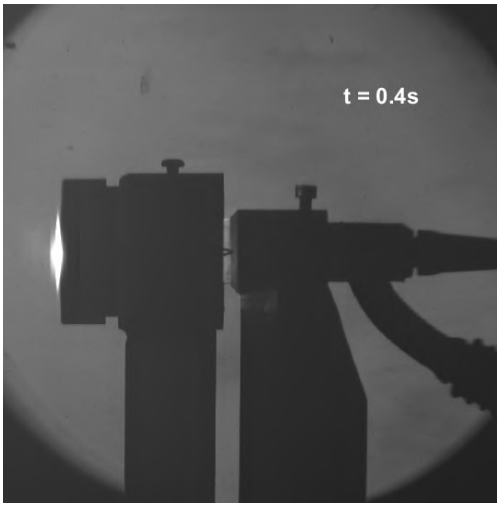


(d) time = 0.4 seconds.

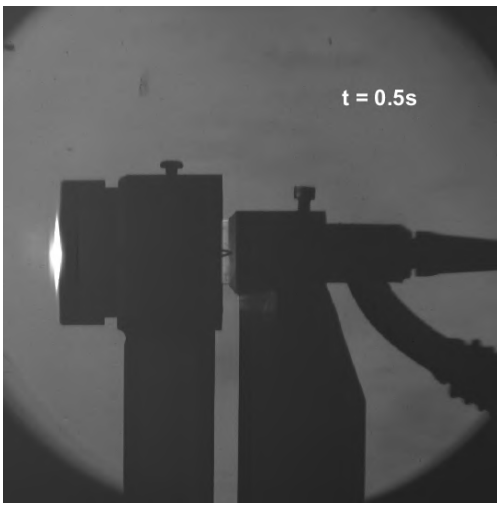


(e) time = 0.5 seconds.

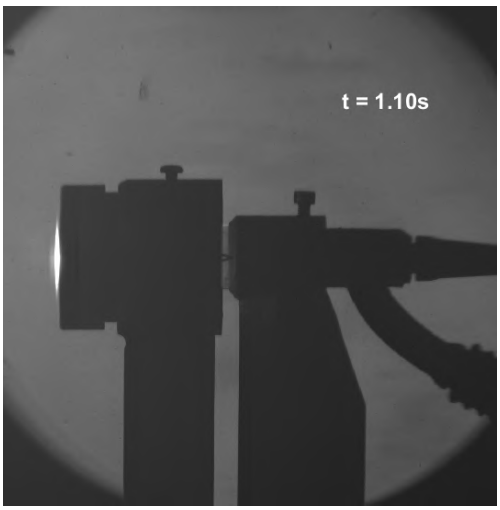


(f) time = 1.10 seconds.

Figure D.4: Schlieren imaging from the high speed camera for heated-only run.


(a) Valve opening.

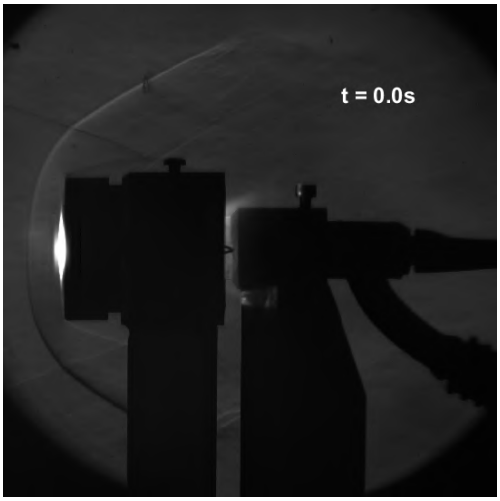


(b) time = 0.0 seconds.

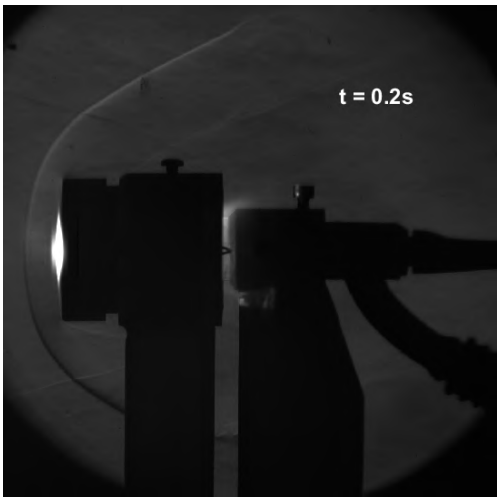


(c) time = 0.2 seconds.

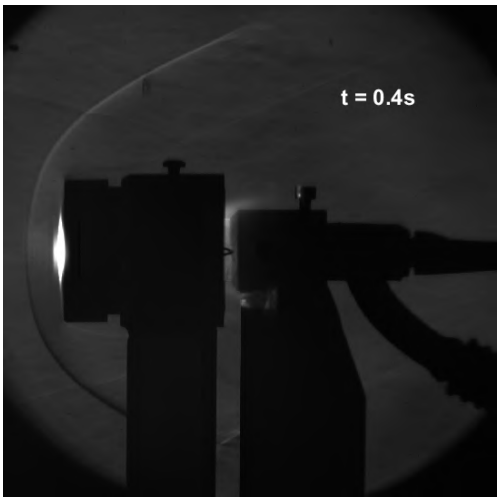


(d) time = 0.4 seconds.

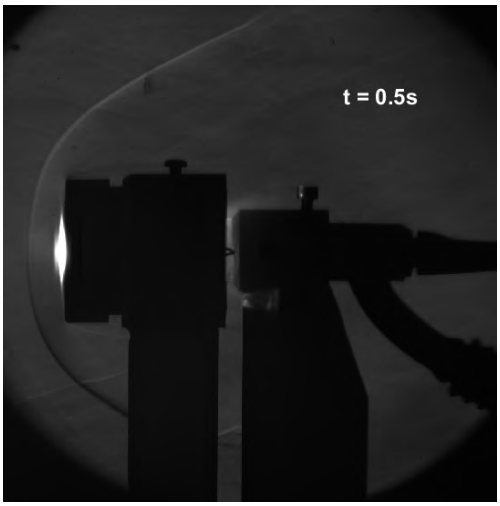


(e) time = 0.5 seconds.


(f) time = 0.53 seconds.

Figure D.5: Schlieren imaging from the high speed camera for heated-with-flow run.

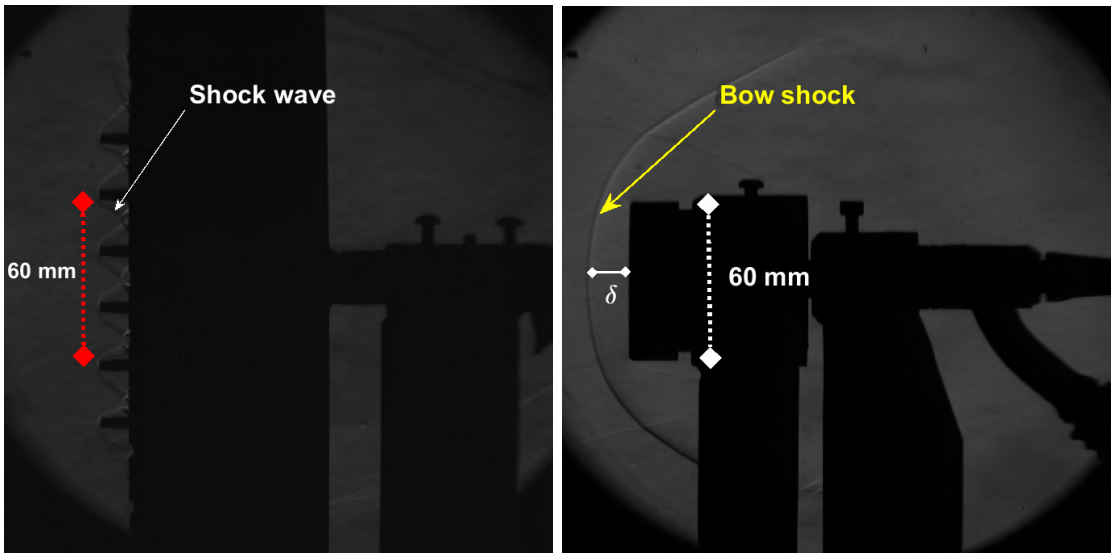


(a) Pressure survey array at Mach 4.5.

(b) Flow-only at Mach 4.5.

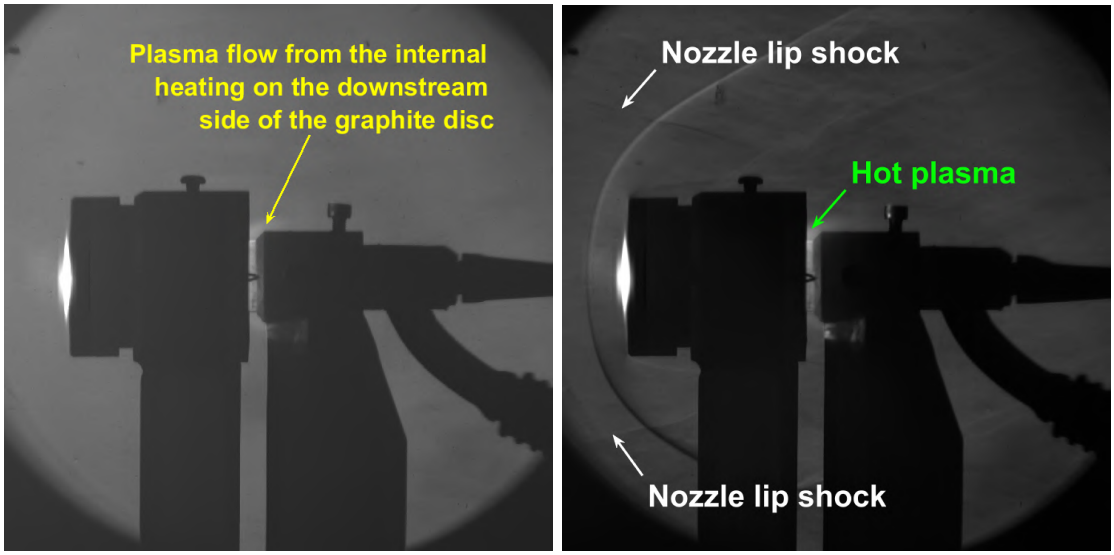


(c) Heated-only.

(d) Heated-with-flow at Mach 4.5.

Figure D.6: High speed camera Schlieren images taken from Mach 4.5 flows at TUSQ, showing typical characteristics of Schlieren high speed video images for the three flowing cases and a frame for the heated-only case at about the time flow would normally be started.

# Appendix E

# Scanning Electron Microscope

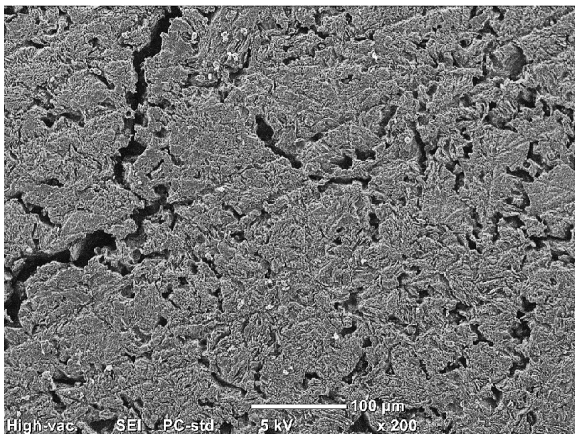


(a) In the proximity of point A

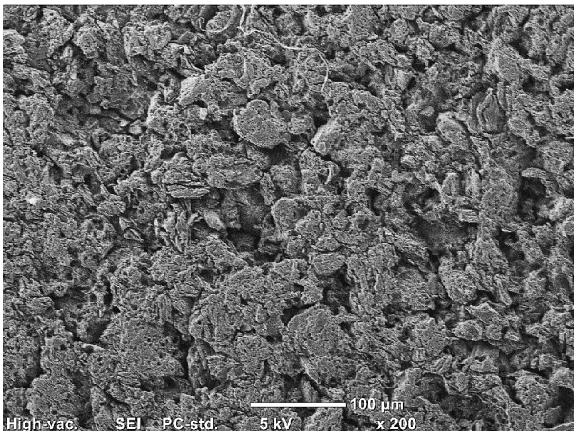


(b) In the proximity of point C

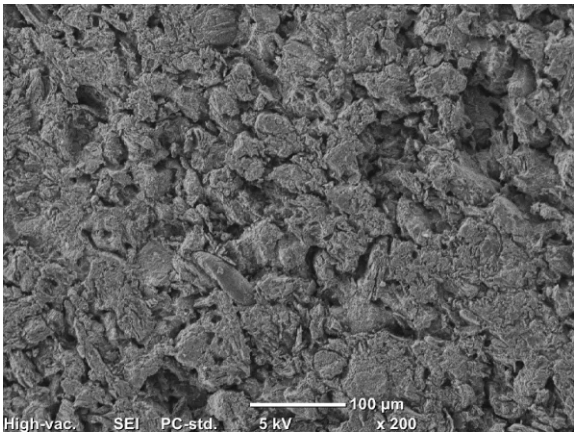


(c) In the proximity of point E

Figure E.1: SEM images after the second heated-with-flow run in the proximity of three points A, C, and E.

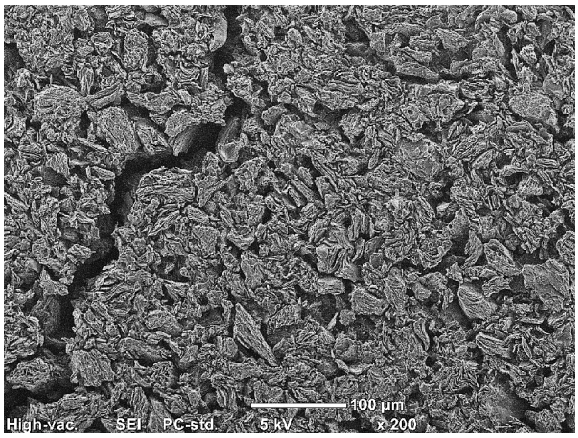


(a) In the proximity of point A

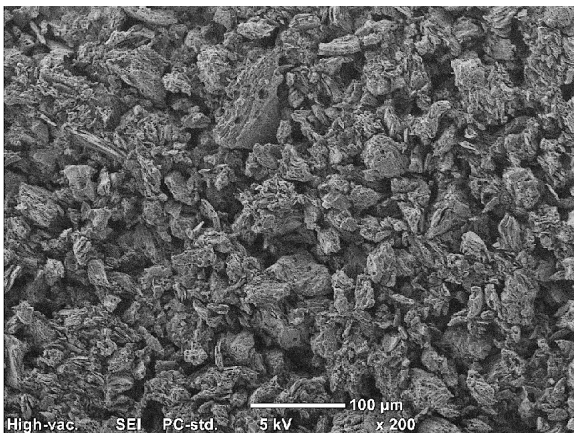


(b) In the proximity of point C

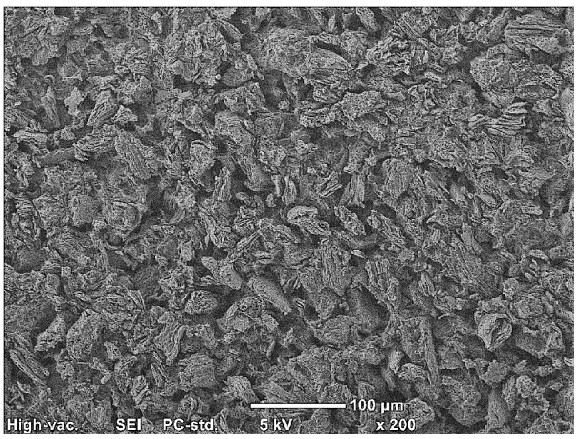


(c) In the proximity of point E

Figure E.2: SEM images after the fourth heated-with-flow run in the proximity of three points A, C, and E.

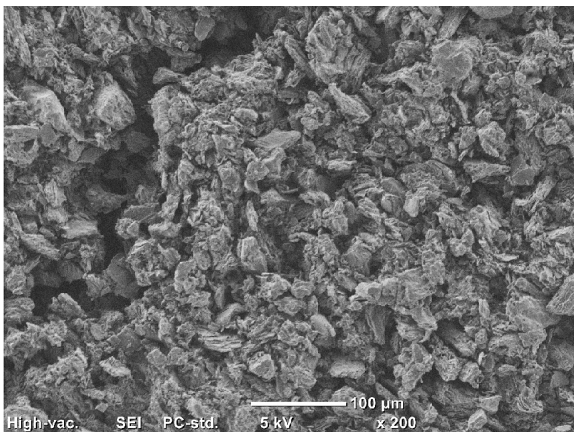


(a) In the proximity of point A

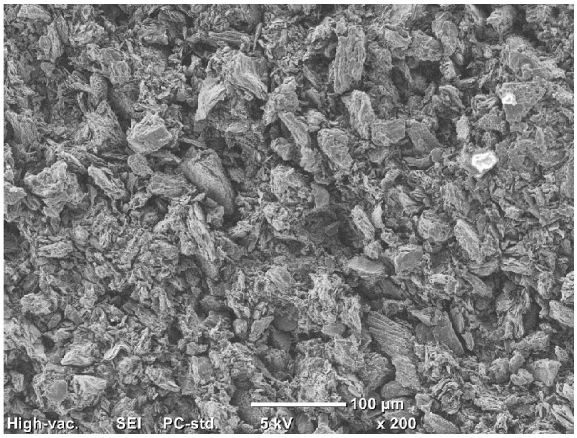


(b) In the proximity of point B

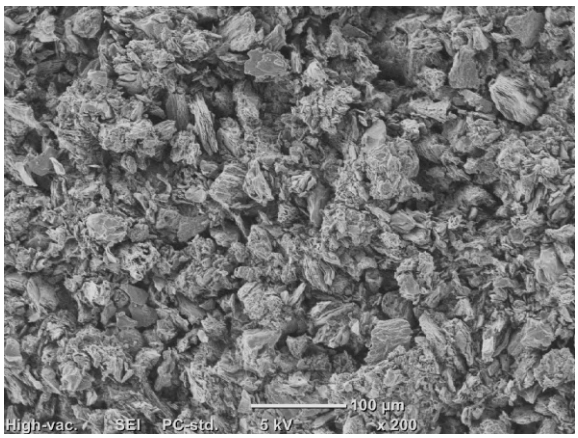


(c) In the proximity of point C

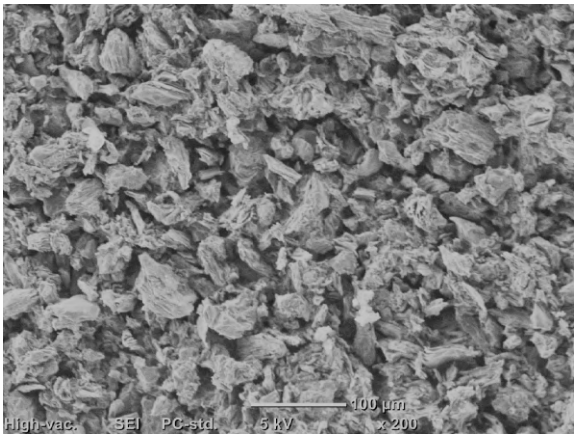


(d) In the proximity of point D

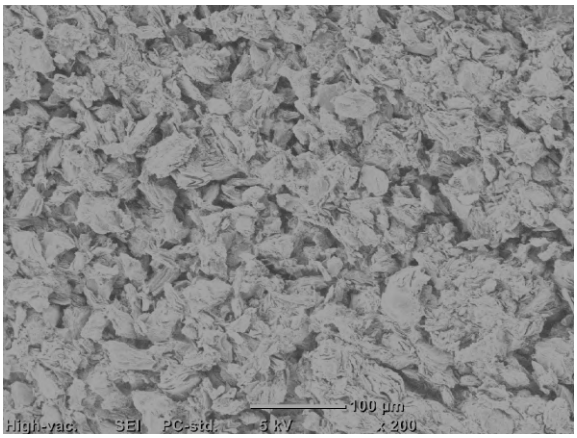


(e) In the proximity of point E

Figure E.3: SEM images after the eighth heated-with-flow run in the proximity of five points A, B, C, D, and E. Substantial surface deterioration is evident. Edges of the crack near the stagnation point show significant deterioration.

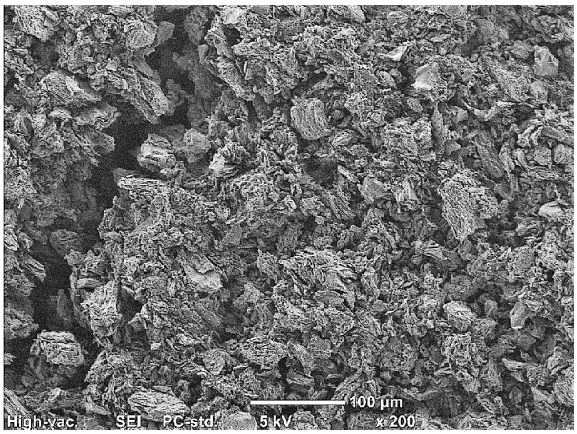


(a) In the proximity of point A

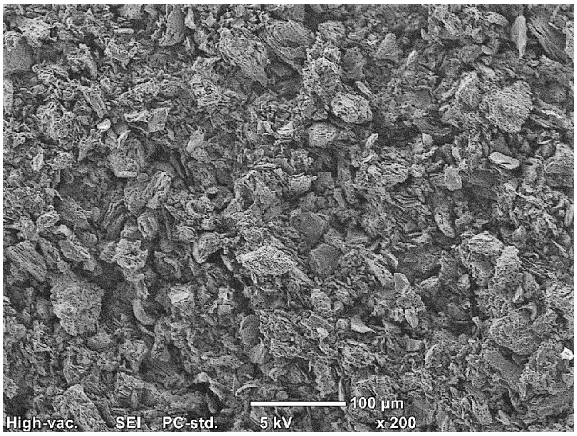


(b) In the proximity of point B

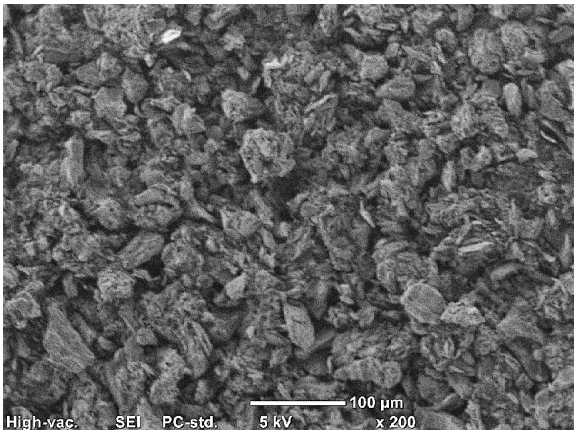


(c) In the proximity of point C

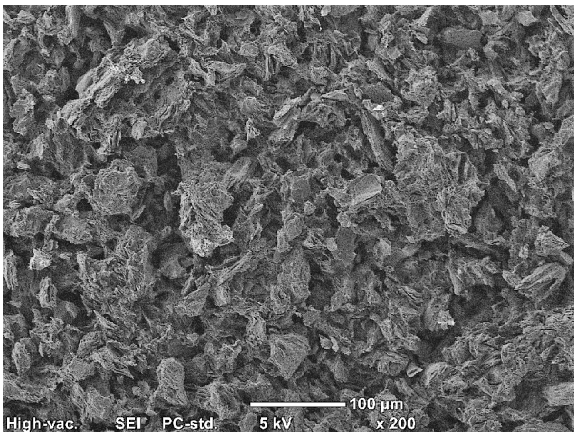


(d) In the proximity of point D

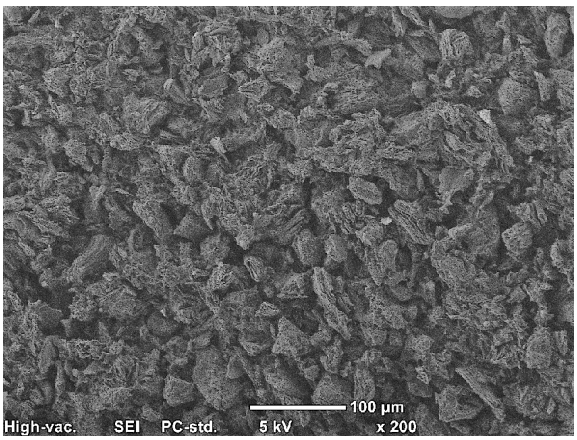


(e) In the proximity of point E

Figure E.4: SEM images after the 12th heated-with-flow run in the proximity of five points A, B, C, D, and E.

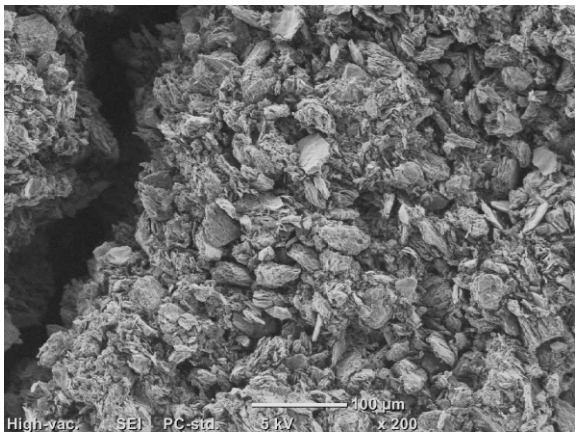


(a) In the proximity of point A

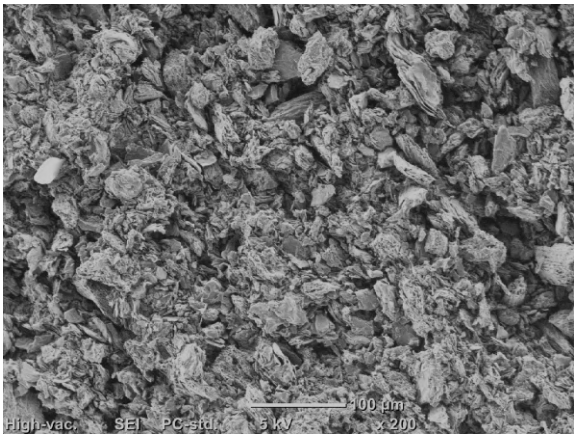


(b) In the proximity of point B

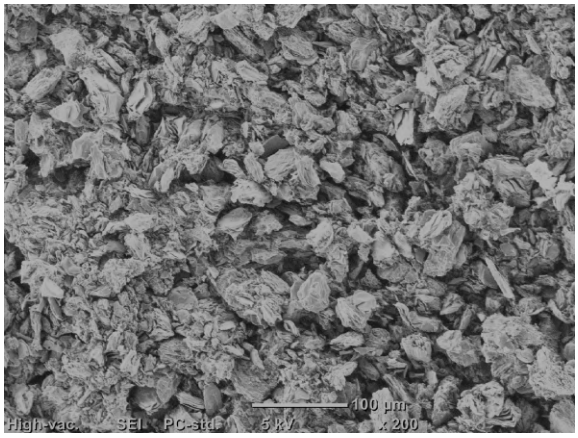


(c) In the proximity of point C

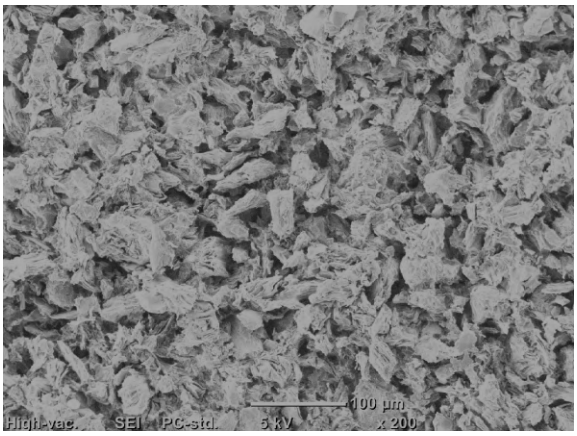


(d) In the proximity of point D

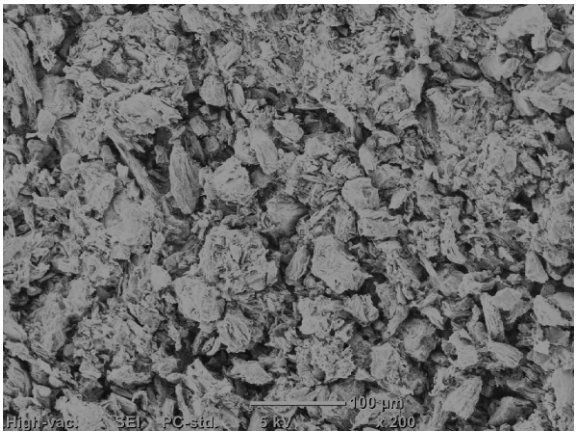


(e) In the proximity of point E

Figure E.5: SEM images after the 16th heated-with-flow run in the proximity of five points A, B, C, D, and E.

## E.1 Back Surfaces

The images in Figure E.6 show the SEM results at the back of the carbon disc after the twelfth heated-with-flow run. Exposure to the plasma has an effect on the surface texture, but the difference between these images and the images of the side exposed to the flow is significant. The edges of the crack on the back of the disc seem relatively sharp, in combination with no sign of a crack at the back after 12 runs, suggests that the crack formed suddenly on cooling after the sixteenth run.


(a) In the proximity of point A

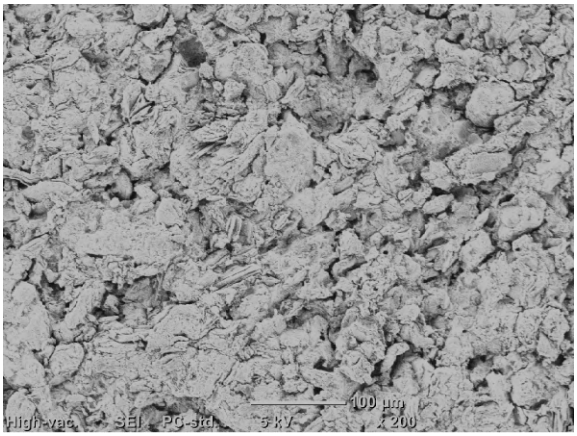


(b) In the proximity of point B

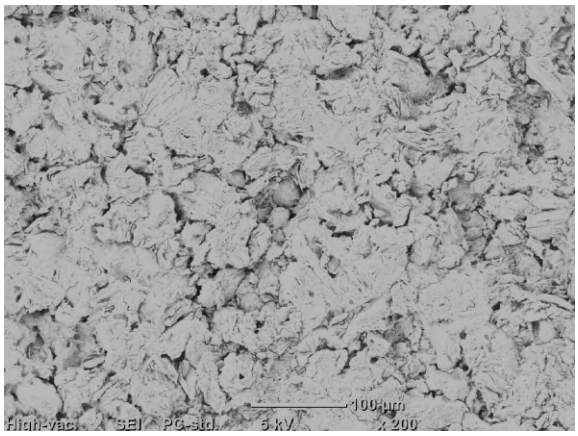


(c) In the proximity of point C

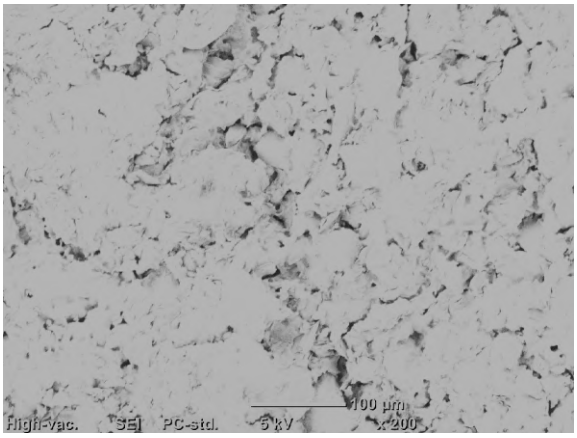


(d) In the proximity of point D

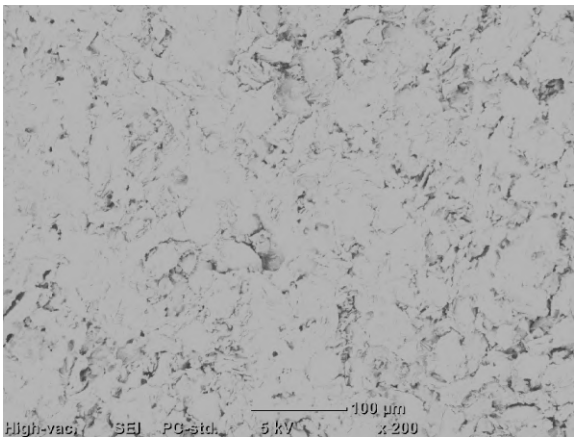


(e) In the proximity of point E

Figure E.6: SEM images (on the back of the disc) after twelfth heated-with-flow run at five points A, B, C, D, and E.

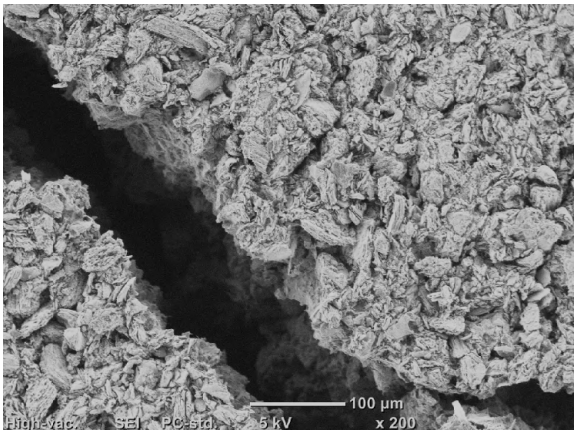


(a) In the proximity of point A

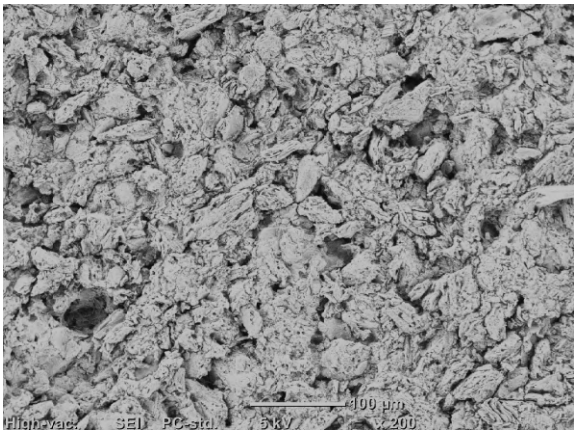


(b) In the proximity of point B

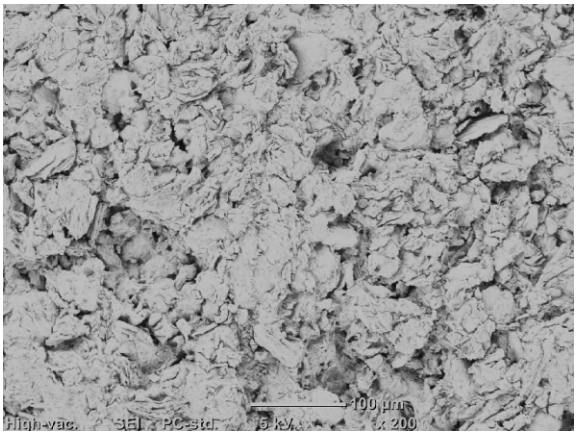


(c) In the proximity of point C

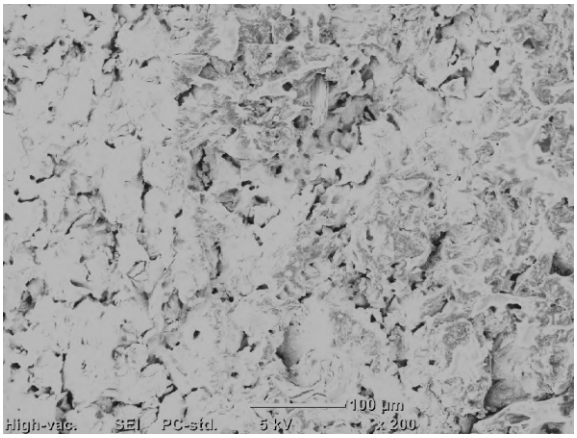


(d) In the proximity of point D

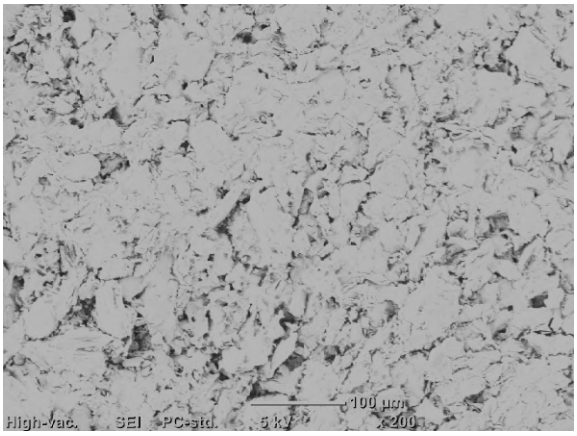


(e) In the proximity of point E

Figure E.7: SEM images (on the back of the disc) after 16th heated-with-flow run at five points A, B, C, D, and E.